ENGINEERING OF PHOTONIC STRUCTURES BASED ON NANOPOROUS ANODIC ALUMINA AS AN OPTICAL SENSING PLATFORM

Laura Karen Acosta Capilla

UNIVERSITAT ROVIRA I VIRGILI
ENGINEERING OF PHOTONIC STRUCTURES BASED ON NANOPOROUS ANODIC ALUMINA AS AN OPTICAL SENSING PLATFORM
Laura Karen Acosta Capilla

UNIVERSITAT ROVIRA I VIRGILI
ENGINEERING OF PHOTONIC STRUCTURES BASED ON NANOPOROUS ANODIC ALUMINA AS AN OPTICAL SENSING PLATFORM
Laura Karen Acosta Capilla

Laura Karen Acosta Capilla

ENGINEERING OF PHOTONIC STRUCTURES BASED ON NANOPOROUS ANODIC ALUMINA AS AN OPTICAL SENSING PLATFORM

Ph.D Thesis

Supervised by:

Prof. Lluís F. Marsal Garví

Departament D'Enginyeria Electrònica Elèctrica i Automàtica

Nanoelectronic and Photonic Systems (NePhoS)

UNIVERSITAT ROVIRA i VIRGILI

Tarragona 2021

UNIVERSITAT ROVIRA I VIRGILI
ENGINEERING OF PHOTONIC STRUCTURES BASED ON NANOPOROUS ANODIC ALUMINA AS AN OPTICAL SENSING PLATFORM
Laura Karen Acosta Capilla

UNIVERSITAT ROVIRA I VIRGILI

Departament d'Enginyeria Electrònica, Elèctrica i Automàtica

Escola Tècnica Superior D'Enginyeria

Campus Sescelades

Avinguda dels Països Catalans, 26

43007 Tarragona

España

Tel. 977 55 96 10

Fax 977 55 96 05

I, Lluís Francesc Marsal Garví state that the present study, entitled "ENGINEERING OF PHOTONIC STRUCTURES BASED ON NANOPOROUS ANODIC ALUMINA AS AN OPTICAL SENSING PLATFORM ", presented by Laura Karen Acosta Capilla for the award of the degree of Doctor, has been carried out under my supervision at the Department of Electronic, Electric and Automatic Control Engineering of this university and that it satisfies all requirements to be eligible for the International Doctorate Award.

Tarragona, June 18th, 2021

Doctoral Thesis Supervisor

Lluís Francesc Marsal Garví

UNIVERSITAT ROVIRA I VIRGILI
ENGINEERING OF PHOTONIC STRUCTURES BASED ON NANOPOROUS ANODIC ALUMINA AS AN OPTICAL SENSING PLATFORM
Laura Karen Acosta Capilla

Acknowledgments

La realización de esta tesis ha sido un camino lleno de aprendizaje, trabajo en equipo, esfuerzo y dedicación que no hubiera sido posible sin la ayuda y apoyo de muchas personas, es por ello, que me gustaría tomarme un pequeño momento para agradecerles por estar conmigo durante todo este tiempo.

En primer lugar, quiero agradecer a mi director de tesis, Prof. Lluis Marsal, por confiar y darme la oportunidad de realizar esta tesis. Muchas gracias por todo su apoyo, comprensión, pero sobre todo por guiarme y darme consejos durante todo este camino. ¡Gracias!

Al Dr. Josep Ferré Borrull, por su ayuda, consejos y colaboración en todos los momentos que los he necesitado. Aprecio mucho todos los comentarios que me ha hecho siempre. ¡Muchas gracias!

Me gustaría agradecer al Dr. Abel Santos por todo su apoyo durante la realización de esta tesis, por dejarme colaborar con él todo este tiempo. ¡He aprendido mucho! Muchas gracias por darme la oportunidad de visitar y trabajar contigo en la Universidad de Adelaida durante el tiempo que la pandemia lo permitió jejeje.

A la Dra. Elisabet Xifré por brindarme su ayuda siempre que lo necesité y ayudarme desde el inicio con cualquier problema que tuve. ¡Muchas gracias, Eli!

Quisiera agradecer a la Dra. Pilar Formentín por su ayuda, apoyo y amistad. Gracias por ayudarme en todo lo que he necesitado.

Quiero agradecer a todos los miembros del grupo NePhos con los que he podido convivir durante este tiempo: Pilar, José, Bea, Laura, Pili, Francesc, Chris, Aurelien, Victor, Pankaj, Jakub, Alfonsina, Anand, Enas, Alejandro, Josep Maria: thank you very much for all these days that we spend in the lab working hard, but specially for all the fun days that we share.

Quiero agradecer a mis amigas Laura y Pili por su amistad y complicidad durante todo este tiempo. Gracias por todos los momentos que

compartimos en el laboratorio, conferencias, café, playa, pero sobre todo por su apoyo durante este tiempo.

También me gustaría agradecer a mis amigos Carlos y Maricarmen por todo este tiempo que hemos compartido juntos, gracias por su amistad y apoyo. ¡Moltes Graciès!

Quiero agradacer a mis grandes amigos: Harold, Lindsay, Javier, Gloria y al pequeño Oliver por ayudarme y compartir conmigo grandes momentos más que amigos somos una Familia.

Especialmente me gustaría agradecer a mi José, sin su apoyo nada de esto hubiera sido posible. Muchas gracias por ayudarme y acompañarme en todo este proceso, por no dejar que me rindiera y tirara la toalla cuando más desesperación sentía. Gracias por nunca soltar mi mano. ¡Te amo!

A mi bebé Damián que me ha dado la fortaleza y el impulso para finalizar todo este camino y seguir adelante. Gracias por ser la luz de mis días.

A mis padres, Paty y Jesús por su amor incondicional, por creer en mí y apoyarme en todo. Porque gracias a ustedes me he convertido en la persona que soy. A mis hermanas y hermanos Lili, Toño, Eri y Fer por apoyarme siempre en todo lo que he necesitado y siempre estar ahí para mí. A mis queridos sobrinos: Ana Pau, Diego, Elisa, Olivia, Jesús, Valentín, Kamilah y Carmelita.

Muchas gracias a toda mi familia que desde México ha estado al pendiente de mí y me han apoyado: Mi Abuelita Coco, Mis tíos Pepe, Enrique, Ramón a mi prima Ceci. A la familia Sánchez López y López Zavala.

Gracias a todas aquellas personas que a pesar de la distancia han estado apoyándome y alentándome a seguir adelante.

This work was supported by:

FPI grant BES-2016-077811 from the Ministerio de Ciencia e innovación TEC 2015 71324-R and RTI2018-094040-B-I00.

List of Contributions

Journal Articles

1. Eckstein, C.; **Acosta, L. K**.; Pol, L.; Xifré-Pérez, E.; Pallares, J.; Ferré-Borrull, J.; Marsal, L. F. "Nanoporous Anodic Alumina Surface Modification by Electrostatic, Covalent, and Immune Complexation Binding Investigated by Capillary Filling." *ACS Applied Materials and Interfaces.* **2018**, 10 (12), 10571–10579.
2. **Laura K Acosta**, Francesc Bertó-Roselló , Elisabet Xifre-Perez, Abel Santos, Josep Ferré-Borrull and Lluis F. Marsal. "Stacked nanoporous anodic alumina gradient-index filters with tunable multi-spectral photonic stopbands as sensing platforms". *ACS Applied Material and interfaces* **2019,** 11, 3360-3371.
3. Laura Pol, Chris Eckstein, **Laura K. Acosta**, Elisabet Xifré-Pérez, Josep Ferré-Borrull and Lluis F. Marsal. "Real-Time Monitoring of Biotinylated Molecules Detection Dynamics in Nanoporous Anodic Alumina for Bio-Sensing". *Nanomaterials*, **2019**, 9 (3), 478.
4. Laura Pol, **Laura K. Acosta,** Josep Ferré-Borrull and Lluis F. Marsal. "Aptamer-Based Nanoporous Anodic Alumina Interferometric Biosensor for Real-Time Thrombin Detection". *Sensors*. **2019**. 19 (20), 4553.
5. **Laura K Acosta**, Francesc Bertó-Roselló, Elisabet Xifre-Perez, Cheryl Suwen Law, Abel Santos, Josep Ferré-Borrull and Lluis F. Marsal. "Tunable Nanoporous Anodic Alumina Photonic Crystals by Gaussian Pulse Anodization". *ACS Applied Materials & Interfaces*. **2020**, 12 (17). 19778-19787

6. Lluis F. Marsal, **Laura K. Acosta**, Josep Ferrè-Borrull. “Recent Advances in Structural Engineering of Nanoporous Anodic Alumina and Applications”. *ECS Transactions*. **2020**. 98 (2). 3-11
7. Siew Yee Lim, Cheryl Suwen Law, Lin Jiang, **Laura K Acosta,** Akash Bachhuka, Lluís F Marsal, Andrew D Abell, Abel Santos. “Enhancing Forbidden Light Propagation in Nanoporous Anodic Alumina Gradient-Index Filters by Alcohol Additives”. *ACS Applied Nanomaterials*. **2020**. 3 (12). 12115-12129
8. Lina Liu, Siew Yee Lim, Cheryl Suwen Law, **Laura K Acosta**, Bo Jin, Andrew D. Abell, Lluis F Marsal, Gang Ni, Abel Santos. “Optical engineering of nanoporous photonic crystals by Gaussian-Like pulse anodization”. *Microporous and Mesoporous Materials*. **2021.** 312. 110770
9. Pankaj Kapruwan, **Laura K. Acosta**, Josep Ferre-Borrull, Lluis F. Marsal. “Optical platform to analyze a model drug loading and releasing profile based on Nanoporous Anodic Alumina Gradient Index Filters”. *Nanomaterials **2021**, 11, 730.*
10. **Laura K Acosta**, Cheryl Suwen Law, Siew Yee Lim, Andrew Abell, Lluis F. Marsal and Abel Santos. "Role of Spectral Resonance Features and Surface Chemistry in Optical Sensitivity of Light-Confining Nanoporous Photonic Crystals". *ACS Applied Materials and Interfaces.* **2021**, 13,12, 14394–14406.
11. **Laura K Acosta**, Cheryl Suwen Law, Abel Santos, Josep Ferré-Borrull and Lluis F. Marsal. “Tuning Intrinsic Photoluminescence from Light-Emitting Multispectral Nanoporous Anodic Alumina Photonic Crystals”. *Submitted*

Conference Contributions

1. **Nanospain 2017.** Design and fabrication of photonic bands in nanoporous anodic alumina based rugate structures. **Laura K. Acosta** Capilla, Elisabet Xifré-Perez, Josep Ferré-Borrull, Lluis F. Marsal. *Poster*
2. **Nanospain 2017.** Surface modification of Nanoporous Alumina towards bio-sensing applications in optical nano-fluidic system. L. Pol, **L. K. Acosta**, J. Ferré-Borrull, E. Xifre-Pérez, L. F. Marsal. *Poster*
3. **NanoBio&Med 2017.** Stacked periodic nanoporous anodic alumina structures for sensing applications. **Laura K. Acosta** Capilla, Elisabet Xifré-Perez, Josep Ferré-Borrull, Lluis F. Marsal. *Poster*
4. **NanoBio&Med 2017.** Interferometric real time monitoring Streptavidin bioconjugation in Nanoporous Anodic Alumina. L. Pol, **L. K. Acosta,** J. Ferré-Borrull, L. F. Marsal. *Poster*
5. **Porous Semiconductures Science and Technology conference (PSST) 2018**. Nanostructured sensing platform based on multiple periodic structures of nanoporous anodic alumina. **Laura K. Acosta** Capilla, Elisabet Xifré-Perez, Josep Ferré-Borrull, Lluis F. Marsal. *Oral presentation*.
6. **Porous Semiconductures Science and Technology conference (PSST) 2018**. Numerical Modelling and Characterization of Nanoporous Anodic Alumina Rugate Filters. Francesc Bertó-Roselló, **Laura K. Acosta Capilla**, Elisabet Xifré-Perez, Josep Ferré-Borrull, Lluis F. Marsal. *Poster*

7. **Porous Semiconductures Science and Technology conference (PSST) 2018.** Influence of incubation time on the surface modification of nanoporous anodic alumina studied by fluid imbibition-coupled laser interferometry. C. Eckstein, l. Pol-Aira, **L. K. Acosta-Capilla**, E. Xifré-Pérez, J. FerréBorrull*. Oral Presentation*
8. **Porous Semiconductures Science and Technology conference (PSST) 2018.** Engineering and analysis of graded-index photonic nanostructures based on mesoporous anodic alumina. E. Xifré-Pérez, **L. K. acosta**, J. Ferre-Borrull, and L. F. Marsal. **Poster**
9. **Porous Semiconductures Science and Technology conference (PSST) 2018.** Interferometric real-time monitoring of streptavidin-biotin conjugation in nanoporous anodic alumina**.** L. Pol, **L. K. Acosta**, J. Ferré-Borrull, E. Xifre-Pérez, L. F. Marsal. *Poster*
10. **Reunion Nacional de óptica (RNO) 2018.** Nanoporous anodic alumina rugate filters for optical biosensing. **Laura K. Acosta Capilla**, Francesc Bertó-Roselló, Elisabet Xifré-Perez, Josep Ferré-Borrull, Lluis F. Marsal. *Oral Presentation*
11. **Conferencia Española de nanofotónica (CEN) 2018**. Structural engineering of one-dimensional nanoporous anodic alumina photonic crystals. **Laura K. Acosta** Capilla, Elisabet Xifré-Perez, Josep Ferré-Borrull, Lluis F. Marsal. *Oral presentation*
12. **Conferencia Española de nanofotónica (CEN) 2018.** Study of Nanoporous Anodic Alumina Gradient-Index Structures by Numerical Modelling. Francesc Bertó-Roselló, **Laura K. Acosta Capilla**, Elisabet Xifré-Perez, Josep Ferré-Borrull, Lluis F. Marsal. *Oral Presentation*

13. **Conferencia Española de nanofotónica (CEN) 2018**. Optical Characterization of the Attachment of Biotinylated Proteins in Nanoporous Anodic Alumina by means of RIfS**.** L. Pol, **L.K. Acosta**, J. Ferré-Borrull, E. Xifre-Pérez, L.F. Marsal. *Poster*
14. **Conferencia Española de nanofotónica (CEN) 2018.** Study of physical and photonic properties of anodized alumina nanotubes. J.T. Domagalski, E. Xifre-Perez, **L. K. Acosta** and L. F. Marsal. *Poster*
15. **NanoSpain 2019.** Stacked and Overlapped Photonic Structures in Nanoporous Anodic Alumina. **Laura. K Acosta**, Elisabet Xifre-Perez, Josep Ferré-Borrull, and Lluis F. Marsal. *Oral presentation*
16. **NanoBio&Med 2019** Complex Nanoporous Anodic Alumina Photonic Structures for Sensing: Design,Fabrication and Application. **Laura. K Acosta**, Elisabet Xifre-Perez, Josep Ferré-Borrull, and Lluis F. Marsal. *Oral presentation*
17. **CDE 2021.** Progress in Engineering Photonic Structures based on Nanoporous Anodic Alumina. **Laura. K Acosta**, Elisabet Xifre-Perez, Josep Ferré-Borrull, and Lluis F. Marsal. *Poster*
18. **SPPM 2021.** Engineering of Photonic Structures in Nanoporous Anodic Alumina. **Laura. K Acosta**, Josep Ferré-Borrull, and Lluis F. Marsal. *Poster*
19. **Conferencia Española de Nanofotónica (CEN) 2021.** Nanoporous Anodic Alumina Photonic Crystals by Gaussian-Like Pulse Anodization. **Laura K. Acosta,** Elisabet Xifré-Pérez, Josep Ferré-Borrull, Abel Santos, Lluis F. Marsal. *Flash talk*

List of Figures

List of Tables

"Nothing in life is to be feared, it is only to be understood. Now is the time to understand more, so that we can fear less. "

-Marie Curie-

UNIVERSITAT ROVIRA I VIRGILI
ENGINEERING OF PHOTONIC STRUCTURES BASED ON NANOPOROUS ANODIC ALUMINA AS AN OPTICAL SENSING PLATFORM
Laura Karen Acosta Capilla

Para Damián

UNIVERSITAT ROVIRA I VIRGILI
ENGINEERING OF PHOTONIC STRUCTURES BASED ON NANOPOROUS ANODIC ALUMINA AS AN OPTICAL SENSING PLATFORM
Laura Karen Acosta Capilla

Table of Content

Chapter 1. Introduction

UNIVERSITAT ROVIRA I VIRGILI
ENGINEERING OF PHOTONIC STRUCTURES BASED ON NANOPOROUS ANODIC ALUMINA AS AN OPTICAL SENSING PLATFORM
Laura Karen Acosta Capilla

1.1 Background

NAA-PSs demonstrate considerable ability as advanced and useful optical sensing platforms due to their exceptional physical, chemical, and optical properties. The geometric properties of nanopores in NAA-PSs can be precisely engineered by different anodization approaches to selectively filter molecules by size-exclusion and increase the available binding functional sites due to the high specific surface area to volume ratio of these nanoporous PSs. Furthermore, the surface chemistry of NAA-PSs can be adjusted with different functional molecules. NAA-PSs are active optical platforms that confine, guide, reflect, emit, and transmit incident light, generating stable optical signals for optical sensing based on different spectral shifts upon exposure to analyte molecules such as reflectivity, photoluminescence, transmittance, waveguiding, absorbance, or color changes. Different forms of NAA-PSs such as distributed Bragg reflectors, grading-index filters, optical microcavities, Fabry–Pérot interferometers can be integrated with various optical techniques such as reflectometric interference spectroscopy (RIfS), reflection and transmission spectroscopy, and photoluminescence spectroscopy (PL). Recent progress in anodization technology has focused on structural engineering of NAA-PSs by distinct forms of pulse-like anodization approaches such as sinusoidal, sawtooth, pseudostepwise, and stepwise. In contrast to pioneering pulse-like anodization combining hybrid pulses between mild and hard anodization regimes, pulse anodization performed under mild conditions moderate electrolyte temperature and anodizing voltage/current density– provide superior controllability over the anodic oxide growth rate and its porosity. Despite

these advances, to date only a limited number of pulse shapes have been implemented into anodization approaches to engineering distinct forms of NAA-PSs including sinusoidal, symmetric and asymmetric stepwise, and sawtooth. Although these strategies have successfully realized the engineering of NAA–PSs with outstanding optical properties, further developments of anodization technology will be needed to tailor-engineer the structure of NAA–PSs with versatility for harnessing specific forms of light–matter interactions and spreading the applicability of these unique photonic structures across light-based technologies.

1.2 Motivation

Motivated by the previous works and the potential of these photonic structures of several applications like sensing, optical encoding, photonics, and photovoltaics. For this reason, this thesis is focused on the fabrication, characterization of Photonic Structures based in nanoporous anodic alumina using different anodization approaches. The obtained Photonic structures were tested as an optical sensing platform.

1.3 Aims of the thesis

The objectives of this PhD thesis are the following:

I. To improve and develop different nanoporous anodic alumina photonic structures.

II. To fabricate nanoporous anodic alumina photonic structures with sinusoidal anodization profile.

III. To fabricate new and advanced nanoporous anodic alumina photonic structures using several anodization approaches.

IV. To apply these nanoporous photonic structures as an optical sensor.

Chapter 2. Basis of Nanoporous Anodic Alumina (NAA)

UNIVERSITAT ROVIRA I VIRGILI
ENGINEERING OF PHOTONIC STRUCTURES BASED ON NANOPOROUS ANODIC ALUMINA AS AN OPTICAL SENSING PLATFORM
Laura Karen Acosta Capilla

2.1 Background of Nanoporous Anodic Alumina

2.1.1 TimeLine of Nanoporous Anodic Alumina.

Nanoporous anodic alumina (NAA) is a self-ordered form of anodic aluminum oxide (AAO). Therefore, it is important to understand the chronological advances related with the engineering of pioneer structures of AAO. Anodized aluminum oxide has been used for the first time in the 20th century with protective and decorative purposes. In 1923, Bengough and Stuart patented a chromic acid-based electrochemical method for protecting aluminum from corrosion[1]. In 1927 the first anodization based on sulfuric acid was patented by Gower and O'Brien[2]. Afterwards, in 1936 Carboni patented a coloring method for aluminum foils by combination of an anodization step in sulfuric acid followed by a second step consisting of the application of alternating current in a metal salt solution[3]. Recently, thanks to the electron microscope invention, in 1953 Keller and co-workers characterized for the first time the honeycomb structure of AAO in the nanometric range, i.e., NAA and placed the groundwork for further NAA studies[4]. Based on this work and taking advantage of new techniques as microtome and electron microscope, Thompson and Wood published several studies providing a deep understanding in the growth mechanisms of aluminum oxide layers and a better knowledge of the anion incorporation and water content in the NAA structure[5-9].

In 1995 Masuda et al. discovered how to fabricate porous alumina whit highly ordered pores by using a two-step anodization process[10-11]. They developed a cheap and highly reproducible strategy of fabrication which permits further studies of NAA in many laboratories. In 2002 Nielsch et al.

published an optimization of this procedure employing sulfuric, oxalic and phosphoric acid as electrolytes. After that many different types of anodization techniques have been established[12-15]. Two different forms of AAO with different morphology are obtained, depending on the electrolytes used for the anodization process. Commonly, with neutral acids (e.g., borate, oxalate...) nonporous-type membranes are formed[16] and with acidic electrolytes (e.g., sulfuric, oxalic, phosphoric...) porous-type membranes are formed. Nonporous AAO membrane is a compact oxide membrane also called barrier-type oxide or barrier layer. Porous AAO membranes consist in a porous membrane with pore sizes within the nanometric scale, also called Nanoporous Anodic Alumina (NAA)[17].

2.1.2 Nanoporous anodic alumina Structure

Nanoporous Anodic Alumina is a honeycomb-like structure in which the hexagon is the unit cell, NAA is formed by several hexagonal cells. Each unit cell includes three different parts:

i. The skeleton, a hexagonal inner layer which is produced of the common internal walls between the unit cells. The inner layer is composed of pure Al_2O_3
ii. An outer layer between the central pores. the outer layer is composed of Al_2O_3 contaminated with impurities (anionic species i.e., phosphate, sulphate, oxalate, etc.) from the electrolyte.
iii. The interstitial rod inside the inner layer at the triple cell junction.

The pore structural parameters are classified six different parts that includes (i) interpore distance (D_{int}), (ii) pore diameter (D_p), (iii) barrier layer thickness (T_b), (iv) pore wall thickness (T_w), (v) pore density (ρ_p) and (vi) porosity (ρ) [4,5,14-18].

Figure 2.1 a) shows schematically an idealized NAA honeycomb-like structure and its parts. **Figure 2.1** b) shows the main parameters which describe NAA structure. The thickness ratio of inner and outer layers (ri/o) depends on the electrolyte in the order: sulfuric acid (H_2SO_4) < oxalic acid ($H_2C_2O_4$) < phosphoric acid (H_3PO_4) < chromic acid (H_2CrO_4)[19]. Also, Han *et al.* demonstrated that the anionic impurities incorporated depend on the anodization time and the electrolyte concentration[20]. They reported that electrolyte concentration decreases along the pore, so the contaminated area will be thicker on the top of the pores. Besides, one important property of these layers is that the outer layer is less resistant to chemical etching than the inner layer, which prevents the structure from collapsing even at high porosity. **Figure 2.2** shows the top and cross-sectional views of NAA pore showing the chemical composition distribution inside the nanopore walls.

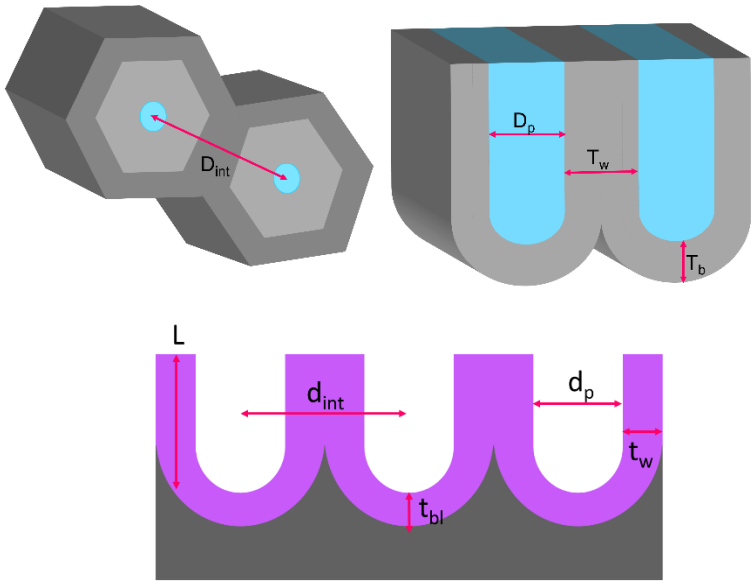

Figure 2.1 Schematic illustration of the NAA Honeycomb structure and its parts (a) honeycomb-like structure (b) Parameters describing the NAA structure.

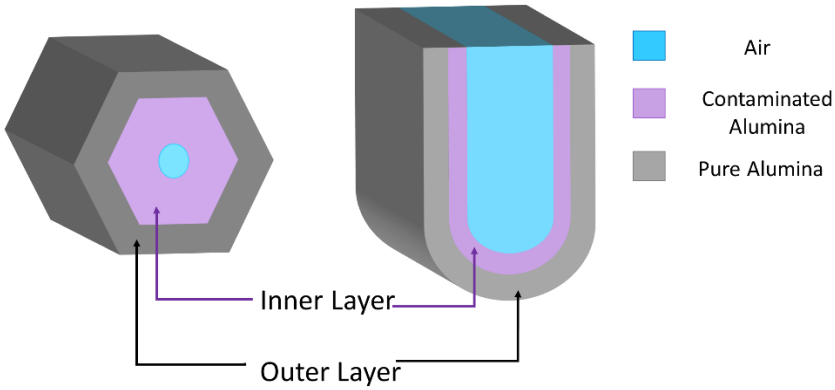

Figure 2.2. Schematic diagram of a nanoporous anodic alumina pore showing the chemical composition distribution inside the pore walls (top and cross-section).

2.1.3 Electrochemistry process of Nanoporous Anodic Alumina

The same as other metals, when aluminum is exposed to air or water is spontaneously oxidized and a thin layer of aluminum oxide is formed over the surface. This thin layer protects the aluminum below from oxidizing more (natural protective layer). Nanoporous anodic alumina is formed by electrochemical oxidation of aluminum by an anodization process. **Figure 2.3** shows the typical electrochemical cell used in the formation of NAA. NAA films are obtained by applying a direct voltage (*U*) through an electrolytic mixture (aqueous solution of acid, e.g., H_2SO_4, $H_2C_2O_4$ and H_3PO_4) into the aluminum substrate. Aluminum is used as an anode and usually a platinum or graphite is used as the cathode (while a material not affected by the electrochemical process). The applied voltage generates a high electric field (*E*) through the thin oxide layer on the surface of aluminum (natural protective layer). Under the electric field the anions of the solution (O^{2-} and OH) travel to the anode in which aluminum is positively charged with resultant electrons lost. When a voltage is applied among the cathode and anode, pores nucleated and start to grow on the

aluminum surface. NAA membranes are generally formed under constant voltage or constant current density (*J*) conditions. Under a constant voltage, a usual anodization *J* versus time (*t*) curve can be divided into four NAA growth stages **(figure 2.4)**[21-25].

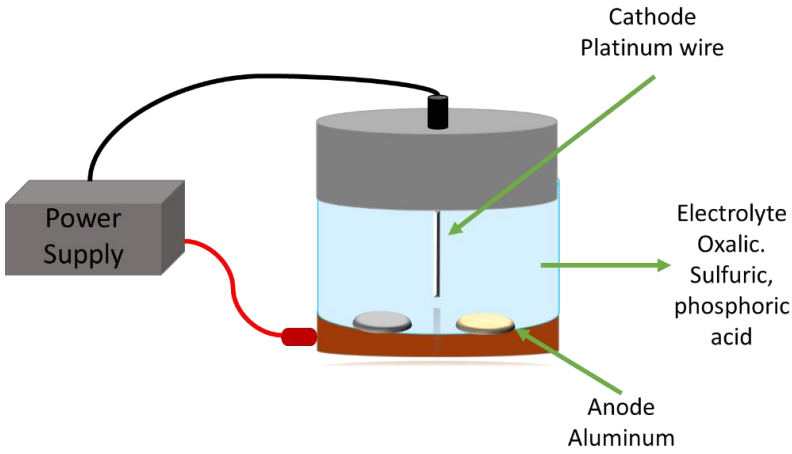

Figure 2.3 Schematic of Anodization system. Aluminum foil is used as anode and platinum as cathode. The anode and cathode are immersed in the acid electrolyte (oxalic, sulfuric, phosphoric or others) and all the system is linked to a power supply.

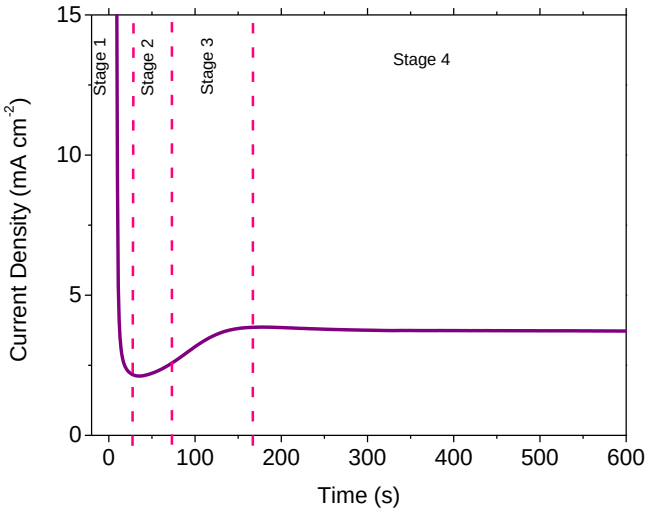

Figure 2.4 Current density (J) versus time (S) during the porous AAO membrane formation divided in four stages. 1) The film of aluminum oxide starts to grow and forms a compact barrier layer, 2) Pores start to grow, 3) The anodizing process continues and 4) Arrangement of pores occurs and continue to grow.

Stage 1. Barrier layer creation. At the moment that is applying a constant voltage, the (J) will reach a high value quickly, that can be attributed to the existence of electrolytic process of water. A thin layer of aluminum oxide starts to grow on the surface of aluminum and creates a compact barrier layer that grows until a specific thickness. While the resistance of the barrier layer is proportional to its thickness, the current density decreases fast until the lowest value.

Stage 2. Pores growth. At the minimum value of current density (J) point, the electric field (E) concentrates on local defects or impurities on the growing aluminum oxide surface to create routes for electrolyte infiltration, which act as pore nucleation sites. Local field enhancement at the saturation routes facilitates oxide decomposition and leads to the formation of further pores.

Stage 3. Gradual increment in the current density (J). The pores continue to form thanks to the easy diffusion of the electrolyte inside pores that is possible due to the advanced anodization process. Finally, an equilibrium between the forming and dissolving aluminum oxide is reached and start stage 4.

Stage 4. Current density (J) achieves a steady-state. During this state, gradual reordering of pores occurs over time until the field (E) is the same for all the pores.

Figure 2.5. shows the schematics of the four NAA growth stages. The growth mechanism in stage 4 (steady-state) is the consequence of competing oxidation i.e., alumina formation at the aluminum-oxide

interface (in the inner layer) and the alumina dissolution at the oxide-electrolyte interface (in the outer layer) during the anodization process. Some possible reactions that are probably taking place have been reported.[35-40]

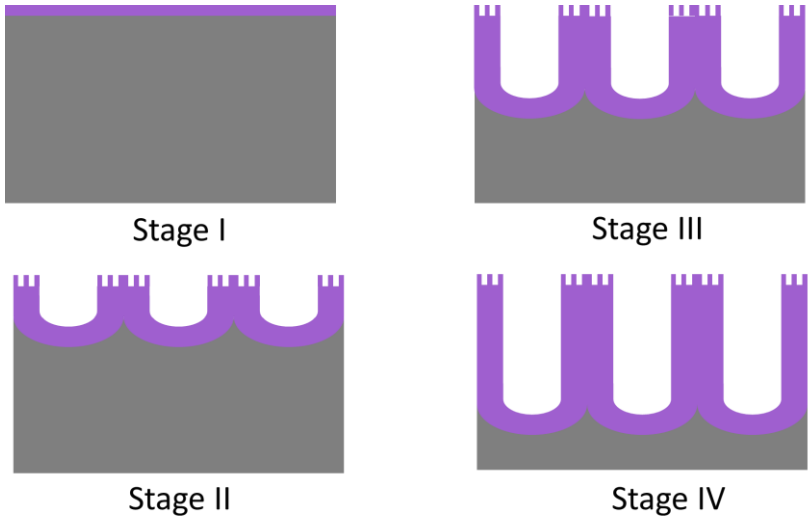

Figure 2.5. Schematic of NAA growth process under constant voltage condition. **I** to **IV** Morphology development with anodization time increasing.

Oxidation-reduction reaction that takes place during the anodization, it is the sum of the separate reactions at each electrode. **(Equation 2.1).**

$$2Al_{(s)} + 3H_2O_{(l)} \rightarrow Al_2O_{3(s)} + 3H_{2\,(g)} \qquad \textbf{(2.1)}$$

The process begins with the heterolytic dissociation of water, **(Equation 2.2**).

$$2H_2O_{(l)} \rightarrow O^{2-}_{(ox)} + OH^{-}_{(ox)} + 3H^{+}_{(aq)} \qquad \textbf{(2.2)}$$

The O^{2-} and OH^{-} anions, under the influence of the electric field (*E*), leave the oxide-electrolyte interface (outer layer) and migrate through the barrier layer until the aluminium-oxide interface (inner layer). When O^{2-}

comes at the aluminium-oxide interface, the metallic aluminium is oxidized and creates Al_2O_3 (**equation 2.3**).

$$Al^{0}_{(s)} \rightarrow Al^{3+}_{(ox)} + 3e^{-} \quad \textbf{(2.3)}$$

The ionic transport of Al^{3+} and O^{2} **(equation 2.4)** at the anode is exemplified in a schematic diagram in **figure 2.6**.

$$2Al^{3+}_{(ox)} + 3O^{2-}_{(ox)} \rightarrow Al_2O_{3\,(s)} \quad \textbf{(2.4)}$$

H^{+} in contact with e^{-} released from the dissociation of water forms H_2 (**equation 2.5**).

$$6H^{+}_{(aq)} + 6e^{-} \rightarrow 3H_{2(g)} \quad \textbf{(2.5)}$$

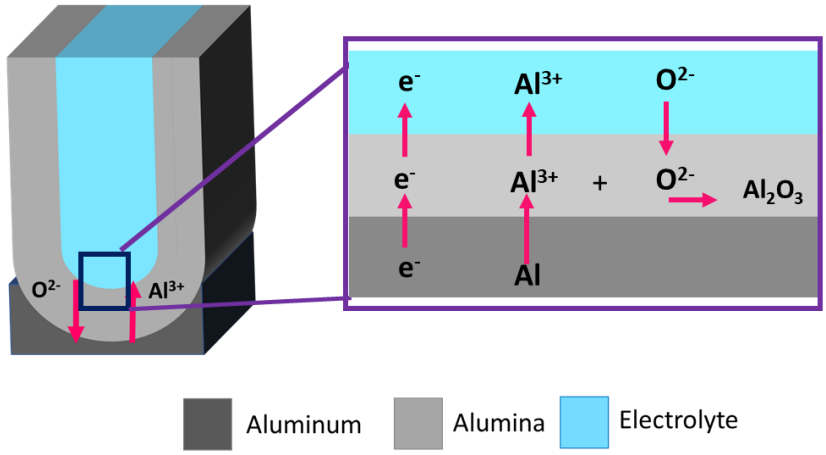

Figure 2.6. Schematics showing the ionic transport of Al^{3+} and O^{2}.

2.1.4 Anodization Techniques

Anodic Aluminum Oxide (AAO) membranes are fabricated using different anodization methods which leads the creation of AAO with specific characteristics. In this section we will describe the mild (MA) and hard anodization (HA).

2.1.4.1 Mild Anodization

In 1995 Masuda and Fukuda publish by the first time the two-step method that allow the manufacturing of self-ordered AAO[10-11]. They observed that after long anodization process, the pores of the bottom start to be ordered in hexagonal arrays becoming a perfect ordered nanoporous structure and they proposed the two-step anodization method (**Figure 2.7**):

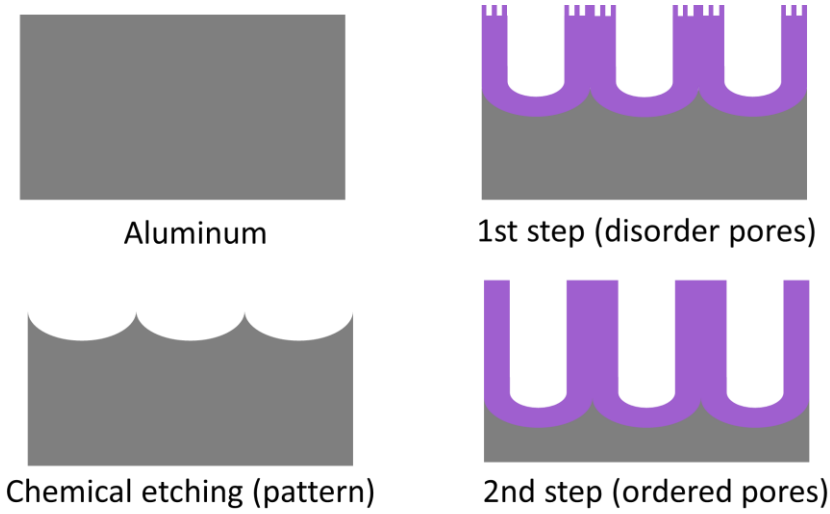

Figure 2.7 Schematics of the two-step anodization process.

1) The first anodization step results in a AAO membrane with disordered pores at the top but with ordered pores at the bottom.
2) After the first anodization step, the NAA membrane is removed and results in an aluminum surface with a honeycomb pattern of concavities.
3) The second anodization step will start to nucleate and grow the pores in a hexagonal ordered way. This procedure is characterized by anodization at low potentials and slow formation of pores due to the

low current density (J). With this technique is possible to obtain uniform pore size (D_p) and interpore distance (D_{int}) that can be easily tuned by selection of appropriate anodization conditions[21].

2.1.4.2. Hard Anodization (HA)

This anodization method consists in the use of high voltages above the breakdown potentials. For a given anodizing electrolyte, there is a breakdown potential (U_B) value (27 V for sulfuric acid, 50 V for oxalic acid and 197 V for phosphoric acid)[22-24] above which stable anodization is difficult to maintain due to the disastrous local current flow and consequent Joule heating which produces local burning and cracking in the growing[21]. This anodization produces NAA films faster and with a higher porous anodic layer growth rate than using MA[25]. Nevertheless, the substrate can be damaged because of the high voltage used. For this reason, HA is not typically used for nanotechnology research because it is difficult to properly maintain the anodization over the breakdown potential[26-29].

2.1.5 Anodization parameters and Geometrical characteristics

The Nanoporous Anodic alumina (NAA) structure is especially different depending on the anodization parameters. Adjusting these specific parameters, it is possible tune the organized NAA structure easily. The anodization parameters which control the structural characteristics of NAA are the anodization voltage (U), anodization time (t) and temperature (T). Additionally, the particular characteristics of the electrolyte have an important effect in the NAA structure[30-39].

2.1.5.1 Anodization Temperature

The electrolyte temperature (T) affects the pore growth rate and pore diameter. High temperatures lead not only to faster growth rates but also high dissolution rate of formed oxide which promotes larger pores. (T) is a critical parameter due to during the anodization process an increment of temperature is probable to take place because of local heating[26-27]. This temperature increment can result in the fast dissolution of the pore walls due to the burning phenomenon. Moreover, the pore growth rate and pore diameter are affected by this parameter, decrease as T is reduced.

2.1.5.2 Anodization Voltage

The pore diameter (D_p) and interpore distance (D_{int}) can be varied mostly by changing the anodization voltage (U)[5,10-11,28-30]. For a given electrolyte, there is a specific voltage (U), above which the breakdown and burning of NAA is most likely to occur due to the electron avalanche phenomenon. This phenomenon occurs due to local heating, increasing in the conductivity and ionization of atoms that leads excessive electron generation. **Table 2.1** shows the typically used electrolytes with their respectively used voltages[40-41].

Table 2.1. Electrolyte voltage commonly used during the anodization process.

Electrolyte	Voltage [V]
Sulfuric acid (H_2SO_4)	20
Oxalic acid ($H_2C_2O_4$)	40
Phosphoric acid (H_3PO_4)	195

2.1.5.3 Electrolyte

One of the most important parameters for the fabrication of NAA films is the electrolyte composition. Moreover, the usual acid electrolytes used for fabricating NAA sulfuric, oxalic and phosphoric acid as was mentioned in **Table 2.1**, though other acids such as tartaric and malonic can be used to obtain NAA with particular characteristics[45-46]. The pH and viscosity of the acid electrolyte strongly affect the structural characteristics of the NAA: a) The pH influences mainly the pore diameter. Low pH values require low anodization voltages, that implicates a reduction of the dissolution of alumina which causes smaller pores. So, the pores are wider with H_3PO_4 and narrower with H_2SO_4[47]. b) The viscosity of the electrolyte affects directly on the final nanostructure. The increment of the viscosity produces a decrement on the current density during the anodization process. This current density reduction generates a decrement of the growth rate but also prevents the localized heating due to the reduction of the Joule effect. High viscosity helps to avoid oxide breakdown specially a high electric field[48].

2.1.5.4 Interpore Distance (D_{int})and Pore Diameter (D_p)

The interpore distance (D_{int}) is the average distance between the centers of two adjacent pores. And the pore diameter D_p is the size radius of the pores. The interpore distance (D_{int}) can be controlled precisely by voltage (U) **(2.6)** and is directly correlated with the pore diameter D_p **(2.7).** Pore diameter (D_p) depends on voltage (U) but also depends on the temperature (T)[20]. The larger these parameters are, the bigger the pore diameter is. The pore sizes obtained by MA can vary between 10 to 400

nm[49]. The relationship between the interpore distance and the anodization potential can be expressed as:

$$D_{int} = KU \quad \textbf{(2.6)}$$

Where D_{int} is the interpore distance, U is the anodization voltage and K is the proportionally constant whose value is between 2.5 and 2.8 nm V^{-1} for Mild Anodization. Additionally, the relationship between the interpore distance, the pore diameter and the pore wall thickness can be expressed as:

$$D_{int} = D_p + t_w \quad \textbf{(2.7)}$$

Where, Dint is the interpore distance, D_p is the pore diameter and t_w is the wall thickness. **Figure 2.8** shows the relationship between the D_p and D_{int} with the voltage and **Table 2.2** shows the most usual anodization parameters for the three acid electrolytes generally used for MA. In addition, the average values of the resulting geometric characteristic are included.

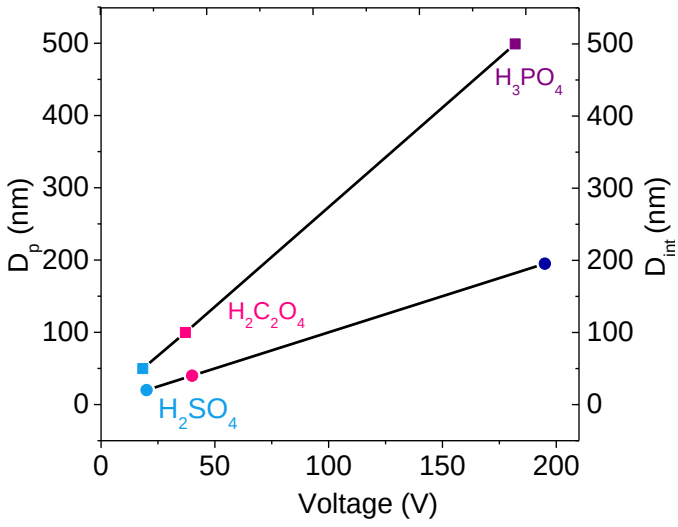

Figure 2.8. Relationship between the geometrical characteristics D_p and D_{int} vs Voltage. D_p vs U (circles) and D_{int} vs U (squares). For each anodization electrolyte.

Table 2.2 Summary of the usual anodization parameters and the geometric characteristics for sulfuric, oxalic, and phosphoric acid.

	H_2SO_4	$H_2C_2O_4$	H_3PO_4
Voltage [V]	20	40	195
Temperature [°C]	5	5	-5
Concentration	0.3 M	0.3 M	1% wt.
Pore diameter [nm]	20	40	195
Interpore distance [nm]	50	100	500

2.1.5.5 Porosity and Pore Density

The ratio of surface occupied by the pores to the total surface of the sample can be defined as porosity (P). Under Mild Anodization conditions, porosity follows the 10% porosity rule and usually is always about 10%[50] and under hard anodization conditions, this value is reduced to 3,3%[51]. The porosity can be correlated with pore diameter and interpore distance by the following equation:

$$P(\%) = \left(\frac{\pi}{2\sqrt{3}}\right)\left(\frac{D_p}{D_{int}}\right) * 100 \qquad \textbf{(2.8)}$$

Where P (%) is the porosity, D_p is the pore diameter and Dint is the interpore distance in nanometers. The pore density is the number of pores that can be found on a specific area. The relationship between pore density and interpore distance can be expressed by the following equation:

$$\rho_p = \left(\frac{2}{\sqrt{3\, D_{int}^2}}\right) * 100 \qquad \textbf{(2.9)}$$

where (ρ_p) is the pore density, and D_{int} is the interpore distance.

2.1.5.6 Barrier Layer Thickness

The barrier layer thickness (tb) is directly proportional to the anodization voltage (U) and is inversely proportional to current density (J). This relationship can be expressed as follows:

$$t_b = KU \quad \textbf{(2.10)}$$

Where (t_b) is the barrier layer thickness value, K is a proportionally constant which depends on the anodization regime (1,3 nm/V for MA), and U is the voltage.

REFERENCES

1. British Patent 223994 **(1923**).
2. British Patent 290901 **(1927**).
3. Italian Patent 741753 **(1936).**
4. F. Keller, M.S. Hunter, D.L. Robinson, Structural features of oxide coatings on aluminum, Journal of the Electrochemical Society 100 (**1953**) 411-419.
5. O'Sullivan, J. P.; Wood, G. C. Proceedings of the Royal Society of London. Series A, Mathematical and Physical Sciences **1970**, 317, 511–543.
6. Thompson, G. E.; Wood, G. C. Nature **1981,** 290, 230.
7. Shimuzu, K.; Kobayashi, K.; Thompson, G. E.; Wood, G. C. Philos. Mag. A **1992,** 66, 643.
8. Thompson, G. E. Thin Solid Films **1997**, 297, 192.
9. Wood, G. C. Journal of The Electrochemical Society **1996**, 143, 74.
10. H. Masuda, K. Fukuda, Ordered metal nanohole arrays made by a two-step replication of honeycomb structures of anodic alumina, Science 268 (**1995**) 1466-1468.
11. H. Masuda, H. Yamada, M. Satoh, H. Asoh, M. Nakao, T. Tamamura, Highly ordered nanochannel-array architecture in anodic alumina, Applied Physics Letters 71 (**1997**) 2770-2772.
12. K. Nielsch, F. Müller, A.P. Li, U. Gösele, Uniform nickel deposition into ordered alumina pores by pulsed electrodeposition, Advanced Materials 12 (**2000**) 582-586.
13. J. Choi, G. Sauer, K. Nielsch, R.B. Wehrspohn, U. Gösele, hexagonally arranged monodisperse silver nanowires with adjustable diameter and high aspect ratio, Chemistry of Materials 15 (**2003**) 776-779.
14. W. Lee, J.-C. Kim. Highly ordered porous alumina with tailor-made pore structures fabricated by pulse anodization, Nanotechnology. 21 (**2010**) 485304.
15. Thompson, G. E. Porous anodic alumina: fabrication, characterization and applications. Thin Solid Films **1997**, 297, 192–201.

16. J.P. O'Sullivan, G.C. Wood, Morphology and mechanism of formation of porous anodic films on aluminum, Proc Roy Soc Ser A Math Phys Sci. 317 **(1970)** 511–543.
17. W. Lee, The anodization of aluminum for nanotechnology applications, JOM. 62 **(2010**) 57–63.
18. Li, F.; Zhang, L.; Metzger, R. M. On the Growth of Highly Ordered Pores in Anodized Aluminum Oxide. Chem. Mater (1998), 10, 2470–2480.
19. G.E. Thompson, G.C. Wood, Anodic films on aluminium, in: J.C. SCULLY (Ed.), Corros. Aqueous Process. Passiv. Film., **1983**: pp. 205–329.
20. H. Han, S.J. Park, J.S. Jang, H. Ryu, K.J. Kim, S. Baik, W. Lee, In situ determination of the pore opening point during wet-chemical etching of the barrier layer of porous anodic aluminum oxide: Nonuniform Impurity Distribution in Anodic Oxide. ACS Appl. Mater. Interfaces. 5 **(2013**) 3441–3448.
21. Lee, W.; Park, S.-J. Porous Anodic Aluminum Oxide: Anodization and Templated Synthesis of Functional Nanostructures. Chemical Reviews **2014**, 114, 7487–7556.
22. S.Ikonopisov, A.Girginov, M.Machkova, Post-breakdown anodization of aluminium, Electrochem. Soc. 22 (**1977**) 1283–1286.
23. J.M. Albella, Electron Injection and Avalanche during the Anodic Oxidation of Tantalum, J. Electrochem. Soc. 131 (1984) 1101.
24. S.Z. Chu, K. Wada, S. Inoue, M. Isogai, Y. Katsuta, A. Yasumori, Large-Scale Fabrication of Ordered Nanoporous Alumina Films with Arbitrary Pore Intervals by Critical-Potential Anodization, J. Electrochem. Soc. 153 **(2006)** B384.
25. J. Ferré-Borrull, J. Pallarès, G. Macías, L.F. Marsal, Nanostructural engineering of nanoporous anodic alumina for biosensing applications, Materials (Basel). 7 **(2014)** 5225–5253.
26. Kikuchi, Tatsuya, Nishinaga, Osamu, Natsui, Shungo, Suzuki, R. O., Self-Ordering Behavior of Anodic Porous Alumina via Selenic Acid Anodizing, Electrochim. Acta. 137 **(2014)** 728–735.

27. T. Aerts, J.B. Jorcin, I. De Graeve, H. Terryn, Comparison between the influence of applied electrode and electrolyte temperatures on porous anodizing of aluminium, Electrochim. Acta. 55 **(2010)** 3957–3965.
28. W. Lee, R. Ji, U. Gösele, K. Nielsch, Fast fabrication of long-range ordered porous alumina membranes by hard anodization, Nat. Mater. 5 **(2006)** 741–747. https://doi.org/10.1038/nmat1717.
29. M. M. Rahman, E. Garcia-Caurel, A. Santos, L.F. Marsal, J. Pallarès, J. Ferré-Borrull, Effect of the anodization voltage on the pore-widening rate of nanoporous anodic alumina, Nanoscale Res. Lett. 7 **(2012**) 1–7.
30. F. Bertó-Roselló, E. Xifré-Pérez, J. Ferré-Borrull, J. Pallarès, L.F. Marsal, Nanoporous Anodic Alumina 3D FDTD Modelling for a Broad Range of Inter-pore Distances, Nanoscale Res. Lett. 11 **(2016).**
31. G.D. Sulka, Highly Ordered Anodic Porous Alumina Formation by Self-Organized Anodizing, **2008**.
32. Ling Z., Li Y., Mechanisms of Nanoporous Alumina Formation and Self-organized Growth, in: D. Losic, A. Santos (Eds.), Nanoporous Alumina, Springer Series in Materials Science Springer, Cham, **2015**.
33. A. Mozalev, S. Magaino, H. Imai, The formation of nanoporous membranes from anodically oxidized aluminium and their application to Li rechargeable batteries, Electrochim. Acta. 46 **(2001)** 2825–2834.
34. W. Lee, S.-J. Park, Porous Anodic Aluminum Oxide: Anodization and Templated Synthesis of Functional Nanostructures, Chem. Rev. 114 **(2014)** 7487–7556.
35. C. Cheng, A.H.W. Ngan, Theoretical Pore Growth Models for Nanoporous Alumina, in: D. Losic, A. Santos (Eds.), Nanoporous Alumina Fabr. Struct. Prop. Appl., Springer Series in Materials Science, **2015**: pp. 31–60.
36. G.E. Thompson, Porous anodic alumina: Fabrication, characterization and applications, Thin Solid Films. 297 **(1997)** 192–201.
37. F. Davies, J. A.; Domeij, B.; Pringle, J. P.; Brown, The migration of metal and oxygen during anodic film formation, Electrochem. Soc. 112 **(1965)** 670–680.
38. J. A. Davies, J.P.S. Pringle, R.L. Graham, F. Brown, A Radiotracer Study of Anodic Oxidation, J. Electrochem. Soc. 109 **(1962)** 99.

39. K. Shimizu, G. Thompson, G. Wood, Y. Xu, Direct observations of ion-implanted Xenon marker layers in anodic barrier films on aluminum, Thin Solid Films. 88 **(1982)** 255–262.
40. F. Brown, W.D. Mackintosh, The Use of Rutherford Backscattering to Study the Behavior of Ion-Implanted Atoms During Anodic Oxidation of Aluminum: Ar, Kr, Xe, K, Rb, Cs, Cl, Br, and l, J. Electrochem. Soc. 120 **(1973)** 1096.
41. Li, A. P.; Müller, F.; Birner, A.; Nielsch, K.; Gösele, U. Journal of Applied Physics 1998, 84, 6023–6026.
42. Masuda, H.; Hasegwa, F. J. Self-ordering of cell arrangement of anodic porous alumina formed in sulfuric acid solution. Electrochem. Soc. **1997**, 144, L127.
43. Masuda, H.; Satoh, M. Fabrication of gold nanodot array using anodic porous alumina as an evaporation mask. Japanese Journal of Applied Physics **1996**, 35, L126–L129.
44. Masuda, H.; Yada, K.; Osaka, A. Self-ordering of cell configuration of anodic porous alumina with large-size pores in phosphoric acid solution. Japanese Journal of Applied Physics **1998**, 37, L1340–L1342.
45. Ono, S.; Saito, M.; Asoh, H. Self-ordering of anodic porous alumina formed in organic acid electrolytes. Electrochim. Acta **2005**, 51, 827–833.
46. Ono, S.; Saito, M.; Ishiguro, M.; Asoh, H. J. Controlling factor of self-ordering of anodic porous alumina. Electrochem. Soc. **2004,** 151, B473–B478.
47. Friedman, A. L.; Brittain, D.; Menon, L. Roles of pH and acid type in the anodic growth of porous alumina. The Journal of Chemical Physics **2007**, 127, 154717.
48. Chen, W.; Wu, J.-S.; Xia, X.-H. Porous anodic alumina with continuously manipulated pore/cell size. ACS Nano **2008**, 2, 959–965.
49. Sulka, G. D., Highly Ordered Anodic Porous Alumina Formation by Self-Organized Anodizing; John Wiley & Sons, Ltd: **2008**; Chapter 1, pp 1–116.
50. Nielsch, K.; Choi, J.; Schwirn, K.; Wehrspohn, R. B.; Gösele, U. Self-ordering regimes of porous alumina: the 10% porosity rule. Nano Letters **2002**, 2, 677–680.
51. Lee, W.; Ji, R.; Gosele, U.; Nielsch, K. Fast fabrication of long-range ordered porous alumina membranes by hard anodization. Nat. Mater. **2006**, 5, 741.

Chapter 2

Chapter 3. Fundamentals of Nanoporous Anodic Alumina Photonic Structures

UNIVERSITAT ROVIRA I VIRGILI
ENGINEERING OF PHOTONIC STRUCTURES BASED ON NANOPOROUS ANODIC ALUMINA AS AN OPTICAL SENSING PLATFORM
Laura Karen Acosta Capilla

This Chapter presents the fundamentals of Photonic structures based on Nanoporous Anodic Alumina. The main concepts, different kind of photonic structures and the potential application of this structures are reviewed.

3.1 Background of Nanoporous Anodic Alumina Photonic Structures

In chapter 2 was explained the structure, fabrication and the design parameters of Nanoporous Anodic Alumina. The optical properties of NAA are very suitable for the formation of Photonic structures. The most attractive property of NAA is its versatile and highly controllable nanoporous structure, which can be readily utilized as an effective medium platform develop unique Photonic structures to modulate and control the flow of electromagnetic waves with precision. Nanoporous anodic alumina (NAA) produced by electrochemical oxidation of aluminum offers a set of unique properties that make it a highly attractive platform material for the fabrication of PSs. These include scalable and cost-effective fabrication process, highly controllable self-organized nanoporous structure based on well-defined cylindrical nanopores of high aspect ratio, chemical resistance, thermal stability, mechanical robustness, and optical properties.[1-2] NAA is considerate as a base material for the development of PCs. Pioneering fundamental studies dealt with the development and assessment of 2D NAA–PSs featuring straight cylindrical nanopores from top to bottom.[3-5] These studies demonstrated that the optical properties of NAA–PCs can be tuned by the geometric features of its nanoporous structure and its chemical composition which can be controlled using different anodization

conditions.[2] The development of anodization approaches directing to modulate the nanoporous structure of NAA in depth opened new opportunities to create multi-dimensional (1D, 2D and 3D) NAA-Photonic Structures. Following these studies Choi et al. studied the reflection spectrum of 2D NAA–PSs in the NIR region and analyzed the effect of the filling factor (i.e., ratio pore radius/interpore distance) on the characteristic PSB.[6] An almost linear blue shift of the PSB position was observed when the nanopores of NAA were widened by wet chemical etching (i.e., increment of filling factor) under controlled conditions. These studies represent the first demonstration and utilization of NAA as a platform for the development of Photonic structures. Nevertheless, the versatility of these PSs to attain light control in the different regions of the spectrum is limited by the range of lattice constants (i.e., d_{int}) in NAA. Another strategy to generate PC structures based on NAA is the in-depth modulation of its nanopores during anodization by structural engineering.

3.2 Photonic Structures.

Photonic structures (PSs) are a class of optical nanostructures with allowed and forbidden photonic bands that modify the movement of photons by altering the dispersion of electromagnetic waves when photons travel across the structure of PS. These light−matter interactions can be tuned with accuracy by engineering the PCs' structure, which features regularly distributed regions of high and low refractive index in one, two, or three dimensions.[7-9] **Figure 3.1** shows the schematics of the three types of Photonic structures in one, two and three dimensions. Nanoporous PSs are particularly good structures to develop ultra-sensitive optical sensing platforms since they supply:

a) Light-modifying capacities to alter and engineer the flow of photons at specific spectral regions from UV to IR.

b) The nanoporous structure that facilitates the transport of molecular species involved in binding events.

c) High specific surface area that increases the number of functional binding sites within the optical platform.[10]

Furthermore, PSs are a promising platform for other kinds of applications like photocatalysis, drug delivery, optical encoding, photovoltaics and others. **Figure 3.1** Schematics of three types of the photonic structures in one, two and three dimensions.

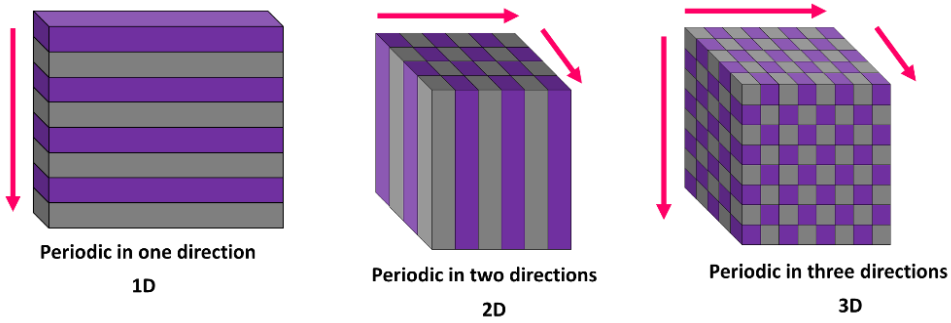

Figure 3.1. Schematics of the three kinds of photonics structures in one, two and three dimensions.

Nanoporous anodic alumina (NAA) is a promising material to developed PSs due to their unique optical properties. The optical properties of NAA rely intrinsically upon its nanoporous architecture. Therefore, to engineer the nanoporous structure of NAA provides novel means of modulating its refractive index in a multidimensional fashion to fabricate advanced materials with unique optical properties to guide, reflect, transmit, emit, and enhance incident light. The nanoporous structure of NAA can be engineered by means of different anodization approaches to produce PC structures with finely tuned optical properties across the spectral regions.

NAA provides controllable and versatile nanopore geometry, chemical and physical stability, stable and tunable optical signals, and mechanical strength. Furthermore, NAA's surface chemistry can be modified with a broad range of functional molecules to achieve chemical selectivity toward analytes of interest.[11-12] Structural engineering of the nanoporous structure of NAA in depth enables the generation of PC structures, the most representative examples of which are Fabry–Perót interferometers, distributed Bragg reflectors, gradient-index filters, apodised gradient index filters, microcavities, and optical bandpass filters.

3.2.1 Fabrication of Photonic Structures

The effective medium of NAA can be engineered in depth with precision during anodization in order to produce photonic structures of high aspect ratio with features of precise regularity and optimal resolution to diffract electromagnetic waves within the UV-visible-NIR spectrum. Even though NAA was used as a matrix for the development of photonic crystals. Recent anodization approaches have made it possible to overcome the intrinsic limitations of NAA fabrication, enabling a new path for the fabrication of a broad range of highly tunable photonic structures, which could open opportunities for all-optical NAA-based optical devices.[13-17] Pioneer studies by Masuda et. al and Gösele et. al revealed that organized NAA-PSs feature a characteristic photonic stopband (PSB) in their optical spectrum, the position of which can be finely tuned by the interpore distance (i.e., lattice constant—distance between the center of adjacent nanopores) and porosity (i.e., pore diameter) of the NAA-PC platform. Structural engineering of the nanoporous structure of NAA in depth enables the formation of PC structures, the most representative examples

of which are Fabry–Pérot interferometers[18-19], distributed Bragg reflectors[20-22], gradient-index filters (Rugate Filters)[23-25], microcavities[26-27], and optical bandpass filters[28]. NAA–PSs, which can be produced with precision by pulse-like anodization strategies trying to engineer the effective medium of NAA.

3.2.1.1. Fabry-Perot Interferometers

Fabry–Perot interferometers based on Nanoporous Anodic Alumina (NAA-FPIs) include a distribution of effective refractive index in depth and have been intensively used as sensing platforms in combination with different techniques. NAA-FPIs interfere constructively with electromagnetic waves, generating a characteristic interference pattern with distinctive fringes, which are a result of the Fabry–Pérot effect. Variations of the effective medium of NAA-FPIs leads to shifts in their typical interference pattern, which can be used as sensing principle to create optical systems with broad applicability[18]. The number, position, and intensity of these oscillations rely on the NAA thickness (i.e., the pore length (Lp)) and its porosity (i.e., the pore diameter (dp))[29].

Therefore, this property offers us an excellent opportunity for designing NAA structures with tunable optical properties by modifying the pore geometry. The fabrication of this kind of structure follows the well-known two-step anodization process developed by Masuda and co-workers[30]. **Figure 3.2** shows the fabrication process used for the formation of Fabry-Pérot interferometer and the characteristic reflection spectrum of these kind of structures.

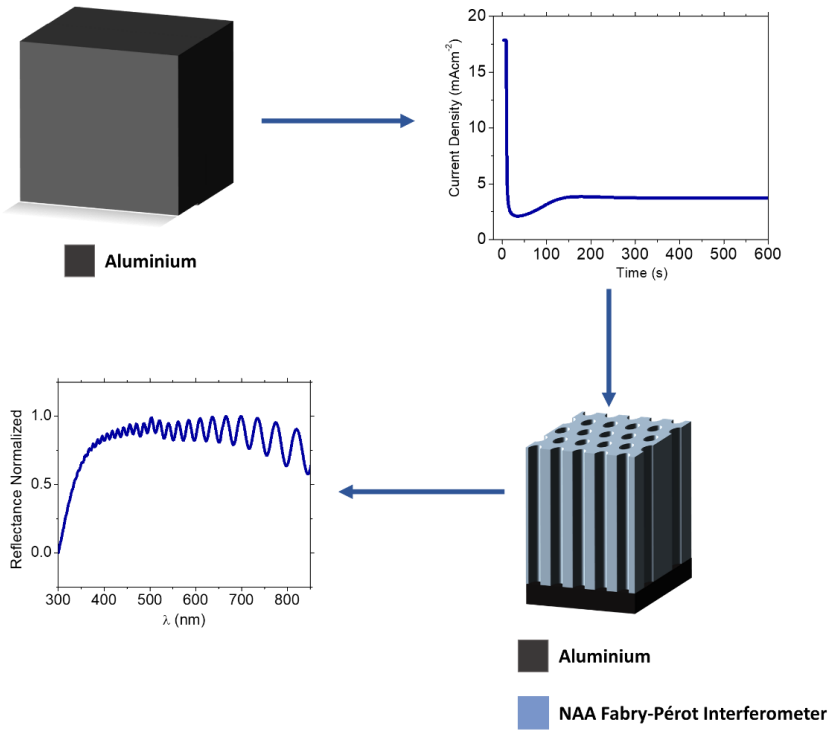

Figure 3.2 Fabrication process of Fabry-Pérot structures by constant anodization. Showing straight pores. The reflection spectrum shows the characteristic optical oscillations.

3.2.1.2 Gradient Index Filters

NAA-GIFs produced by sinusoidal pulse anodization feature a characteristically well-resolved, intense, and narrow PSB associated with a smooth and periodic modulation of the effective refractive index in depth, which is ~π/4 narrower than that of their quarter-wave NAA-DBR.[31] Well-resolved and narrow PSBs are desirable for different light-based applications requiring a precise control over electromagnetic waves such as optical sensing and biosensing,[32-33] optical encoding[34], and photocatalysis.[23] Recent developments in pulse anodization technology have aimed at improving the quality of light control of NAA-PCs. A variety of sinusoidal pulse anodization strategies have been explored to improve

the quality of light control in NAA-GIFs, including implementation of apodization functions into anodization profiles[35] and application of anodizing voltage as a function of optical path length.[36] NAA-GIFs produced by these and other approaches have achieved high quality PSBs, with quality factors. **Figure 3.3** shows the fabrication process of NAA-GIFs by sinusoidal pulse anodization and the representative reflection spectrum of the characteristic reflection bands.

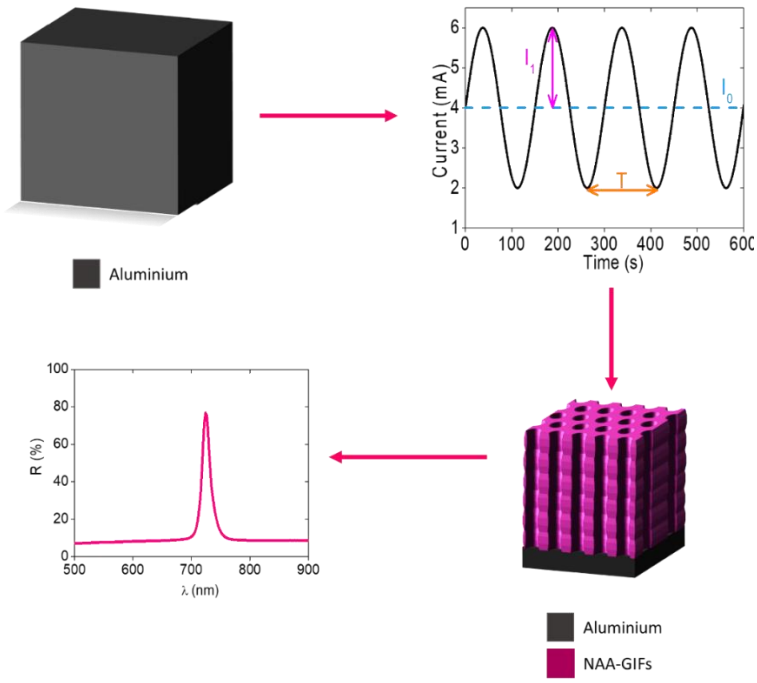

Figure 3.3 Fabrication process of Nanoporous Anodic Alumina Gradient Index Filters using sinusoidal pulse anodization.

3.2.1.3. Distributed Bragg Reflectors (DBR)

The distributed Bragg reflector (DBR) is a multilayered structure that consists of periodically stacked layers with different refractive indexes. The main optical property of a DBR is that it can block light propagation in the direction perpendicular to the refractive index variation for a certain

wavelength range, called the stop band.[22,37] The central wavelength of this stop band depends on the refractive index and thickness of the layers composing the DBR, whereas the stopband width depends basically on the contrast between the refractive indexes and the relative thicknesses between the layers within one period, although it also depends on the total number of layers. DBRs are structures that can control the incident light (completely or partially) inside the material. This interesting photonic property makes DBRs potential candidates for the fabrication of various optoelectronic devices: light filters,[38] vertical cavity surface-emitting laser,[39-40] reflector mirrors,[41] electro absorptive reflection modulators,[42] and others. To obtain DBR structures exists different kind of anodization process like cycling anodization voltage[22] and current density pulse anodization[43]. Figure 3.4 shows the fabrication process of NAA-DBR using cycling anodization and the reflection spectrum of the obtained band.

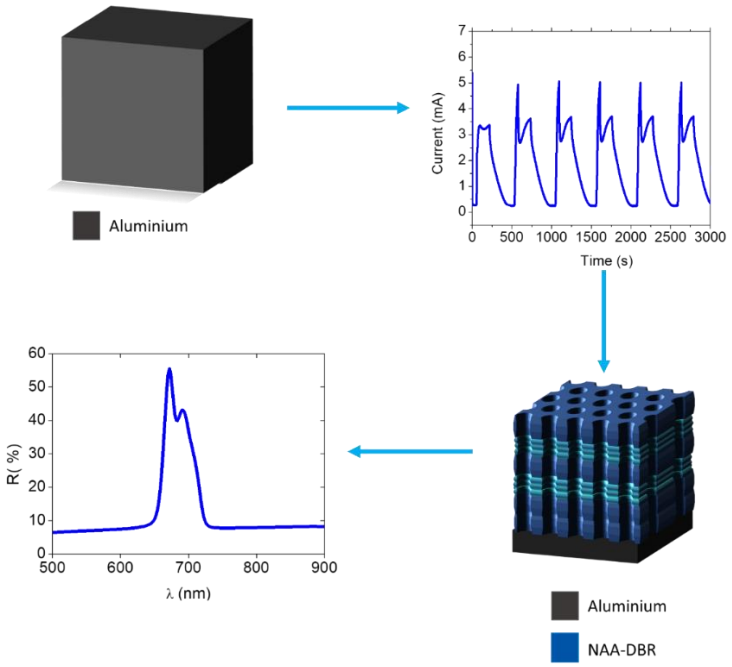

Figure 3.4. Fabrication process of NAA-DBR by cyclic anodization and the reflection spectrum of the characteristic photonic band.

3.2.1.4 Microcavities

The fabrication of Nanoporous Anodic alumina microcavities (NAA-μCVs) involves the introduction of defect modes in the Photonic Structure, which can be achieved by various approaches such as the insertion of a thin layer of nanopores with constant effective refractive index between two highly reflective Bragg mirrors, a phase shift of the effective refractive index between Bragg mirrors, or a progressive asymmetric modulation of the effective medium in depth.[44-46] However, the maximum quality factors of NAA-μCVs reported by Wang et al. and Yan et al., [46] were found to be significantly lower than those of porous silicon-based μCVs[47-49] because of the low refractive index of alumina (Al_2O_3; n-Alumina $\sim$ 1.70).[44-46]

Despite this limitation, the development of new pulse-like anodization strategies and novel NAA-PC architectures provides new opportunities to improve the quality of NAA-μCVs and explore new strategies to attain strong light confinements by precise control of light−matter interactions at the nanoscale.[27] Recent studies identified sharp resonance bands within the photonic stopband (PSB) of NAA-PCs produced by stepwise pulse anodization when a logarithmic negative apodization function was applied under certain conditions.[27,50-51]

However, only a few studies have explored the potential of these emerging optical transducers as sensing platforms. Yan et al.,[46] and Lee et al.,[61] demonstrated that NAA−μCVs are sensitive PC structures to changes in refractive index, while Wang et al. proved that NAA−μCVs' RB undergoes dynamic spectral shifts upon exposure to humidity from water vapor.[62] Despite these advances, there remain fundamental questions concerning the design and engineering of NAA−μCVs to maximizing

sensitivity of light confined within their structure for practical sensing applications. Previous studies on nanoporous PCs[63-64] point that sensitivity of NAA−µCVs is critically determined by:

a) size of analyte molecules,
b) degree to which analyte molecules increase the refractive index of the medium filling the nanopores
c) molecule−surface interaction strength
d) spectral position and quality of light confinement.

Figure 3.5 shows the fabrication process of NAA-µCVs by stepwise pulse anodization and the reflection spectrum showing the NAA-µCV.

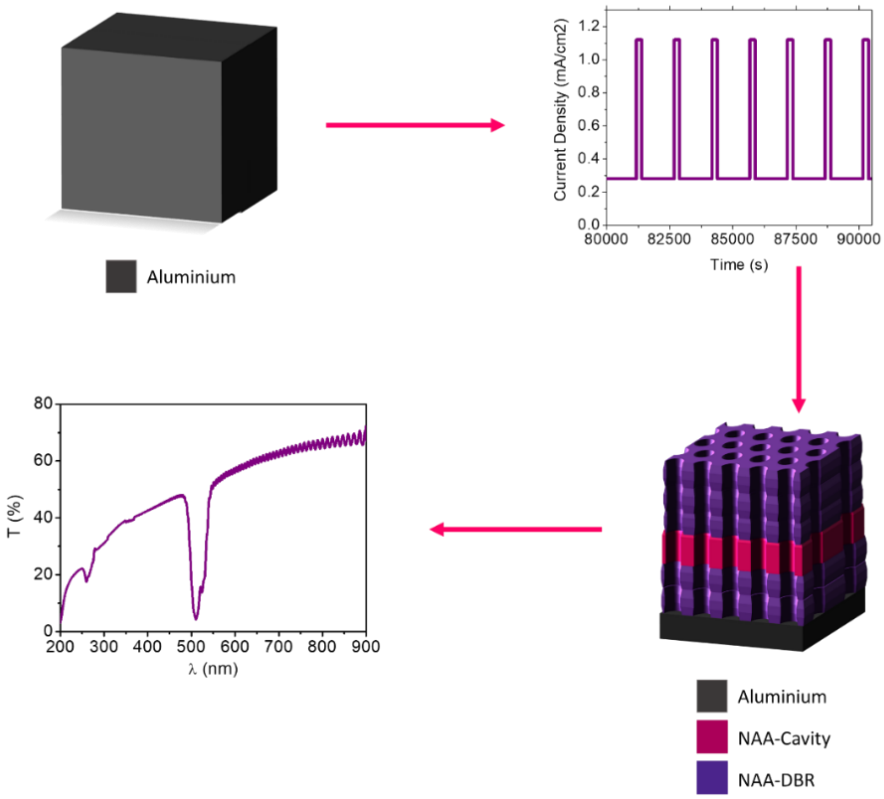

Figure 3.5. Fabrication process of optical microcavities NAA-µCvs.

3.2.2 Multispectral Photonic Structures

To fabricate PCs with multiple narrow photonic stopbands at different spectral positions remains challenging, and to date, only a few proof-of-concept studies have realized this class of PCs. For instance, Sailor et al.,[52,53] and Santos et al.,[54] developed porous silicon and NAA-PC structures, respectively, with multiple photonic stopbands at different spectral positions. These PCs were obtained by averaging the sum of multiple sinusoidal waves into a single complex waveform, which was subsequently translated into anodization profiles to engineer the nanoporous structure of these PCs in depth. Each sinusoidal wave determines the position and the reflectance amplitude of a forbidden photonic band or photonic stopband.

Multiple-band NAA structures have interesting applications such as optical encoding, optical sensing, photonics and photovoltaics.[55-60] However, the average sum of multiple sinusoidal waves and their implementation into anodization processes that are effectively translated into modulations of effective refractive index present some limiting drawbacks. When the number of forbidden bands is increased, the reflectance amplitude of each band is reduced. The reflectance amplitude of each forbidden band is proportional to the amplitude of the sinusoidal wave. Therefore, when the number of bands increases, the multiple averaging reduces the amplitude of each sinusoidal wave proportionally to the number of bands, thus decreasing the reflectance amplitude of all the bands in the spectrum of these PCs. **Figure 3.6** shows the fabrication process of the NAA- multispectral-PSs, the anodization profile shows a part of the current process of each layer. The reflection spectra show

three photonic sop bands corresponding with each layer fabricated. This anodization approach is very useful for the formation of sensing platforms, drug delivery systems, optical encoding, photocatalysis, band pass filters and others.

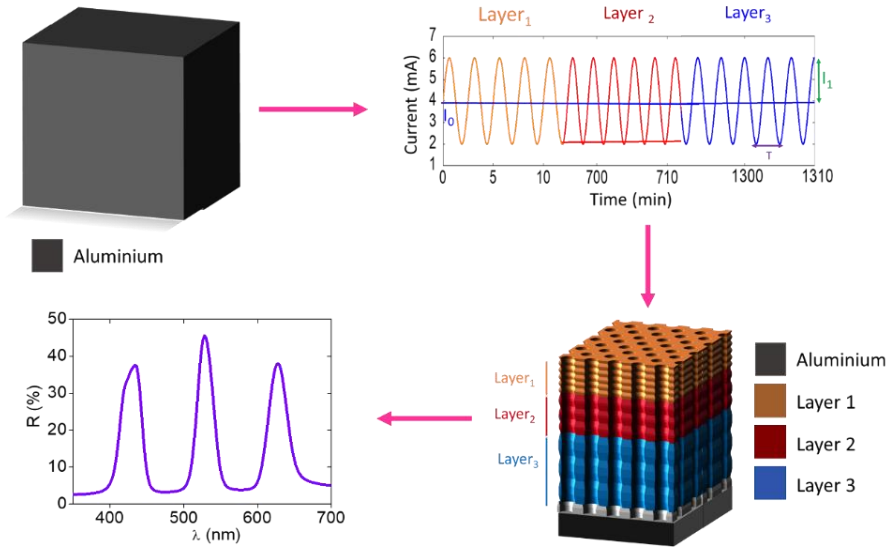

Figure 3.6. Fabrication process of NAA-multispectral-PSs. The reflection spectrum shows three PSB corresponding with the three stacked layers.

3.2.2.1. Optical Bandpass Filters

Optical bandpass filters (BPFs) are photonic structures that allow the transmission of a specific portion of the light spectrum in a selective manner while impeding the passing of light of all other wavelengths.[65] BPFs are extensively used across a broad range of disciplines and industries, including photography, astronomy, the pharmaceutical industry, medicine, physics, and chemistry. Generally, BPFs are classified into three categories according to the range of allowed wavelengths:

a) long-pass filters, which allow the transmission of light of long wavelengths,
b) short-pass filters, which allow the passing of light of short wavelengths,
c) bandpass filters, which allow the transmission of a band of wavelengths while blocking the passing of light of shorter and longer wavelengths.

The first obtained Bandpass filters based on nanoporous anodic alumina (NAA-BPF) were carried out by Santos and Co-workers. Bandpass filters (NAA–BPFs) produced by a pseudo-stepwise asymmetric pulse anodization approach under galvanostatic conditions in sulfuric acid electrolyte at low temperature.[66] The anodization approach was based on asymmetric stepwise current density pulses. The effect of the anodization period over the position and FWHM of the PSB of NAA–BPFs was first established. Using this rationale, the combination of stacked NAA–BPFs produced with different anodization periods can be readily used to create different transmission bands at specific positions across the transmission spectrum of the PC heterostructures. Besides, the progressive modification of the anodization period in the stacked NAA–BPF structure can be used to engineer the width of the PSB.

Table 3.1 shows a compilation of anodization approaches for the formation of the most characteristic photonic structures. This table includes the references of the principal studies involved in this anodization approaches.

Table 3.1 Summary of the main anodization approaches.

Photonic Structure	Anodization approach	Reference
NAA-FPI	One step anodization Two-step anodization	3-5 67,76-78,112
NAA-GIFs	Sinusoidal pulse anodization Pseudo-stepwise pulse anodization	24-25,32 83-84
NAA-DBR	Stepwise pulse anodization Pseudo stepwise pulse anodization	20,26-27,43-46 50,76,89,113
NAA-µCVs	Stepwise pulse anodization Sinusoidal pulse anodization Pseudostepwise pulse anodization Sawtoth pulse anodization	26 27 44-46 89
NAA-BPF	Stepwise pulse anodization Pseudo stepwise anodization Stepwise pulse anodization + sinusoidal pulse anodization	28
NAA-multispectral-PS	Sinusoidal Pulse anodization	91, 119

3.3 Potential Applications of Nanoporous Anodic Alumina Photonic Structures

The promising optical properties of NAA-PSs make it an innovative platform. Since the first pioneering works NAA-PS have been used as platforms for optical sensors[67-72], recently they have also been used for photocatalysis[90], drug delivery[91], optical encoding[34], photovoltaics and lasing systems.

3.3.1 Optical sensors

Optical sensors are devices that use different kinds of light–matter interactions to detect and quantify molecules for multiple applications. They contain a light source to generate electromagnetic signals, a sensing platform in which light–matter interactions appear, and a detector to identify and quantify spectral shifts in electromagnetic waves upon interaction and exposure to analytes.[73-75] Usually, the sensing principle in optical sensors depend on shifts in the characteristic spectral property of

the optical platform upon interaction with molecules. NAA-PSs show much potential as advanced and versatile optical sensing platforms due to their excellent physical, chemical, and optical properties. To engineer the effective medium and surface chemistry of NAA-PSs enhances the sensing performance and capabilities of NAA-based optical sensing system in terms of selectivity, sensitivity, and specificity. The geometric features of nanopores in NAA-PSs can be precisely engineered by different anodization approaches to selectively filter molecules by size-exclusion and increase the available binding functional sites due to the high specific surface area to volume ratio of these nanoporous PSs.

NAA-PSs are active optical platforms that confine, guide, reflect, emit, and transmit incident light, generating stable optical signals for sensing applications based on different spectral shifts upon exposure to analyte molecules such as reflectivity, photoluminescence, transmittance, waveguiding, absorbance, or color changes. Recent research advances in NAA-PSs as an optical sensing platform demonstrated that the NAA-PSs are an excellent platform due to their high controllable and tune the effective medium and versatile surface chemistry, which can be precisely engineering to achieve performance for an extensive molecules and analytes. Several researches are focus on the fabrication of photonic structures for develop optical sensor systems showing selectivity, sensitivity and Low Limit of detection.

Table 3.2 shows a compilation of the recent sensing performances for the different Photonic structure. All of these studies demonstrated the ability of the NAA-PSs structures for been used as optical sensing platforms for a broad range of analytes.

Table 3.2 Recent sensing performances for different photonic structures (NAA-PSs)

Photonic Structure	Analyte	Reference
Fabry Pérot Interferometeres	D-Glucose	76
	Proteinase K	77
	Hg	76
	Gold iones	19, 78
	Cancer cells	79
	TNF	80
	Cysteine	67
	Trypsin	81
	Galactosidase	82
GIFs	D-Glucose	32
	Indomethacin	25
	HSA	83
	Salicylic acid	83
	Metal ions (Hg, Cu, Pb)	84
	Ethanol	24
	Alcohols mixtures	24
	Sulfadymethoxine	85
	Warfarin	85
	Coumarin	85
DBR	D-Glucose	87
	Ethanol-IPA	43,87
	Gold Iones	87
	Vitamin C	43
	Hg	43
	Alkanes	87,88
	Organic molecules	88
	Au	87
Optical microcavities	Humidity sensor	45
	gas sensor	46
	Alcohols mixture	89, 27
	Hexane	89
	Nacl	27
	Au ions	43

3.3.2 Photocatalysis

Photocatalysis is a light process in which photons interact with atoms (matter–semiconductor) to generate electron–hole pairs that produce free radicals able to undertake secondary reactions. Photocatalytic processes involve a photoactive material (e.g., semiconductor, noble

metal) with a well-defined energy bandgap[91]. When the energy of the incoming photons is higher than the energy bandgap of the platform material, electrons and holes are generated in the materials conduction and valence bands, respectively.

Typical photocatalyst materials have fundamental constraints such as low photon-to-electron conversion rates due to limited utilization of high-irradiance solar spectral zones and low effective surface area[91]. The efficiency of photocatalysts system can be improved by engineering their structure at the nanoscale in the form of nanoporous photonic structures (PSs), which provide high specific surface area, improved utilization of incoming photons, and efficient mass transport of ionic and molecular species involved in photocatalytic reactions[94-97]. Inverse opal PC photocatalysts feature a characteristic photonic stopband (PSB) that can be engineered with precision across the spectral regions to harvest incoming photons from high-irradiance spectral regions [99-102]. Although these PC structures have been explored as platform material for photocatalysis, they present several inherent drawbacks, including long fabrication process, restriction to 3D nanostructures, constraints to small domain areas and formation of structural defects[103]. Among other alternatives, electrochemically engineered nanoporous materials are promising photocatalyst platforms due to their versatile, highly controllable and self-organized nanoporous structure. Advances in electrochemical oxidation of aluminum and titanium enable new opportunities to precisely modulate and engineer the effective medium of semiconductor oxides to harness light–matter interactions for photocatalysis.

NAA-PSs such as gradient-index filters, optical microcavities, and distributed Bragg reflectors present as ideal platforms to utilize the "slow photon" effect for enhanced photocatalytic reactions. However, the wide energy band gap of NAA[104, 105] prevents the direct use of NAA-PSs for photocatalysis. Despite this intrinsic limitation, the chemical-modification of NAA-PSs with photoactive materials such as TiO_2 does provide an opportunity to develop new platform materials as highly efficient photocatalysts by a rational management of photons at the nanoscale

The research advances in nanoporous PSs have been demonstrated the ability of these structures to be efficient for photocatalysis systems. Santos and co-workers have been demonstrated the use of different photonic structures by photocatalysis system. **Table 3.3** summarize the most recent advances in photocatalysis using NAA-PSs this table includes the optical mechanism used in each study.

Table 3.3. Summary of the recent studies in photocatalysis with NAA-PSs.

Photonic structure	Optical mechanism	Reference
TiO_2-NAA-GiFs	Slow photon	23
TiO_2-NAA-DBR	Slow photon	98
TiO_2-NAA-μQVs	Light recirculation	26
TiO2-NAA-BDBR	Slow photon	106
Au-TiO_2-NAA-DBRs	Slow photon + surface plasmon resonance	107

3.2.3 Drug delivery

In drug delivery advances, the release of the target molecule has been a major challenge; consequently, different stimuli are currently used to maintain the drug molecules and release them only when triggered by any specific stimulus. In this regards, pH-sensitive mechanisms draw huge

attention as they are similar to the pH variations inside the human body. From Now, polyelectrolyte multilayers (PEM) have been frequently used to cover the surface of nanoporous structures for the continued delivery of drug molecules[108-110]. One of the principal problems when PEM are used in NAA nanostructures is the determination of the degree of drug loading into the pores and the rate of release of the drug-loaded into the nanostructure. Recently, was developed an optical platform based on Nanoporous Anodic Alumina Gradient Index filters (NAA-GIFs). The study developed by Kapruwan et. al demonstrates successfully the ability of these nanostructures for analyzing the loading and release of a cargo molecule. To achieve this, NAA-GIFs composed of two photonic stopbands have been obtained, infused with the cargo molecule, and monitored optically for their loading and releasing patterns.[111]

3.3.4 Optical encoding

This innovative anodization approach, so-called multi-sinusoidal pulse anodization based on the combination of multiple sinusoidal waves into a single complex waveform, which corresponds to the average sum of several sinusoidal waves. This electrochemical nanofabrication method is demonstrated as a unique means of engineering the photonic stop band of nanoporous anodic alumina in depth. photonic structures based on Nanoporous Anodic Alumina can be used to encode information within their optical transmission spectrum. Santos et.al developed as a proof-of-concept, an 8-bit encoding system with ON (1)/OFF (0) states is for the first time implemented and demonstrated in NAA-based photonic structures, opening new opportunities for robust and reliable nanoscale platforms for secure information storage and optical encoding[28].

REFERENCES

1. G. D. Sulka, Highly Ordered Anodic Porous Alumina Formation by Self-Organized Anodizing, in Nanostructured Materials in Electrochemistry, Wiley-VCH Verlag Gmbh&Co. KGaA, 2008, pp. 1–116.
2. W. Lee and J. S. Park, Chem. Rev., 2014, 114, 7487
3. H. Masuda, M. Ohya, H. Asoh, M. Nakao, M. Nohtomi and T. Tamamura, Jpn. J. Appl. Phys., 1999, 38, L1403.
4. H. Masuda, M. Ohya, K. Nishio, H. Asoh, M. Nakao, M. Nohtomi, A. Yokoo and T. Tamamura, Jpn. J. Appl. Phys., 2000, 39, L1039.
5. H. Masuda, M. Ohya, H. Asoh and K. Nishio, Jpn. J. Appl.Phys., 2001, 40, L1217.
6. J. Choi, Y. Luo, R. B. Wehrspohn, R. Hillebrand, J. Schilling and U. Gösele, J. Appl. Phys., 2003, 8, 4757.
7. López, C. Materials aspects of photonic crystals. Adv. Mater. 2003, 15, 1680–1704.
8. Yablonovitch, E. Inhibited spontaneous emission in solid-state physics and electronics. Phys. Rev. Lett. 1987,58, 2059.
9. John, S. Strong localization of photons in certain disordered dielectric superlattices. Phys. Rev. Lett. 1987, 58,2486.
10. Xia, Y.; Gates, B.; Li, Z.-Y. Self-assembly approaches to three-dimensional photonic crystals. Adv. Mater. 2001, 13, 409–413
11. Lee, W.; Park, S.-J. Porous anodic aluminum oxide: Anodization and templated synthesis of functional nanostructures. Chem. Rev. 2014, 114, 7487–7556.
12. Santos, A. Nanoporous anodic alumina photonic crystals: Fundamentals, developments and perspectives. J. Mater. Chem. C 2017, 5, 5581–5599
13. W. Lee and J.-C. Kim, Nanotechnology, 2010, 21, 485304.
14. W. Lee, K. Schwirn, M. Steinhart, E. Pippel, R. Scholz and U. Gosele, Nat. Nanotechnol., 2008, 3, 234.
15. W. Lee, R. Scholz and U. Gosele, Nano Lett., 2008, 8, 2155.
16. W. Lee, J. C. Kim and U. Gosele, Adv. Funct. Mater., 2009, 19, 1.
17. R. C. Furneaux, W. R. Rigby and A. P. Davidson, Nature,1989, 337, 47.

18. Ferré-Borrull, J., Pallarès, J., Macías, G. & Marsal, L. F. Nanostructural engineering of nanoporous anodic alumina for biosensing applications. Materials (Basel). 7, 5225-5253 (2014).
19. Law, C. S. et al. Engineering of Surface Chemistry for Enhanced Sensitivity in Nanoporous Interferometric Sensing Platforms. (2017)
20. SPIE, G. D. & Hnida, K. Distributed Bragg reflector based on porous anodic alumina fabricated by pulse anodization. Nanotechnology 23, 075303 (2012).
21. Ferré-Borrull, J., Rahman, M. M., Pallarès, J. & Marsal, L. F. Tuning nanoporous anodic alumina distributed-Bragg reflectors with the number of anodization cycles and the anodization temperature. Nanoscale Res. Lett. 9, 416 (2014).
22. Rahman, M. M., Marsal, L. F., Pallares andJosep & Ferre-Borrull. Tuning the photonic stop bands of nanoporous anodic alumina-based distributed bragg reflectors by pore widening. ACS Appl. Mater. Interfaces 5, 13375–13381 (2013).
23. Lim, S. Y. et al. Engineering the Slow Photon Effect in Photoactive Nanoporous Anodic Alumina Gradient-Index Filters for Photocatalysis. ACS Appl. Mater. Interfaces 10, 24124–24136 (2018).
24. Macias, G., Ferré-Borrull, J., Pallarès, J. & Marsal, L. F. 1-D nanoporous anodic alumina rugate filters by means of small current variations for real-time sensing applications. Nanoscale Res. Lett. 9, 315 (2014).
25. Santos, A. et al. Realisation and advanced engineering of true optical rugate filters based on nanoporous anodic alumina by sinusoidal pulse anodisation. Nanoscale 8, 1360–1373 (2016).
26. Liu, L.; Lim, S. Y.; Law, C. S.; Jin, B.; Abell, A. D.; Ni, G.; Santos, A. Light-Confining Semiconductor Nanoporous Anodic Alumina Optical Microcavities for Photocatalysis. J. Mater. Chem. A 2019, 7 (39), 22514–22529.
27. Acosta, L. K.; Law, C. S.; Lim, S. Y.; Abell, A. D.; Marsal, L. F.; Santos, A. Role of Spectral Resonance Features and Surface Chemistry in the Optical Sensitivity of Light-Confining Nanoporous Photonic Crystals. ACS Appl. Mater. Interfaces 2021.

28. Santos, A.; Pereira, T.; Law, C. S.; Losic, D. Rational Engineering of Nanoporous Anodic Alumina Optical Bandpass Filters. Nanoscale 2016, 8 (12), 14846–14857.
29. Santos, A.; Balderrama, V. S.; Alba, M.; Formentín, P.; Ferré-Borrull, J.; Pallarès, J.; Marsal, L. F. Tunable Fabry-Pérot Interferometer Based on Nanoporous Anodic Alumina for Optical Biosensing Purposes. Nanoscale Res. Lett. 2012, 7, 370.
30. Masuda, Hideki and Fukuda, K. Ordered Metal Nanohole Arrays Made by a Two-Step Replication of Honeycomb Structures of Anodic Al ... Science (80). 1995, 268, 1466–1468.
31. E. Lorenzo, C. J. Oton, N. E. Capuj, M. Ghulinyan, D. Navarro-Urrios, Z. Gaburro and L. Pavesi, Appl. Opt.,2005, 44, 5415–5421.
32. Kumeria, T.; Rahman, M. M.; Santos, A.; Ferre-Borrull, J.; Marsal, L. F.; Losic, D. Structural and Optical Nanoengineering of Nanoporous Anodic Alumina Rugate Filters for Real-Time and Label-Free Biosensing Applications. Anal. Chem. 2014, 86 (3), 1837–1844.
33. Eckstein, C.; Law, S.; Lim, Y.; Kaur, S.; Kumeria, T.; Ferré-Borrull, J.; Abell, A. D.; Marsal, L. F.; Santos, A. Nanoporous Photonic Crystals with Tailored Surface Chemistry for Ionic Copper Sensing . J. Mater. Chem. C 2019, 7, 12278–12289.
34. Santos, A.; Law, C. S.; Pereira, T.; Losic, D. Nanoporous Hard Data: Optical Encoding of Information within Nanoporous Anodic Alumina Photonic Crystals. Nanoscale 2016, 8 (15), 8091–8100.
35. A. Santos, C. S. Law, D. W. C. Lei, T. Pereira and D. Losic, Nanoscale, 2016, 8, 18360–18375.
36. S. E. Kushnir, T. Y. Pchelyakova and K. S. Napolskii. J. Mater. Chem. C, 2018, 6, 12192–12199.
37. López, C. Materials Aspects of Photonic Crystals. Adv. Mater. 2003, 15 (20), 1679–1704.
38. Avrutina, E. A.; Gorfinkel, V. B.; Luryi, S.; Shore, K. A. Appl. Phys. Lett. 1993, 63, 2460−2462.
39. Yoon, J.; Lee, W.; Thomas, E. L. Nano Lett. 2006, 6, 2211−2214.
40. Chena, L.; Toweb, E. Appl. Phys. Lett. 2006, 89, 053125-1− 053125-3.

41. Yan, R. H.; Simes, R. J.; Coldren, L. A. Appl. Phys. Lett. 1989, 55,1946−1948.
42. Zheng, W. J.; Fei, G. T; Wang, B.; Zhang, L. D. Nanoscale Res. Lett. 2009, 4, 665−667
43. Chen, Y.; Santos, A.; Wang, Y.; Kumeria, T.; Li, J.; Wang, C.; Losic, D. Biomimetic Nanoporous Anodic Alumina Distributed Bragg Reflectors in the Form of Films and Microsized Particles for Sensing Applications. ACS Appl. Mater. Interfaces 2015, 7 (35), 19816–19824.
44. Lee, J.; Bae, K.; Kang, G.; Choi, M.; Baek, S.; Yoo, D.-S.; Lee, C.-W.; Kim, K. Graded-lattice AAO photonic crystal heterostructure for high Q refractive index sensing. RSC Adv. 2015, 5, 71770−71777.
45. Wang, Y.; Chen, Y.; Kumeria, T.; Ding, F.; Evdokiou, A.; Losic,D.; Santos, A. Facile synthesis of optical microcavities by a rationally designed anodization approach: tailoring photonic signals by nanopore structure. ACS Appl. Mater. Interfaces 2015, 7, 9879−9888.
46. Yan, P.; Fei, G.-T.; Li, H.; Shang, G.-L.; Wu, B.; Zhang, L.-D. Alumina photonic crystals with defect modes for sensor application. Chin. J. Chem. Phys. 2014, 27, 121−124.
47. Akahane, Y.; Asano, T.; Song, B.-S.; Noda, S. High-Qphotonic nanocavity in a two-dimensional photonic crystal. Nature 2003, 425, 944−947.
48. Ghulinyan, M.; Oton, C. J.; Bonetti, G.; Gaburro, Z.; Pavesi, L. Free-standing porous silicon single and multiple optical cavities. J. Appl. Phys. 2003, 93, 9724−9729.
49. Reece, P. J.; Lérondel, G.; Zheng, W. H.; Gal, M. Optical microcavities with subnanometer linewidths based on porous silicon. Appl. Phys. Lett. 2002, 81, 4895−4897
50. Law, C. S.; Lim, S. Y.; Santos, A. On the precise tuning of optical filtering features in nanoporous anodic alumina distributed Bragg reflectors. Sci. Rep. 2018, 8, 4642.
51. Law, C. S.; Lim, S. Y.; Macalincag, R. M.; Abell, A. D.; Santos, A. Light-Con Fi Ning Nanoporous Anodic Alumina Microcavities by Apodized Stepwise Pulse Anodization. ACS Appl. Nano Mater. 2018, 1, 4418–4434.

52. Ruminski, A. M.; Moore, M. M.; Sailor, M. J. Humidity-Compensating Sensor for Volatile Organic Compounds Using Stacked Porous Silicon Photonic Crystals. Adv. Funct. Mater. 2008, 18 (21), 3418−3426.
53. Meade, S. O.; Yoon, M. S.; Ahn, K. H.; Sailor, M. J. PorousSilicon Photonic Crystals as Encoded Microcarriers. Adv. Mater. 2004, 16 (20), 1811−1814.
54. Santos, A. Nanoporous Anodic Alumina Photonic Crystals: Fundamentals, Developments and Perspectives. J. Mater. Chem. C 2017, 5 (23), 5581−5599.
55. Macias, G.; Ferré-Borrull, J.; Pallarès, J.; Marsal, L. F. 1-D Nanoporous Anodic Alumina Rugate Filters by Means of Small Current Variations for Real-Time Sensing Applications. Nanoscale Res. Lett. 2014, 9 (1), 315.
56. Kumeria, T.; Santos, A.; Losic, D. Nanoporous Anodic Alumina Platforms: Engineered Surface Chemistry and Structure for Optical Sensing Applications. Sensors 2014, 14 (7), 11878−11918.
57. Sahel, S.; Amri, R.; Gamra, D.; Lejeune, M.; Benlahsen, M.; Zellama, K.; Bouchriha, H. Effect of Sequence Built on Photonic Band Gap Properties of One-Dimensional Quasi-Periodic Photonic Crystals: Application to Thue-Morse and Double-Period Structures. Superlattices Microstruct. 2017, 111, 1−9.
58. Shen, H.; Wang, Z.; Wu, Y.; Yang, B. One-Dimensional Photonic Crystals: Fabrication, Responsiveness and Emerging Applications in 3D Construction. RSC Adv. 2016, 6 (6), 4505−4520.
59. Kelly, T. L.; Garcia Sega, A.; Sailor, M. J. Identification and Quantification of Organic Vapors by Time-Resolved Diffusion in Stacked Mesoporous Photonic Crystals. Nano Lett. 2011, 11 (8), 3169−3173.
60. Santos, A.; Yoo, J. H.; Rohatgi, C. V.; Kumeria, T.; Wang Y.; Losic, D. Realisation and Advanced Engineering of True Optical Rugate Filters Based on Nanoporous Anodic Alumina by Sinusoidal Pulse Anodisation. Nanoscale 2016, 8 (3), 1360−1373.
61. Lee, J.; Bae, K.; Kang, G.; Choi, M.; Baek, S.; Yoo, D.-S.; Lee, C.-W.; Kim, K. Graded-Lattice AAO Photonic Crystal Heterostructure for High Q Refractive Index Sensing. RSC Adv. 2015, 5, 71770−71777.

62. Wang, Y.; Chen, Y.; Kumeria, T.; Ding, F.; Evdokiou, A.; Losic, D.; Santos, A. Facile Synthesis of Optical Microcavities by a Rationally Designed Anodization Approach: Tailoring Photonic Signals by Nanopore Structure. ACS Appl. Mater. Interfaces 2015, 7, 9879−9888.
63. Santos, A.; Yoo, J. H.; Rohatgi, C. V.; Kumeria, T.; Wang, Y.; Losic, D. Realisation and Advanced Engineering of True Optical Rugate Filters Based on Nanoporous Anodic Alumina by Sinusoidal Pulse Anodisation. Nanoscale 2016, 8, 1360−1373.
64. Eckstein, C.; Law, C. S.; Lim, S. Y.; Kaur, S.; Kumeria, T. Ferré-Borrull, J.; Abell, A. D.; Marsal, L. F.; Santos, A. Nanoporous Photonic Crystals with Tailored Surface Chemistry for Ionic Copper Sensing. J. Mater. Chem. C 2019, 7, 12278−12289.
65. H. A. Macleod, Thin-film optical filters, CRC Press, Taylor & Francis Group, Florida, 2010
66. Santos, A.; Pereira, T.; Law, C. S.; Losic, D. Rational Engineering of Nanoporous Anodic Alumina Optical Bandpass Filters. Nanoscale 2016, 8 (12), 14846–14857.
67. Santos, A.; Kumeria, T.; Losic, D. Optically Optimized Photoluminescent and Interferometric Biosensors Based on Nanoporous Anodic Alumina: A Comparison. 2013.
68. Santos, A.; Kumeria, T.; Losic, D. Nanoporous Anodic Alumina: A Versatile Platform for Optical Biosensors. Materials (Basel). 2014, 7 (6), 4297–4320.
69. Kumeria, T.; Santos, A.; Losic, D. Nanoporous Anodic Alumina Platforms: Engineered Surface Chemistry and Structure for Optical Sensing Applications. Sensors 2014, 14 (7), 11878–11918. https://doi.org/10.3390/s140711878.
70. Kumeria, T.; Santos, A.; Losic, D. Nanoporous Anodic Alumina Platforms: Engineered Surface Chemistry and Structure for Optical Sensing Applications. Sensors 2014, 14 (7), 11878–11918.
71. Shang, G. L.; Fei, G. T.; Zhang, Y.; Yan, P.; Xu, S. H.; Zhang, L. De. Preparation of Narrow Photonic Bandgaps Located in the near Infrared Region and Their Applications in Ethanol Gas Sensing. J. Mater. Chem. C 2013, 1 (34), 5285–5291.

72. Shang, G.; Fei, G.; Li, Y.; Zhang, L. Influence of Dielectrics with Light Absorption on the Photonic Bandgap of Porous Alumina Photonic Crystals. Nano Res. 2016, 9 (3), 703–712.
73. Homola, J.; Yee, S.S.; Gauglitz, G. Surface plasmon resonance sensors: Review. Sens. Actuators B Chem. 1999, 54, 3–15.
74. Holtz, J.H.; Asher, S.A. Polymerized colloidal crystal hydrogel films as intelligent chemical sensing materials. Nature 1997, 389, 829–832.
75. Dickinson, T.A.; White, J.; Kauer, J.S.; Walt, D.R. A chemical-detecting system based on a cross-reactive optical sensor array. Nature 1996, 382, 697–700.
76. Kumeria, T.; Santos, A.; Rahman, M.M.; Ferré-Borrull, J.; Marsal, L.F.; Losic, D. Advanced structural engineering of nanoporous photonic structures: nanopore architecture to enhance sensing properties. ACS Photonics 2014, 1, 1298–1306
77. Krismastuti, F.S.H.; Bayat, H.; Voelcker, N.H.; Schönherr, H. Real time monitoring of layer-by-layer polyelectrolyte deposition and bacterial enzyme detection in nanoporous anodized aluminum oxide. Anal. Chem. 2015, 87, 3856–3863.
78. Jani, A.M.M.; Kempson, I.M.; Losic, D.; Voelcker, N.H. Dressing in layers: Layering surface functionalities in nanoporous aluminum oxide membranes. Angew. Chem. Int. Ed. 2010, 49, 7933–7937.
79. Ferro, L.M.; Lemos, S.G.; Ferreira, M.; Trivinho-Strixino, F. Use of multivariate analysis on Fabry–Pérot interference spectra of nanoporous anodic alumina (NAA) for optical sensors purposes. Sens. Actuators B Chem. 2017, 248, 718–723.
80. Rajeev, G.; Xifre-Perez, E.; Simon, B.P.; Cowin, A.J.; Marsal, L.F.; Voelcker, N.H. A label-free optical biosensor based on nanoporous anodic alumina for tumour necrosis factor-alpha detection in chronic wounds. Sens. Actuators B Chem. 2018, 257, 116–123.
81. Nemati, M.; Santos, A.; Kumeria, T.; Losic, D. Label-free real-time quantification of enzyme levels by interferometric spectroscopy combined with gelatin-modified nanoporous anodic alumina photonic films. Anal. Chem. 2015, 87, 9016–9024

82. Lee, J.C.; An, J.Y.; Kim, B.W. Application of anodized aluminium oxide as a biochip substrate for a Fabry-Perot interferometer. J. Chem. Technol. Biotechnol. 2007, 82, 1045–1052
83. Pujari, S.P.; Scheres, L.; Marcelis, A.T.; Zuilhof, H. Covalent surface modification of oxide surfaces. Angew. Chem. Int. Ed. 2014, 53, 6322–6356ion
84. Kumeria, T.; Rahman, M.M.; Santos, A.; Ferré-Borrull, J.; Marsal, L.F.; Losic, D. Nanoporous anodic alumina rugate filters for sensing of ionic mercury: Toward environmental point-of-analysis systems. ACS Appl. Mater Inter. 2014, 6, 12971–12978
85. Nemati, M.; Santos, A.; Law, C.S.; Losic, D. Assessment of binding affinity between drugs and human serum albumin using nanoporous anodic alumina photonic crystals. Anal. Chem. 2016, 88, 5971–5980.
86. Chen, Y.; Santos, A.; Wang, Y.; Kumeria, T.; Wang, C.; Li, J.; Losic, D. Interferometric nanoporous anodic alumina photonic coatings for optical sensing. Nanoscale 2015, 7, 7770–7779.
87. Pacholski, C. Photonic crystal sensors based on porous silicon. Sensors 2013, 13, 4694–4713.
88. Guo, D.-L.; Fan, L.-X.; Wang, F.-H.; Huang, S.-Y.; Zou, X.-W. Porous anodic aluminum oxide Bragg stacks as chemical sensors. J. Phys. Chem. C 2008, 112, 17952–17956.
89. An, Y.-Y.; Wang, J.; Zhou, W.-M.; Jin, H.-X.; Li, J.-F.; Wang, C.-W. The preparation of high-quality alumina defective photonic crystals and their application of photoluminescence enhancement. Superlattices Microstruct. 2018, 119, 1–8.
90. Lim, S. Y.; Law, C. S.; Liu, L.; Markovic, M.; Hedrich, C.; Blick, R. H.; Abell, A. D.; Zierold, R.; Santos, A. Electrochemical Engineering of Nanoporous Materials for Photocatalysis: Fundamentals, Advances, and Perspectives. Catalysts 2019, 9 (12), 1–34.
91. Kapruwan, P.; Acosta, L. K.; Ferré-Borrull, J.; Marsal, L. F. Optical Platform to Analyze a Model Drug-Loading and Releasing Profile Based on Nanoporous Anodic Alumina Gradient Index Filters. Nanomaterials 2021, 11 (3), 1–16.

92. Fox, M. A.; Dulay, M. T. Heterogeneous Photocatalysis. Chem. Rev. 1993, 93, 341−35.
93. Qu, Y.; Duan, X. Progress, challenge and perspective of heterogeneous photocatalysts. Chem. Soc. Rev. 2013, 42, 2568–2580
94. Lim, S. Y.; Law, C. S.; Markovic, M.; Kirby, J. K.; Abell, A. D.; Santos, A. Engineering the Slow Photon Effect in Photoactive Nanoporous Anodic Alumina Gradient-Index Filters for Photocatalysis. ACS Appl. Mater. Interfaces 2018, 10, 24124−24136.
95. Lim, S.Y.; Law, C.S.; Liu, L.; Markovic, M.; Abell, A.D.; Santos, A. Integrating surface plasmon resonance and slow photon effects in nanoporous anodic alumina photonic crystals for photocatalysis. Catal. Sci. Technol. 2019, 9, 3158–3176.
96. Zhang, Z.; Wang, P. Optimization of photoelectrochemical water splitting performance on hierarchical TiO2 nanotube arrays. Energy Environ. Sci. 2012, 5, 6506–6512
97. Meng, S.; Li, D.; Fu, X.; Fu, X. Integrating photonic bandgaps with surface plasmon resonance for the enhancement of visible-light photocatalytic performance. J. Mater. Chem. A 2015, 3, 23501–23511
98. Lim, S. Y.; Law, C. S.; Markovic, M.; Marsal, L. F.; Voelcker, N. H.; Abell, A. D.; Santos, A. Rational Management of Photons for Enhanced Photocatalysis in Structurally-Colored Nanoporous Anodic Alumina Photonic Crystals. ACS Appl. Energy Mater. 2019, 2, 1169−1184.
99. Zheng, X.; Meng, S.; Chen, J.; Wang, J.; Xian, J.; Shao, Y.; Fu, X.; Li, D. Titanium dioxide photonic crystals with enhanced photocatalytic activity: Matching photonic band gaps of TiO2 to the absorption peaks of dyes. J. Phys. Chem. C 2013, 117, 21263–21273.
100. Zhang, L.; Baumanis, C.; Robben, L.; Kandiel, T.; Bahnemann, D. Bi2WO6 inverse opals: Facile fabrication and efficient visible-light driven photocatalytic and photoelectrochemical water-splitting activity. Small 2011, 7, 2714–2720.

101. Li, X.; Zhen, X.; Meng, S.; Xian, J.; Shao, Y.; Fu, X.; Li, D. Structuring β-Ga2O3 photonic crystal photocatalyst for efficient degradation of organic pollutants. Environ. Sci. Technol. 2013, 47, 9911–9917.
102. Meng, S.; Li, D.; Wang, P.; Zheng, X.; Wang, J.; Chen, J.; Fang, J.; Fu, X. Probing photonic effect on photocatalytic degradation of dyes based on 3D inverse opal ZnO photonic crystal. RSC Adv. 2013, 3, 17021–17028.
103. Curti, M.; Schneider, J.; Bahnemann, D.W.; Mendive, C.B. Inverse opal photonic crystals as a strategy to improve photocatalysis: Underexplored questions. J. Phys. Chem. Lett. 2015, 6, 3903–3910.
104. Lee, C.-Y.; Schmuki, P. Engineering of Self-Organizing Electrochemistry: Porous Alumina and Titania Nanotubes. In Electrochemical Engineering Across Scales: From Molecules to Proceses; Alkire, R. C., Bartlett, P. N., Lipkowski, J., Eds.; John Wiley & Sons: Weinheim, 2015; Vol. 15, pp 145−192.
105. Wu, J.; Liu, B.; Ren, Z.; Ni, M.; Li, C.; Gong, Y.; Qin, W.; Huang, Y.; Sun, C. Q.; Liu, X. CuS/RGO Hybrid Photocatalyst for Full Solar Spectrum Photoreduction from UV/Vis to Near-Infrared Light. J. Colloid Interface Sci. 2018, 517,80−85.
106. Liu, L.; Lim, S. Y.; Law, C. S.; Jin, B.; Abell, A. D.; Ni, G.; Santos, A. Engineering of Broadband Nanoporous Semiconductor Photonic Crystals for Visible-Light-Driven Photocatalysis. ACS Appl. Mater. Interfaces 2020, 12 (51), 57079–57092.
107. S. Y. Lim, C. S. Law, L. Liu, M. Markovic, A. D. Abell and A. Santos, Catal. Sci. Technol., 2019, 9, 3158–3176.
108. Porta-i-Batalla, M.; Eckstein, C.; Xifré-Pérez, E.; Formentín, P.; Ferré-Borrull, J.; Marsal, L.F. Sustained, Controlled and Stimuli- Responsive Drug Release Systems Based on Nanoporous Anodic Alumina with Layer-by-Layer Polyelectrolyte. Nanoscale Res. Lett. 2016, 11, 1–9
109. Deshmukh, P.K.; Ramani, K.P.; Singh, S.S.; Tekade, A.R.; Chatap, V.K.; Patil, G.B.; Bari, S.B. Stimuli-sensitive layer-by-layer (LbL) self-assembly systems: Targeting and biosensory applications. J. Control. Release 2013, 166, 294–306

110. Ariga, K.; McShane, M.; Lvov, Y.M.; Ji, Q.; Hill, J.P. Layer-by-layer assembly for drug delivery and related applications. Expert Opin. Drug Deliv. 2011, 8, 633–644.
111. Kapruwan, P.; Acosta, L. K.; Ferré-Borrull, J.; Marsal, L. F. Optical Platform to Analyze a Model Drug-Loading and Releasing Profile Based on Nanoporous Anodic Alumina Gradient Index Filters. Nanomaterials 2021, 11 (3), 1–16.
112. Ter Maat, J.; Regeling, R.; Ingham, C.J.; Weijers, C.A.; Giesbers, M.; de Vos, W.M.; Zuilhof, H. Organic modification and subsequent biofunctionalization of porous anodic alumina using terminal alkynes. Langmuir 2011, 27, 13606–13617.
113. Chen, Y.; Santos, A.; Wang, Y.; Kumeria, T.; Ho, D.; Li, J.; Wang, C.; Losic, D. Rational design of photonic dust from nanoporous anodic alumina films: A versatile photonic nanotool for visual sensing. Sci. Rep. 2015, 5, 12893.
114. Guo, D.-L.; Fan, L.-X.; Wang, F.-H.; Huang, S.-Y.; Zou, X.-W. Porous anodic aluminum oxide Bragg stacks as chemical sensors. J. Phys. Chem. C 2008, 112, 17952–17956.
115. Ruiz-Clavijo, A.; Tsurimaki, Y.; Caballero-Calero, O.; Ni, G.; Chen, G.; Boriskina, S.V.; Martín-González, M. Engineering a full gamut of structural colors in all-dielectric mesoporous network metamaterials. ACS Photonics 2018, 5, 2120–2128.
116. Acosta, L. K.; Bertó-Roselló, F.; Xifre-Perez, E.; Santos, A.; Ferré-Borrull, J.; Marsal, L. F. Stacked Nanoporous Anodic Alumina Gradient-Index Filters with Tunable Multispectral Photonic Stopbands as Sensing Platforms. ACS Appl. Mater. Interfaces 2019, 11 (3), 3360–3371.

Chapter 4. Nanoporous Anodic Alumina Photonic Structures with Multi-Spectral Photonic Bands

UNIVERSITAT ROVIRA I VIRGILI
ENGINEERING OF PHOTONIC STRUCTURES BASED ON NANOPOROUS ANODIC ALUMINA AS AN OPTICAL SENSING PLATFORM
Laura Karen Acosta Capilla

This chapter presents the development and optical engineering of stacked nanoporous anodic alumina photonic structures with multispectral bands. (NAA-MPSs) with tunable multi-spectral photonic stopbands for sensing applications. The structure of these photonic crystal (PC) is formed by stacked layers of NAA produced with sinusoidally modified effective medium. The progressive modification of the sinusoidal period during the anodization process enables the generation and precise tuning of the characteristic photonic stopbands (PSB) (i.e., one per sinusoidal period in the anodization profile) of these PC structures.

4.1 Introduction

The design and engineering of nanostructures with innovative architectures and materials can pave the way for controlling light-matter interactions at the nanoscale in novel ways. These nanostructures would enable new opportunities to develop advanced materials for a plethora of applications, including optical chemical and biosensing[1–4], drug delivery[5,6], and photonic encryption[7]. Photonic crystals (PCs) are a class of optical nanostructures with allowed and forbidden photonic bands that modify the movement of photons by altering the dispersion of electromagnetic waves when photons travel across de PC´s structure.

PCs modulate the flow of light when photons travel across the material. These light-matter interactions can be tuned with accuracy by engineering the PC´s structure, which features regularly distributed regions of high and low refractive index in one, two or three dimensions [8–16]. PCs can be produced with different architectures and materials to attain light modulation across the broad range of spectral regions (from UV to IR),

depending on the application needs [17–22]. Of all PC architectures, gradient index filters (GIFs) are PCs that are typically used as selective filters due to their narrow photonic band.[23] These photonic structures have also been explored as platforms to develop highly sensitive optical sensors.[24] When the effective medium of gradient-index filters is changed, the characteristic band undergoes spectral shifts that can be used as sensing principle for a variety of optical sensing systems.[25]

Nanoporous anodic alumina (NAA) is a promising base material for the fabrication of PCs. NAA is formed by the electrochemical oxidation (anodization) of aluminum, a cost-effective and fully scalable process compatible with conventional micro- and nanofabrication approaches that allows the precise control over the geometry and distribution of the pores[26,27]. The optical properties of NAA rely intrinsically upon its nanoporous architecture. Therefore, to engineer the nanoporous structure of NAA provides novel means of modulating its refractive index in a multi-dimensional fashion to fabricate advanced materials with unique optical properties to guide, reflect, transmit, emit, and enhance incidence light.[28,29].

Furthermore, NAA has high chemical and physical stability, provides stable optical signals without further surface passivation and its surface chemistry can be easily modified with a broad range of functional molecules for multiple applications, including chemo- and biosensing, drug delivery, optical encoding, theranostics implants[30,31], catalysis and electromagnetism[32,33]. NAA is particularly interesting for the development of optical sensing platforms since it is optically active (i.e., can alter the motion of photons in different ways) and its nanopores can work as

nanocontainers to accommodate analytes of interest. NAA can be modified with functional molecules to provide selectivity toward a broad range of analytes and its nanopore geometry can be engineered to increase the effective surface area for binding events.[34–43] To fabricate PCs with multiple narrow photonic stopbands at different spectral positions remains challenging and to date, only a few proof-of-concept studies have realized this class of PCs. For instance, Sailor et al[44,45], and Santos et al[46] developed porous silicon and NAA-PC structures respectively with multiple photonic stopbands at different spectral positions.

These PCs were obtained by averaging the sum of multiple sinusoidal waves into a single complex waveform, which was subsequently translated into anodization profiles to engineer the nanoporous structure of these PCs in depth. Each sinusoidal wave determines the position and the reflectance amplitude of a forbidden photonic band or photonic stopband. Multiple-band NAA structures have interesting applications such as optical encoding tags, optical sensing, photonics and photovoltaics [44,47–53]. However, the average sum of multiple sinusoidal waves and their implementation into anodization processes that are effectively translated into modulations of effective refractive index present some limiting drawbacks. When the number of forbidden bands is increased, the reflectance amplitude of each band is reduced. The reflectance amplitude of each forbidden band is proportional to the amplitude of the sinusoidal wave.

Therefore, when the number of bands increases, the multiple averaging reduces the amplitude of each sinusoidal wave proportionally to the number of bands, thus decreasing the reflectance amplitude of all the

bands in the spectrum of these PCs. Therefore, this fabrication approach is amplitude-limited and do not offer enough controllability to generate multiple spectral forbidden bands with high intensity. To overcome this limitation, in this chapter we devise an alternative fabrication method that enables the production of NAA-based PCs featuring multiple forbidden bands at specific spectral positions with higher intensity. Multiple sinusoidal current density waveforms of different period are applied sequentially during anodization to produce composite NAA-PC structures composed of stacked NAA-MPSs. In contrast to previous methods using complex averaged waveforms, the sequential application of sinusoidal anodizing current density periods provides a suitable means of creating NAA-PCs with multiple forbidden bands with high intensity. The flexibility of this novel fabrication method to design and engineer the tunability of multi-spectral photonic stopband in these NAA-PCs is evaluated in real-time. The sensitivity of the effective medium of these PC structures upon changes of the medium filling the pores is systematically assessed to demonstrate the potential of these NAA-PCs as optical sensing platforms.

4.2 Experimental details

4.2.1 Fabrication of Photonic Structures with multi-spectral photonic bands (NAA-MPSs)

Aluminum substrates were cleaned with acetone, water, and ethanol in order to remove all the impurities and grease. Before anodization, aluminum substrates were electropolished in a solution 4:1 v/v of ethanol-perchloric acid at 20 V and 5°C for 6 min, with the stirring direction alternated every 60 s. Subsequently, anodization of aluminum substrates

was carried out in oxalic acid 0.3 M at 5°C by applying a current density–time anodization waveform that modulates the pore diameter in depth, as the NAA layer grows. Finally, the remaining aluminum was removed from the backside of the NAA-MPSs by chemical etching with a saturated solution of HCl and $CuCl_2$ for optical characterization. A set of anodization profiles were generated to produce NAA-MPSs with three forbidden bands positioned at specific wavelengths within the visible region of the spectrum following Equation 4.1.

$$J(t)\begin{cases} J_1 \sin\left(\frac{2\pi}{T_1}t\right) + J_0 & 0 \le t < NT_1 \\ J_1 \sin\left(\frac{2\pi}{T_2}t\right) + J_0 & NT_1 \le t < NT_1 + NT_2 \\ J_1 \sin\left(\frac{2\pi}{T_3}t\right) + J_0 & NT_1 + NT_2 \le t < NT_1 + NT_2 + NT_3 \end{cases} \quad (4.1)$$

where J(t) is the anodization current density at time t, J_1 is the current density amplitude, T_i (i = 1, 2, 3) is the anodization period and J_0 is the offset current density. For this purpose, the anodization current density waveform was formed by three sequential sinusoids with three different pulse periods (i.e., T_1, T_2 and T_3). The rest of the sinusoid parameters such as offset current density (J_0), current density amplitude (J_1) and number de periods (N) were kept constants for all the sinusoids. **Figure 4.1a** shows a conceptual illustration of the fabrication process used to generate multi-spectral NAA-MPSs including a representative anodization profile (**Figure 4.1b**) and schematics of the different layers composing the structure of NAA-MPSs with the corresponding anodization period and the reflection spectrum of a NAA-MPSs with J_0 = 2.6 $mAcm^{-2}$, J_1= 1.3 $mAcm^{-2}$, T_1 = 150, T_2 = 175 and T_3 = 200 s, and N = 100 periods and J_0 = 2.6 $mAcm^{-2}$, J_1= 1.3 $mAcm^{-2}$, T_1 = 170, T_2 = 175 and T_3 = 180 s, and N = 100 periods, with details of the characteristics reflection stop bands (**Figure 4.1c**).

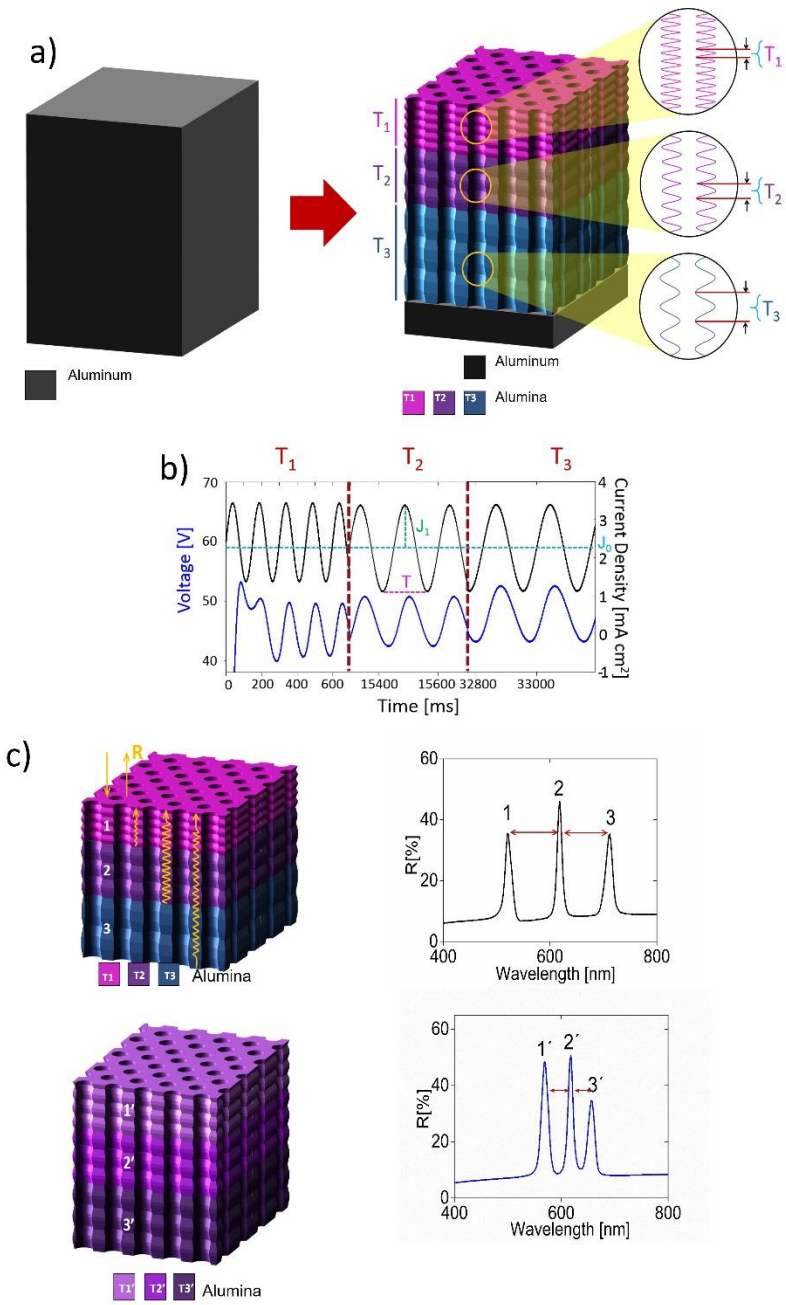

Figure 4.1. Conceptual illustration of the electrochemical approach used to produce multi-spectral NAA-MPSs by sinusoidal current density profile for three photonic stopbands. (a) Fabrication process of multi-spectral NAA-MPSs. (b) Sinusoidal anodization profile of a representative multi-spectral NAA-MPS. (c) Schematics showing the existing relationship between nanoporous architecture and optical properties of multi-spectral NAA-MPSs for the samples produced with J_0= 2.6 mAcm^{-2}, J_1= 1.3 mAcm^{-2}, T_1 =150, T_2 =175 and T_3 =200 s, and N = 100 periods, and J_0= 2.6 mAcm^{-2}, J_1= 1.3 mAcm^{-2}, T_1 =170, T_2 =175 and T_3 =180 s, and N = 100 periods.

Table 4.1 summarizes the fabrication conditions of the different NAA-MPSs produced in this study. The anodization current density waveform profile follows equation 4.1. A pore widening treatment was performed after anodization in order to widen the nanopore diameter in each NAA-MPSs and study the influence of the porosity on their optical properties by wet chemical etching in H_3PO_4 5% wt at 35ºC. The pore widening treatment was applied for different times, from 0 to 25 min, in an interval of 5 min.

Table 4.1. Summary of fabrication conditions and period thickness of samples NAA-MPSs-A, B, C, and D.

Sample	J_0 [$mAcm^2$]	J_1 [$mAcm^2$]	T_1 [s]	T_2 [s]	T_3 [s]	N	Period Thickness [nm]		
							Layer 1	**Layer 2**	**Layer 3**
A	2.6	1.3	150	175	200	1	180	210	240
B	2.6	1.3	160	175	190	1	192	210	228
C	2.6	1.3	165	175	185	1	198	210	222
D	2.6	1.3	170	175	180	1	204	210	216

4.2.2 Optical Characterization of Multi-Spectral Photonic Structures

The reflection spectra of multi-spectral NAA-MPSs across the UV-visible-NIR spectrum were measured at 8º of incidence angle with a resolution of 2 nm in a Perkin Elmer UV-Visible-NIR Lambda 950 spectrophotometer. The effective medium of these NAA-PCs was assessed in real-time by quantifying spectral shifts in the positions of the characteristics photonic stopbands of NAA-MPSs upon infiltration with D-glucose solutions of different refractive index. This process was performed in real-time in a

flow cell made of acrylic plastic. Reflectance spectra of multi-spectral NAA-MPSs were obtained using a halogen light source and a spectrometer. Light was directed onto the surface of NAA-MPSs at normal angle through a bifurcated fiber optic cable consisting of six illuminating waveguides and one reading waveguide coupled to an optical lens that focused the light on the top of the NAA-MPSs. The light reflected was collected by the spectrometer, which recorded one spectrum every 2 s. Reflectance spectra were acquired for the wavelength range 400-800 nm.

The sensitivity of the effective medium of the NAA-MPSs was assessed by infiltrating their nanoporous structure with glucose solutions at different concentrations (0.025, 0.05, 0.125, 0.250, 0.50, 0.75, and 1M). Upon the infiltration, the characteristic forbidden bands undergo spectral shifts due to changes in the refractive index of the medium filling the nanopores. These changes are quantified in real time using deionized water (DI) as a baseline at constant rate of 500 µl min^{-1}, between each infiltration a washing step with (DI).

The interferometric color of multi-spectral NAA-MPSs was characterized by digital pictures, acquired by a Canon EOS 700D digital camera equipped with Tamron 90 mm F2.8 VC USD macro mount lens with autofocus function under natural light illumination.

4.2.3 Structural Characterization of NAA-MPSs

The structural characterization of multi-spectral NAA-MPSs was performed using an environmental scanning electron microscope (ESEM FEI Quanta 600) operating at an accelerating voltage between 20 and 25 keV. ESEM images were analyzed by ImageJ software.

4.2.4 Modelling of NAA-MPSs

The optical properties of multi-spectral NAA-MPSs were modelled using an effective medium approximation (EMA) and the transfer matrix method (TMM). The effective refractive index of each layer in the structure of NAA-MPSs was calculated using the Looyenga-Landau-Lifshitz (3L) formula in combination with that reported from Bartzsch et al.[54,55] Calculation of the reflectance spectra was performed by means of the transfer matrix method using MatLab® software.

4.3 Results and Discussion

4.3.1 Fabrication and structural Characterization of NAA-MPSs

Figure 4.2 shows a representative anodization current density profile for each T_i applied during the fabrication of multi-spectral NAA-MPSs and the measured voltage response of the system. This graph reveals that the anodization voltage (output) follows the sinusoidal variations of the applied anodization current density (input) with a certain delay.

Anodization is an electrochemical process that relies on the flow of the electronic and ionic species across the oxide barrier layer located at the nanopores' bottom. Dynamic modifications of the anodizing current density alter the steady flow of electronic and ionic species across the oxide barrier layer, which needs a recovery time to achieve its equilibrium state again. This time delay depends on the thickness of the oxide barrier layer and the level of anodizing current density change[20,56,57].

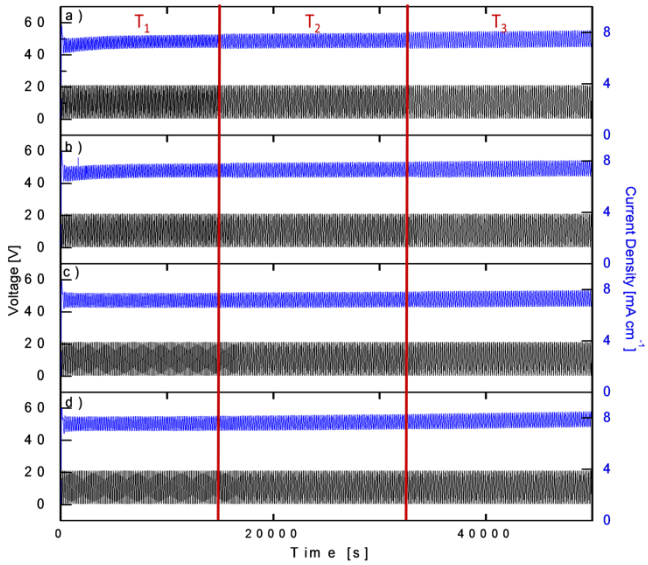

Figure 4.2. Evolution of the anodization current density and voltage during the fabrication of NAA-MPSs. (a) Anodization voltage and current density profile of sample NAA-MPSs-A J_0 = 2.6 mAcm^{-2}, J_1= 1.3 mAcm^{-2}, T_1 = 150, T_2 = 175 and T_3 = 200 s and N = 100 periods. (b) NAA-MPSs-B J_0 = 2.6 mAcm^{-2}, J_1= 1.3 mAcm^{-2}, T_1= 160, T_2= 175 and T_3 =190 s and N= 100 periods. (c) NAA-MPSs-C J_0 = 2.6 mAcm^{-2}, J_1= 1.3 mAcm^{-2}, T_1= 165, T_2= 175 and T_3 =185 s and N= 100 periods. (d) NAA-MPSs-D J_0 = 2.6 mAcm^{-2}, J_1= 1.3 mAcm^{-2}, T_1= 170, T_2 = 175 and T_3 = 180 s and N= 100 periods.

It is remarkable that the amplitude of the measured voltage increases with the anodization period (i.e., T_1, T_2 and T_3) despite of keeping constant the rest of the parameters (J_0 and J_1). From this analysis, it is inferred that the porous layer growth has a dynamic behavior governed by a characteristic reaction time established by the anodization period. The anodization current density sinusoidal waves featuring three sequentially increasing anodization periods are translated into the material's structure as stacked PCs based on NAA-MPSs in the same structure.

For each NAA-PC embedded within the structure of the multi-spectral NAA-MPS, the pore diameter varies sinusoidally in depth. The optical response of the composite NAA-MPSs presents several forbidden bands, one for each NAA-MPS composing the overall PC structure**. Figure 4.3**

shows representative ESEM images of a representative multi-spectral NAA-MPS produced in this study. The top view image shows nanopores randomly distributed across the surface of the PC structure **(Figure 4.3a)** the pore average of this sample (NAA-MPSs-A) is ~45 nm due to the pore widening treatment of 10 minutes. The general cross section of the samples shown in **Figure 4.3b** reveals the oscillating pattern in depth of the pore diameter**. Figure 4.3c** shows a magnified view of the yellow circle in **figure 4.3b**. The pore morphology of the NAA-MPSs induces a modification in depth of the porosity, which results in a sinusoidal variation of the effective refractive index in depth.

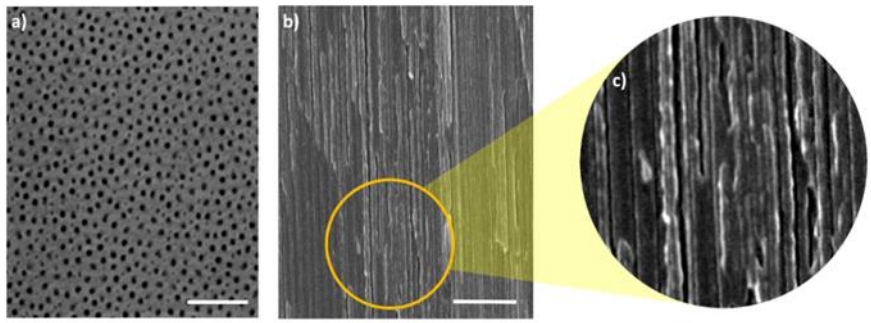

Figure 4.3. Structural characterization of a NAA-MPSs- produced with offset density current J_0= 2.6 mAcm^{-2}, amplitude density current J_1=1.3 mAcm^{-2}, N = 100 periods, T_1= 150, T_2=175, T_3= 200 s and pore widening time of 10 min (a) ESEM top view (scale bar: 1 µm). (b) ESEM General cross section (scale bar: 2 µm). (c) Magnified view of yellow circle of NAA-MPSs.

An EMA (effective medium approximation) model was employed to design the NAA-MPSs structure as a multilayer system and provide a mechanistic explanation of the optical properties of multi-spectral NAA-MPSs. The pore diameter can be precisely controlled by the pore widening time from 0, 5, 10, 15, 20 and 25 min, which correspond to pore diameters of 35, 40, 45, 50, 55 and 60 nm, respectively **(Figure 4.4).**

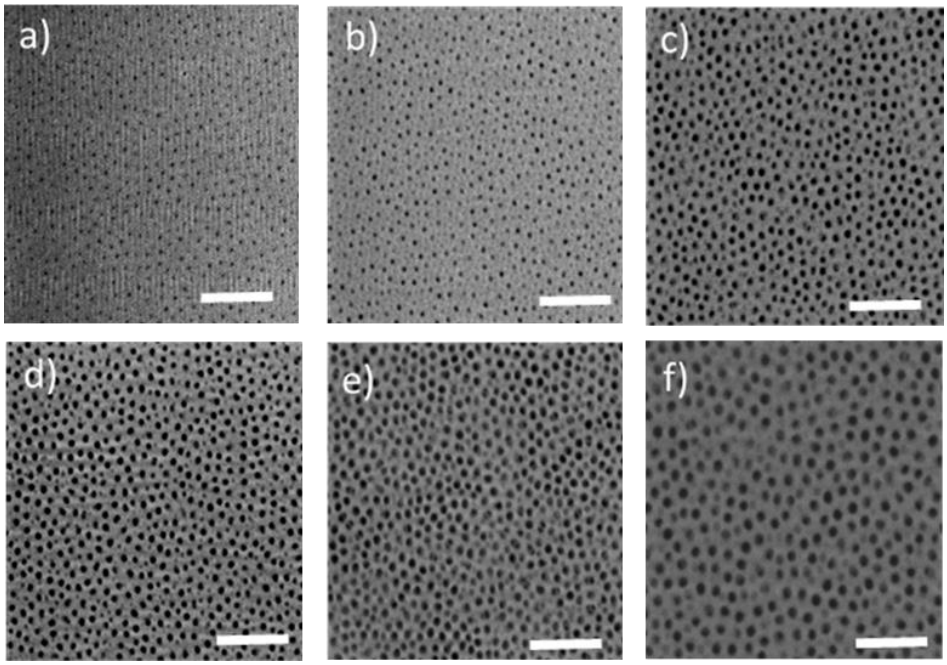

Figure 4.4. Structural characterization of a NAA-MPSs- produced with offset density current J_0= 2.6 mAcm^{-2}, amplitude density current J_1=1.3 mAcm^{-2}, N = 100 periods, T_1= 170, T_2=175, T_3= 180 s (a) ESEM top view of sample with t_{pw}= 0 min (pore diameter= 35 nm) (scale bar: 1 µm). (b) sample with t_{pw}= 5 min (pore diameter= 40 nm), (c) sample with t_{pw}= 10 min (pore diameter= 45 nm), (d) sample with t_{pw}= 15 min (pore diameter= 50 nm), (e) sample with t_{pw}= 20 min (pore diameter= 55 nm), (f) sample with t_{pw}= 25 min (pore diameter= 60 nm).

Figure 4.5 shows an illustration of the transition of the NAA-MPSs pore morphology into an effective graded-index model that follows the pore growth direction. This system is composed of multiple layers with constant refractive index which oscillates between a high refractive index and a low refractive index value along the nanopore's length. NAA-MPSs fabricated in this study present three different forbidden bands, the spectral position of which is established by the anodization period T_i (i=1,2,3). The central anodization period T_2 is kept constant (T_2= 175 s), which means that the position of the central band is approximately the same for all the NAA-MPSs. However, the values of the other two periods

(T_1 and T_3 were systematically modified in each NAA-MPSs in order to demonstrate the tuneability of the bands separation and its effect on the sensitivity of these composite PCs.

As summarized in **Table 4.1**, NAA-MPSs-A were produced with T_1= 150, T_2= 175 and T_3= 200 s, NAA-MPSs-B were fabricated with T_1= 160, T_2= 175 and T_3= 190 s, NAA-MPSs-C with T_1= 165, T_2= 175 and T_3= 185 s, and NAA-MPSs-D with T_1= 170, T_2= 175 and T_3=180 s.

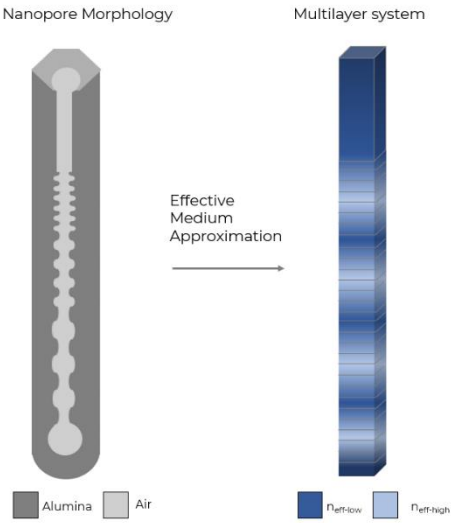

Figure 4.5. Transition of the NAA-MPS nanopore morphology towards a multilayered system in which the constant effective refractive index of each layer varies between $n_{eff-low}$ and $n_{eff-high}$.

4.3.2 Optical characterization and modelling of NAA-MPSs

All the studied multi-spectral NAA-MPSs were fabricated with J_0=2.6 $mAcm^{-2}$, J_1= 1.3 $mAcm^{-2}$ with constant number of periods (N = 100 periods) whereas the values of the three periods T_i vary from one to the other. Figure 5a shows the reflectance spectra of multi-spectral NAA-MPSs with varying T_i. Three forbidden bands can be clearly observed for all these

NAA-MPSs, which show a narrow width, with an average of full width and half maximum (FWHM) between 12 to 20 nm. It can be observed that the central forbidden band is positioned at the same wavelength for all the multi-spectral NAA-MPSs since all of them were fabricated with the same T_2 (175 s).

On the contrary, T_1 and T_3 were systematically modified to demonstrate the tuneability of this class of PC system across the visible spectrum. The position of the forbidden bands depends on the anodization period, which can be precisely tuned by increasing or decreasing T_1 and T_3 (i.e., red shift –move towards longer wavelengths or blue shift move towards shorter wavelengths).

Figure 4.6a shows the position of the forbidden bands for four different combinations of anodization periods. The excellent repeatability and controllability of the anodization system is observed in this graph as all the NAA-MPSs- present a central forbidden band at 618 ± 1 nm, which is associated with the NAA-MPS produced with T_2= 175 s. For the NAA-MPSs-A, the position of the reflection bands for T_1 = 150 s, T_2 = 175 s, T_3 = 200 s were located at in the 520, 618 and 712 nm, respectively. In the case of NAA-MPSs-B, the forbidden bands were located in 553, 616 and 673 nm, which correspond to T_1=160 s, T_2 = 175 s and T_3 = 190 s, respectively. The position of the forbidden bands of NAA-MPSs-C produced with T_1= 165 s T_2= 175 s and T_3= 185 s were in 570, 618 and 660 nm, respectively. Finally, the reflection bands of NAA-MPSs-D were located in 596, 619 and 640 nm, which correspond to the embedded NAA-MPSs fabricated with T_1= 170 s, T_2= 175 s and T_3= 180 s.

Figure 4.6b shows that the position of the three forbidden bands have a linear dependence with the corresponding anodization period (T_1, T_2 and T_3). These linear fitting make it possible to design the spectral fingerprint of each multi-spectral NAA-MPS (i.e. position of the forbidden bands) across the entire spectrum to fulfil the requirement of different applications. Digital images of these multi-spectral NAA-MPSs reveal that these PCs display vivid interferometric color, which is established by the position of the characteristic reflection bands.

For the samples NAA-MPSs-A, C and D the interferometric color is red while the sample NAA-MPSs-B is green. The interferometric color exhibit by these photonics structures is established by the band located at longer wavelengths 712, 660 and 640 nm for samples NAA.GIFs-A, C, and D respectively and in the case of sample B the interferometric color is given by the closer wavelength 553 nm.

Figure 4.6c shows a compilation of experimental and simulated reflection spectra for the multi-spectral NAA-MPSs fabricated in this study. The simulation results show that the three reflection bands of the multi-spectral NAA-MPS (cyan lines) are in good agreement with the experimental reflection spectra of the samples. These graphs show that the transfer matrix model developed in this study can precisely predict the spectral fingerprint of these complex PCs. This model provides a mechanistic explanation of the light–matter interactions occurring within these PCs, opening new opportunities to design novel PC architectures for specific applications.

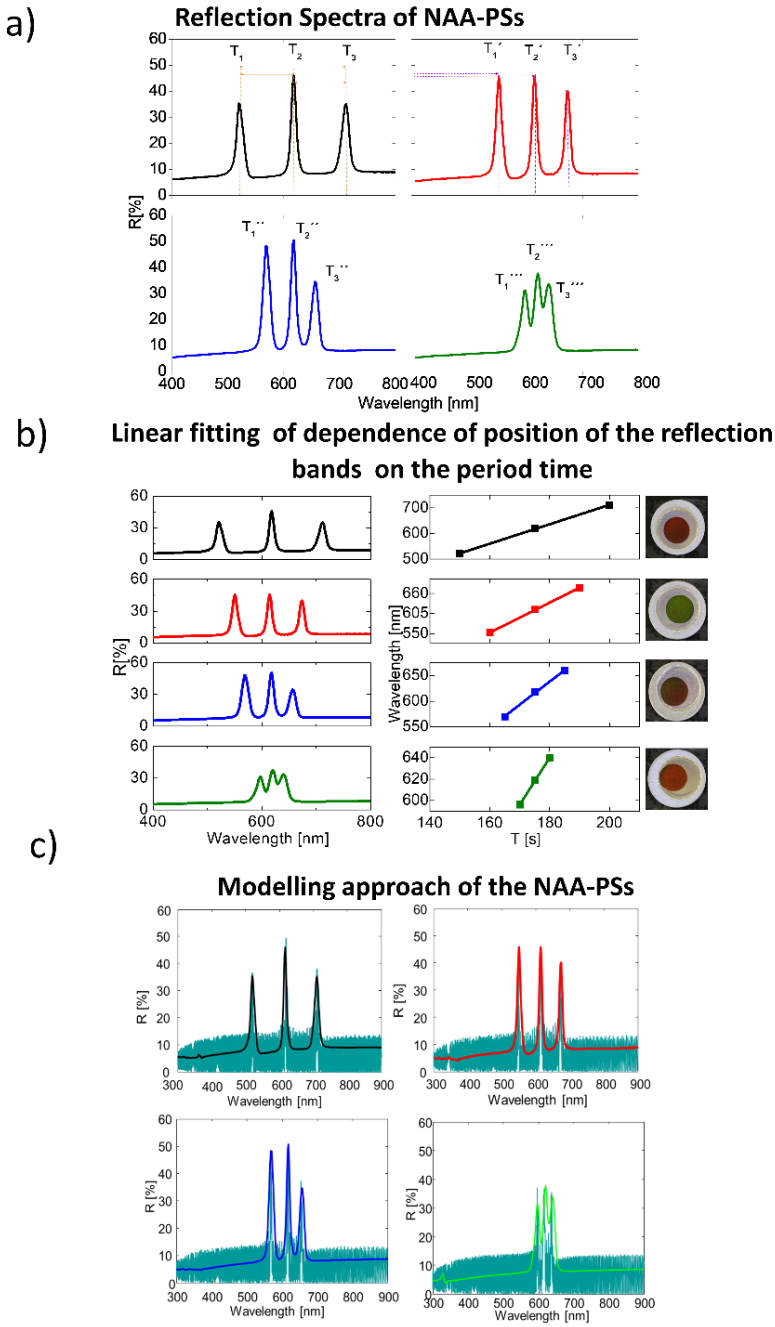

Figure 4.6. Reflection spectra of NAA-MPSs of samples A-D (Described in table 1). (a) Reflection spectra of all samples (NAA-MPS-A-D). (b) Position of the reflection bands of NAA-MPSs in (a-d) as a function of period time (T). The linear regression is plotted for each NAA-MPSs. Digital pictures of NAA-MPSs A-D (c) Modelling approach of all the samples (NAA-MPSs-A-D) cyan lines represent the modelling approximation of the NAA-MPSs spectra and the black, red, blue and green represent de experimental spectra of samples.

4.3.3 Pore Widening Effect in the Optical Properties of Multi-Spectral NAA-MPSs.

To study the effect of the pore widening time on the optical properties of multi-spectral NAA-MPSs, the reflectance spectrum of these NAA-MPSs fabricated with J_0= 2.6 mAcm^{-2}, J_1= 1.3 mAcm^{-2} and T_1= 165, T_2 =170 and T_3=175 s was measured at different pore widening times (t_{pw}): 5, 10, 15, 20 and 25 min, which correspond to nanopore diameters of 35, 40, 45, 50, 55 and 60 nm, respectively **(Figure 4.7).**

Figure 4.7a shows the reflection spectra with t_{pw}. At t_{pw} = 0 (i.e., as-produced NAA-MPSs, average of pore diameter ~35 nm) the position of the reflection bands was located at 578, 606 and 628 nm for T_1= 165 s, T_2= 170 s and T_3= 175 s, respectively. The reflection bands present a maximum reflection intensity of 32.3, 51.8 and 57.8 %, respectively, and a FWHM of 24, 18 and 16 nm. At t_{pw}= 5 min (i.e., pore diameter ~ 40nm), the reflection bands are blue-shifted to 568, 598 and 622 nm, the maximum reflection for these bands were 34.8, 55.2, 60.3 % and their FWHM were 31, 18 and 18 nm, respectively. In the case of t_{pw} = 10 min (i.e., average of pore diameter of 45 nm), the position of the forbidden bands was located at 558, 592 and 618 nm, the maximum reflection for these bands were 46.0, 54.8 and 46.5 %, and the FWHM were 32, 20 and 20 nm, respectively.

For t_{pw} = 15 min (average of pore diameter ~50 nm), the position of the forbidden bands was 546, 582 and 612 nm, the maximum reflection for these bands were 45.4, 52.8, and 43.8 %, and the FWHM of the bands were 35, 21 and 22 nm respectively. The position of the reflection bands for t_{pw} = 20 min (i.e., pore diameter ~55 nm) were 532, 572 and 602 nm,

with a maximum reflection of 42.2, 49.7 and 44.3 % and FWHM of 42, 23 and 23 nm, respectively. At t_{pw}= 25 min (average pore diameter of 60 nm), the position of the forbidden bands was situated at 520, 560 and 590 nm, the maximum reflection of the bands were 38.8, 46.1 and 41.3 % and the FWHM for these forbidden bands were 44, 24 and 24 nm, respectively.

Figure 4.7b shows the linearity between t_{pw} and the position of the three forbidden bands. This graph indicates that the position of the forbidden bands blue shifts linearly when tpw increases from 0 to 25 min. However, the blue shift rate (i.e., slope of linear fitting) depends on the position of the forbidden band: the slope of band 1 is greater than that of bands 2 and 3. The slopes of the fitting lines for the three forbidden bands of multi-spectral NAA-MPSs produced were found to be -2.34 (T_1= 165 s), -1.46 (T_2 = 170 s) and -1.81 (T_3 = 175 s) nm min^{-1}.

The relation between the t_{pw} and the FWHM is presented in **Figure 4.7c**. For band 1, we can observe that a high increment of the FWHM with t_{pw}, whereas for bands 2 and 3 the increment is less marked. For the three bands, the increment of FWHM depends linearly on the pore widening time. The slopes of the fitting lines for the FWHM of the three forbidden bands of multi-spectral NAA-MPSs produced with T_1 = 165 s, T_2 = 170 s and T_3 = 175 s, were found to be 0.78, 0.32 and 0.26 nm min^{-1}, respectively. The difference observed between band 1 and the rest of bands can be explained by observing the NAA structure of the multi-spectral NAA-MPSs. The three bands of these NAA-PCs are generated by three different NAA-MPSs stacked one over another.

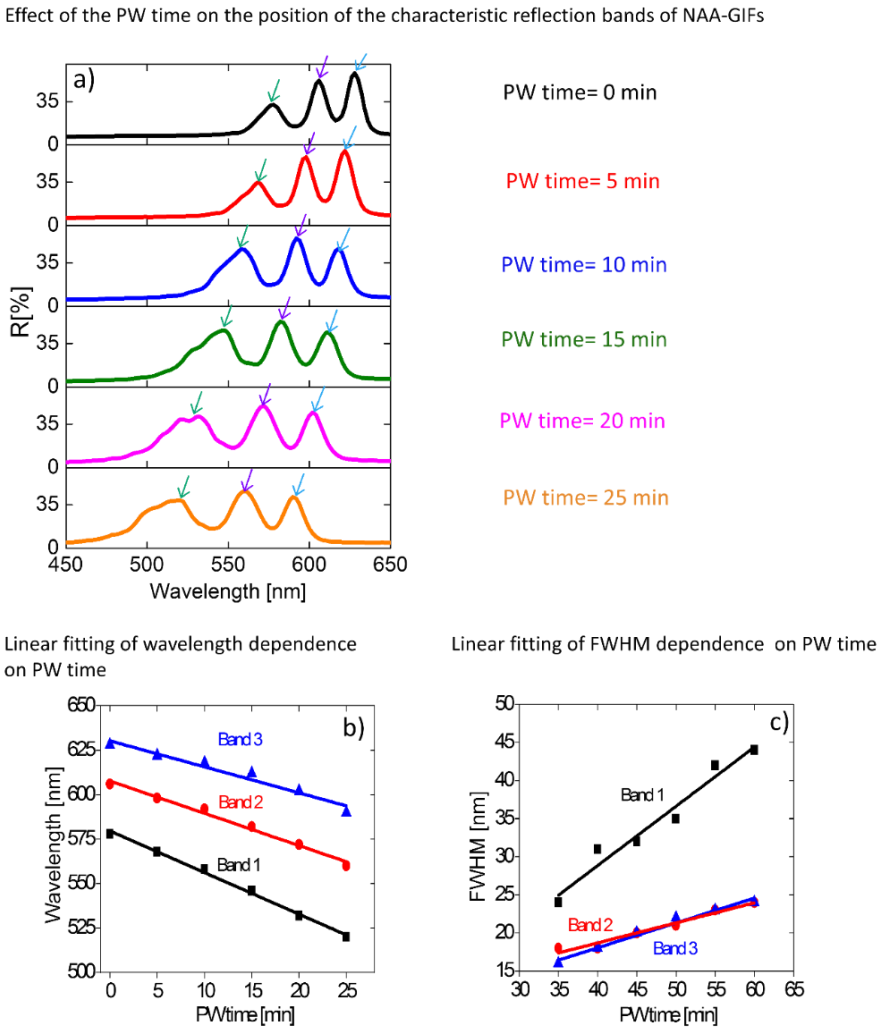

Figure 4.7. (a) Effect of the pore widening on the reflection spectrum of a NAA-MPSs with J_0= 2.6 mAcm^{-2}, J_1= 1.3 mAcm^{-2} and T_1= 165, T_2= 170 and T_3= 175 s was measured for different pore widening times: 0, 5, 10, 15, 20 and 25 min. (b) linear fitting lines showing the dependence between the position of the reflection bands and pore widening time (c) Linear fitting showing the dependence between Full width at half maximum (FWHM) and pore widening time.

Table 4.2 summarizes the effect of the six different t_{pw} on the position of the forbidden bands, their intensity, and their FWHM. The position of the characteristic forbidden bands undergoes a blue shift when the PC structure is etched and the size of its nanopores is widened. The NAA-MPS that generates band 1 is at the top of the composite multi-spectral NAA-

MPSs structure. Chemical etching at the top part of the composite NAA-MPS is more effective than within the nanoporous structure due to limited diffusion of chemical species. Therefore, the top NAA-MPS structure is etched at a slightly faster rate than its counterparts located at lower positions within the composite NAA-MPS. This results in a differential etching rate that leads to distinct blue shifts in the position of the characteristic forbidden bands of the multi-spectral NAA-MPSs. Whereas the other two NAA-MPSs, generating bands 2 and 3, are underneath and their complete NAA structure is affected by the etching dissolution in a similar way.

Table 4.2. Summary of the effect of the pore widening on the reflectance spectrum of NAA-MPSs.

Pore widening time (min)	Average Pore diameter (nm)	Band	λ_{band} (nm)	R_{max} (%)	FWHM (nm)
0	35	1	578	32.3	24
		2	606	51.8	18
		3	628	57.8	16
5	40	1	568	34.8	31
		2	598	55.2	18
		3	622	60.3	18
10	45	1	558	46.0	32
		2	592	54.8	20
		3	618	46.5	20
15	50	1	546	45.4	35
		2	582	52.8	21
		3	612	43.8	22
20	55	1	532	41.2	42
		2	572	49.7	23
		3	602	44.3	23
25	60	1	520	38.8	44
		2	560	46.1	24
		3	590	41.3	24

The average pore diameter also affects the amplitude of the forbidden band and it's FWHM **(Table 4.2).** When increasing the average pore diameter from 35 to 60 nm, the FWHM of band 1 increases from 24 to 44 nm, for band 2 increases from 18 to 24 nm and for band 3 from 16 to 24 nm. The maximum reflectance of the bands increases with the pore diameter until 50 nm, after which the reflectance intensity decreases.

Therefore, two different response regions can be differentiated: the pore diameter increases the maximum reflectance of the forbidden band until 50 nm and decreases beyond this pore size. This phenomenon can be associated with diffusive light scattering by the overall PC structure due to increased porosity.

4.3.4 Assessment of the Sensitivity of the Effective Medium of NAA-MPSs

To study the potential use of multi-spectral NAA-MPSs structures as sensing platforms, we assessed in real-time the spectral shifts in the three characteristic forbidden bands of these NAA-MPSs by filling the pores with analytical solutions D-glucose with different concentrations. The variation of the effective refractive index of the medium filling the nanopores of multi-spectral NAA-MPSs red-shifts the position of the characteristic forbidden bands. These experiments were performed for different pore diameters in order to study the sensitivity of the PC structure when the pore diameter is increased. To this end, first a base line was obtained using deionized water, which was injected into the flow cell for 10 min until a stable base line was achieved. Then, analytical solutions of D-glucose 0.025 – 1.0 M were flowed at a constant rate of 500 µL min^{-1}.

A cleaning step flowing fresh deionized water was carried out between each analytical solution of D-glucose in order to clean the remaining glucose molecules within the pores. **Figure 4.8** shows the assessment of sensitivity of the effective medium of multi-spectral NAA-MPSs. We can observe that the shift of the forbidden band positions increases when the D-glucose concentration increases, which indicates the utility of these PCs for sensing applications.

Figure 4.8a shows a scheme of the infiltration of multi-spectral NAA-MPSs nanopores with different concentration of D-glucose. This infiltration produces a red shift (shift toward higher wavelengths) in the position of the forbidden bands. **Figure 4.8b** shows the real-time measurements of a multi-spectral NAA-MPS with pore diameter of 40 nm (t_{pw} = 5 min). **Figures 4.8c-e** show the linear dependence between the shift of the forbidden bands and the concentration D-glucose for each pore diameter and band structure.

Figure 4.8c shows the fitting lines for band 1 with reflection bands situated between 435 and 500 nm, which correspond to each pore widening time. The sensitivity (S) for each pore diameter in band 1 was 0.91 (35 nm), 1.64 (40 nm), 2.23 (45 nm), 3.15 (50 nm) and 3.07 (55 nm) nm M^{-1} and with a limit of detection of (LOD) 6.8, 1.3, 5.2, 3.5 and 5.5 mM, respectively**.** **Figure 4.8d** shows the results for band 2 (525-590 nm), the sensitivity (S) for each pore diameter of band 2 were 0.97 (35 nm), 1.64 (40 nm), 2.13 (45 nm), 2.90 (50 nm) and 3.23 (55 nm) nm M^{-1}, with a limit of detection of (LOD) 2.2, 1.9, 5.3, 3.7 and 2.8 mM, respectively.

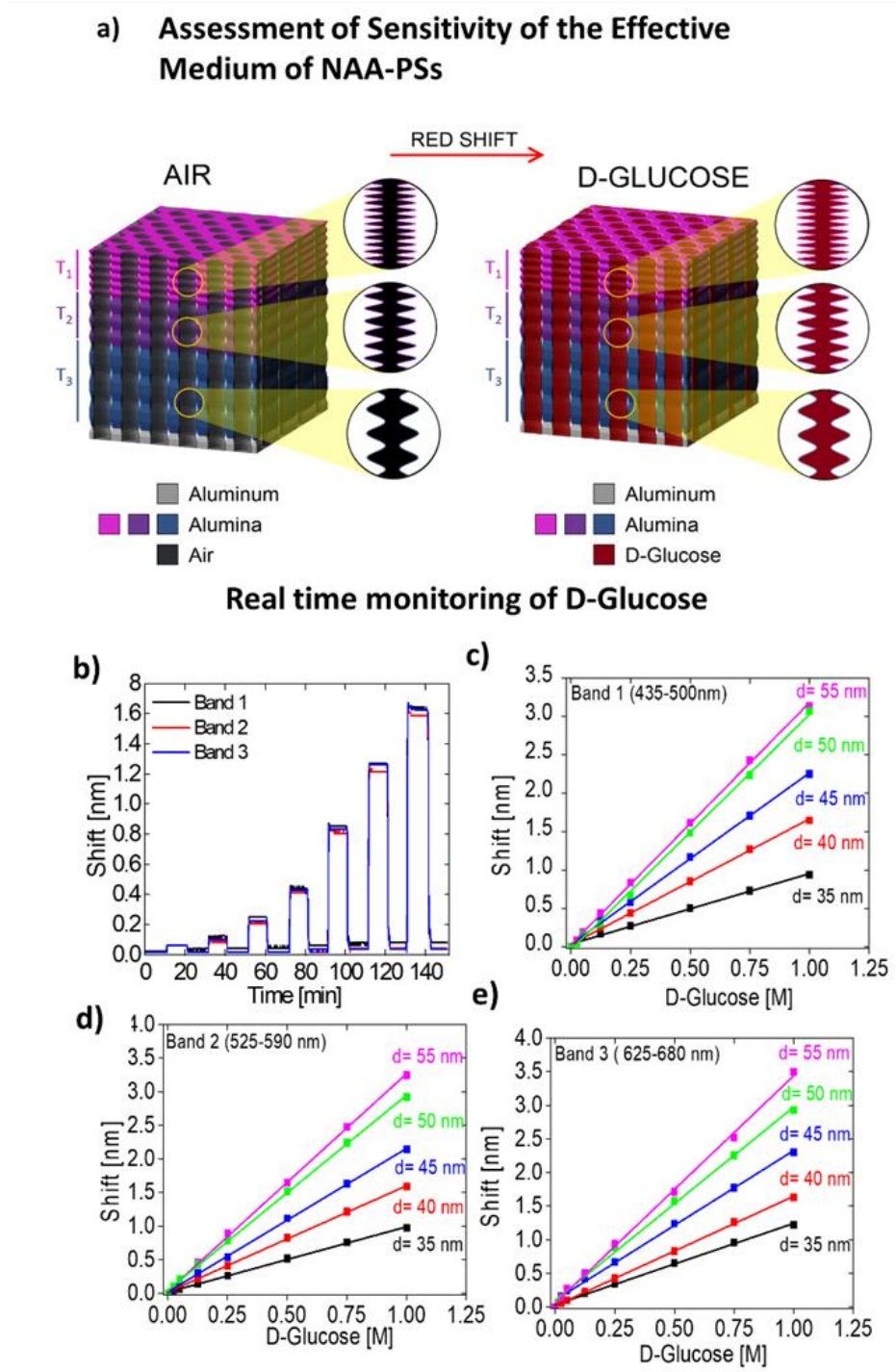

Figure 4.8. (a) Assessment of the effective medium assessment of NAA- GIFs. (b) Real time monitoring of D-Glucose concentrations 0.025, 0.05, 0.125, 0.25, 0.5, 0.75 and 1.0 M for 40 nm of pore diameter. Sensitivity approach for different pore diameters (35, 40, 45, 50 and 55 nm) for (c) band 1, (d) band 2, and (e) band 3.

Figure 4.8e summarizes the results for the band 3 (625-680 nm). The sensitivity (S) of each pore diameter of band 3 were 1.21 (35 nm), 1.63 (40 nm), 2.22 (45 nm), 2.87 (50 nm) and 3.38 (55 nm) nm M^{-1}, with a limit of detection of (LOD) 1.7, 1.8, 6.4, 3.7 and 1.7 mM, respectively.The results of the average of pore diameters of 35 (t_{pw}=0 min), 45(t_{pw}=10 min), 50 (t_{pw}=15 min) and 55 (t_{pw}=20 min) nm are shown in **Figure 4.9.** The infiltration of each analytical solution of D-glucose produces a redshift in the position of the bands. However, this change was reversible due to the lack of a chemical interaction between glucose molecules and the NAA-MPSs surface. **Table 4.3** summarizes the sensitivity and LOD characteristics of the multi-spectral NAA-MPSs obtained from the effective medium assessment.

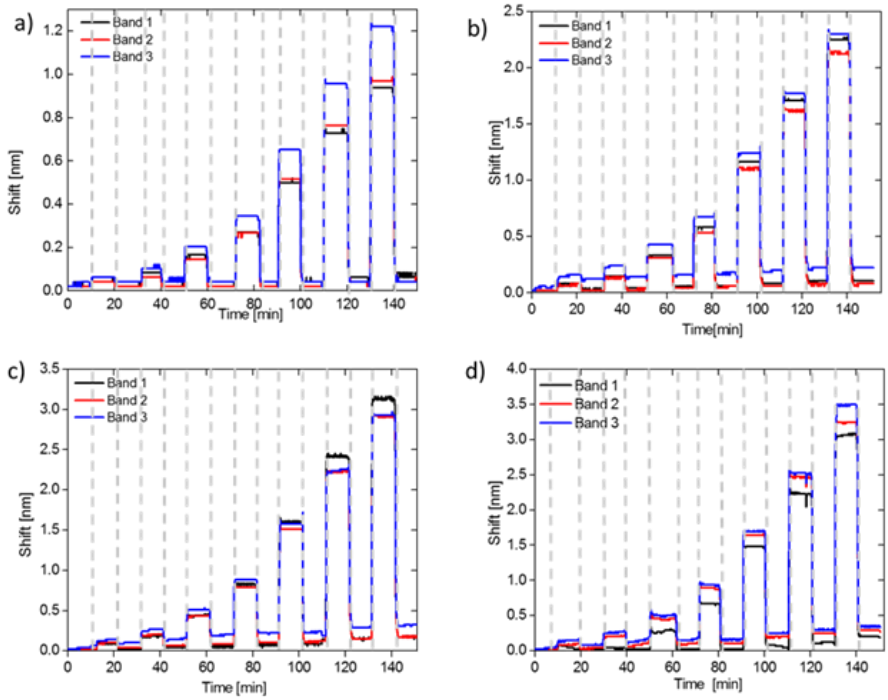

Figure 4.9. Real time monitoring of D-Glucose concentrations 0.025, 0.05, 0.125, 0.25, 0.5, 0.75 and 1M. (a) Pore diameter = 35 nm (t_{pw}= 0min), (b) Pore diameter = 45 nm (t_{pw}= 10min), (c) Pore diameter = 50 nm (t_{pw}= 15min) and (d) Pore diameter = 55 nm (t_{pw}= 20 min).

Table 4.3. Sensitivity and limit of detection (LOD) of NAA-MPSs in the real time monitoring experiments.

Average Pore	Band	S [nm M^{-1}]	LOD [mM]
D = 35 nm (t_{pw} = 0min)	1	0.91	6.8
	2	0.97	2.2
	3	1.21	1.7
D = 40 nm (tpw = 5 min)	1	1.64	1.3
	2	1.58	1.9
	3	1.63	1.8
D = 45 nm (tpw= 10 min)	1	2.23	5.2
	2	2.13	5.3
	3	2.22	6.4
D = 50 nm (tpw= 15 min)	1	3.15	3.5
	2	2.90	3.7
	3	2.87	3.7
D = 55 nm (tpw= 20 min)	1	3.07	5.5
	2	3.23	2.8
	3	3.38	1.7

Figure 4.10 provides a bar chart comparing the sensitivity of the different PC structures. From these results, we can conclude that when the pore diameter in the structure of multi-spectral NAA-MPSs is increased, the shift of the forbidden band position increases linearly in all the cases, being more than three times greater for 55 nm than for 35 nm. Also, it is worthwhile noting that band 3 is in general more sensitive to effective refractive index variations than bands 1 and 2.

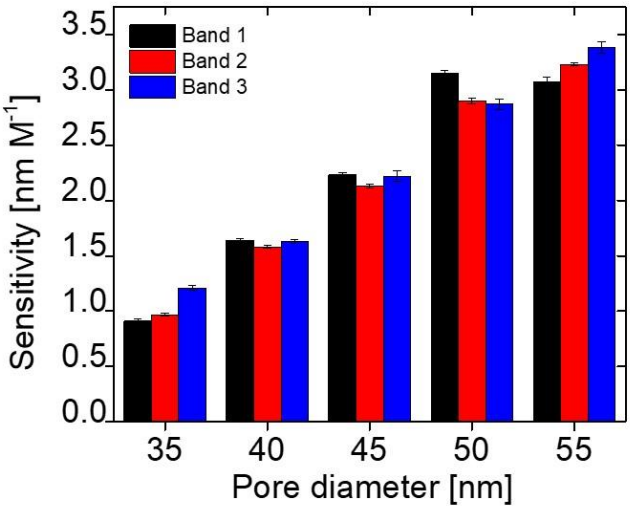

Figure 4.10. Sensitivity of each forbidden band of the NAA-MPSs for the different pore diameters (35, 40, 45, 50 and 55 nm) for the three bands.

4.4 Conclusion

In this chapter, we fabricated stacked photonic crystals based on nanoporous anodic alumina gradient-index filters (NAA-MPSs) with complex optical response by the application of successive sinusoidal anodization current density profiles. The position of the forbidden bands presented by these multi-spectral NAA-MPSs can be accurately tuned by varying the anodization period of the anodization current density waveform. Furthermore, we assess the effect of the porosity of the structure on the reflection spectrum by applying a pore widening chemical etching treatment from 0 to 25 min. The increment of the pore diameter blue-shifts the position of the forbidden bands. A lineal relation between the increments of the pore widening times and the position of the forbidden bands can be observed. The intensity and width of the bands also increases with the pore widening.

We also demonstrated the ability of multi-spectral NAA-MPSs structures for sensing applications by detecting small changes of the effective refractive index due to the fluid filling of the pores. Different concentrations of D-glucose have been successfully detected and quantified in real-time. These real-time experiments, carried out by increasing the average pore diameter from 35 nm to 55 nm, indicate that the sensitivity is different for each forbidden band and it depends on the pore diameter of the multi-spectral NAA-MPS structure: the increment of the pore diameter leads to an enhancement in sensitivity of the photonic crystal structure.

REFERENCES

(1) Yan, P.; Fei, G. T.; Shang, G. L.; Wu, B.; De Zhang, L. Fabrication of One-Dimensional Alumina Photonic Crystals with a Narrow Band Gap and Their Application to High-Sensitivity Sensors. *Journal of Materials Chemistry C* **2013**, *1* (8), 1659–1664.

(2) Bonanno, L. M.; Segal, E. Nanostructured Porous Silicon-Polymer-Based Hybrids: From Biosensing to Drug Delivery. *Nanomedicine* **2011**, *6* (10), 1755.

(3) Santos, A.; Macías, G.; Ferré-Borrull, J.; Pallarès, J.; Marsal, L. F. Photoluminescent Enzymatic Sensor Based on Nanoporous Anodic Alumina. *ACS Appl. Mater. Interfaces* **2012**, *4* (7), 3584–3588.

(4) Lee, J.; Bae, K.; Kang, G.; Choi, M.; Baek, S.; Yoo, D. S.; Lee, C. W.; Kim, K. Graded-Lattice AAO Photonic Crystal Heterostructure for High Q Refractive Index Sensing. *RSC Advances* **2015**, *5* (88), 71770–71777.

(5) Bonifacio, L. D.; Lotsch, B. V.; Puzzo, D. P.; Scotognella, F.; Ozin, G. A. Stacking the Nanochemistry Deck: Structural And Compositional Diversity in One-Dimensional Photonic Crystals. *Advanced Materials* **2009**, *21* (16), 1641–1646.

(6) Anglin, E. J.; Cheng, L.; Freeman, W. R.; Sailor, M. J. Porous Silicon in Drug Delivery Devices and Materials. *Advanced Drug Delivery Reviews* **2008**, *60* (11), 1266–1277.

(7) Santos, A.; Law, C. S.; Pereira, T.; Losic, D. Nanoporous Hard Data: Optical Encoding of Information within Nanoporous Anodic Alumina Photonic Crystals. *Nanoscale* **2016**, *8* (15), 8091–8100.

(8) Zaraska, L.; Stępniowski, W. J.; Ciepiela, E.; Sulka, G. D. The Effect of Anodizing Temperature on Structural Features and Hexagonal Arrangement of Nanopores in Alumina Synthesized by Two-Step Anodizing in Oxalic Acid. *Thin Solid Films* **2013**, *534*, 155–161.

(9) Yagur-Kroll, S.; Schreuder, E.; Ingham, C. J.; Heideman, R.; Rosen, R.; Belkin, S. A Miniature Porous Aluminum Oxide-Based Flow-Cell for Online Water Quality Monitoring Using Bacterial Sensor Cells. *Biosensors and Bioelectronics* **2014**, *64*, 625–632.

(10) Wang, G.; Wang, J.; Li, S. Y.; Zhang, J. W.; Wang, C. W. One-Dimensional Alumina Photonic Crystals with a Narrow Band Gap and Their Applications to High-Sensitivity Concentration Sensor and Photoluminescence Enhancement. *Superlattices and Microstructures* **2015**, *86*, 546–551.

(11) Wang, B.; Fei, G. T.; Wang, M.; Kong, M. G.; Zhang, L. De. Preparation of Photonic Crystals Made of Air Pores in Anodic Alumina. *Nanotechnology* **2007**, *18* (36), 1–4.

(12) Shu, S. W.; Zhang, J.; Tsang, C. K.; Shi, L. G.; Li, Y. Y. Metal-Based Rugate Filters with Strong Visible and near-Infrared Reflectivity. *Applied Physics B: Lasers and Optics* **2012**, *107* (3), 669–673.

(13) Pacholski, C. Photonic Crystal Sensors Based on Porous Silicon. *Sensors* **2013**, *13* (4), 4694–4713.

(14) Masuda, H.; Ohya, M.; Asoh, H.; Nakao, M.; Nohtomi, M.; Tamamura, T. Photonic Crystal Using Anodic Porous Alumina. *Japanese Journal of Applied Physics, Part 2: Letters* **1999**, *38*, 1403–1405.

(15) Macias, G.; Ferré-Borrull, J.; Pallarès, J.; Marsal, L. F. Effect of Pore Diameter in Nanoporous Anodic Alumina Optical Biosensors. *The Analyst* **2015**, *140*, 4848–4854.

(16) Gorelik, V. S.; Sverbil, P. P.; Filatov, V. V.; Bi, D.; Fei, G. T.; Xu, S. H. Transmission Spectra of One-Dimensional Porous Alumina Photonic Crystals. *Photonics and Nanostructures - Fundamentals and Applications* **2018**, *32*, 6–10.

(17) Toccafondi, C.; Thorat, S.; La Rocca, R.; Scarpellini, A.; Salerno, M.; Dante, S.; Das, G. Multifunctional Substrates of Thin Porous Alumina for Cell Biosensors. *Journal of Materials Science: Materials in Medicine* **2014**, *25* (10), 2411–2420.

(18) Santos, A.; Alba, M.; Rahman, M. M.; Formentin, P.; Ferre-Borrull, J.; Pallares, J.; Marsal, L. F. Structural Tuning of Photoluminescence in Nanoporous Anodic Alumina by Hard Anodization in Oxalic and Malonic Acids. *Nanoscale Research Letters* **2012**, *7* (1), 1–12.

(19) Law, C. S.; Lim, S. Y.; Santos, A. On the Precise Tuning of Optical Filtering Features in Nanoporous Anodic Alumina Distributed Bragg Reflectors. *Scientific Reports* **2018**, *8* (4642), 1–16.

(20) Montero-Moreno, J. M.; Belenguer, M.; Sarret, M.; Müller, C. M. Production of Alumina Templates Suitable for Electrodeposition of Nanostructures Using Stepped Techniques. *Electrochimica Acta* **2009**, *54* (9), 2529–2535.

(21) Sweetman, M. J.; Voelcker, N. H. Chemically Patterned Porous Silicon Photonic Crystals towards Internally Referenced Organic Vapour Sensors. *RSC Advances* **2012**, *2* (11), 4620–4622.

(22) Rahman, M. M.; Marsal, L. F.; Pallares, J.; Ferre-Borrull, J. Tuning the Photonic Stop Bands of Nanoporous Anodic Alumina-Based Distributed Bragg Reflectors by Pore Widening. *ACS Applied Materials and Interfaces* **2013**, *5* (24), 13375–13381.

(23) Lorenzo, E.; Oton, C. J.; Capuj, N. E.; Ghulinyan, M.; Navarro-Urrios, D.; Gaburro, Z.; Pavesi, L. Porous Silicon-Based Rugate Filters. *Applied optics* **2005**, *44* (26), 5415–5421.

(24) Nemati, M.; Santos, A.; Law, C. S.; Losic, D. Assessment of Binding Affinity between Drugs and Human Serum Albumin Using Nanoporous Anodic Alumina Photonic Crystals. *Analytical Chemistry* **2016**, *88* (11), 5971–5980.

(25) Siraji, A. A.; Zhao, Y. High-Sensitivity and High-Q-Factor Glass Photonic Crystal Cavity and Its Applications as Sensors. *Optics Letters* **2015**, *40* (7), 1508–1511.

(26) Masuda, Hideki and Fukuda, K. Ordered Metal Nanohole Arrays Made by Two-Step Replication of Honeycomb Structures of Anodic Alumina. *Science* **1995**, *268* (3), 1466–1468.

(27) Ferré-Borrull, J.; Pallarès, J.; Macías, G.; Marsal, L. F. Nanostructural Engineering of Nanoporous Anodic Alumina for Biosensing Applications. *Materials* **2014**, *7* (7), 5225–5253.

(28) Kumeria, T.; Santos, A.; Rahman, M. M.; Ferré-Borrull, J.; Marsal, L. F.; Losic, D. Advanced Structural Engineering of Nanoporous Photonic Structures: Tailoring Nanopore Architecture to Enhance Sensing Properties. *ACS Photonics* **2014**, *1* (12), 1298–1306.

(29) Md Jani, A. M.; Losic, D.; Voelcker, N. H. Nanoporous Anodic Aluminium Oxide: Advances in Surface Engineering and Emerging Applications. *Progress in Materials Science* **2013**, *58* (5), 636–704.

(30) Briggs, E. P.; Walpole, A. R.; Wilshaw, P. R.; Karlsson, M.; Pålsgård, E. Formation of Highly Adherent Nano-Porous Alumina on Ti-Based Substrates: A Novel Bone Implant Coating. *Journal of Materials Science: Materials in Medicine* **2004**, *15* (9), 1021–1029.

(31) McCarthy, J. R.; Jaffer, F. A.; Weissleder, R. A Macrophage-Targeted Theranostic Nanoparticle for Biomedical Applications. *Small* **2006**, *2* (8–9), 983–987.

(32) Lim, S. Y.; Law, C. S.; Markovic, M.; Kirby, J. K.; Abell, A. D.; Santos, A. Engineering the Slow Photon Effect in Photoactive Nanoporous Anodic Alumina Gradient-Index Filters for Photocatalysis. *ACS Applied Materials and Interfaces* **2018**, *10* (28), 24124–24136.

(33) Law, C. S.; Lim, S. Y.; Abell, A. D.; Voelcker, N. H.; Santos, A. Nanoporous Anodic Alumina Photonic Crystals for Optical Chemo- and Biosensing: Fundamentals, Advances, and Perspectives. *Nanomaterials* **2018**, *8* (10), 1–47.

(34) Krismastuti, F. S. H.; Bayat, H.; Voelcker, N. H.; Schönherr, H. Real Time Monitoring of Layer-by-Layer Polyelectrolyte Deposition and Bacterial Enzyme Detection in Nanoporous Anodized Aluminum Oxide. *Analytical Chemistry* **2015**, *87* (7), 3856–3863.

(35) Kumeria, T.; Santos, A.; Losic, D. Ultrasensitive Nanoporous Interferometric Sensors for Label-Free Detection of Gold (III) Ions. *ACS Applied Materials & Interfaces* **2013**, *5*, 11783–11790.

(36) Popat, K. C.; Mor, G.; Grimes, C. A.; Desai, T. A. Surface Modification of Nanoporous Alumina Surfaces with Poly (Ethylene Glycol). *Langmuir* **2004**, *20* (19), 8035–8041.

(37) Santos, A.; Formentín, P.; Pallarès, J.; Ferré-Borrull, J.; Marsal, L. F. Structural Engineering of Nanoporous Anodic Alumina Funnels with High Aspect Ratio. *Journal of Electroanalytical Chemistry* **2011**, *655* (1), 73–78.

(38) Vojkuvka, L.; Santos, A.; Pallarès, J.; Ferré-Borrull, J.; Marsal, L. F.; Celis, J. P. On the Mechanical Properties of Nanoporous Anodized Alumina by Nanoindentation and Sliding Tests. *Surface and Coatings Technology* **2012**, *206* (8–9), 2115–2124.

(39) Marsal, L. F.; Vojkuvka, L.; Formentin, P.; Pallarés, J.; Ferré-Borrull, J. Fabrication

and Optical Characterization of Nanoporous Alumina Films Annealed at Different Temperatures. *Optical Materials* **2009**, *31* (6), 860–864.

(40) Santos, A.; Vojkuvka, L.; Alba, M.; Balderrama, V. S.; Ferré-Borrull, J.; Pallarès, J.; Marsal, L. F. Understanding and Morphology Control of Pore Modulations in Nanoporous Anodic Alumina by Discontinuous Anodization. *Physica Status Solidi (A) Applications and Materials Science* **2012**, *209* (10), 2045–2048.

(41) Macias, G.; Hernandez-Eguia, L. P.; Ferre-Borrull, J.; Pallares, J.; Marsal, L. F. Gold-Coated Ordered Nanoporous Anodic Alumina Bilayers for Future Label-Free Interferometric Biosensors. *ACS Applied Materials and Interfaces* **2013**, *5* (16), 8093–8098.

(42) Santos, A.; Ferré-Borrull, J.; Pallarès, J.; Marsal, L. F. Hierarchical Nanoporous Anodic Alumina Templates by Asymmetric Two-Step Anodization. *Physica Status Solidi (A) Applications and Materials Science* **2011**, *208* (3), 668–674.

(43) Eckstein, C.; Acosta, L. K.; Pol, L.; Xifré-Pérez, E.; Pallares, J.; Ferré-Borrull, J.; Marsal, L. F. Nanoporous Anodic Alumina Surface Modification by Electrostatic, Covalent, and Immune Complexation Binding Investigated by Capillary Filling. *ACS Applied Materials and Interfaces* **2018**, *10* (12), 10571–10579.

(44) Ruminski, A. M.; Moore, M. M.; Sailor, M. J. Humidity-Compensating Sensor for Volatile Organic Compounds Using Stacked Porous Silicon Photonic Crystals. *Advanced Functional Materials* **2008**, *18* (21), 3418–3426.

(45) Meade, S. O.; Yoon, M. S.; Ahn, K. H.; Sailor, M. J. Porous Silicon Photonic Crystals as Encoded Microcarriers. *Advanced Materials* **2004**, *16* (20), 1811–181.

(46) Santos, A. Nanoporous Anodic Alumina Photonic Crystals: Fundamentals, Developments and Perspectives. *J. Mater. Chem. C* **2017**, *5* (23), 5581–5599.

(47) Macias, G.; Ferré-Borrull, J.; Pallarès, J.; Marsal, L. F. 1-D Nanoporous Anodic Alumina Rugate Filters by Means of Small Current Variations for Real-Time Sensing Applications. *Nanoscale research letters* **2014**, *9* (1), 315.

(48) Kumeria, T.; Santos, A.; Losic, D. Nanoporous Anodic Alumina Platforms: Engineered Surface Chemistry and Structure for Optical Sensing Applications. *Sensors* **2014**, *14* (7), 11878–11918.

(49) Sahel, S.; Amri, R.; Gamra, D.; Lejeune, M.; Benlahsen, M.; Zellama, K.; Bouchriha, H. Effect of Sequence Built on Photonic Band Gap Properties of One-Dimensional Quasi-Periodic Photonic Crystals: Application to Thue-Morse and Double-Period Structures. *Superlattices and Microstructures* **2017**, 1–9.

(50) Shen, H.; Wang, Z.; Wu, Y.; Yang, B. One-Dimensional Photonic Crystals: Fabrication, Responsiveness and Emerging Applications in 3D Construction. *RSC Adv.* **2016**, *6* (6), 4505–4520.

(51) Kelly, T. L.; Garcia Sega, A.; Sailor, M. J. Identification and Quantification of Organic Vapors by Time-Resolved Diffusion in Stacked Mesoporous Photonic Crystals. *Nano Letters* **2011**, *11* (8), 3169–3173.

(52) Santos, A.; Yoo, J. H.; Rohatgi, C. V.; Kumeria, T.; Wang, Y.; Losic, D. Realisation and Advanced Engineering of True Optical Rugate Filters Based on Nanoporous Anodic Alumina by Sinusoidal Pulse Anodisation. *Nanoscale* **2016**, *8* (3), 1360–1373.

(53) Calvo, M. E.; Colodrero, S.; Hidalgo, N.; Lozano, G.; López-López, C.; Sánchez-Sobrado, O.; Míguez, H. Porous One Dimensional Photonic Crystals: Novel Multifunctional Materials for Environmental and Energy Applications. *Energy and Environmental Science* **2011**, *4* (12), 4800–4812.

(54) Bartzsch, H.; Lange, S.; Frach, P.; Goedicke, K. Graded Refractive Index Layer Systems for Antireflective Coatings and Rugate Filters Deposited by Reactive Pulse Magnetron Sputtering. *Surface and Coatings Technology* **2004**, *180–181*, 616–620.

(55) Alekseev, S. A.; Lysenko, V.; Zaitsev, V. N.; Barbier, D. Application of Infrared Interferometry for Quantitative Analysis of Chemical Groups Grafted onto the Internal Surface of Porous Silicon Nanostructures. *Journal of Physical Chemistry C* **2007**, *111* (42), 15217–15222.

(56) Cheng, W.; Steinhart, M.; Gösele, U.; Wehrspohn, R. B. Tree-like Alumina Nanopores Generated in a Non-Steady-State Anodization. *Journal of Materials Chemistry* **2007**, *17* (33), 3493–3495.

(57) Lee, W.; Kim, J. C. Highly Ordered Porous Alumina with Tailor-Made Pore Structures Fabricated by Pulse Anodization. *Nanotechnology* **2010**, *21* (48), 1.

Chapter 4

Chapter 5. Nanoporous Anodic Alumina Photonic Structures by Gaussian Pulse Anodization

UNIVERSITAT ROVIRA I VIRGILI
ENGINEERING OF PHOTONIC STRUCTURES BASED ON NANOPOROUS ANODIC ALUMINA AS AN OPTICAL SENSING PLATFORM
Laura Karen Acosta Capilla

This Chapter presents a Gaussian pulse anodization approach to generate nanoporous photonic crystals with highly tunable and controllable optical properties across the visible–NIR spectrum. Nanoporous anodic alumina Gaussian photonic crystals (NAA-GPSs) are fabricated in oxalic acid electrolyte by Gaussian pulse anodization –a novel form of pulse-like anodization. The effect of the Gaussian pulse width in the anodization profile on the optical properties of these photonic crystals is assessed by systematically varying this fabrication parameter from 5 to 60 s. The effective medium of NAA-GPSs is assessed by monitoring spectral shifts in their characteristic PSB upon infiltration of their nanoporous structure with analytical solutions of D-glucose of varying concentration

5.1 Introduction

Photonic structures (PSs) are dielectric optical forms with specifically engineered photonic bands to modify the group velocity of photons when these flow through the PC. Light–matter interactions in PCs can be tuned with precision by engineering the PC's architecture so regions with high and low refractive index are periodically and spatially distributed [1-8]. Distinct forms of PCs based on a wide range of materials can be produced to harness versatile control over electromagnetic waves across the broad spectrum, from UV to IR. PCs have found multiple applications, including photonic encoding[9], chemical sensing and biosensing[10-14], lasing[8], and photocatalysis[15,16]. Since the pioneering works by Masuda and co-workers, nanoporous anodic alumina (NAA) is an ideal base material to generate nanoporous PCs[17-19] due to its cylindrical nanopores with well-defined and highly controllable geometric features. NAA is produced by anodization of aluminum films, which is a cost-effective and fully scalable

top–down industrial process compatible with traditional micro- and nanofabrication[20-22]. The optical properties of NAA are intrinsically dependent on the architecture, dimensions and distribution of its nanopores, which can be precisely engineered during the anodization process. Therefore, structural engineering of NAA enables new paths to modulate its effective refractive index in 1D, 2D or 3D distributions to form PC structures such as distributed Bragg reflectors[23-26], microcavities[27], and gradient index filters[15,16,28-30]. NAA-PC structures have demonstrated unique optical properties to guide, reflect, transmit, emit, and enhance incident photons for specific applications. Recent progress in anodization technology has focused on structural engineering of NAA-PCs by distinct forms of pulse-like anodization approaches such as sinusoidal[14,28,29-33], sawtooth[34], pseudostepwise[35], and stepwise[27].

In contrast to pioneering pulse-like anodization combining hybrid pulses between mild and hard anodization regimes[37-40], pulse anodization performed under mild conditions[41] moderate electrolyte temperature and anodizing voltage/current density– provide superior controllability over the anodic oxide growth rate and its porosity, enabling new paths to engineering the structure of NAA with precision to achieve versatile control of light for specific applications such as optical sensing [42,43], and biosensing[22,44-47] and photocatalysis[15]. Despite these advances, to date only a limited number of pulse shapes have been implemented into anodization approaches to engineering distinct forms of NAA-based PCs, including sinusoidal, symmetric and asymmetric stepwise, and sawtooth. Although these strategies have successfully realized the engineering of NAA–PCs with outstanding optical properties, further developments of

anodization technology will be needed to tailor-engineer the structure of NAA–PCs with versatility for harnessing specific forms of light–matter interactions and spreading the applicability of these unique PC structures across light-based technologies. Motivated by these efforts, herein we present an innovative pulse-like anodization approach that makes it possible to engineer a novel form of NAA-PCs using Gaussian current density pulses.

The position of central wavelength, full width at half maximum and intensity of the characteristic photonic stopband (PSB) of NAA-PCs in their reflection spectrum are demonstrated to rely strongly on the Gaussian pulse width, the incidence angle of light and the porosity of NAA-PCs. We also demonstrate that Gaussian NAA-PCs (NAA-GPSs) produced by Gaussian pulse anodization are highly sensitive to alterations in their effective medium, showing promising potential to be integrated as platform materials for optical sensing and biosensing systems. The findings establish a rationale to better understand the effect of key anodization parameters on the optical properties of NAA-GPSs, providing exciting opportunities to engineer NAA–PCs with finely tuned optical properties for specific light-based technologies.

5.2 Fabrication Details

5.2.1 Fabrication of NAA-GPSs by Gaussian Pulse Anodization

Impurities and grease in as-received aluminum substrates were removed by thoroughly sequential washing in acetone, ethanol, and water. Prior to anodization, aluminum substrates were electropolished in an electrolyte 4:1 v/v ethanol–perchloric acid at 20 V and 5°C for 6 min, with the stirring

direction alternated from clockwise to anticlockwise every 60 s. Electropolished aluminum discs were then anodized in 0.3 M aqueous oxalic acid electrolyte at 5°C using a current density–time anodization profile featuring Gaussian pulses generated according to Equation 1, for a number of pulses *N*:

$$J(t) = J_0 + J_1 exp^{\frac{-[t-\frac{T}{2}]^2}{2c^2}} \quad (5.1)$$

where *J(t)* is the anodization current density at time *t*, J_1 is the current density amplitude, *T* is the anodization period, J_0 is the offset current density and *C* is the width of the Gaussian pulse. **Figure 5.1a** illustrates the fabrication process used to generate NAA-GPSs via gaussian pulse anodization, including a representative anodization profile with a graphical description of the fabrication parameters (current density offset – J_0 = 1.13 mA cm^{-2}, current density amplitude – J_1 = 2.26 mA cm^{-2}, anodization period – T = 250 s, number of pulses- N = 150 periods and Gaussian pulse width – C = 20 s), and the schematic description of the most representative structural features defining the structure of NAA-GPSs (i.e., pore length – $L_{NAA\text{-}GPSs}$ and period length – $d_{NAA\text{-}GPSs}$).

Figure 5.1b shows interlink between the nanoporous structure and the optical properties of NAA-GPSs, with a representative reflection spectrum of a NAA-GPS produced with J_0 = 1.13 mA cm^{-2}, J_1 = 2.26 mA cm^{-2}, *T* = 250 s, *N* = 150 pulses and *C* = 20 s. Notice that, the inset shows a digital picture acquire with dark background of that NAA–GPS displaying vivid red-orange interferometric color) (center), and magnified view of the photonic stopband (PSB) of that NAA-GPS with a graphical description of its optical

features (i.e., reflection intensity – $R_{PSB,}$ central wavelength – λ_{PSB} and full width and half maximum – $FWHM_{PSB}$) (right).

For optical characterization purposes, after anodization the remaining aluminum substrate was chemically etched from the backside of NAA-GPSs by selective chemical etching in a saturated HCl–$CuCl_2$ solution for optical characterization. To study the effect of porosity on the optical properties of NAA-GPSs, the nanopores of these PCs were widened after anodization via wet chemical etching in an aqueous solution of H_3PO_4 5 wt% at 35°C and varying time, from 0 to 20 min, with a time interval of 5 min.

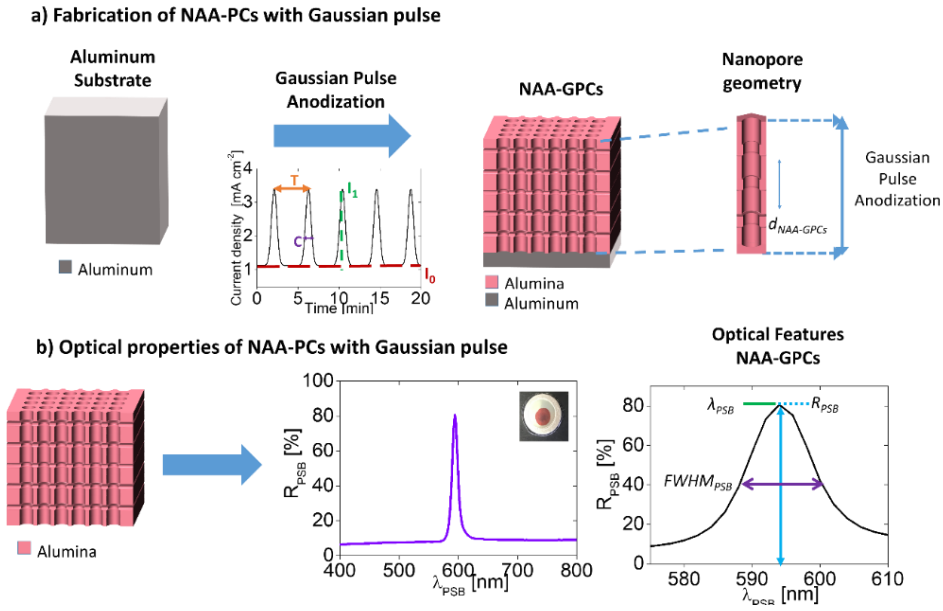

Figure 5.1. Fabrication of nanoporous anodic alumina Gaussian photonic structures (NAA-GPSs) using Gaussian pulse anodization. (a) Representative Gaussian pulse anodization profile used to produce NAA-GPSs. (b) Schematics showing relationship between structure (left), optical reflection spectrum of a representative NAA-GPS produced.

5.2.2 Optical Characterization of NAA-GPSs Produced by Gaussian Pulse Anodization

Reflection spectra of NAA-GPSs were measured from 250 to 900 nm with a resolution of 2 nm at varying incidence angle from 8 to 60° in a PerkinElmer UV−visible−NIR Lambda 950 spectrophotometer. The reflection intensity (R_{PSB}), quality factor (Q_{PSB}) and full width at half maximum ($FWHM_{PSB}$) of the PSB of NAA-GPSs were estimated from the reflection spectra, using Gaussian fittings. The effective medium of NAA-GPSs was assessed by measuring spectral shifts in the position of their PSB upon infiltration with analytical solutions of D-glucose with varying refractive index. This process was performed under continuous fluidic flow conditions at a fixed rate of 500 µL min^{-1} in real-time using an acrylic plastic-based flow cell. Reflectance spectra from NAA-GPSs were acquired using a setup combining a halogen light source (Spectligth DH-c) and an optical fiber spectrometer (Avantes, AvaSpec-3648).

Light from the source was focused onto the surface of NAA-GPSs at normal incidence using a bifurcated fiber optic probe with six illuminating waveguides assembled around one central reading waveguide. The Optical probe was coupled to an optical lens to focus light within a ~1 mm-diameter circular spot on the top of NAA-GPSs. Collection of reflected light was performed by the optical fiber probe and guided to the spectrometer, which recorded one spectrum every 2 s with and integration time of 50 ms. Reflectance spectra were measured for the wavelength range of 400−900 nm. The resulting data were processed by a custom-made program in MATLAB software.

5.2.3 Structural Characterization of NAA-GPSs Produced by Gaussian Pulse Anodization

The structure of Gaussian NAA-GPSs was characterized by a field-emission gun scanning electron microscopy (FEG-SEM FEI Quanta 450) and an environmental scanning electron microscopy (ESEM FEI Quanta 600) operating at an accelerating voltage between 20 and 25 keV. ESEM and FEG-SEM images were analyzed by ImageJ [48].

5.2.4 Modeling of Gaussian NAA-GPSs

The optical properties of Gaussian NAA-GPSs were modeled by combining an effective medium approximation (EMA) model and the transfer matrix method (TMM). The effective refractive index of each layer within NAA-GPSs' structure was estimated by the Looyenga−Landau−Lifshitz (3L) EMA model in combination with that reported from Bartzsch[31,49] and Kuang[50].

Figure 5.2 shows an illustration of the discretization of effective refractive index in NAA-GPSs as a 1D-effective graded-index system in the pore growth direction. The pore morphology of the NAA-GPSs induces a modification in depth of the porosity, which in turn results in a variation of the refractive index in depth. The resulting system is a composition of multiple layers with varying constant refractive index between high and low values. The effective refractive index of each layer was calculated using the Looyenga-Landau-Lifshitz formula adapted to NAA-GPSs. The dimension in the Z direction of the 1D-effective graded-index system was determined by the physical thickness of one period (Δ) by the number of cycles (N). The optical source was an incident plane wave perpendicular to the surface of the structure (XY plane), which propagated perpendicular

to the Z axis from 350 to 1200 nm at an angle of incidence of 8°. The reflectance spectra were calculated by the TMM method, where the above multi-layered thin film model was implemented. Calculations were performed using a custom-designed program in MATLAB software.

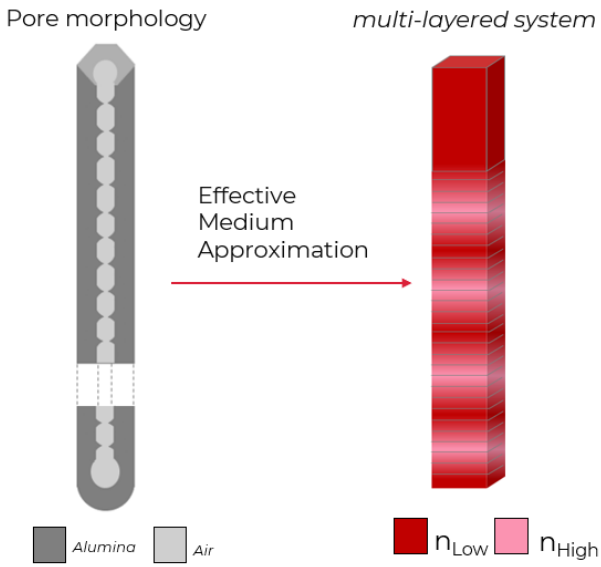

Figure 5.2. Illustration of the transition of the NAA-GPSs pore morphology towards a multilayered system in which the constant effective refractive index of each layer varies between n_{low} and n_{high}.

5.3. Results and Discussion

5.3.1 Fabrication of NAA-GPSs

Figure 5.3 shows a set of representative Gaussian pulse anodization profiles used to produce NAA-GPSs. Six types of NAA-GPSs were produced with fixed J_0 = 1.13 mA cm^{-2}, J_1 = 2.26 mA cm^{-2}, T = 250 s, N = 150 pulses, and systematically varied C = 5, 10, 20, 30, 40 and 60 s. **Table 5.1** summarizes the fabrication conditions of the assessed NAA-GPSs, labelled as NAA-GPS-1 (C = 5 s), NAA-GPS-2 (C = 10 s), NAA-GPS-3 (C = 20 s), NAA-GPS-4 (C = 30 s), NAA-GPS-5 (C = 40 s) and NAA-GPS-6 (C = 60 s) as a

function of the value of *C* used in their fabrication. While the voltage anodization profile (output) shows an asymmetric Gaussian shape with the current density input for *C*= 5–30 s, it turns into a quasi-symmetric Gaussian bell for *C* > 30 s.

Analysis of the anodization profiles reveal the output voltage follows closely the input current density profile, with a delay of ~0.4 min. This short delay is attributable to the dynamic modification of the anodization current density, which disturbs the continuous flow of the electrolytic species across of the oxide barrier layer. Such alteration leads to a recovery time until the electrochemical equilibrium is reached again.[37,51-52] The voltage output profiles shown in **Figure 5.3** reveal voltage Gaussian pulses with asymmetric shape of Gaussian pulses, the asymmetry of which increases with decreasing width of the anodizing Gaussian current density pulse input. This phenomenon is due to the capacitor effect in the oxide barrier layer located at the nanopore bottom tips, which separates the electrolyte/oxide and the oxide/metal interfaces.

When the current density input is suddenly altered, the oxide barrier layer – an electrical insulator – accumulates charge carriers (electrons and electrolytic species). These charge carriers are slowly released during the voltage recovery time, when the current density input is reduced from high to low level. The reduction of current density input in wider Gaussian pulses is smoother than that of their counterparts with narrower width, which in turns minimizes the asymmetry of the Gaussian voltage pulse output.

Table 5.1. Summary of fabrication parameters used to produce Gaussian NAA-GPSs.

Sample	J_0 [mA cm^{-2}]	J_1 [mA cm^{-2}]	T [s]	N [Pulses]	C [s]
NAA-GPS-1	1.13	2.26	250	150	5
NAA-GPS-2	1.13	2.26	250	150	10
NAA-GPS-3	1.13	2.26	250	150	20
NAA-GPS-4	1.13	2.26	250	150	30
NAA-GPS-5	1.13	2.26	250	150	40
NAA-GPS-6	1.13	2.26	250	150	60

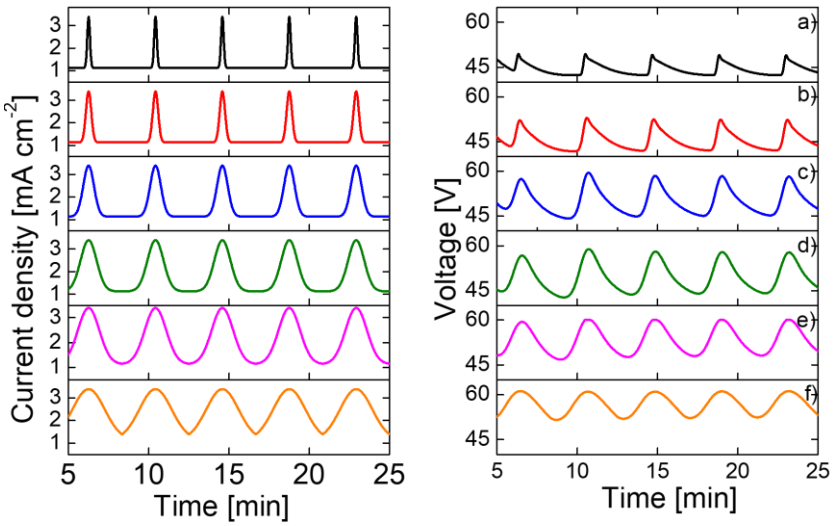

Figure 5.3. Analysis of Gaussian pulse anodizing current density (input) and voltage (output) profiles used to fabricate NAA-GPSs (NB: fixed anodization parameters – J_0 = 1.13 mA cm^{-2}, J_1 = 2.26 mA cm^{-2}, T = 250 s and N = 150 pulses). (a) NAA-GPS-1 (C = 5 s). (b) NAA-GPS-2 (C = 10 s). (c) NAA-GPS-3 (C = 20 s). (d) NAA-GPS-4 (C = 30 s). (e) NAA-GPS-5 (C = 40 s). (f) NAA-GPS-6 (C = 60 s).

5.3.2 Structural characterization of NAA-GPSs

Figure 5.4 shows representative FEG-SEM images of NAA-GPSs produced with J_0 = 1.13 mA cm^{-2}, J_1 = 2.26 mA cm^{-2}, T = 250 s, N = 150 pulses and C = 5, 10, 20, 30, 40 and 60 s. The general top view FEG-SEM image shows nanopores randomly distributed across the surface of the Gaussian NAA-PC (**Figure 5.4a)**, the average diameter of which is ~17 nm (see a magnified top view with details of nanopores in **Figure 5.4b)**. The general cross-sectional FEG-SEM image reveals nanopore diameter modulations along the nanopore length, which are induced by the input Gaussian current density pulses **(Figure 5.4c).** Nanopore diameter modulations are translated into effective medium modulations in depth, leading to the top–down generation of an 1D NAA-GPS structure. **Figure 5.4d** shows a cross-sectional view of the period length ($d_{NAA\text{-}GPSs}$) in NAA-GPSs, as graphically defined in **Figure 5.4f**.

The period length corresponds to the length of the stacked layers of NAA generated during each Gaussian pulse. FEG-SEM analysis reveals that, for C = 5, 10, 20, 30, 40 and 60 s, the period length are 166 ±10, 176 ± 9, 195 ± 17, 211 ± 18, 234 ± 24, 319 ± 15 respectively. **Figure 5.4.e** shows the dependence of $d_{NAA\text{-}GPSs}$ with C, in which the former structural feature increased with the latter anodization parameter. This graph reveals two growth regimes, from C= 5 to 40 s and from 40 to 60 s. While the period length grows at a rate of 1.88 nm s^{-1} within the first regime, it becomes more dependent on C>40 s, which a growth rate of 4.25 nm s^{-1}.

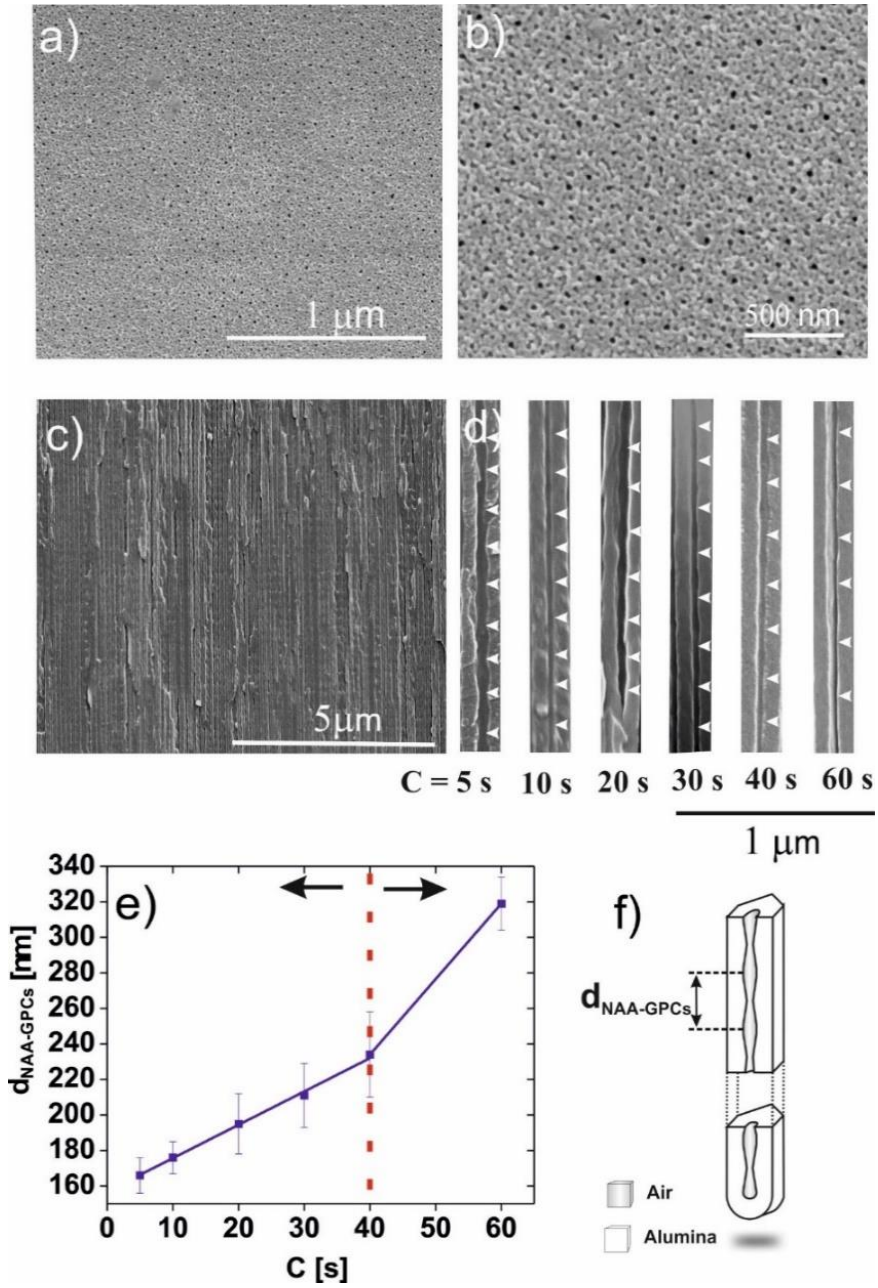

Figure 5. 4. Structural characterization of NAA-GPSs produced by Gaussian pulse anodization (NB: NAA-GPS produced with J_0 = 1.13 mA cm^{-2}, J_1 = 2.26 mA cm^{-2}, N = 150 pulses, T = 250 s and C = 5, 10,20, 30, 40 and 60 s). (a) General top view FEG-SEM image of a representative NAA-GPS (b) Magnified view of a representative NAA-GPS. (c) General cross-sectional FEG-SEM view of a representative NAA-GPS). (d) Cross-view of NAA-GPSs with C= 5, 10, 20, 30, 40 and 60 s. (e) relation between C and period length ($d_{NAA-GPSs}$). (f) Illustration of period length of NAA-GPSs .

5.4 Optical Characterization of NAA-GPSs

5.4.1 Effect of Gaussian Pulse Width on the Optical Features of the Characteristic PSB of NAA-GPSs

To study the effect of the Gaussian width (i.e. *C* parameter) on the optical properties of NAA-GPSs, a set of these PC structures was fabricated by Gaussian pulse anodization with fixed J_0 = 1.13 mA cm^{-2}, J_1 = 2.26 mA cm^{-2}, *T* = 250 s, *N* = 150 pulses, and varying *C* = 5, 10, 20, 30, 40 and 60 s. **Figure 5.5a** shows reflectance spectra of NAA-GPSs produced with *C* = 5, 10, 20, 30, 40 and 60 s, which feature narrow characteristic PSBs with an average full width at half maximum ($FWHM_{PSB}$) of 21 ± 9 nm. It is apparent that the position of the PSB red-shifts with increasing *C* following a linear dependence, in which λ_{PSB} red-shifts at a rate of 9.8 ± 0.3 nm s^{-1} with *C*, with a linearity correlation coefficient of 0.994 **(Figure 5.5b**). Analysis of the anodization profiles shown in **Figure 5.3** reveals that both the amplitude and offset of the anodizing voltage output increase with *C*. Previous studies have demonstrated that increasing voltage offset in NAA-PCs produced under current density control conditions results in a red-shift in the characteristic PSB of the PCs[30] due to increment in the period length within the PC structure. **Figure 5.5c** shows the dependence between the maximum reflection intensity of the PSB of NAA-GPSs and *C*. It can observe that NAA-GPSs produced with *C* = 20 s achieve the maximum intensity (~80%), whereas those NAA-GPSs produced with *C* = 5 s have the lowest intensity (~10%). A cubic polynomial fitting was used establish a correlation between the intensity of the PSB and *C*, which was found to describe precisely the dependence between optical feature and fabrication parameter, as denoted by the correlation coefficient of R^2 =

0.995. **Figure 5.5d** depicts the relationship between $FWHM_{PSB}$ of NAA-GPSs and C. This graph indicates that $FWHM_{PSB}$ increases exponentially with increasing C, from 10 nm at C = 5 s (narrowest PSB) to 37 nm at C = 60 s (broadest PSB).

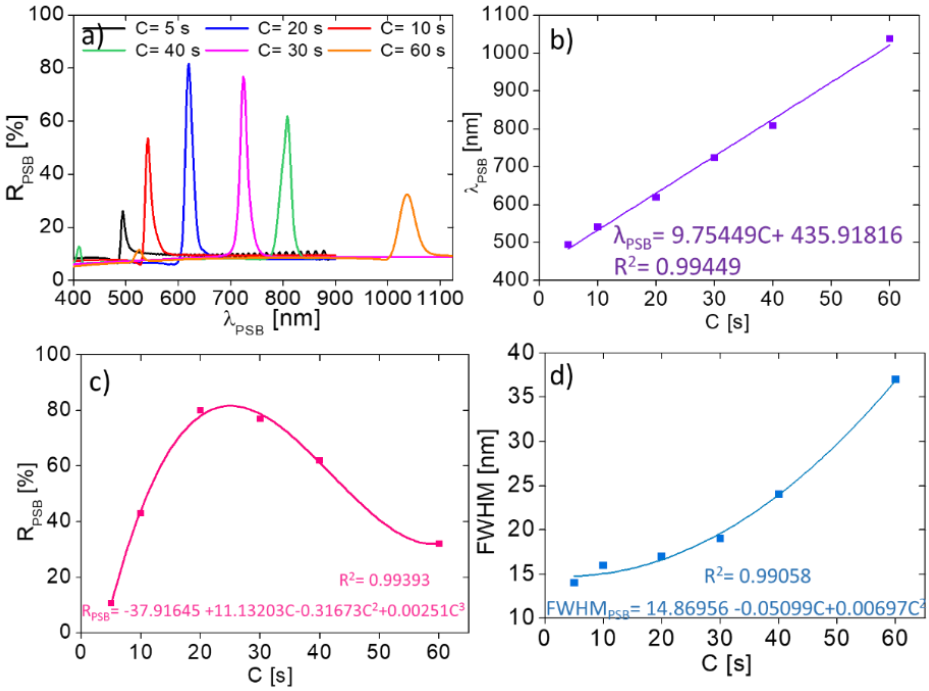

Figure 5.5. Effect of Gaussian width (C) on the features of the PSB of NAA-GPSs fabricated by Gaussian pulse anodization at fixed J_0 = 1.13 mA cm^{-2}, J_1 = 2.26 mA cm^{-2}, T = 250 s and N = 150 at ϑ = 8º. (a) Reflection spectra of NAA-GPSs as a function of C = 5, 10, 20, 30, 40 and 60 s. (b) Position of the reflection band of NAA-GPSs (λ_{PSB}) (c) Intensity reflection (R_{PSB}) of NAA-GPSs (d) Full width at half maximum ($FWHM_{PSB}$) NAA-GPSs.

5.4.2 Effect of Angle of Incidence on the Optical Features of the Characteristic PSB of NAA-GPSs

The combinational effect of the incidence angle and C on the optical features of the characteristic PSB of NAA-GPSs was investigated. **Table 5.2** provides a detailed summary of the effect of each of these parameters on the optical features (i.e., λ_{PSB}, R_{PSB}, $FWHM_{PSB}$ and quality factor – Q_{PSB} =

λ_{PSB}/ $FWHM_{PSB}$) of NAA-GPSs produced by Gaussian pulse anodization. **Figure 5.6a** shows the reflection spectra of a NAA-GPS-3 at different incidence angles (ϑ = 8, 20, 30, 45, 50 and 60°). It is apparent that the position of the PSB of NAA-GPSs undergoes a blue-shift when the incidence angle increases. This result is in good agreement with the Bragg–Snell law, in which the wavelength of the diffracted light depends on the incidence angle, the periodicity and the effective refractive index[36, 53-57] of the nanoporous PC, as expressed in Equation 2:

$$m\lambda_{PSB} = 2d_{NAA-GPCs}\sqrt{n_{eff}^2 - sin^2\theta} \quad (5.2)$$

where λ_{PSB} is wavelength of the PSB, m is the order of the PSB, $d_{NAA\text{-}GPS}$ is the structure periodicity, ϑ is the incidence angle, n_{eff} is the effective refractive index. **Figure 5.6b** shows that the position of the PSB of NAA-GPSs is shifted toward shorter wavelengths (i.e., blue-shift) with increasing incidence angle and increasing C, as revealed by linear fittings. Analysis of the fitting lines denotes that λ_{PSB} blue-shifts at rates of –1.51, –1.66, –2.10, –2.25, –2.59 and –3.30 nm/° for C = 5, 10, 20, 30, 40 and 60 s, respectively. Analysis of **Figure 5.6c** indicates that the reflection intensity of the PSB decreases as the incidence angle increases. Analysis of the fitting lines denotes that R_{PSB} decreases at rates of –0.02, –0.03, –0.39, –0.34, –0.27 and –0.25 %/° for C = 5, 10, 20, 30, 40 and 60 s, respectively. **Figure 5.6d** shows the $FWHM_{PSB}$ dependence with the angle of incidence. It is apparent that the $FWHM_{PSB}$ remains almost constant when the incidence angle increases.

Table 5.2. Summary of the effect of C parameter and the incidence angle on the reflectance spectrum of Gaussian NAA-PCs.

Sample	Parameter	8°	20°	30°	45°	50°	60°
G1 C= 5s	λ_{PSB} [nm]	494	483	470	444	435	417
	$R_{PSB\ [\%]}$	10.6	10.6	10.3	10	9.9	9.09
	$FWHM_{PSB}$ [nm]	14	15	15	14	14	13
	Q_{PSB}	31	28	27	29	30	34
G2 C= 10s	λ_{PSB}	542	531	516	487	477	458
	$R_{PSB\ [\%]}$	43	41	38	35	35	31
	$FWHM_{PSB}$ [nm]	16	17	17	15	14	13
	Q_{PSB}	39	35	35	34	33	34
G3 C= 20s	λ_{PSB}	620	603	584	550	537	512
	$R_{PSB\ [\%]}$	80	76	70	68	66	61
	$FWHM_{PSB}$ [nm]	17	17	17	16	16	15
	Q_{PSB}	39	35	35	34	33	34
G4 C= 30s	λ_{PSB}	724	709	676	655	635	610
	$R_{PSB\ [\%]}$	77	74	67	64	63	55
	$FWHM_{PSB}$ [nm]	19	19	19	19	18	19
	Q_{PSB}	40	37	35	35	35	32
G5 C= 40s	λ_{PSB}	808	792	768	723	708	677
	$R_{PSB\ [\%]}$	62	58	54	51	50	48
	$FWHM_{PSB}$ [nm]	24	24	23	23	22	20
	Q_{PSB}	34	33	33	31	32	33
G6 C= 60s	λ_{PSB}	1037	1016	985	929	908	870
	$R_{PSB\ [\%]}$	32	32	28	24	22	20
	$FWHM_{PSB}$ [nm]	37	37	40	37	35	29
	Q_{PSB}	28	27	24	25	26	30

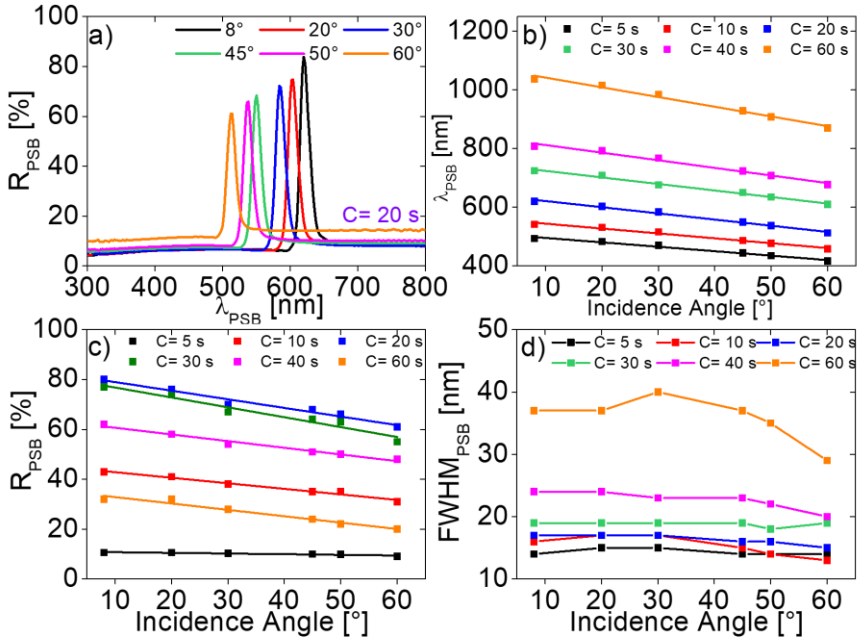

Figure 5.6 Combinational effect of incidence angle and Gaussian width on the PSB's features of NAA-GPSs (NB: NAA-GPSs produced at fixed J_0 = 1.13 mA cm^{-2}, J_1 = 2.26 mA cm^{-2}, T = 250 s and N = 150, and varying C = 5, 10, 20, 30, 40 and 60 s and ϑ = 8, 20, 30, 45, 50 and 60º). (a) Representative reflection spectra of NAA-GPS-3 (C = 20 s) at varying ϑ. (b) Position of PSB (λ_{PSB}) as a funciton of C and ϑ. (c) Reflection intensity of PSB (R_{PSB}) as a funciton of C and ϑ. (d) Full width at half maximum of PSB ($FWHM_{PSB}$) as a funciton of C and ϑ.

5.4.3 Effect of Pore Widening on the Optical Features of the Characteristic PSB of NAA-GPSs

To assess the effect of the internal porosity on the optical properties of NAA-GPSs, the nanopores of a set of these PC structures, fabricated with J_0 = 1.13 mA cm^{-2} J_1 = 2.26 mA cm^{-2}, T = 250 s, C = 20 s and N = 150 pulses, were widened by wet chemical etching at different pore widening times (t_{pw} = 0, 5, 10, 15 and 20 min). ESEM image analysis established a direct correlation between t_{pw} and the nanopores diameter, which was found to be ~20, 30, 40, 50, 60 nm at t_{pw} = 0, 5, 10, 15 and 20 min, respectively **(Figure 5.7**).

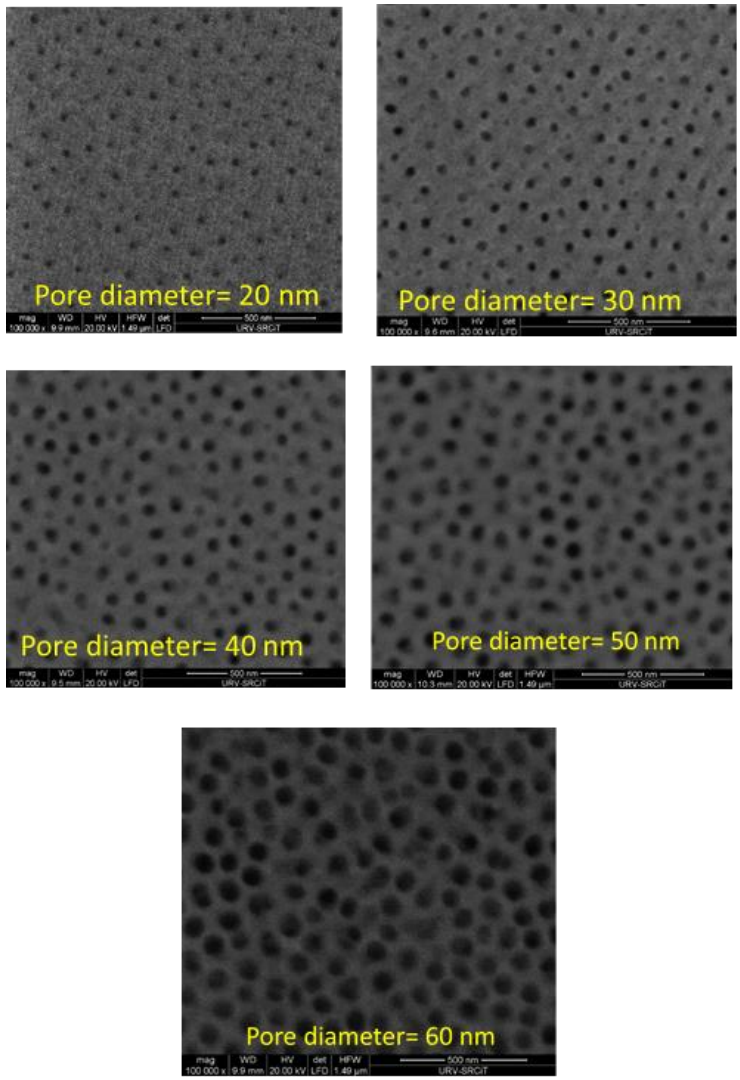

Figure 5.7. Top view of NAA-GPS after Pore widening treatment

Figures 5.8a–d show the dependence of λ_{PSB}, R_{PSB} and $FWHM_{PSB}$ of the characteristic PSB of NAA-GPSs with t_{pw}. **Figure 5.8a** shows the reflection spectra of a representative NAA-GPS (C = 20 s) with t_{pw}, from 0 to 20 min. It is apparent that the position of the characteristic PSB in the reflection spectrum of NAA-GPSs is blue-shifted when their nanoporous structure is widened. The reflection band is shifted toward shorter wavelengths due to the reduction of the fraction of alumina ($n_{Alumina}$ ~1.7 RIU) with respect

to air (n_{air} = 1.0 RIU) in the effective refractive index of the PC structure. **Figure 5.8b** shows the dependence of λ_{PSB} with t_{pw}, in which the former optical feature is blue-shifted with the latter fabrication parameter at a rate of –5.7 ± 0.4 nm min^{-1}. **Figure 5.8c** shows the dependence of R_{PSB} with t_{pw}. This behavior is observed for all angles of incidence measured. **Figure 5.8d** shows the dependence of $FWHM_{PSB}$ with t_{pw}, in which this optical feature increases at a rate of 1.48 nm min^{-1} as the nanoporous structure is widened.

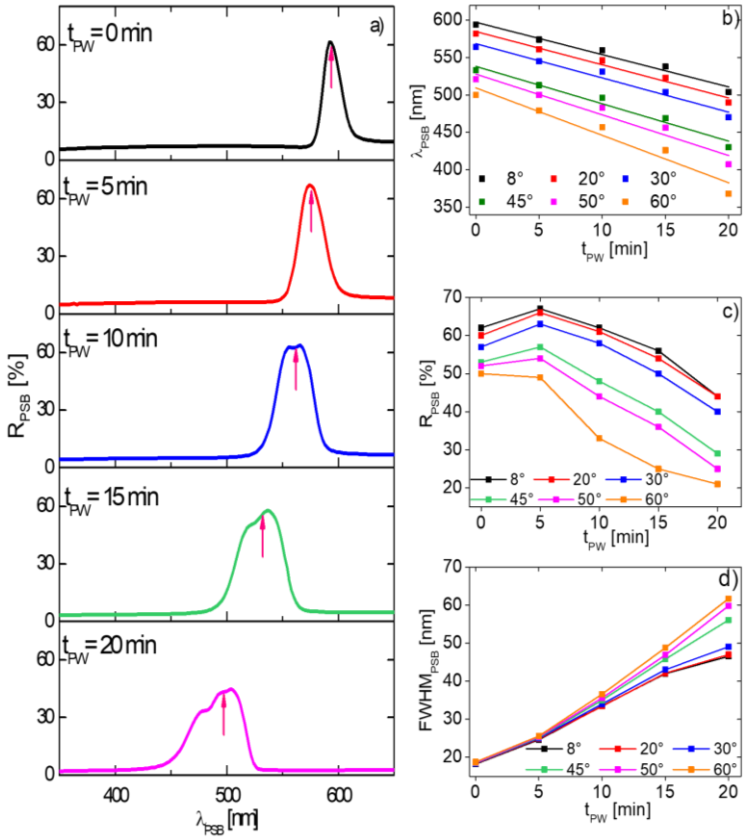

Figure 5.8. Effect of pore widening time (t_{pw} = 0, 5, 10, 15 and 20 min) on the optical features of the PSB of NAA-GPSs (NB: NAA-GPSs produced at fixed J_0 = 1.13 mA cm^{-2}, J_1 = 2.26 mA cm^{-2}, T = 250 s and N = 150 and ϑ = 8, 20, 30, 45, 50 and 60°). (a) Representative reflection spectrum of a NAA-GPS produced with C = 20 s at ϑ = 8° as a function of t_{pw} from 0 to 20 min. (b) Linear fitting lines showing the dependence between λ_{PSB} and t_{pw}. (c) Lines showing the dependence between R_{PSB} and t_{pw}. (d) Linear fitting lines showing the dependence between $FWHM_{PSB}$ and t_{pw}.

5.4.4 Assessment of Effective Medium of NAA-GPSs

In order to evaluate the optical sensitivy of NAA-GPSs, spectral shifts in the characteristic PSB of these PCs upon infiltration of their nanoporous network with double-distilled water-based D-glucose solutions of varying concentration (i.e. 0.0125, 0.0250, 0.050, 0.125, 0.250, 0.50, 0.75 and 1.0 M) were measured in real-time using a flow system.The correlation between D-glucose concentration and refractive index is show in **Figure 5.9.**

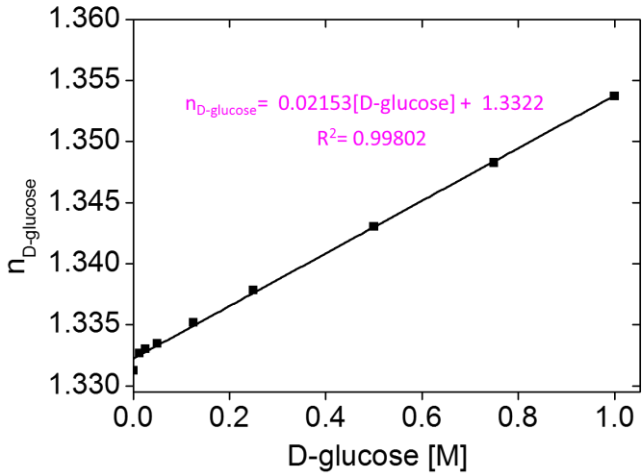

Figure 5.9. Correlation between D-glucose concentration and refractive index

Dynamic variations of the refractive index of the medium inside the nanopores shift in the position of the PSB of NAA-GPSs (i.e. increment in refractive index – red shift; decrement in refractive index – blue shift) **(Figure 5.10a). Figure 5.10b** illustrates a representative example of real-time monitoring of PSB shifts in a NAA-GPS-2 upon infiltration of its nanoporous structure with analytical solutions of D-glucose. First, a stable baseline was obtained by flowing water for 10 min.

Then, analytical solutions of D-glucose with varying concentration (0.0125, 0.0250, 0.050, 0.125, 0.250, 0.50, 0.75 and 1.0 M) were flowed through the system at 500 µL min^{-1}. Washing steps with fresh doble-distilled water were introduced between each analytical solution to remove remaining glucose molecules from the nanopores. The infiltration of the nanoporous structure of NAA-GPSs with aqueous solutions of D-glucose of increasing refractive index red-shifts the position of the characteristic PSB to longer wavelengths. The position of the PSB returns to its original baseline when water is flowed through the system, indicating that changes in the effective medium of these PSs are exclusively attributable to alterations in the refractive index of the medium filling the nanopores, without permanent chemical interaction between the inner surface of NAA-GPSs and glucose molecules in the analytical solution.

Figures 5.10c–f summarize linear correlations between the concentration of D-glucose and the red-shift of the PSB of NAA-GPS-2–NAA-GPS-5, and **Table 5.3** compiles the values of the most representative sensing parameters. The sensitivitie (*S*) of NAA-GPS-2–5, expressed in terms of slope of these linear fittings, were 0.83 ± 0.02, 0.77 ± 0.02, 1.04 ± 0.02 and 1.08 ± 0.05 nm M^{-1}, respectively. These results indicate that the most sensitive NAA-GPS structure is that produced with *C* = 40 s. The low limit of detection (LOD– 3σ = 3 times the standard deviation of the lowest D-Glucose concentration divided by S) was found for the sample *C* = 10 s. These NAA-GPSs show excellent linearity (R^2 – correlation coefficient) with an average of 0.994.

Table 5.4 provides a summary compiling the sensing performance of the most relevant examples combining NAA-PCs in real -time for sensing application using D-glucose.

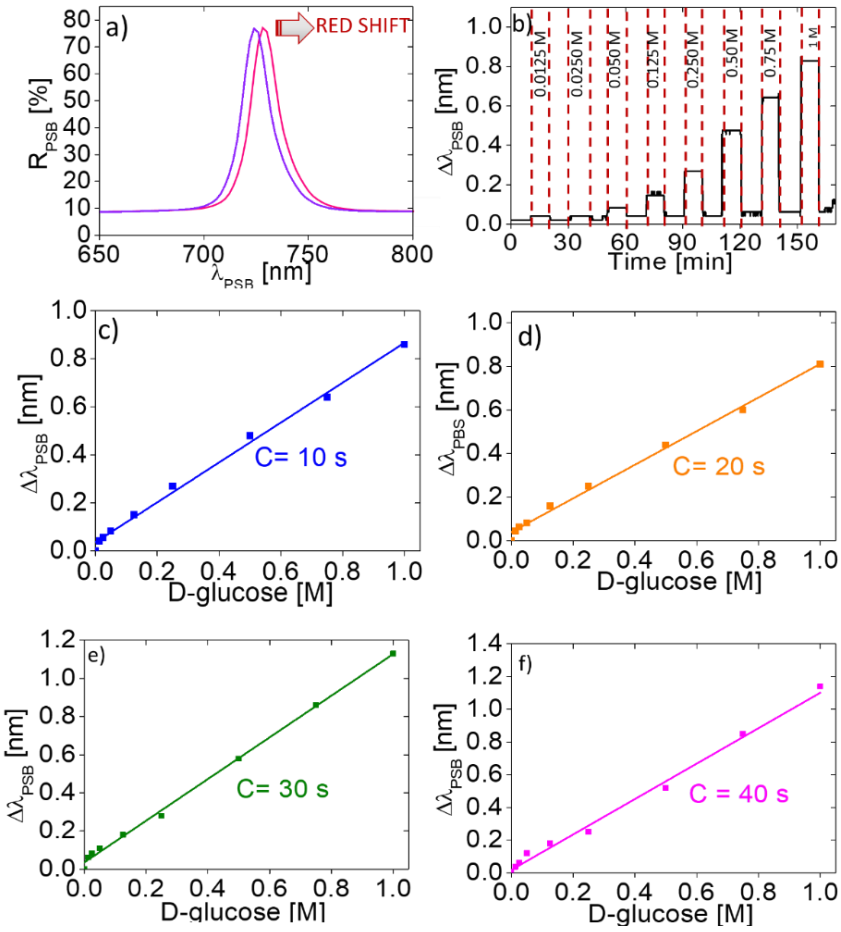

Figure 5.10. Effective medium assessment of NAA-GPSs. (a) Reflection spectrum of NAA-GPSs in water (purple) and D-Glucose (pink) showing the sensing principle (red-shift) used in Real-time experiments (b) Representative real-time shits in λ_{PSB} of NAA-GPSs upon selective infiltration of their nanoporous structure with analytical solutions of D-glucose with varying concentration, from 0.0125 to 1.0 M (NB: NAA-GPS produced at fixed J_0 = 1.13 mA cm^{-2}, J_1 = 2.26 mA cm^{-2}, T = 250 s and N = 150, C = 10 and ϑ = 0°. (c–f). Linear correlations summarizing the dependence between λ_{PSB} in NAA-GPSs (C = 10. 20, 30 and 40 s) and D-glucose concentration.

Table 5.3. Sensitivity and low limit of detection of NAA-GPSs produced by Gaussian pulse anodization upon infiltration of their effective medium with analytical solutions of D-glucose.

Sample	*S* [nm M^{-1}]	*LOD* [mM]	R^2
NAA-GPS-2 (C = 10 s)	0.83 ± 0.02	7.49 ± 0.26	0.995
NAA-GPS-3 (C = 20 s)	0.77 ± 0.02	16.3 ± 0.18	0.994
NAA-GPS-4 (C = 30 s)	1.04 ± 0.02	28.8 ± 0.20	0.997
NAA-GPS-5 (C = 40 s)	1.08 ± 0.05	29.6 ± 0.32	0.985

Table 5.4. Comparison of the sensing performance for different NAA-PCs

NAA Structure	Analyte	LOD [mM]	S	Reference
NAA-GPS	D-Glucose	7.49-29.6	0.77-1.08 [nm M^{-1}]	This work
Rugate Filters	D-Glucose	10-15	1.95-4.93 [nm M^{-1}]	12
DBR	D-Glucose	0.0042	0.0115 % [μM^{-1}]	58
Fabry- Pérot	D-Glucose	100	0.007 % [mM^{-1}]	59

To validate the experimental results, we adapted the Looyenga–Landau–Lifshitz (3L) EMA model to describe the distribution of effective refractive index in NAA-GPSs. This model can be easily implemented to describe the effective medium of composite photonic crystal systems. In particular, the Looyenga−Landau−Lifshitz model adapted to NAA-GPSs can be expressed by Equation 5.3[49-57].

$$n^{\frac{2}{3}}_{eff-NAA-GPCs} = f_{Al_2O_3} * n^{\frac{2}{3}}_{Al_2O_3} + f_{med} * n^{\frac{2}{3}}_{medium} \qquad (5.3)$$

where $n^{2/3}_{eff\text{-}NAA\text{-}GPSs}$ is the effective refractive index of NAA-GPSs, $n^{2/3}_{Al2O3}$, is the refractive index of alumina, f_{medium} volume fraction of filling medium, $n^{2/3}_{medium}$ is the refractive index of filling medium, and f_{Al2O3} is the volume fraction of alumina.

Furthermore, the reflection of light in each layer of NAA within the structure of NAA-GPSs follows the Fabry-Perót relationship shown in Equation 5.4:

$$\lambda_{PSB} = 2n_{eff-NAA-GPCs} * \ d_{NAA-GPCs} * \cos\theta \qquad (5.4)$$

where λ_{PSB} is the position of the PSB, $n_{eff\text{-}NAA\text{-}GPSs}$ is the effective refractive index of NAA-GPSs, $d_{NAA\text{-}GPSs}$ in the period length and ϑ is the incidence angle of light. Equation 5.4 can be reorganized as Equation 5.5 taking into account $f_{Al2O3} + f_{med}$ = 1 and θ = 0°:

$$\lambda_{PSB} = (2d_{NAA-GPCs})^{\frac{2}{3}} * (1 - f_{med}) * n_{Al_2O_3}^{\frac{2}{3}} + 2d_{NAA-GPCs}^{\frac{2}{3}} * f_{med} * \ n_{med}^{\frac{2}{3}} \qquad (5.5)$$

Figure 5.11 shows the obtained values and linear fittings after substituting the experimental data in the 3L model adapted for NAA-GPSs. A linear fitting between $\lambda_{PSB}^{2/3}$ and $n^{2/3}_{medium}$ made it possible to estimate $d_{NAA\text{-}GPSs}$ and f_{medium}, which for instance were found to be 170 ± 5 nm and 0.11 ± 0.02 for NAA-GPS-2, respectively. This result is in good agreement with simulations using the transfer matrix method, which gave an estimation for $d_{NAA\text{-}GPSs}$ of 160 nm (i.e., ~6% deviation between experimental and simulated results). This result demonstrates that the effective medium of NAA-GPSs produced by Gaussian pulse anodization can be precisely described by the 3L EMA model. The comparison of experimental data and simulations is summarized in **Table 5.5** and **Table 5.6**, respectively**. Figure 5.12** shows a direct comparison between simulated and experimental reflection spectra of NAA-GPSs assessed in this study. It is apparent that simulated (blue lines) and experimental (red lines) spectra of NAA-GPS-2, NAA-GPS-3, NAA-GPS-4 and NAA-GPS-5 are in excellent agreement.

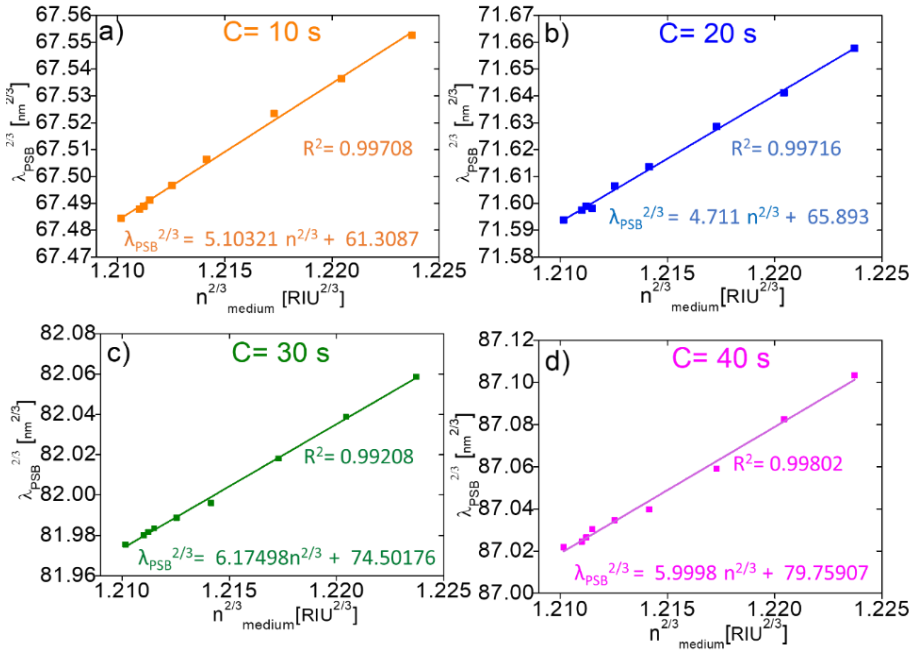

Figure 5.11. Assessment of effective medium of NAA-GPSs using the Looyenga-Landau-Lifshtz model (3L) (NB: NAA-GPS produced at fixed J_0 = 1.13 mA cm^{-2}, J_1 = 2.26 mA cm^{-2}, T = 250 s, N = 150 pulses and varying C). (a) C = 10 s. (b) C = 20 s. (c) C = 30 s. (d) C = 40 s.

Table 5.5 Comparison of the experimental results.

	Looyenga-Landau-Lifshitz model			Optical Characterization				Structural characterization		
C [s]	$d_{NAA\ GAUSS}$ [nm]	f medium [%]	$L_{NAA\text{-}GPCs}$ [nm]	λ_{PSB} [nm]	$FWHM_{PSB}$ [nm]	Q	R_{PSB} [%]	Pore diameter [nm]	Porosity [%]	L_{Total} [nm]
5	-	-	-	494	14	35	10.6	17	10.3	
10	170	10.5	25500	542	16	34	43	17	11.3	22800
20	185	10.5	27750	620	17	36	80	17	9.5	24100
30	227	10.5	34050	724	19	39	77	17	9.1	30500
40	248	9.5	37200	808	24	34	62	17	9.3	34200
60	-	-	-	1037	37	28	32	17	10	

Table 5.6 Comparison of the simulation results**.**

C [s]	$d_{NAA\ GAUSS}$ [nm]	λ_{PSB} [nm]	$FWHM_{PSB}$ [nm]	Q	R_{PSB} [%]	f medium [%]	L_{total} [nm]
5	145	497	14	35	19	10	21750
10	160	542	15	36	49	10	24000
20	185	621	16	40	71	10	27500
30	217	725	19	38	72	10	32550
40	240	804	22	36	61	10	36000
60	305	1040	38	27	34	10	45750

This result further demonstrates that the transfer matrix model developed in this study can be precisely predict the reflection bands of NAA-GPSs. **Figures 5.12g–j** compiles a comparative summary of the experimental (triangles) and simulation (circles) results for λ_{PSB}, $FWHM_{PSB}$, R_{PSB} and Q_{PSB} as a function of *C*. **Figure 5.12g** shows the experimental and simulated values of λ_{PSB} for NAA-GPS-1 to NAA-GPS-6. These data demonstrate that simulations can predict the spectral position of the PSB of NAA-GPSs with excellent accuracy, with almost negligible deviations of 0.60% (*C* = 5 s), 0.00% (*C* = 10 s), 0.16% (*C* = 20 s), 0.13% (*C* = 30 s), 0.49% (*C* = 40 s), and 0.29% (*C* = 60 s).

Figure 5.12h shows a comparative analysis between experimental and simulated values for $FWHM_{PSB}$. These results show a close correlation between experimental and simulated values, with a small average deviation of ~3.8%. It is also apparent that our model can precisely describe the intensity of the PSB for *C* = 30–60 s, with a deviation ranging between 1.6–6.9% (**Figure 5.12i**).

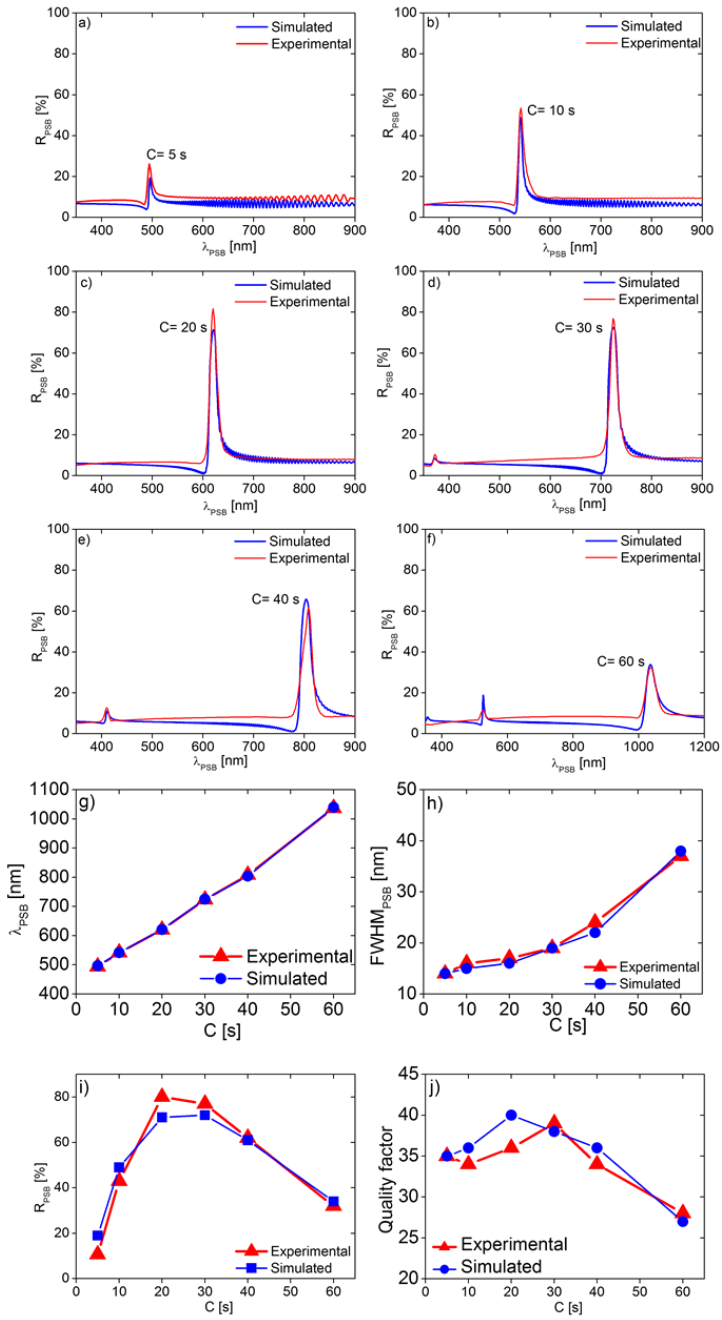

Figure 5.12. Effective medium model validation through comprehensive comparison between experimental values and simulation estimations for NAA-GPSs (NB: red lines and dots – experimental values; blue lines and dots – simulated estimations). (a–f) Experimental and simulated reflection spectra of NAA-GPSs as a function of C = 5, 10, 20, 30, 40 and 60 s. (g) Comparison between experimental and simulated values for λ_{PSB} at C = 5–60 s. (h) Comparison between experimental and simulated values for $FWHM_{PSB}$ at C = 5–60 s. (i) Comparison between experimental and simulated values for R_{PSB} at C = 5–60 s. (j) Comparison between experimental and simulated values for Q_{PSB} at C = 5–60 s.

However, discrepancy between simulations and experimental values is observed with a ~14.1% deviation at *C* = 20 s. Comparison between experimental and simulated estimations of Q_{PSB} for NAA-GPSs is shown in **Figure 5.12j**. Small discrepancy between experimental values and simulated estimations are observed with an average deviation ~3.4%. However, a disagreement of 10% is found for NAA-GPSs produced with *C* = 20 s. To summarize, analysis of the optical features of NAA-GPSs estimated from experimental data and simulations further demonstrate that our effective medium model can precisely describe the optical properties of these PC structures, providing new opportunities to design high-quality NAA-GPSs with tunable PSBs across the visible–NIR spectrum.

5.5. Conclusion

In this chapter, we fabricated photonic crystals based in nanoporous anodic alumina using a novel pulse-like anodization approach consisting of current density Gaussian pulses. The effect of the Gaussian pulse width on the optical features of the characteristic photonic stopband of these nanoporous PCs –position of central wavelength, full width at half maximum, reflection intensity and quality factor– was systematically assessed at varying angle of incidence. The position of the PSB of these PCs can be precisely tuned varying by the width of the Gaussian pulse, from λ_{PSB} = 494 nm to 1037 nm from C = 5 to 60 s, respectively. The reflection presented a highest intensity when *C* = 20 s (80%) and lowest when *C* = 5 s (20%) and $FWHM_{PSB}$ increase exponentially when *C* increases. Furthermore, we evaluated the effect of the angle of incidence angle in the reflection bands and we observe a blue-shift when the incidence angle

increases according with the Bragg-Snell law. The reflection intensity was also affected, as the incidence angle increases the intensity decreases. The $FWHM_{PSB}$ was not affected for the incidence angle. In addition, we report the effect of the porosity of the Gaussian-NAA-GPSs applying a pore widening chemical etching from 0 to 20 minutes increasing the nanopore diameter from 20 to 60 nm. The position of the reflection band blue-shifted from 594 to 495 nm also was observed an increment in the intensity and the width of the reflection bands. The potential applicability of these PC structures as optical platform for sensing applications was evaluated by monitoring in real-time spectral shifts in their characteristic PSB upon selective infiltration of their medium with analytical solutions of D-glucose. These observations indicate that NAA-GPSs can achieve high optical sensitivity (1.08 ± 0.05 nm M^{-1}), low limit of detection (7.5 ± 0.26 mM) and excellent linearity (R^2 = 0.994). We also demonstrated that the effective medium of NAA-GPSs can be mechanistically explained by the Looyenga-Landau-Lifshitz EMA model, as confirmed by correlations between experimental data and model predictions of structural parameters ($d_{NAA\text{-}GPSs}$ and f_{medium}). The experimental observations were further validated and mechanistically described by developing a theoretical effective medium model, using the transfer matrix approach, and performing a comprehensive comparison between experimental values and simulated estimations. The model can be used to precisely predict the experimental data and optical features of NAA-GPSs, opening exciting opportunities to engineer innovative PCs architectures for specific light-based applications.

REFERENCES

1. Santos, A. Nanoporous Anodic Alumina Photonic Crystals: Fundamentals, Developments and Perspectives. *J. Mater. Chem. C* **2017**, 5 (23), 5581–5599.
2. Law, C. S.; Lim, S. Y.; Abell, A. D.; Voelcker, N. H.; Santos, A. Nanoporous Anodic Alumina Photonic Crystals for Optical Chemo- and Biosensing: Fundamentals, Advances, and Perspectives. *Nanomaterials* **2018**, 8 (10), 1–47.
3. Leonard, S. W.; Mondia, J. P.; Driel, H. M. Van; Toader, O.; John, S.; Busch, K.; Birner, a.; Gosele, U.; Lehmann, V. Tunable Two-Dimensional Photonic Crystals Using Liquid-Crystal Infiltratio. *Phys Rev B* **2000**, 61 (4), 2389–2392.
4. Gorelik, V. S.; Sverbil, P. P.; Filatov, V. V.; Bi, D.; Fei, G. T.; Xu, S. H Transmission Spectra of One-Dimensional Porous Alumina Photonic Crystals. *Photonics Nanostruct. Fundam. Appl.* **2018**, 32, 6–10.
5. Wang, B.; Fei, G. T.; Wang, M.; Kong, M. G.; Zhang, L. De. Preparation of Photonic Crystals Made of Air Pores in Anodic Alumina. *Nanotechnology* 2**007**, 18 (36), 1–4.
6. Sadykov, A. I.; Kushnir, S. E.; Roslyakov, I. V.; Baranchikov, A. E.; Napolskii, K. S. Selenic Acid Anodizing of Aluminium for Preparation of 1D Photonic Crystals. *Electrochem Commun* **2019**, 100, 104–107.
7. Choi, J.; Luo, Y.; Wehrspohn, R. B.; Hillebrand, R.; Schilling, J.; Gösele, U. Perfect Two-Dimensional Porous Alumina Photonic Crystals with Duplex Oxide Layers *J. Appl Phys* **2003,** 94 (8), 4757–4762.
8. Masuda, H.; Yamada, M.; Matsumoto, F.; Yokoyama, S.; Mashiko, S.; Nakao, M.; Nishio, K. Lasing from Two-Dimensional Photonic Crystals Using Anodic Porous Alumina. *Adv, Mater* **2010**, 2492 (18), 213–216.
9. Santos, A.; Law, C. S.; Pereira, T.; Losic, D. Nanoporous Hard Data: Optical Encoding of Information within Nanoporous Anodic Alumina Photonic Crystals. *Nanoscale* **2016**, 8 (15), 8091–8100.
10. Wang, G.; Wang, J.; Li, S. Y.; Zhang, J. W.; Wang, C. W. One-Dimensional Alumina Photonic Crystals with a Narrow Band Gap and Their Applications to High-

Sensitivity Concentration Sensor and Photoluminescence Enhancement. *Superlattices Microstruct* **2015**, 86, 546–551.

11. Kumeria, T.; Santos, A.; Losic, D. Nanoporous Anodic Alumina Platforms: Engineered Surface Chemistry and Structure for Optical Sensing Applications. *Sensors* **2014**, 14 (7), 11878–11918.
12. Kumeria, T.; Rahman, M. M.; Santos, A.; Ferre-Borrull, J.; Marsal, L. F.; Losic, D. Structural and Optical Nanoengineering of Nanoporous Anodic Alumina Rugate Filters for Real-Time and Label-Free Biosensing Applications. *Anal. Chem* **2014**, 86 (3), 1837–1844.
13. Kumeria, T.; Rahman, M. M.; Santos, A.; Ferre-Borrull, J.; Marsal, L. F.; Losic, D. Nanoporous Anodic Alumina Rugate Filters for Sensing of Ionic Mercury: Toward Environmental Point-of-Analysis Systems. *ACS Appl. Mater. Interfaces* **2014**, 6 (15), 12971–12978.
14. Macias, G.; Ferré-Borrull, J.; Pallarès, J.; Marsal, L. F. 1-D Nanoporous Anodic Alumina Rugate Filters by Means of Small Current Variations for Real-Time Sensing Applications. *Nanoscale Res. Lett.* **2014**, 9 (1), 315.
15. Lim, S. Y.; Law, C. S.; Markovic, M.; Kirby, J. K.; Abell, A. D.; Santos, A. Engineering the Slow Photon Effect in Photoactive Nanoporous Anodic Alumina Gradient-Index Filters for Photocatalysis. *ACS Appl. Mater. Interfaces* **2018**, 10 (28), 24124–24136.
16. Liu, L.; Lim, S. Y.; Law, C. S.; Jin, B.; Abell, A. D.; Ni, G.; Santos, A. Light-Confining Semiconductor Nanoporous Anodic Alumina Optical Microcavities for Photocatalysis. *J. Mater. Chem. A* **2019**, 7 (39), 22514–22529.
17. Masuda, H.; Ohya, M.; Asoh, H.; Nakao, M.; Nohtomi, M.; Tamamura, T. Photonic Crystal Using Anodic Porous Alumina. *J. Appl. Phys., Part 2* **1999**, 38, 1403–1405.
18. Masuda, H.; Ohya, M.; Masuda, H.; Ohya, M.; Nishio, K.; Nakao, M. Photonic Band Gap in Anodic Porous Alumina with Extremely High Aspect Ratio Formed in Phosphoric Acid Solution. *J. Appl. Phys., Part 2* **2000**, 39 (L1039), 2–5.

19. Masuda, H.; Ohya, M.; Masuda, H.; Ohya, M.; Nishio, K.; Nakao, M. Photonic Band Gap in Naturally Occurring Ordered Anodic Porous Alumina. *J. Appl. Phys., Part 2* **2001**, 40, 1217–1219.
20. Müller, F.; Birner, A.; Schilling, J.; Li, A.; Nielsch, K.; Go, U. High Aspect Ratio Microstructures Based on Anisotropic Porous Materials. *Microsyst. Technol.* **2002**, 8, 7–9.
21. Montero-Rama, M. P.; Viterisi, A.; Eckstein, C.; Ferré-Borrull, J.; Marsal, L. F. In-Situ Removal of Thick Barrier Layer in Nanoporous Anodic Alumina by Constant Current Re-Anodization. *Surf. Coat. Technol* **2019**, 380, 1-7.
22. Ferré-Borrull, J.; Pallarès, J.; Macías, G.; Marsal, L. F. Nanostructural Engineering of Nanoporous Anodic Alumina for Biosensing Applications. *Materials* **2014**, 7 (7), 5225–5253.
23. Chen, Y.; Santos, A.; Wang, Y.; Kumeria, T.; Li, J.; Wang, C.; Losic, D. Biomimetic Nanoporous Anodic Alumina Distributed Bragg Reflectors in the Form of Films and Microsized Particles for Sensing Applications. *ACS Appl. Mater. Interfaces* **2015**, 7 (35), 19816–19824.
24. Rahman, M. M.; Marsal, L. F.; Pallares, J and Ferre-Borrull, J. Tuning the Photonic Stop Bands of Nanoporous Anodic Alumina-Based Distributed Bragg Reflectors by Pore Widening. *ACS Appl. Mater. Interfaces* **2013**, 5 (24), 13375–13381.
25. Ferré-Borrull, J.; Rahman, M. M.; Pallarès, J.; Marsal, L. F. Tuning Nanoporous Anodic Alumina Distributed-Bragg Reflectors with the Number of Anodization Cycles and the Anodization Temperature. *Nanoscale Res. Lett* **2014**, 9 (1), 1-6
26. Zhu, T.; Liu, Y.; Ding, T.; Fu, W. Y.; Jarman, J.; Ren, C. X.; Kumar, R. V.; Oliver, R. A. Wafer-Scale Fabrication of Non-Polar Mesoporous GaN Distributed Bragg Reflectors via Electrochemical Porosification. Sci. Rep. **2017**, 7, 1–8.
27. Law, C. S.; Lim, S. Y.; Macalincag, R. M.; Abell, A. D.; Santos, A. Light-Con Fi Ning Nanoporous Anodic Alumina Microcavities by Apodized Stepwise Pulse Anodization. *ACS Appl. Nano Mater* **2018**, 1, 4418–4434.
28. Acosta, L. K.; Bertó-Roselló, F.; Xifre-Perez, E.; Santos, A.; Ferré-Borrull, J.; Marsal, L. F. Stacked Nanoporous Anodic Alumina Gradient-Index Filters with

Tunable Multispectral Photonic Stopbands as Sensing Platforms. *ACS Appl. Mater. Interfaces* **2019**, 11 (3), 3360–3371.

29. (29) Kumeria, T.; Rahman, M. M.; Santos, A.; Ferre-Borrull, J.; Marsal, L. F.; Losic, D. Nanoporous Anodic Alumina Rugate Filters for Sensing of Ionic Mercury: Toward Environmental Point-of-Analysis Systems. *ACS Appl. Mater. Interfaces* **2014**, 6 (15), 12971–12978.
30. Santos, A.; Yoo, J. H.; Rohatgi, C. V.; Kumeria, T.; Wang, Y.; Losic, D. Realisation and Advanced Engineering of True Optical Rugate Filters Based on Nanoporous Anodic Alumina by Sinusoidal Pulse Anodisation. *Nanoscale* **2016**, 8 (3), 1360–1373.
31. Santos, A.; Law, C. S.; Chin Lei, D. W.; Pereira, T.; Losic, D. Fine Tuning of Optical Signals in Nanoporous Anodic Alumina Photonic Crystals by Apodized Sinusoidal Pulse Anodisation. *Nanoscale* **2016**, 8 (43), 18360–18375.
32. Bartzsch, H.; Lange, S.; Frach, P.; Goedicke, K. Graded Refractive Index Layer Systems for Antireflective Coatings and Rugate Filters Deposited by Reactive Pulse Magnetron Sputtering. *Surf. Coat. Technol* 2004, 180–181, 616–620.
33. Salem, M. S.; Sailor, M. J.; Sakka, T.; Ogata, Y. H. Electrochemical Preparation of a Rugate Filter in Silicon and Its Deviation from the Ideal Structure. *J. Appl. Phys* **2007**, 101 (6), 1–6.
34. Law, C. S.; Santos, A.; Nemati, M.; Losic, D. Structural Engineering of Nanoporous Anodic Alumina Photonic Crystals by Sawtooth-like Pulse Anodization. *ACS Appl. Mater. Interfaces* **2016**, 8 (21), 13542–13554.
35. Xu, B.; Zhang, D.; Zeng, X.; Wang, Y.; Dong, Z. Transmission Characteristics of Photonic Crystal Waveguide with Array Square Al_2O_3 Rods Lattice in Millimeter Wave. *Opt. Mater* **2019**, 97 (July), 1-4.
36. Kushnir, S. E.; Napolskii, K. S. Thickness-Dependent Iridescence of One-Dimensional Photonic Crystals Based on Anodic Alumina. *Mater. Des* **2018**, 144, 140–150.
37. Lee, W.; Kim, J. Highly Ordered Porous Alumina with Tailor-Made Pore Structures Fabricated by Pulse Anodization. *Nanotechnology* **2010**, 21, 1-8

38. Lee, W.; Schwirn, K.; Steinhart, M.; Pippel, E.; Scholz, R. Structural Engineering of Nanoporous Anodic Aluminium Oxide by Pulse Anodization of Aluminium. *Nat. Nanotechnol,* **2008**, 3 (April), 234–239.
39. Lee, W.; Scholz, R.; Go, U. A Continuous Process for Structurally Well-Defined Al_2O_3 Nanotubes Based on Pulse Anodization of Aluminum. *Nano Lett* **2008**, 8 (8), 2155–2160.
40. Lee, W.; Kim, J.; Go, U. Spontaneous Current Oscillations during Hard Anodization of Aluminum under Potentiostatic Conditions. *Adv. Funct. Mater* **2010**, 20, 21–27.
41. Wang, Y.; Santos, A.; Evdokiou, A.; Losic, D. Rational Design of Ultra-Short Anodic Alumina Nanotubes by Short-Time Pulse Anodization. Electrochim. Acta **2015**, 154, 379−386
42. Chen, Y.; Santos, A.; Wang, Y.; Kumeria, T.; Wang, C.; Li, J.; Losic, D. Interferometric Nanoporous Anodic Alumina Photonic Coatings for Optical Sensing. *Nanoscale* **2015**, 7, 7770–7779.
43. Eckstein, C.; Xifre-Perez, E.; Porta-I-Batalla, M.; Ferre-Borrull, J.; Marsal, L. F. Optical Monitoring of the Capillary Filling Dynamics Variation in Nanoporous Anodic Alumina toward Sensing Applications. *Langmuir* **2016**, 32 (41), 10467–10472.
44. Pol, L.; Acosta, L. K.; Ferré, J.; Marsal, L. F. Aptamer-Based Nanoporous Anodic Alumina Interferometric Biosensor for Real-Time Thrombin Detection. *Sensors* **2019**, 19 (4543), 1–11.
45. Pol, L.; Eckstein, C.; Acosta, L. K.; Xifre, E.; Josep, F.; Marsal, L. F. Real-Time Monitoring of Biotinylated Molecules Detection Dynamics in Nanoporous Anodic Alumina for Bio-Sensing. *Nanomaterials* **2019**, 9 (478), 1–12.
46. Rajeev, G.; Simon, B. P.; Marsal, L. F.; Voelcker, N. H. Advances in Nanoporous Anodic Alumina-Based Biosensors to Detect Biomarkers of Clinical Significance: A Review. Adv. Healthcare Mater **2018**, 7 (7), 1–18.
47. Hernández-Eguía, L. P.; Ferré-Borrull, J.; Macias, G.; Pallarès, J.; Marsal, L. F. Engineering Optical Properties of Gold-Coated Nanoporous Anodic Alumina for Biosensing. *Nanoscale Res. Lett* **2014**, 9 (1), 414, 1-8.

48. Schneider, C.A., Rasband, W.S., Eliceiri, K.W. NIH Image to ImageJ: 25 years of image analysis. Nature Methods **2012**, 9, 671-675.
49. Alekseev, S. A.; Lysenko, V.; Zaitsev, V. N.; Barbier, D. Application of Infrared Interferometry for Quantitative Analysis of Chemical Groups Grafted onto the Internal Surface of Porous Silicon Nanostructures. J. Phys. Chem. C **2007**, 111 (42), 15217–15222.
50. Kuang, P.; Bhattacharya, S.; Hsieh, M.-L.; John, S.; Lin, S.-Y. Photonic Crystals with a Continuous, Gaussian-Type Surface Profile for near-Perfect Light Trapping. *J.Nanophotonics* **2018**, 12 (2), 1-12
51. Cheng, W.; Steinhart, M.; Gösele, U.; Wehrspohn, R. B. Tree-like Alumina Nanopores Generated in a Non-Steady-State Anodization. *J. Mater. Chem* **2007**, 17 (33), 3493–3495.
52. Montero-Moreno, J. M.; Belenguer, M.; Sarret, M.; Müller, C. M. Production of Alumina Templates Suitable for Electrodeposition of Nanostructures Using Stepped Techniques. *Electrochim. Acta* **2009**, 54 (9), 2529–2535.
53. Morandi, V.; Marabelli, F.; Amendola, V.; Meneghetti, M.; Comoretto, D. Colloidal Photonic Crystals Doped with Gold Nanoparticles: Spectroscopy and Optical Switching Properties. *Adv. Funct. Mater***, 2007**, 17 (15), 2779–2786.
54. Vos, W. L.; Sprik, R.; van Blaaderen, A.; Imhof, A.; Lagendijk, A.; Wegdam, G. H. Strong Effects of Photonic Band Structures on the Diffraction of Colloidal Crystals. *Phys Rev B* **1996**, 53 (24), 16231–16235.
55. Astratov, V. N.; Vlasov, Y. A.; Karimov, O. Z.; Kaplyanskii, A. A.; Musikhin, Y. G.; Bert, N. A.; Bogomolov, V. N.; Prokofiev, A. V. Photonic Band Gaps in 3D Ordered Fee Silica Matrices. *Phys. Lett. A* **1996**, 222 (5), 349–353.
56. Sadykov, A. I.; Kushnir, S. E.; Sapoletova, N. A.; Ivanov, V. K.; Napolskii, K. S. Anodic Titania Photonic Crystals with High Reflectance within Photonic Band Gap via Pore Shape Engineering. *Scr. Mater.* **2020**, 178, 13–17.
57. Spanier, J. E.; Herman, I. P. Use of Hybrid Phenomenological and Statistical Effective-Medium Theories of Dielectric Functions to Model the Infrared Reflectance of Porous SiC Films. *Phys Rev B*,**2000**, 61 (15), 437–450.

58. Kumeria, T.; Santos, A.; Rahman, M. M.; Ferré-Borrull, J.; Marsal, L. F.; Losic, D. Advanced Structural Engineering of Nanoporous Photonic Structures: Tailoring Nanopore Architecture to Enhance Sensing Properties. ACS Photonics **2014**, 1 (12), 1298− 1306
59. Santos, A.; Kumeria, T.; Losic, D. Optically Optimized Photoluminescent and Interferometric Biosensors Based on Nano- porous Anodic Alumina: A Comparison. Anal. Chem. **2013**, 85, 7904− 791.

Chapter 6. Photonic Crystals Microcavities: Fabrication, Chemical surface sensitivity and light confining

UNIVERSITAT ROVIRA I VIRGILI
ENGINEERING OF PHOTONIC STRUCTURES BASED ON NANOPOROUS ANODIC ALUMINA AS AN OPTICAL SENSING PLATFORM
Laura Karen Acosta Capilla

In this Chapter Nanoporous anodic alumina optical microcavities (NAA–μQVs) with spectrally tunable resonance band and surface chemistry are used as model light-confining photonic crystal (PC) platforms to elucidate the combined effect of spectral light confinement features and surface chemistry on optical sensitivity nm^{-1} in water- and organic-based analytical solutions, respectively. These advances provide new insights into critical factors determining optical sensitivity in light-confining nanoporous PC structures, with implications across optical sensing applications, and other photonic technologies.

6.1 Introduction

Photonic crystals (PCs) are a class of structured materials that enable precise molding of electromagnetic waves flow for a plethora of applications.[1,2] Light propagation across PCs is governed by interference between multiply Bragg scattered waves, the energy dispersion of which is formally described by a photonic band diagram featuring allowed and forbidden bands.[3] As such, PCs enable precise control over a variety of light–matter interactions by engineering their architecture, composition, and structural features.[4,5] Of all forms of light–matter interactions, confinement of light is an indispensable process for a wide range of applications such as astrophysics[6], quantum computing[7,8], lasing[9], telecommunications[10], and sensing[11]. Optical microcavities are a type of PCs that confine light into small volumes by resonant recirculation of electromagnetic waves.[12,13]

Strong light confinement within these PC structures is characterized by a narrow, well-resolved spectral resonance band (RB), the width of which would ideally correspond to a single wavelength. However, in practice, the

resonance band of optical microcavities spans a relatively narrow range of wavelengths due to energy loss per optical cycle associated with structural defects and optical absorption. Similarly, minute perturbations of the environment within optical microcavities introduce changes in the properties of confined light, either in linewidth, frequency shift, or resonance splitting.[14] These alterations of confined waves are characteristically proportional to the induced perturbation magnitude, making optical microcavities prime candidates for many daily life sensing applications such as magnetometers for mineral exploration[15], opto-mechanical transducers in mobile phones[16], and single-particle/molecule detectors for environmental and medical diagnosis[17,18]. Porous optical microcavities are particularly suitable transducers for sensing since these PCs provide light-confining capabilities, high surface-to-volume ratio to increase functional binding sites and frequency of molecule-to-surface interactions, and nanochannels that facilitate transport of analyte molecules to minimize detection time.[19] 1D nanoporous optical microcavities can be prepared with precisely engineered optical properties across the broad spectrum, from UV to IR, by anodization—electrochemical oxidation. This top–down nanofabrication technique is also simple, cost-competitive, scalable, and controllable.[20—22] Porous silicon-based optical microcavities produced by anodization of silicon are the most mature and controllable technology to date. Recent advances in pulse-like anodization of aluminum have realized several architectures of nanoporous anodic alumina-based optical microcavities (NAA–μQVs).[23-30] However, only a few studies have explored the potential of these emerging optical transducers as sensing platforms. Yan *et al*.[28] and Lee *et al*.[25] demonstrated that NAA–μQVs are sensitive PC structures to changes

in refractive index, while Wang *et al*. proved that NAA–μQVs' RB undergoes dynamic spectral shifts upon exposure to humidity from water vapor.[26] Despite these advances, there remain fundamental questions concerning the design and engineering of NAA–μQVs to maximizing sensitivity of light confined within their structure for practical sensing applications. Previous studies on nanoporous PCs[31,32] point that sensitivity of NAA–μQVs is critically determined by i) size of analyte molecules, ii) degree to which analyte molecules increase the refractive index of the medium filling the nanopores, iii) molecule-to-surface interaction strength, and iv) spectral position and quality of light confinement.

Herein, the combined effect of spectral light confinement features and surface chemistry on optical sensitivity of NAA–μQVs has been analyzed for the first time. The architecture of these 1D NAA–PC structures is engineered by stepwise pulse anodization (STPA) under current density control conditions (**Figure 6.1a**). Model NAA–μQVs feature two highly reflective distributed Bragg mirrors with a physical cavity layer in between (**Figure 6.1b**). The optical spectrum of NAA–μQVs show well-resolved, spectrally tunable RBs, the central wavelength of which is engineered from ~400 to 800 nm by STPA (**Figure 6.1c**). The surface chemistry of NAA–μQVs is selectively modified to alter their wettability. The characteristic RB of hydrophilic and hydrophobic NAA–μQVs undergoes quantifiable spectral shifts upon infiltration of their nanoporous structure with organic- and aqueous-based analytical solutions of equally varying refractive index. Analysis of refractive index-induced spectral shifts of NAA–μQVs' RB allows us to generate fundamental knowledge about how spectral resonance features and surface chemistry determine optical sensitivity in these model optical microcavities.

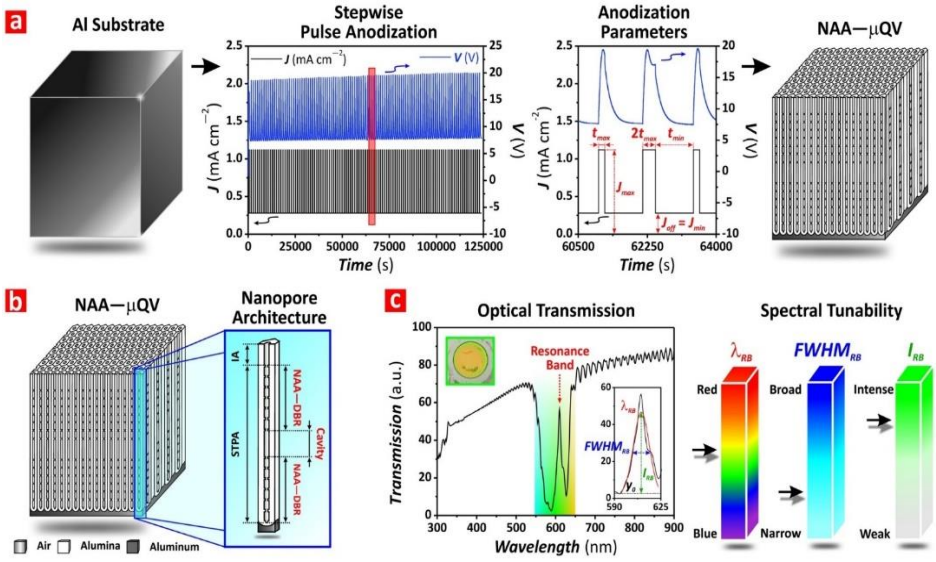

Figure 6.1. Fabrication and optical engineering of nanoporous anodic alumina optical microcavities (NAA–μQVs) by stepwise pulse anodization (STPA). (a) Schematic of the fabrication process of NAA–μQVs by STPA under current density control conditions with: aluminum substrate (left), representative STPA profile with a definition of anodization parameters (center), and idealized structure of NAA–μQVs (right) (NB: anodization profile used to produce a NAA–μQV_{600}, with a magnified view of red rectangle defining graphically the main anodization parameters including maximum current density – J_{max} = 1.120 mA cm^{-2}, minimum or offset current density – J_{min} = J_{off} = 0.280 mA cm^{-2}, time at J_{max} – t_{max} = 160 s, and time at J_{min} – t_{min} = 962 s). (b) Schematic representing the idealized nanopore architecture of NAA–μQVs formed by two NAA distributed Bragg reflectors (NAA–DBRs) with a physical cavity in between (NB: IA = initial anodization). (c) Representative transmission spectrum of a NAA–μQV_{600} showing details of the characteristic resonance band (RB) and a graphical description of the main optical features (inset) including central wavelength position – λ_{RB}, full width at half maximum – $FWHM_{RB}$, and intensity – I_{RB}, which can be precisely tuned across the UV–visible spectrum by the input anodization period in the STPA profile.

6.2 Experimental Details

6.2.1. Fabrication of NAA–μQVs by STPA.

1.5 × 1.5 cm square Al chips were cleaned in ethanol and water under sonication for 15 min each, dried, and stored until further use. Prior to anodization, Al chips were electropolished in a 4:1 (*v*:*v*) EtOH:$HClO_4$ electrolyte at 5 ^{o}C and 20 V for 3 min. After electropolishing, Al chips were anodized under current density control conditions in 1 M aqueous H_2SO_4

acid electrolyte at -2 °C. The acid electrolyte composition was modified with 25 *v*% of EtOH to prevent it from freezing at sub-zero temperature.[33,34] Electrolyte temperature inside custom-built electrochemical reactors was kept constant throughout anodization, using a system of cold plates connected to liquid refrigerated circulators (AC150–A25, Thermo Fisher Scientific, Australia). The anodizing electrolyte was stirred at a rate of ~300 rpm to homogenize the temperature and composition of the reactant solution during anodization. The anodization process started with a constant current density (*J*) step at 1.120 mA cm^{-2} for 10 min to achieve a constant nanopore growth rate before switching anodization to STPA. After that, this top–down fabrication process started with the generation of a NAA–DBR featuring a total of 55 NAA stacks with a stepwise modulated porosity. This structure was fabricated by switching the input current density between J_{max} = 1.120 mA cm^{-2} and $J_{min} = J_{off}$ = 0.280 mA cm^{-2} in a stepwise fashion, for a duration of t_{max} and t_{min}, respectively, and for a total of 55 STPA pulses. Then, a physical cavity layer featuring straight nanopores was created by applying a constant current density step at $J_{max} = J_Q$ = 1.120 mA cm^{-2}, for a given time of $t_Q = 2 \cdot t_{max}$. The process was then switched back to STPA mode to create another NAA–DBR structure with as many NAA stacks as those of the top NAA–DBR, under the same fabrication conditions. Input current density-time STPA profiles were generated by a custom-designed Labview-based application. The anodization period (T_P) for each STPA pulse was defined as the total time duration at J_{max} and J_{min}, where $T_P = t_{max} + t_{min}$ and $t_{max} = 6 \cdot t_{min}$. **Table 6.1** summarizes the conditions used to fabricate the five types of NAA–µQVs assessed in this study.

Table 6.1. Fabrication conditions used to produce NAA–μQVs by STPA including anodization period (T_P), maximum current density (J_{max}), minimum current density (J_{min}), time at J_{max} (t_{max}), time at J_{min} (t_{min}), cavity current density ($J_Q = J_{max}$), and time at J_Q (t_Q).

NAA–µQV	T_P (s)	t_{max} (s) J_{max} (mA cm^{-2})	t_{min} (s) J_{min} (mA cm^{-2})	t_Q (s) J_Q (mA cm^{-2})
NAA–µQV$_{400}$	748	107 1.120	641 0.280	**214** **1.120**
NAA–µQV$_{500}$	935	134 1.120	801 0.280	**268** **1.120**
NAA–µQV$_{600}$	1122	160 1.120	962 0.280	**320** **1.120**
NAA–µQV$_{700}$	1309	187 1.120	1122 0.280	**374** **1.120**
NAA–µQV$_{800}$	**1496**	**214** **1.120**	**1282** **0.280**	**428** **1.120**

6.2.2. Surface Functionalization of NAA–µQVs.

The inner surface of a set of freshly prepared NAA–µQVs was chemically functionalized with dichlorodimethysilane via chemical vapor deposition.[35] In brief, NAA–µQVs were hydroxylated in 30 *wt* % H_2O_2 at 100 ^oC for 10 min and dried under air stream. Hydroxylated NAA–µQVs were subsequently functionalized with dichlorodimethysilane by chemical vapor deposition under vacuum at 110 ^oC for 3 h. After this, NAA–µQVs were washed with ultrapure water and ethanol to remove unbounded dichlorodimethysilane molecules. Contact angle of as-produced and dichlorodimethysilane-functionalized NAA–µQVs was measured by an optical tensiometer (Attension Theta Flex, Biolin Scientific, Sweden), using the sensile drop technique. Briefly, a water droplet (~15 mL) was formed on the end of a syringe and approached to NAA–µQVs' surface until

contact. Upon contact, the needle was withdrawn, and image analysis was performed to establish the contact angle on the surface of NAA–μQVs.

6.2.3. Optical Characterization of NAA–μQVs.

Before optical characterization, Al substrate remaining after fabrication was selectively removed from the backside of NAA–μQVs by wet chemical etching in a mix HCl–$CuCl_2$ solution (2.4 M HCl and 0.2 M $CuCl_2$) to create a transparent window, using a 5 mm-diameter circular etching mask. Transmission spectra of NAA–μQVs were acquired at normal incidence, from 200 to 900 nm, using a UV–visible spectrophotometer (Cary 300, Agilent, USA). Optical features of the characteristic resonance band (RB) in the transmission spectra of NAA–μQVs (i.e., central wavelength – λ_{RB}, full width at half maximum – $FWHM_{RB}$, intensity – I_{RB}, and quality factor – $Q_{RB} = \lambda_{RB}/FWHM_{RB}$) were estimated from Gaussian fittings performed in OriginPro 8.5, using the lower lobe of the RB as a baseline (y_0)—graphical description in **Figure 6.1c**. The anodic oxide growth rate (G_R) and effective refractive index (n_{eff}) of NAA stacks forming the structure of NAA–μQVs were quantified by a set of reference NAA films produced under constant current density control conditions at J_{min} and J_{max}, using 1 M H_2SO_4 acid electrolyte at –2 ^oC.

The growth rate of NAA at J_{min} and J_{max} (i.e. $G_{R–min}$ and $G_{R–max}$) was determined via FEG-SEM image analysis from reference NAA films produced in 1 M H_2SO_4 acid electrolyte at –2 ^oC for 5, 10, 15, and 20 h. NAA films used to characterize the effective refractive index of NAA at J_{min} and J_{max} (i.e. $n_{eff–min}$ and $n_{eff–max}$) were fabricated for a fixed total charge density of 5 C cm^{-2}—integrated current density per unit area and time. Specular reflection spectra from these NAA films were acquired at varying

angles of incidence (q_{Inc} = 15º, 25º, 35º and 45º) in a system comprising a variable angle reflection stage (RSS–VA, Ocean Optics, USA) coupled to a miniature visible optical fiber spectrometer (FLAME–T–VIS–NIR–ES, Ocean Optics, USA) and a tungsten light source (LS–1LL, Ocean Optics, USA) via optical fibers (QP200–2–UV–VIS, Ocean Optics, USA). Reflection spectra, from 400 to 900 nm, were acquired with an integration time of 10 ms and 20 average measurements, and processed by applying fast Fourier transform (FFT) in IgorPro (WaveMetrics, USA) to quantify the effective optical thickness (OT_{eff}) of these NAA films by Equation 6.1:

$$OT_{eff} = 2 \cdot n_{eff} \cdot L_P \cdot \cos\theta \qquad (6.1)$$

where OT_{eff} is the effective optical thickness of the NAA film (in nm), n_{eff} is its effective refractive index, L_P is its physical thickness (in nm) and q is the angle of refraction of light. Digital photographs of NAA–µQVs were acquired by a Canon EOS 700D digital camera equipped with a Tamron 90 mm F2.8 VC USD macro mount lens under natural illumination.

6.2.4. Simulations of Transmission Spectra of NAA–µQVs.

Simulated transmission spectra of NAA–µQVs were calculated by implementing and executing a tailored transfer matrix method (TMM) algorithm in a customized MATLAB application. Experimental values of effective refractive index of each NAA stack in the structure of NAA–µQVs and central wavelength of their characteristic resonance band were used as inputs to validate our model.[36—38]

6.2.5. Assessment of Optical Sensitivity of NAA–µQVs.

Refractive index sensitivity of hydrophilic and hydrophobic NAA–µQVs was assessed by quantification of spectral shifts of their characteristic resonance band (Dl_{RB}) upon infiltration of their nanoporous structure with aqueous- and organic-based analytical solutions of equally varying refractive index, from $n_{medium–low}$ = 1.333 ± 0.001 RIU to $n_{medium–high}$ = 1.345 ± 0.001 RIU. Aqueous analytical solutions were prepared by dissolution of controlled concentrations of NaCl in Milli-Q water at *[NaCl]* = 0.00, 0.30, 0.45, 0.70, 0.90, and 1.20 M. Organic analytical solutions were prepared by mixing methanol and ethanol at volume ratios of *[MeOH]*:*[EtOH]* (*v*:*v*) = 0.80:0.20, 0.70:0.30, 0.67:0.33, 0.60:0.40, 0.50:0.50, and 0.45:0.55 to achieve a variation of n_{medium} from 1.333 to 1.345 RIU. Hydrophilic and hydrophobic NAA–µQVs were sandwiched in a custom-built, transparent, acrylic plastic-based flow cell system, through which analytical solutions were flowed at a rate of 100 µL min^{-1}, using a peristaltic pump (LongerPump, Thermoline Scientific, Australia).

Real-time optical transmission spectra of hydrophilic and hydrophobic NAA–µQVs were obtained using a transmission setup comprising a transmission stage (STAGE–RTL–T, Ocean Optics, USA) coupled to two optical fibers (QP200–2–UV–VIS, Ocean Optics, USA) connecting a tungsten light source (LS–1LL, Ocean Optics, USA) with a high-resolution optical fiber spectrometer (HDX–XR, Ocean Optics, USA). White light was focused and illuminated onto NAA–µQVs over a circular spot size of ~2 mm in diameter and collected at their backside using a collimating lenses system (74–VIS, Ocean Optics, USA). Transmission spectra were acquired from 400 to 900 nm with an integration time of 10 ms and 20 average

measurements and processed by applying real-time Gaussian fittings to the characteristic resonance band in IgorPro (WaveMetrics, USA) to quantify DI_{RB}.

6.2.6. Structural Characterization of NAA–µQVs.

NAA–µQVs and reference NAA films were characterized by field emission gun scanning electron microscopy (FEG-SEM Quanta 450, FEI, USA), and their geometric features estimated by FEG-SEM image analysis performed in ImageJ.[39]

6.3. Results and Discussion

6.3.1. Structural Features of NAA–µQVs by STPA.

Figure 6.2a shows a schematic of the idealized nanoporous structure of NAA–µQVs with a graphical definition of the main geometric and optical features of these PCs. These include the total thickness (L_P), period length at J_{min} ($L_{TP–min}$) and J_{max} ($L_{TP–max}$), period length ($L_{TP} = L_{TP–min} + L_{TP–max}$), cavity length ($L_{TP–Q}$), and effective refractive indexes at J_{min} ($n_{eff–min}$), J_{max} ($n_{eff–max}$), and J_Q ($n_{eff–Q}$). Note that, under the design conditions used in this study, $L_{TP–Q} = 2L_{TP–max}$ and $n_{eff–Q} = n_{eff–max}$. The architecture of NAA–µQVs can be divided into three main substructures: i) two symmetric NAA–DBRs at their top and bottom featuring nanopores with modulated porosity in depth, and ii) a physical cavity layer in between them with straight cylindrical nanopores. **Figure 6.2b–d** depict a set of FEG-SEM images of a representative NAA–µQV_{800}. These NAA-based PCs feature homogeneously distributed nanopores at their top surface, the average diameter of which is 22 ± 4 nm (**Figure 6.2b**).

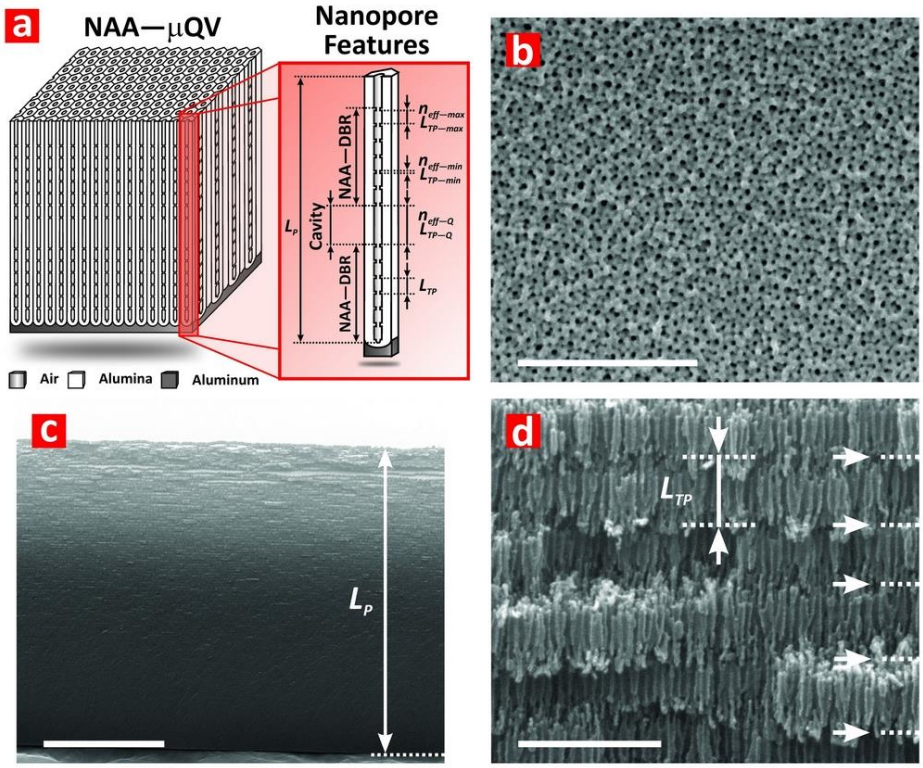

Figure 6.2. Structural engineering of NAA–μQVs by stepwise pulse anodization (STPA). (a) Schematic showing the idealized structure of NAA–μQVs formed by two NAA–DBRs with a physical cavity layer in between, and a graphical definition of the main geometric and optical features (NB: total thickness – L_P, nanopore length at minimum current density – L_{TP-min}, nanopore length at maximum current density – L_{TP-max}, period length – $L_{TP} = L_{TP-min} + L_{TP-max}$, cavity length – L_{TP-Q}, effective refractive index at minimum current density – $n_{eff-min}$, effective refractive index at maximum current density – $n_{eff-max}$, and effective refractive index at cavity current density – n_{eff-Q}). (b) Top view FEG-SEM image of a representative NAA–μQV$_{800}$ showing details of randomly distributed nanopores with an average diameter of 22 ± 4 nm (scale bar = 500 nm). (c) General cross-sectional view FEG-SEM image of a representative NAA–μQV$_{800}$ revealing NAA stacks with modulated porosity along their length (scale bar = 10 mm). (d) Magnified cross-sectional view FEG-SEM image of (c) showing details of nanopore modulations and period length (L_{TP}) denoted by white dotted lines and arrows (scale bar = 500 nm) (NB: the structure of the NAA–μQV$_{800}$ shown in (c) and (d) was widened by wet chemical etching in a 5 *wt %* aqueous solution of H_3PO_4 at 35 °C for 6 min for imaging purposes).

The full-view cross-sectional image of the NAA–μQV structure shown in **Figure 6.2c** reveals stacked layers of NAA, the periodicity of which is controlled by the input STPA profile. A magnified view of this structure

shows details of NAA layers stacked one over another. NAA layers feature periodically modulated porosity in depth, the period or lattice constant of which is defined as the period length (L_{TP})—length of NAA stacks within the NAA–μQV structure (**Figure 6.2d**).

6.3.2. Design of NAA–μQVs by STPA.

The optical properties of NAA–μQVs are critically defined by the geometric and optical features of nanopores in the NAA stacks forming their structure. The Bragg condition for constructive light recirculation in a NAA–μQV formed by two highly reflective NAA–DBRs is such that the optical thickness of each NAA stack—product of effective refractive index and physical thickness—is equal to a quarter of the resonance band central wavelength of the cavity (l_{RB}), according to Equation 6.2[26]:

$$\frac{\Delta\lambda_{RB}}{4} = n_{eff-max} \cdot L_{TP-max} = n_{eff-min} \cdot L_{TP-min} \qquad (6.2)$$

If we reorganize terms, then we get Equations 6.3 and 6.4:

$$\frac{\Delta\lambda_{RB}}{4} = n_{eff-max} \cdot L_{TP-max} \qquad (6.3)$$

$$\frac{\Delta\lambda_{RB}}{4} = n_{eff-min} \cdot L_{TP-min} \qquad (6.4)$$

The period lengths at J_{min} and J_{max} (i.e. L_{TP-min} and L_{TP-max}) can be estimated as the product between the anodic oxide growth rates (i.e. G_{R-min} and G_{R-max}) and time durations (i.e. t_{min} and t_{max}) at J_{min} and J_{max}, respectively. Therefore, if we substitute these expressions in Equations 6.3 and 6.4, this then gives us Equations 6.5 and 6.6:

$$\frac{\Delta\lambda_{RB}}{4} = n_{eff-max} \cdot G_{R-max} \cdot t_{max} \qquad (6.5)$$

$$\frac{\Delta\lambda_{RB}}{4} = n_{eff-max} \cdot G_{R-min} \cdot t_{min} \quad (6.6)$$

Rearranging terms, then we obtain Equations 6.7 and 6.8:

$$t_{max} = \frac{\Delta\lambda_{RB}}{4} \cdot \left(\frac{1}{n_{eff-max} \cdot G_{R-max}}\right) \quad (6.7)$$

$$t_{min} = \frac{\Delta\lambda_{RB}}{4} \cdot \left(\frac{1}{n_{eff-min} \cdot G_{R-min}}\right) \quad (6.8)$$

Considering that $T_P = t_{max} + t_{min}$ and combining Equations 6.7 and 6.8, then we get Equation 6.9:

$$T_P = \frac{\Delta\lambda_{RB}}{4} \cdot \left(\frac{1}{n_{eff-max} \cdot G_{R-max}} + \frac{1}{n_{eff-min} \cdot G_{R-min}}\right) \quad (6.9)$$

This expression provides a simple and direct means of engineering the spectral position of the resonance band of NAA–µQVs by modifying the anodization period in the input STPA profile.A set of reference NAA films was fabricated under the same anodization conditions used in this study to determine G_{R-max}, G_{R-min}, $n_{eff-max}$, and $n_{eff-min}$). The anodic oxide growth rates (i.e., G_{R-min} and G_{R-max}) at J_{min} and J_{max} were determined from FEG-SEM image analysis. The refractive indexes at J_{min} and J_{max} (i.e. $n_{eff-max}$, and $n_{eff-min}$) were quantified from FFT-processed reflection spectra of these reference NAA films at q_{Inc} = 15º, 25º, 35º and 45º, combining Equation 6.1 (Fabry–Pérot) and Equation 6.10 (Snell), through an iterative calculation process:

$$n_{air} \operatorname{Sin} \theta_{Inc} = n_{eff} \operatorname{Sin} \theta \quad (6.10)$$

where n_{air} is the refractive index of air (1.000 RIU), q is the angle of refraction, and q_{Inc} is the external angle of incidence. Values of G_{R-max}, G_{R-}

$_{min}$, $n_{eff–max}$, and $n_{eff–min}$ under the conditions of study were measured to be 0.41 ± 0.03 nm s^{-1}, 0.09 ± 0.1 nm s^{-1}, 2.263 ± 0.002 RIU, and 1.773 ± 0.003 RIU, respectively. If we substitute these values in Equation 6.9, this then gives T_P ~1.84·l_{RB}. This expression provides a direct relationship between anodization period and position of resonance band of NAA–µQVs.

6.3.3. Structural and Optical Engineering of NAA–µQVs by STPA.

A set of NAA–µQVs featuring resonance bands across the visible spectrum was engineered by systematic variation of the anodization period in the input STPA profile, from T_P = 748 to 1496 s with DT_P = 187 s (**Table 6.1**). **Figure 6.3** shows anodization profiles, cross-sectional view FEG-SEM images, and transmission spectra of representative NAA–µQV_{400}, NAA–µQV_{600}, and NAA–µQV_{800}, while (**Figure 6.4)** compiles these details for all NAA–µQVs assessed in this study (i.e., NAA–µQV_{400}–NAA–µQV_{800}). A qualitative analysis of full-view anodization profiles shown in **Figures 6.3a–c** reveals that a stepwise pulsed input current density profile, with an amplitude of $A_J = J_{max} – J_{min}$ = 0.840 mA cm^{-2}, results in a pulsed output voltage profile with an average amplitude of ~12.5 V and a frequency that follows closely that of the input current density waveform.

Magnified views of these anodization profiles show an electrochemical output in the form of asymmetric voltage pulses featuring capacitor-like charge-discharge regions, which correspond to the sections at J_{max} and J_{min} of the input STPA pulses, respectively. This electrochemical response is associated with the hemispherical barrier oxide layer closing the tip of NAA's nanopores at the anodic oxide growth front (i.e., interface anodic oxide–metal).[40,41]

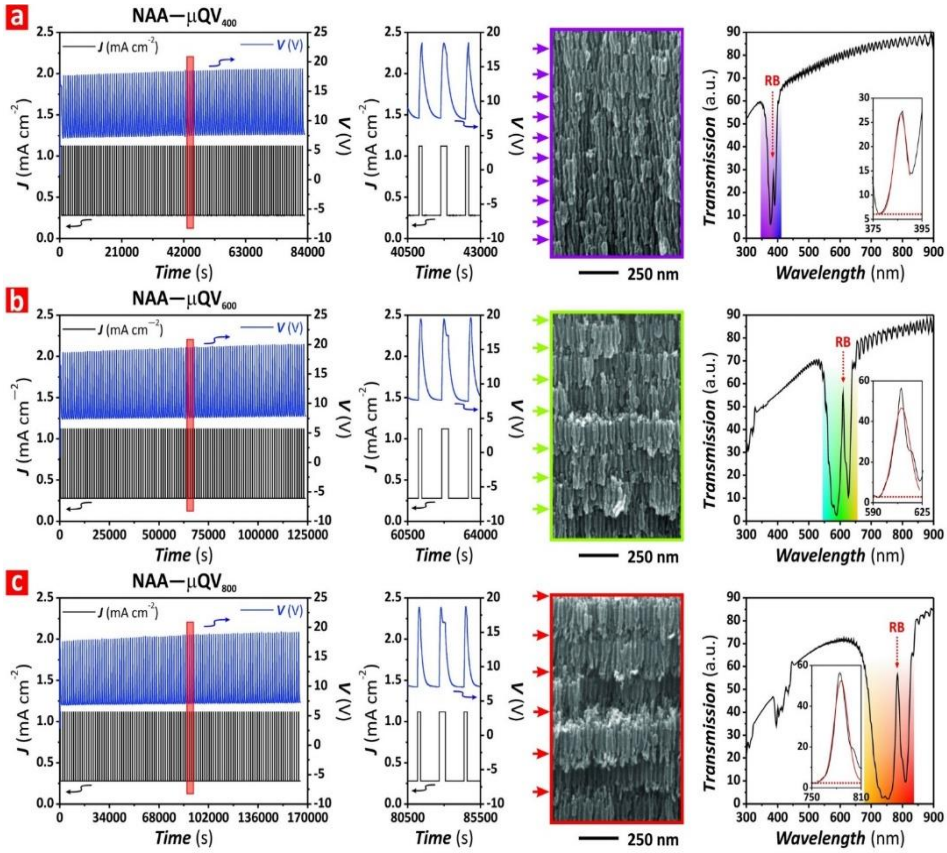

Figure 6.3. Structural and optical engineering of NAA–μQVs by STPA (NB: the structure of NAA–μQVs shown in these FEG-SEM images was widened by wet chemical etching in a 5 *wt* % aqueous solution of H_3PO_4 at 35 ^oC for 6 min for imaging purposes). (a) Full-view of anodization profile used to fabricate NAA–μQV_{400} with a magnified view of red rectangle showing details of the input current density and output voltage response (left), magnified cross-sectional view FEG-SEM image of a representative NAA–μQV_{400} with purple arrows indicating the period length (center), and full-view transmission spectrum of a NAA–μQV_{400} with details of the RB (inset) (right). (b) Full-view of anodization profile used to fabricate NAA–μQV_{600} with a magnified view of red rectangle showing details of the input current density and output voltage response (left), magnified cross-sectional view FEG-SEM image of a representative NAA–μQV_{600} with green arrows indicating the period length (center), and full-view transmission spectrum of a NAA–μQV_{600} with details of the RB (inset) (right). (c) Full-view of anodization profile used to fabricate NAA–μQV_{800} with a magnified view of red rectangle showing details of the input current density and output voltage response (left), magnified cross-sectional view FEG-SEM image of a representative NAA–μQV_{800} with red arrows indicating the period length (center), and full-view transmission spectrum of a NAA–μQV_{800} with details of the RB (inset) (right).

Anodic aluminum oxide is an electrical insulator that delays the flow of electrons and ionic species (i.e., Al^{3+}, O^{2-}, and OH^{-}) driven by the applied electric field across the barrier oxide layer during anodization. Dynamic change in input current density, results in an adjustment of the barrier oxide layer thickness to counterbalance the induced change in electric field. Analysis of anodization profiles reveals a short time delay (~10–18 s) between change in input current density and output voltage response for all NAA–μQVs developed in this study (**Figure 6.4**). This indicates that these anodization conditions make it possible to precisely engineer nanopore morphology modulations in depth by judicious modification of the input current density.

FEG-SEM cross-sectional analysis of representative NAA–μQV_{400}, NAA–μQV_{600}, and NAA–μQV_{800} films upon mechanical fracture reveals a layered structure of NAA stacks featuring periodically modulated porosity along their length (**Figures 6.3a–c**). The structural periodicity or lattice constant of these 1D NAA–μQVs is defined as the period length (L_{TP})—thickness of NAA stacks within the NAA–μQV structure. It is apparent from color arrows in **Figures 6.3a–c** and **Figure 6.4** that L_{TP} increases with anodization period in the input STPA pulses. Optical transmission spectra of NAA–μQVs shown in **Figures 6.3a–c** and **Figure 6.4** is characterized by an intense, broad photonic stopband (PSB), the features of which are determined by the two NAA–DBRs forming this PC structure. Magnified views of these PBSs reveal well-resolved, narrow resonance bands (RBs) at approximately their center. This optical feature is attributable to constructive light recirculation within NAA–μQVs, which results from the intercalation of a physical cavity layer between the two NAA–DBRs.

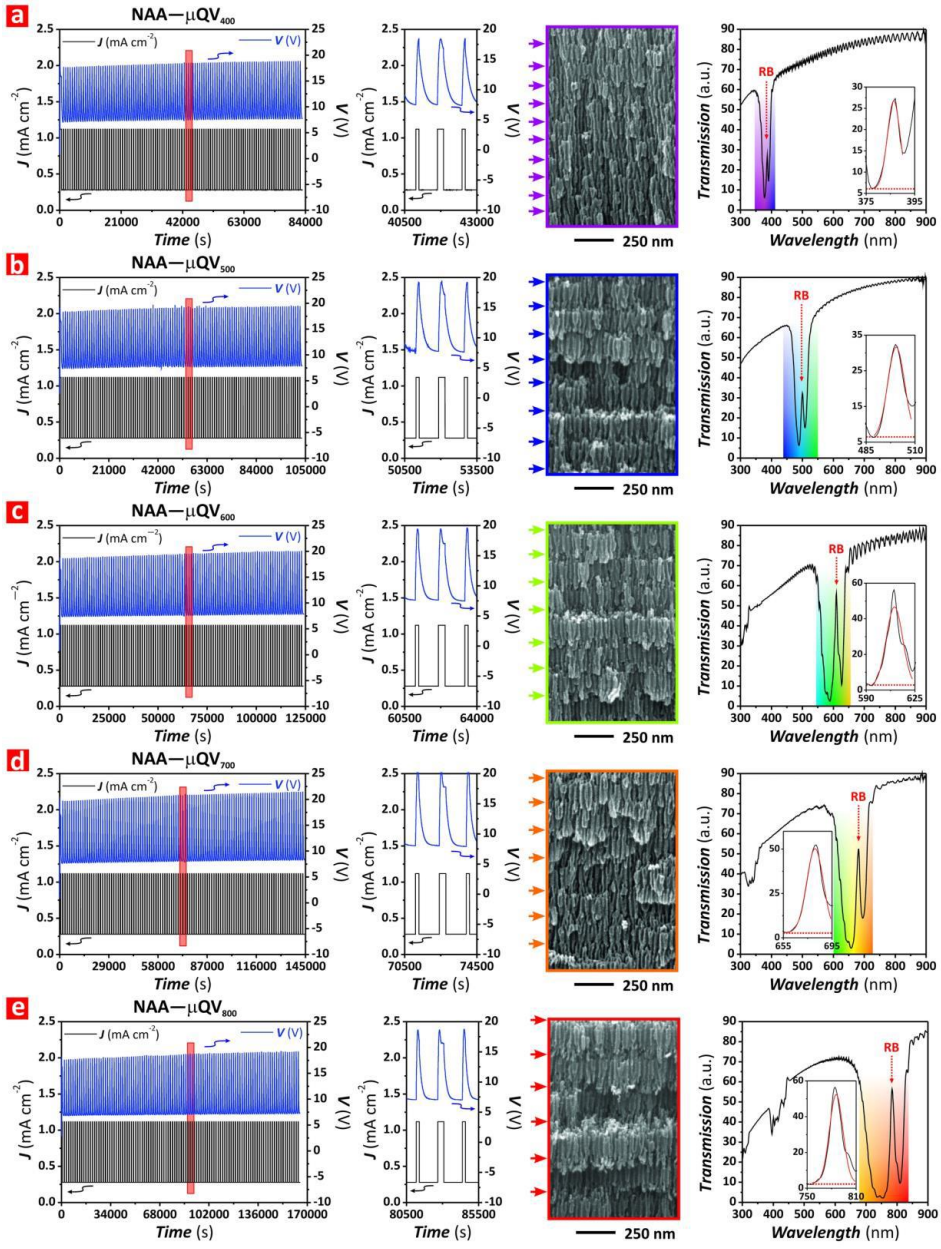

Figure 6.4. Structural and optical engineering of NAA–μQVs by STPA (NB: the structure of NAA–μQVs shown in these FEG-SEM images was widened by wet chemical etching in a 5 wt % aqueous solution of H_3PO_4 at 35°C for 6 min for imaging purposes). (a–e) Full-view of anodization profile used to fabricate NAA–μQV_{400}—NAA–μQV_{800} with a magnified view of red rectangle showing details of the input current density and output voltage response (left), magnified cross-sectional view FEG-SEM image of a representative NAA–μQV_{400}—NAA–μQV800 with color arrows indicating the period length (center), and full-view transmission spectrum of NAA–μQV_{400}—NAA–μQV_{800} with details of RBs (inset) (right).

It is also apparent from these graphs that RB red-shifts (shift toward longer wavelengths) its position with increasing anodization period. Note that the resonance band spectral position is determined by the intrinsic relationship between the geometric and optical properties of the cavity layer and the NAA stacks forming the structure of NAA–DBRs, which is designed to fulfil the conditions $L_{TP-Q} = 2 \cdot L_{TP-max}$ and $n_{eff-Q} = n_{eff-max}$.[26] An increment in T_P in the input current density results in longer L_{TP} and L_{TP-Q} within the NAA–DBRs and the cavity layer composing the PC structure, respectively (**Figure 6.5a**). As such, the resonance band position (l_{RB}) can be precisely engineered across the broad spectrum by modification of T_P in the input STPA profile. **Figure 6.5b** shows the intrinsic dependence of the total thickness (L_P) and period length (L_{TP}) in NAA–μQVs with T_P, from 748 to 1496 s. It is apparent from this graph that both L_P and L_{TP} increase linearly with increasing T_P at rates of 8.6 ± 3.4 and 0.10 ± 0.01 nm s^{-1}, respectively. **Figure 6.5b** (inset) shows the dependence of nanopore diameter at the top of NAA–μQVs (D_P) with the anodization period, where this geometric parameter increases exponentially with T_P according to the expression D_P (nm) = 15 + 0.06·Exp[(T_P (s) – 373)/241)]. This finding is reasonable since the longer T_P the more time the NAA–μQV structure is exposed to the acid electrolyte, which inevitably leads to progressive etching of its structure. **Figure 6.5c** summarizes the dependence of the optical features of the characteristic resonance band of NAA–μQVs with T_P. It is apparent that λ_{RB} red-shifts its position linearly with increasing T_P at a rate of 0.52 ± 0.01 nm s^{-1}. For instance, l_{RB} shifts its position from 386 ± 1 nm at T_P = 748 nm to 786 ± 1 nm at T_P = 1496 s, which correspond to NAA–μQV_{400} and NAA–μQV_{800}, respectively.

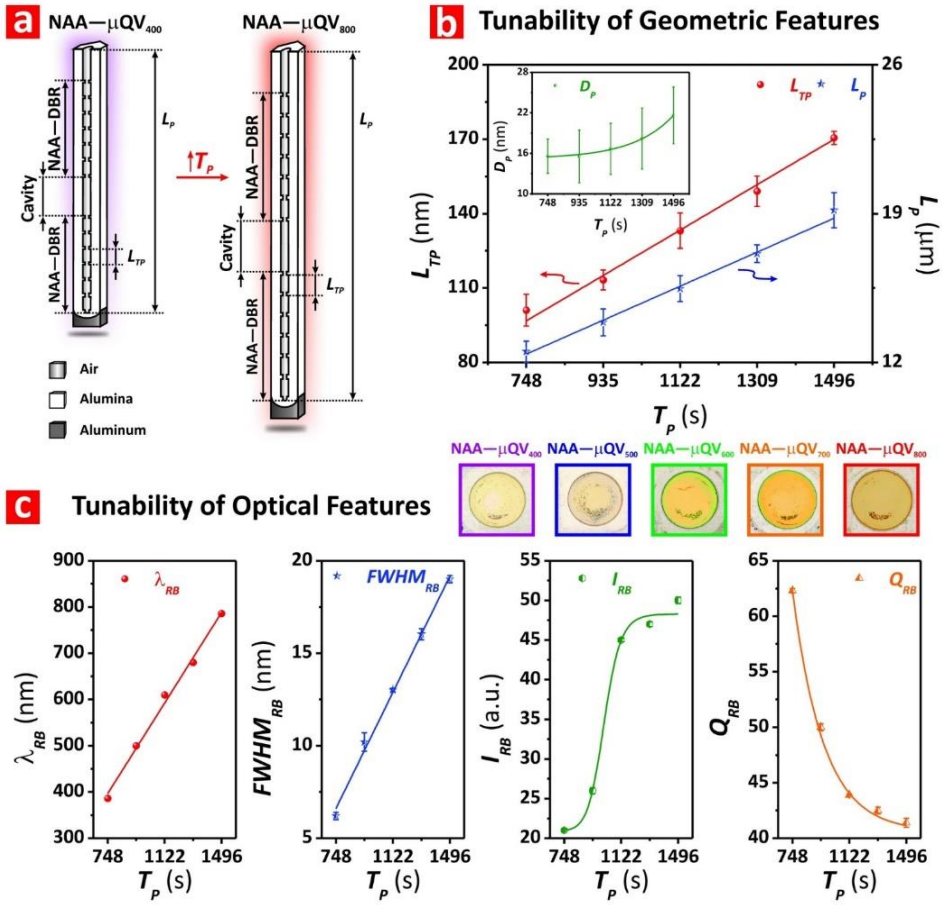

Figure 6.5 Tunability of structural and optical features of NAA–μQVs by modification of anodization period in the input STPA profile. (a) Schematics of idealized nanopores of NAA–μQVs produced at distinct anodization periods (T_P) showing details of the effect of this fabrication parameter on the structural features of these NAA-based PCs. (b) Dependence of total thickness (L_P), period length (L_{TP}), and nanopore diameter (D_P) with anodization period, from T_P = 748 to 1496 s with DT_P = 187 s, for NAA–μQV_{400}—NAA–μQV_{800}. (c) Dependence of central wavelength position (I_{RB}), full width at half maximum ($FWHM_{RB}$), intensity (I_{RB}), and quality factor (Q_{RB}) with anodization period, from T_P = 748 to 1496 s with DT_P = 187 s, for NAA–μQV_{400}—NAA–μQV_{800}, with inset showing digital pictures of these NAA–PCs featuring interferometric colors (NB: the diameter of NAA–μQVs was ~1 cm).

Comparative analysis between measured and calculated values of l_{RB} using **Equation 6.9** reveals a residual deviation that oscillates between 0.1 and 5 %, which demonstrates the suitability of our model to tune the position of the resonance band of NAA–µQVs by the input anodization period in the STPA profile.

To further validate the model, a custom-built MATLAB application using the TMM approach was used generate simulated optical spectra of NAA–µQVs, using experimentally quantified values of $n_{eff–max}$, $n_{eff–min}$, and l_{RB} as inputs.[36—38] However, an analysis of simulated and experimentally estimated values of $L_{TP–max}$ and $L_{TP–min}$ for NAA-µQV$_{400}$-NAA-µQV$_{800}$ shown in **Table 6.2** reveals a minimum deviation of ~0.1–5 %.

Table 6.2. Comparison between experimental and simulated values of period length at J_{min} (LTP_{min}) and $Jmax$ (LTP_{max}).

	***Experimental*†**		***Simulated*‡**		***Deviation****	
NAA–µQV	LTP_{min} (nm)	LTP_{max} (nm)	LTP_{min} (nm)	LTP_{max} (nm)	LTP_{min} (%)	LTP_{max} (%)
NAA–µQV400	44	58	42	54	5.4	5.7
NAA–µQV500	55	72	54	71	2.2	2.2
NAA–µQV600	66	87	66	86	0.1	0.7
NAA–µQV700	77	101	73	96	4.7	5.1
NAA–µQV800	88	115	84	111	3.7	4.0

†Values estimated as $L_{TP–min} = t_{min}·G_{R–min}$ and $L_{TP–max} = t_{max}·G_{R–max}$
‡Values estimated from simulations
*Values estimated as:
$L_{TP—min—deviation} = 100·|L_{TP—min—experimental} — L_{TP—min—simulated}|/= L_{TP—min—experimental}$
$L_{TP—max—deviation} = 100·|L_{TP—max—experimental} — L_{TP—max—simulated}|/= L_{TP—max—experimental}$

This demonstrates that our model can mechanistically describe the optical properties of these NAA-based PCs with precision, providing a useful tool to design NAA–μQVs with well-resolved resonance bands across the visible spectrum by modification of the input anodization period. It is also apparent that the width of the resonance band ($FWHM_{RB}$) increases linearly with increasing T_P at a rate of 0.017 ± 0.001 nm s^{-1}. $FWHM_{RB}$ increases from 6.2 ± 0.2 nm for NAA–μQV_{400} to 19.0 ± 0.3 nm for NAA–μQV_{800}. This analysis also indicates that the intensity of the resonance band (I_{RB}) increases with increasing T_P following a sigmoidal trend. It is worthwhile noting that an interesting characteristic of NAA–μQVs is their interferometric color, which results from efficient light reflection—forbidden light—at those visible spectral regions where their characteristic PSB and RB are located. Digital images of NAA–μQVs shown in **Figure 6.5c** reveal that, while NAA–μQV_{400} and NAA–μQV_{500} are transparent, their analogues produced at longer T_P feature vivid interferometric colors (i.e., green for NAA–μQV_{600}, orange for NAA–μQV_{700}, and red for NAA–μQV_{800}). This result is attributable to the highest I_{RB} values achieved by these NAA–μQVs, which were found to be 45 ± 1, 47 ± 1, and 50 ± 1 a.u., respectively. The quality factor (Q_{RB})—ratio of I_{RB} to $FWHM_{RB}$— is parameter that quantifies how good a given optical microcavity confines light within its structure. **Figure 6.5c** demonstrates that Q_{RB} decreases exponentially T_P according to the expression Q_{RB} = 41 + 865·Exp[—T_P (s)/203]. For instance, Q_{RB} for NAA–μQV_{400} and NAA–μQV_{800} are estimated to be 62.3 ± 0.2 and 41.4 ± 0.4, respectively. Decrease in Q_{RB} with T_P is attributable to the progressive etching of the nanoporous structure with increasing anodization time. At a fixed number of STPA pulses, NAA–μQVs produced with longer anodization period are

exposed to the acid electrolyte for longer time. Extended anodization time results in increased light scattering and an unbalanced distribution of effective optical thickness between NAA stacks at the top and bottom of the NAA–μQVs due to extensive and progressive chemical etching. As such, quality of light confinement within these NAA–PCs is worsened with anodization time. This observation will be addressed elsewhere by a new methodology to enhance controllability of Q_{RB} with anodization time.

6.3.4. Surface Chemistry Engineering and Sensing Principle of NAA–μQVs.

As-produced NAA is an amorphous, hydrophilic, amphoteric metal oxide that features an onion-like chemical composition with concentrically decreasing concentration of acid electrolyte-incorporated impurities, from the outer nanopore wall or inner surface—surface exposed to acid electrolyte—to the inner cell boundary formed of pure Al_2O_3.[44,45] The inner surface of NAA is rich in Al^{3+} and O^{2-} vacancies, and OH^- groups, which enable facile anchoring of functional molecules to tailor NAA-based PCs for selective optical sensing purposes.[22] The hydrophilic or hydrophobic character of the surface of a solid-state sensing platform can dramatically determine its sensing performance. As such, understanding the role of wettability on the sensitivity of NAA–μQVs is a critical step to enabling this technology for real-life sensing applications. With this in mind, we engineered two types of NAA–μQVs with spectrally tunable resonance bands across the visible spectrum: i) as-produced or 'hydrophilic' NAA–μQVs, and ii) dichlorodimethysilane-functionalized or 'hydrophobic' NAA–μQVs (**Figure 6.6a**). It is worthwhile nothing that, in the context of this study, the terms 'hydrophilic' and 'hydrophobic' do not

refer to the conventional contact angle classification of 90º. Contact angle (CA) measurements in hydrophilic and hydrophobic NAA–µQVs (**Figure 6.6a** insets) indicate an increasing CA upon surface chemistry functionalization, from ~15 to 44º, for as-produced and dichlorodimethysilane-functionalized NAA–µQVs, respectively.

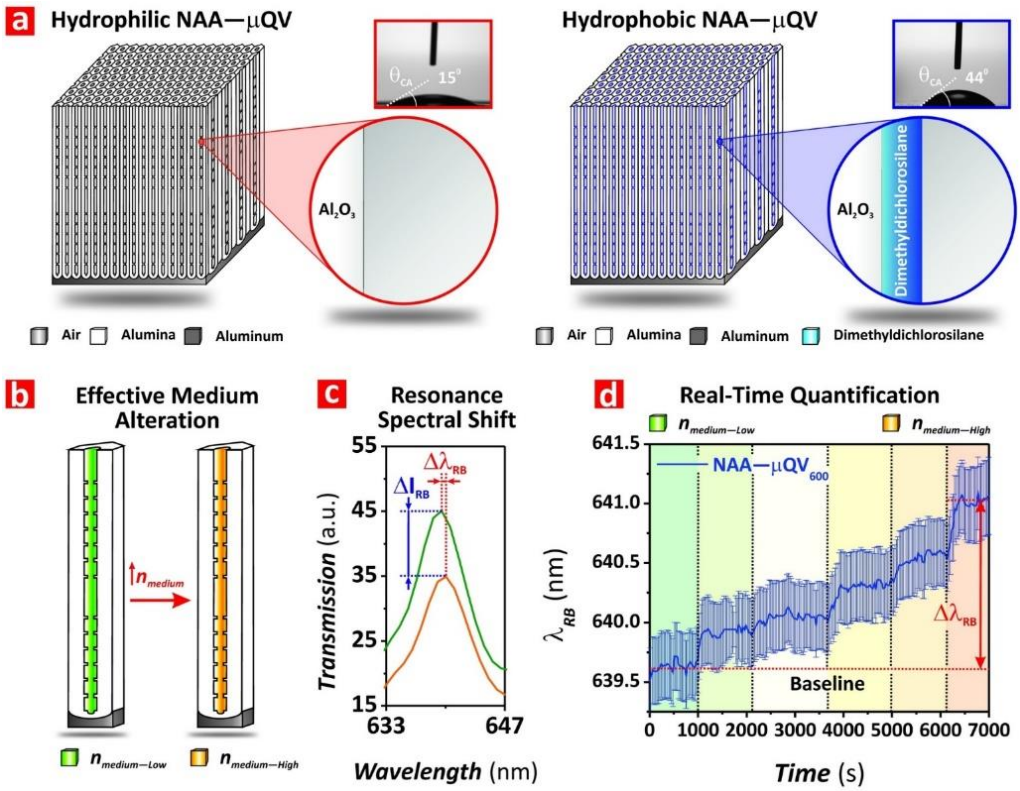

Figure 6.6. Chemical functionalization and optical sensing principle of NAA–µQVs fabricated by STPA. (a) Schematics showing the idealized structure of as-produced ('hydrophilic') and dichlorodimethysilane-functionalized ('hydrophobic') NAA–µQVs with insets displaying contact angle (CA) measurements of ~15 and 44º, respectively. (b) Schematic showing details of the nanoporous structure of NAA–µQVs upon infiltration with solutions of varying refractive index. (c) Optical transmission spectra of a representative NAA–µQV$_{600}$ showing details of its resonance band in the baseline solution (n_{medium} = 1.333 RIU, green line) and in the analytical solution with highest refractive index (n_{medium} = 1.345 RIU, orange line), including a graphical description of I_{RB} shift (DI_{RB}) and I_{RB} decay (DI_{RB}). (d) Real-time monitoring of resonance band shift with increasing n_{medium}, from $n_{medium–low}$ = 1.333 RIU to $n_{medium–high}$ = 1.345 RIU, for a representative NAA–μQV$_{600}$.

Incoming electromagnetic waves of specific wavelengths are confined with the structure of NAA–µQVs by resonant, constructive recirculation. As such, any perturbation of the effective medium of these nanoporous PCs alters the properties of confined light—core sensing principle (**Figure 6.6b**). **Figure 6.6c** shows an example of how changes in refractive index of the medium filling the nanopores of NAA–µQVs lead to quantifiable shifts in position (DI_{RB}) and decays in intensity (DI_{RB}) of their characteristic resonance band. Proportionality between induced perturbation and optical response makes NAA–µQVs a suitable class of optical sensing transducer platforms for sensing applications.

Figure 6.6d demonstrates how dynamic alterations of the effective medium of NAA–µQVs by infiltration of their nanoporous structure with media of increasing refractive index (n_{medium}) are translated into real-time, quantifiable shifts in l_{RB}, where this optical feature red-shifts its position with increasing n_{medium}, from $n_{medium–low}$ = 1.333 RIU to $n_{medium–low}$ = 1.345 RIU. Prior to injection of aqueous- and organic-based analytical solutions of equally varying refractive index (i.e., from 1.333 to 1.345 RIU) into the flow cell system, a stable baseline is obtained in the corresponding reference solution (i.e., n_{medium} = 1.333 RIU) for ~15 min.

Increasing the refractive index of the medium filling the nanoporous structure of NAA–µQVs by injecting analytical solutions of increasing n_{medium} into the flow cell results in an almost instantaneous red shift to l_{RB}. Spectral shifts of NAA–µQVs' RB are found to be proportional to the increment in n_{medium}.

6.3.5. Effect of Surface Chemistry and Resonance Band Features on Sensitivity of NAA–μQVs.

To elucidate the combined effect of spectral resonance position and surface chemistry on the sensitivity of NAA–μQVs, quantification and comparison of sensing performance indicators (i.e., sensitivity – *S* and linearity – R^2) was performed using DI_{RB} as a reference sensing parameter. **Figure 6.7** summarizes spectral shifts in resonance band position for hydrophilic and hydrophobic NAA–μQVs upon variation of n_{medium} in aqueous- and organic-based analytical solutions. It is apparent from these results that sensitivity of both hydrophilic and hydrophobic NAA–μQVs, defined as the slope of linear fittings shown in **Figures 6.8a–d**, increases with I_{RB}, in both organic and aqueous analytical solutions. Linear trends indicate a strong proportionality between effective medium perturbation and optical response in NAA–μQVs. **Table 6.3** summarizes the sensing performance parameters obtained from linear fittings shown in **Figure 6.8**. These results indicate that hydrophilic NAA–μQV_{800} in organic-based solutions, are the most sensitive structure under the conditions of study. These achieve a sensitivity of 186.5 ± 5.6 nm RIU^{-1} and a linearity of 0.9955. Further qualitative analysis of these fittings also indicates that hydrophilic NAA–μQVs are more sensitive than their hydrophobic counterparts, in both aqueous and organic media. **Figure 6.8** provides a comprehensive summary of the sensitivity of hydrophilic and hydrophobic NAA–μQVs in aqueous and organic media as a function of I_{RB}. **Figures 6.8a and b** demonstrate that sensitivity of hydrophilic and hydrophobic NAA–μQVs toward changes in refractive index of the medium filling the nanopores increases linearly with I_{RB}. However, the optical response of

these optical transducers varies significantly with surface chemistry and nature of the medium filling the nanopores for a specific range of n_{medium}. **Figure 6.8c** summarizes values of sensitivity per unit of resonance band position, defined as $S_{IRB} = S/I_{RB}$.

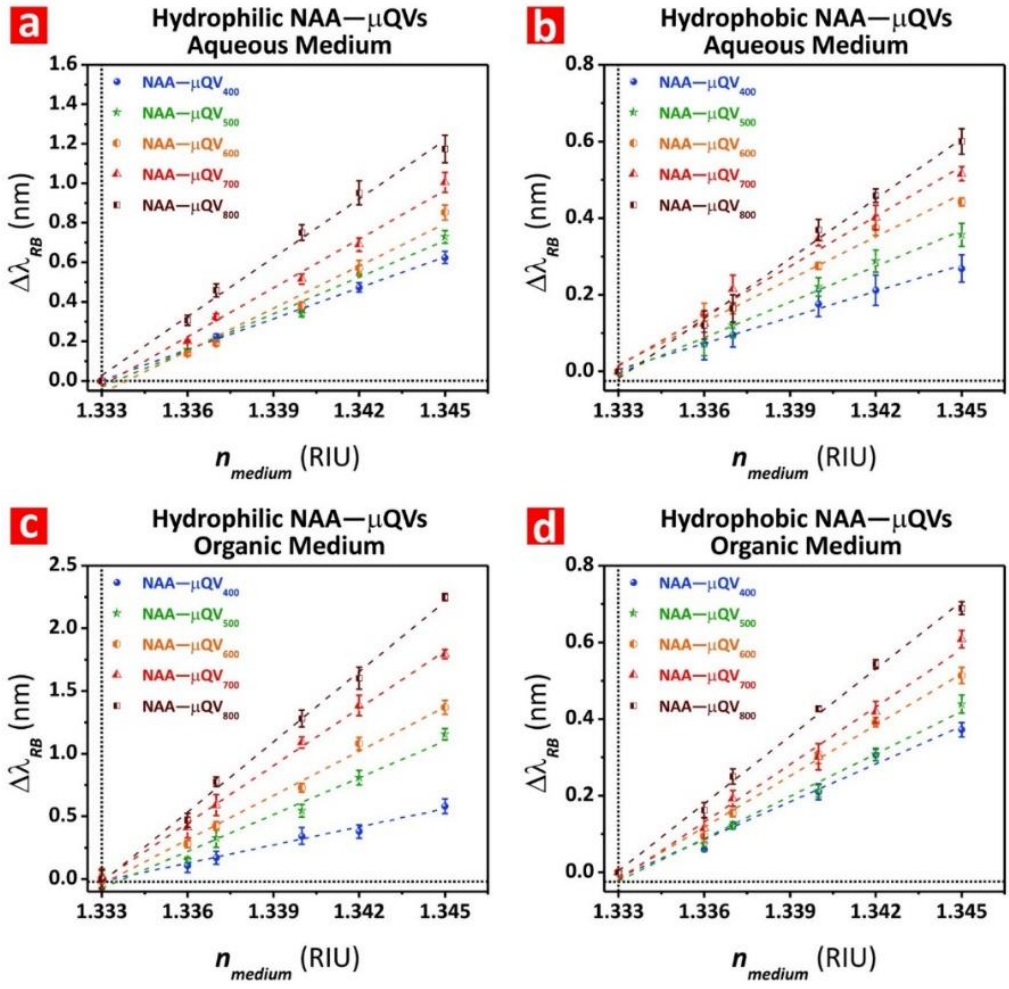

Figure 6.7. Assessment of sensing performance of hydrophilic and hydrophobic NAA–μQVs with tunable resonance bands upon exposure to aqueous- and organic-based analytical solutions of varying refractive index (n_{medium} = 1.333–1.345 RIU) using spectral shifts in their characteristic resonance band (DI_{RB}) as a core sensing principle. (a) Sensing performance of hydrophilic NAA–μQV$_{400}$—NAA–μQV$_{800}$ in aqueous medium. (b) Sensing performance of hydrophobic NAA–μQV$_{400}$—NAA–μQV$_{800}$ in aqueous medium. (c) Sensing performance of hydrophilic NAA–μQV$_{400}$—NAA–μQV$_{800}$ in organic medium. (d) Sensing performance of hydrophobic NAA–μQV$_{400}$—NAA–μQV$_{800}$ in organic medium.

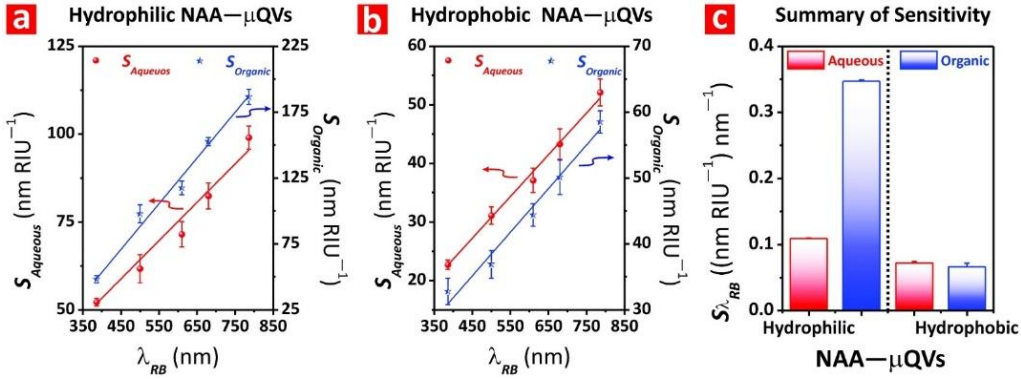

Figure 6.8. Optical sensitivity of hydrophilic and hydrophobic NAA–μQVs with tunable resonance band across the visible spectrum in aqueous- ($S_{Aqueous}$) and organic-based ($S_{Organic}$) solutions. (a) Optical sensitivity of hydrophilic NAA–μQVs in aqueous solutions as a function of l_{RB}. (b) Optical sensitivity of hydrophilic NAA–μQVs in organic solutions as a function of l_{RB}. (c) Summary of sensitivity per unit of resonance band position (S_{lRB}) for hydrophilic and hydrophobic NAA–μQVs.

Hydrophilic NAA–μQVs are clearly more sensitive than their hydrophobic analogues, in both aqueous- and organic-based solutions, with S_{lRB} values of 0.109 ± 0.001 and 0.347 ± 0.002 (nm RIU^{-1}) nm^{-1}, respectively. Hydrophilic NAA–μQVs are found to be more than three-fold more sensitive to changes in refractive index when sensing is performed in organic-based liquid matrices. Conversely, hydrophobic NAA–μQVs are found to be slightly more sensitive to alterations of refractive index in aqueous medium, with sensitivities of 0.072 ± 0.002 and 0.066 ± 0.006 (nm RIU^{-1}) nm^{-1} in aqueous- and organic-based media, respectively. Sensitivity of NAA–based PCs relies on i) size of analyte molecules, ii) degree to which analyte molecules increase the refractive index of the medium filling the nanopores, iii) molecule-to-surface interaction strength, and iv) spectral position and quality of light confinement. Previous studies on porous silicon-based PCs have pointed that optical sensitivity of these optical structures is inversely and directly proportional to the $FWHM_{RB}$ and Q_{RB}, respectively, where PCs featuring narrower and

higher quality bands provide more sensing resolution upon modification of their effective medium.[46] Conversely, sensitivity of NAA–μQVs toward changes in n_{medium} is found to increase with increasing $FWHM_{RB}$ and decreasing Q_{RB}. As such, it is necessary to consider other contributing factors that might play a more significant role than that of $FWHM_{RB}$ and Q_{RB} in determining the sensitivity of this type of nanoporous PCs. Aqueous solutions of NaCl contain Na^+ and Cl^- ions, and H_2O molecules, while organic analytical mixtures used in this study are composed of MeOH and EtOH molecules. The size of these molecules and ions (< 1 nm) is much smaller than the visible light wavelength. Therefore, it is possible to assume that the size of analyte molecules does not contribute to the differences in sensitivity observed in hydrophilic and hydrophobic NAA–μQVs. Values of refractive index for both aqueous- and organic based analytical solutions used in this study were the same (i.e., n_{medium} = 1.333, 1.336, 1.337, 1.340, 1.342, and 1.345 RIU). Analysis of optical absorbance of these solutions from 400 to 800 nm indicates that both NaCl and MeOH–EtOH solutions absorb more light at higher wavelengths within a comparable range of absorbance (~0.40–0.42 a.u.) As such, increasing sensitivity per unit of resonance band position in hydrophilic and hydrophobic NAA–μQVs for both aqueous- and organic-based solutions can be attributed to increasing optical absorbance of analytical solutions with wavelength, where this parameter is found to be more critical than that of $FWHM_{RB}$ and Q_{RB} in determining the sensitivity of NAA–μQVs under the conditions of study. Analysis of S_{IRB} also reveals that, while sensitivity in hydrophobic NAA–μQVs is statistically the same in aqueous and organic media (i.e., 0.072 ± 0.002 and 0.066 ± 0.006 (nm RIU^{-1}) nm^{-1}, respectively), hydrophilic NAA–μQVs show considerable variation in sensitivity with

media, where S_{IRB} is higher when changes in n_{medium} are induced by an organic medium (i.e., 0.109 ± 0.001 and 0.347 ± 0.002 (nm RIU^{-1}) nm^{-1} for aqueous and organic solutions, respectively). Ghazzal et al. developed opal-like SiO_2–TiO_2 PCs with tunable hydrophilic–hydrophobic balance to investigate the effect of this parameter on optical sensitivity upon infiltration with water and hexane.[47] These opal PCs showed decreasing and increasing sensitivity toward water and hexane with increasing hydrophobic character, respectively.

Table 6.3. Summary of optical sensing performance parameters (sensitivity — *S* and linearity — *R2*) for hydrophilic and hydrophobic NAA-µQVs in aqueous- and organic-based analytical solutions of varying refractive index.

NAA–µQV	Surface Chemistry	Medium	S (nm RIU^{-1})	R^2
NAA–µQV400	Hydrophilic	Aqueous	52.2 ± 1.1	0.9991
NAA–µQV500			61.7 ± 4.3	0.9764
NAA–µQV600			71.5 ± 5.6	0.9697
NAA–µQV700			82.4 ± 3.7	0.9901
NAA–µQV800			99.3 ± 4.0	0.9920
NAA–µQV400	Hydrophilic	Organic	48.2 ± 2.8	0.9834
NAA–µQV500			97.9 ± 6.8	0.9763
NAA–µQV600			117.5 ± 5.0	0.9909
NAA–µQV700			152.6 ± 3.1	0.9979
NAA–µQV800			186.5 ± 5.6	0.9955
NAA–µQV400	Hydrophobic	Aqueous	22.7 ± 0.8	0.9934
NAA–µQV500			31.1 ± 1.3	0.9909
NAA–µQV600			37.1 ± 2.1	0.9841
NAA–µQV700			43.3 ± 2.6	0.9828
NAA–µQV800			52.1 ± 2.2	0.9908
NAA–µQV400	Hydrophobic	Organic	32.8 ± 2.0	0.9816
NAA–µQV500			38.9 ± 2.1	0.9845
NAA–µQV600			44.4 ± 1.7	0.9929
NAA–µQV700			50.1 ± 2.6	0.9869
NAA–µQV800			58.5 ± 1.7	0.9959

However, it is worth noting that these nanoporous PCs featured a ~5–7 times smaller diameter (~3–6 nm) than that of NAA–μQVs. As such, these PCs are more susceptible to infiltration constraints due to flow retention of water and hexane molecules when these solutions flow through hydrophilic and hydrophobic nanopores. **Figure 6.5d** reveals a fast, almost instantaneous rise in DI_{RB} upon exchange of analytical solution flowing through the flow cell system, in both aqueous and organic solutions. This suggests that no flow constraints occur within NAA–μQVs under the conditions of study. Some et al. studied the effect of wettability on the optical sensitivity of hydrophilic graphene and hydrophobic reduced graphene oxide layers.[48] Hydrophilic graphene showed higher sensitivity to volatile organic compounds that its hydrophobic counterpart.

Differences in sensitivity were attributed to the presence of polar functional groups on the surface of hydrophilic graphene, which increase the strength of molecule-to-surface interactions between organics and graphene. We hypothesize that sensitivity differences between hydrophilic and hydrophobic NAA–μQVs in aqueous and organic analytical solutions are critically determined by molecule-to-surface interactions. The surface of as-produced NAA–μQVs features aluminum and oxygen vacancies, and hydroxyl groups. These charged functionalities would favor polar interactions with organics, enhancing the overall sensitivity of the PC structure. Upon functionalization with dichlorodimethylsilane, the inner surface of NAA–μQVs is homogeneously coated with a layer of Cl groups, which would minimize the strength of molecule-to-surface interactions and homogenize the optical response of the nanoporous PC structure upon infiltration with aqueous and organic solutions. To conclude, analysis of the overall sensitivity of NAA–μQVs demonstrates

that the performance of these light-confining nanoporous photonic crystal structures is comparable to that of other nanoporous microcavity structures produced by anodization.[25,26,28] Although emerging high-Q plasmonic resonance structures can provide much higher sensitivities (one order of magnitude superior ~1,000 nm RIU^{-1})[49,50], NAA–μQVs could open exciting new opportunities to further enhance these performances through hybrid composite structures, harnessing phenomena such as Tamm plasmon resonance.

6.4. Conclusion

In summary, we have determined for the first time the combined effect of spectral light confinement features and surface chemistry on optical sensitivity using nanoporous anodic alumina optical microcavities as model light-confining photonic crystal structures. The nanoporous architecture of NAA–μQVs featuring two distributed Bragg mirrors with a physical cavity layer in between was engineered by stepwise pulse anodization. Model NAA–μQVs showed well-resolved, spectrally tunable resonance bands ~400 to 800 nm by judicious modification of the anodization period in the input STPA profile. A theoretical model for precise engineering of NAA–μQVs' resonance band across the visible spectrum was developed. Comparison between simulated and experimental optical transmission spectra demonstrated that our model can accurately predict the optical properties of these NAA-based PC structures, using experimental values of effective refractive index and anodic oxide growth rate. Optical sensitivity of as-produced (hydrophilic) and dichlorodimethylsilane-functionalized (hydrophobic) NAA–μQVs was

assessed by analyzing dynamic spectral shifts of NAA–μQVs' resonance band upon infiltration with organic- and aqueous-based analytical solutions of equally varying refractive index, from 1.333 to 1.345 RIU. The findings demonstrated that optical sensitivity of both hydrophilic and hydrophobic NAA–μQVs increases linearly with the position of their characteristic resonance, in both organic and aqueous solutions, due to increasing optical absorbance.

Analysis of sensitivity also revealed that hydrophilic NAA–μQVs show ~81 and 35 % superior sensitivity to their hydrophobic counterparts for organic- and aqueous-based analytical solutions, respectively. We hypothesize that homogeneity in sensitivity of hydrophobic NAA–μQVs in organic and aqueous solutions was attributable to stabilization by Cl groups deposited onto the inner surface of these nanoporous PCs. In contrast, the presence of charged functionalities on the surface of hydrophilic NAA–μQVs enables strong molecule-to-surface interactions that enhance sensitivity toward organic- and aqueous-based solutions of varying refractive index. In this chapter we present a new avenue to explore the unique light-confining properties of NAA-based PC structures for optical sensing applications. Precise design and engineering of structural, optical, and chemical properties of these PCs provide exciting new opportunities to harness distinct forms of light–matter interactions for a broad range of photonic technologies and sensing applications.

REFERENCES

1. Yablonovitch, E. Inhibited Spontaneous Emission in Solid-State Physics and Electronics. *Phys. Rev. Lett.*, **1987**, *58*, 2059–2062.
2. John, S. Strong Localization of Photons in Certain Disordered Dielectric Superlattices. *Phys. Rev. Lett.*, **1987**, *58*, 2486–2489.
3. López, C. Materials Aspects of Photonic Crystals. *Adv. Mater.*, **2003**, *15*, 1680–1704.
4. Baba, T. Slow Light in Photonic Crystals. *Nat. Photonics*, **2008**, *2*, 465–473.
5. Noda, S.; Chutinan, A.; Imada, M. Trapping and Emissions of Photons by a Single Defect in a Photonic Bandgap Structure. *Nature*, **2000**, *407*, 608–610.
6. Abramovici, A.; Althouse, W. E.; Drever, R. W. P.; Gürsel, Y.; Kawamura, S.; Raab, F. J.; Shoemaker, D.; Sievers, L.; Spero, R. E.; Thorne, K. S.; Vogt, R. E.; Weiss, R.; Whitcomb, S. E.; Zucker, M. E. LIGO: The Laser Interferometer Gravitational-Wave Observatory. *Science*, **1992**, *256*, 325–333.
7. Azuma, H. Quantum Computation with Kerr-Nonlinear Photonic Crystals. *J. Phys. D: Appl. Phys.*, **2007**, *41*, article no 025102.
8. Langford, N. K.; Ramelow, S.; Prevedel, R.; Munro, W. J.; Milburn, G. J.; Zeilinger, A. Efficient Quantum Computing using Coherent Photon Conversion. *Nature*, **2011**, *478*, 360–363.
9. Cao, W.; Muñoz, A.; Palffy–Muhoray, P.; Taheri, B. Lasing in a Three-Dimensional Photonic Crystal of the Liquid Cristal Blue Phase II. *Nat. Mater.*, **2002**, *1*, 111–113.
10. Shalaev, M. I.; Walasik, W.; Tsukernik, A.; Xu, Y.; Litchinitser, N. M. Robust Topologically Protected Transport in Photonic Crystals at Telecommunication Wavelengths. *Nat. Nanotechnol.*, **2019**, *14*, 31–34.
11. Meade, S. O.; Yoon, M. S.; Ahn, K. H.; Sailor, M. J. Porous Silicon Photonic Crystals as Encoded Microcarriers. *Adv. Mater.*, **2004**, *16*, 1811–1814.
12. Vahala, K. J.; Optical Microcavities. *Nature*, **2003**, *424*, 839–846.

13. Armani, A. M.; Kulkarni, R. P.; Fraser, S. E.; Flagan, R. C.; Vahala, K. J. Label-Free, Single-Molecule Detection with Optical Microcavities. *Science*, **2007**, *317*, 783–787.
14. Chen, W.; Özedemir, S. K.; Zhao, G.; Wiersig, J.; Yang, L. Exceptional Points Enhance Sensing in an Optical Microcavity. *Nature*, **2017**, *548*, 192–196.
15. Forstner, S.; Prams, S.; Knittel, J.; van Ooijen, E. D.; Swaim, J. D.; Harris, G. I.; Szorkovszky, A.; Bowen, W. P.; Rubinsztein–Dunlop, H. Cavity Optomechanical Magnetometer. *Phys. Rev. Lett.*, **2012**, *108*, article no 120801.
16. Gavartin, E.; Verlot, P.; Kippenberg, T. J. A Hybrid On-Chip Optomechanical Transducer for Ultrasensitive Force Measurements. *Nat. Nanotechnol.*, **2012**, *7*, 509–514.
17. He, L.; Özedemir, S. K.; Zhu, J.; Kim, J.; Yang, L. Detecting Single Viruses and Nanoparticles using Whispering Gallery Microlasers. *Nat. Nanotechnol.*, **2011**, *6*, 428–432.
18. Basske, M. D.; Vollmer, F. Optical Observation of Single Atomic Ions Interacting with Plasmonic Nanorods in Aqueous Solutions. *Nat. Photon.*, **2016**, *10*, 733–739.
19. Mulloni, V.; Pavesi, L. Porous Silicon Microcavities as Optical Chemical Sensors. *Appl. Phys. Lett.*, **2000**, *76*, 2523–2525.
20. Lee, W.; Park, S. –J. Porous Anodic Aluminum Oxide: Anodization and Templated Synthesis of Functional Nanostructures. *Chem. Rev.*, **2014**, *114*, 7487–7556.
21. Santos, A. Nanoporous Anodic Alumina Photonic Crystals: Fundamentals, Developments and Perspectives. *J. Mater. Chem. C*, **2017**, *5*, 5581–5599.
22. Law, C. S.; Lim, S. Y.; Abell, A. D.; Voelcker, N. H.; Santos, A. Nanoporous Anodic Alumina Photonic Crystals for Optical Chemo- and Biosensing: Fundamentals, Advances, and Perspectives. *Nanomaterials*, **2018**, *8*, article no 788.
23. Law, C. S.; Lim, S. Y.; Macalincag, R. M.; Abell, A. D.; Santos, A. Light-Confining Nanoporous Anodic Alumina Microcavities by Apodized Stepwise Pulse Anodization. *ACS Appl. Nano Mater.*, **2018**, *1*, 4418–4434.

24. Law, C. S.; Lim, S. Y.; Abell, A. D.; Marsal, L. M.; Santos, A. Structural Tailoring of Nanoporous Anodic Alumina Optical Microcavities for Enhanced Resonant Recirculation of Light. *Nanoscale*, **2018**, *10*, 14139–14152.
25. Lee, J.; Bae, K.; Kang, G.; Choi, M.; Baek, S.; Yoo, D. –S.; Lee, C. –W.; Kim, K. Graded-Lattice AAO Photonic Crystal Heterostructure for High *Q* Refractive Index Sensing. *RSC Adv.*, **2015**, *5*, 71770–71777.
26. Wang, Y.; Chen, Y.; Kumeria, T.; Ding, F.; Evdokiou, A.; Losic, D.; Santos, A. Facile Synthesis of Optical Microcavities by a Rationally Designed Anodization Approach: Tailoring Photonic Signals by Nanopore Structure. *ACS Appl. Mater. Interfaces*, **2015**, *7*, 9879–9888.
27. Shang, G. L.; Fei, G. T.; De Zhang, L. Experimental Realization of Tunable Defect Mode in Photonic Crystal. *J. Phys. D: Appl. Phys.*, **2015**, *48*, article no 435304.
28. Yan, P.; Fei, G. –T.; Li, H.; Shang, G. –L.; Wu, B.; Zhang, L. –D. Alumina Photonic Crystals with Defect Modes for Sensor Application. *Chin. J. Chem. Phys.*, **2014**, *27*, 121–124.
29. An, Y. –Y.; Wang, J.; Zhou, W. –M.; Jin, H. –X.; Li, J. –F.; Wang, C. –W. The Preparation of High Quality Alumina Defective Photonic Crystals and Their Application of Photoluminescence Enhancement. *Superlattice. Microst.*, **2018**, *119*, 1–8.
30. Kushnir, S. E.; Komarova, T. Y.; Napolskii, K. S. High-Quality-Factor Anodic Alumina Optical Microcavities Prepared by Cyclic Anodizing with Voltage *versus* Optical Path Length Modulation. *J. Mater. Chem. C*, **2020**, *8*, 3991–3995.
31. Santos, A.; Yoo, J. H.; Rohatgi, C. V.; Kumeria, T.; Wang, Y.; Losic, D. Realisation and Advanced Engineering of True Optical Rugate Filters Based on Nanoporous Anodic Alumina by Sinusoidal Pulse Anodisation. *Nanoscale*, **2016**, *8*, 1360–1373.
32. Eckstein, C.; Law, C. S.; Lim, S. Y.; Kaur, S.; Kumeria, T.; Ferré–Borrull, J.; Abell, A. D.; Marsal, L. F.; Santos, A. Nanoporous Photonic Crystals with Tailored Surface Chemistry for Ionic Copper Sensing. *J. Mater. Chem. C*, **2019**, *7*, 12278–12289.

33. Wang, Y.; Santos, A.; Evdokiou, A.; Losic, D. Rational Design of Ultra-Short Anodic Alumina Nanotubes by Short-Time Pulse Anodization. *Electrochim. Acta*, **2015**, *154*, 379–386.
34. Santos, A.; Formentín, P.; Ferré–Borrull, J.; Pallarès, J.; Marsal, L. F. Nanoporous Anodic Alumina Obtained without Protective Oxide Layer by Hard Anodization. *Mater. Lett.*, **2012**, *67*, 296–299.
35. Law, C. S.; Sylvia, G. M.; Nemati, M.; Yu, J.; Losic, D.; Abell, A. D.; Santos, A. Engineering of Surface Chemistry for Enhanced Sensitivity in Nanoporous Interferometric Sensing Platforms. *ACS Appl. Mater. Interfaces*, **2017**, *9*, 8929–8940.
36. Gorelik, V. S.; Svervil, P. P.; Filatov, V. V.; Bi, D.; Fei, G. T.; Xu, S. H. Transmission Spectra of One-Dimensional Porous Alumina Photonic Crystals. *Photonics and Nanostructures — Fundamentals and Applications*, **2018**, *32*, 6–10.
37. Acosta, L. K.; Bertó–Roselló, F.; Xifre–Perez, E.; Law, C. S.; Santos, A.; Ferré–Borrull, J.; Marsal, L. F. Tunable Nanoporous Anodic Alumina Photonic Crystals by Gaussian Pulse Anodization. *ACS Appl. Mater. Interfaces*, **2020**, *12*, 19778–19787.
38. Teare, S. W. *Optical Interference Filters Using MATLAB*, Society of Photo-Optical Instrumentation Engineers (SPIE), Washington, USA, 2019.
39. Abràmoff, M. D.; Magalhaes, P. J.; Ram, S. J. Image Processing with ImageJ. *Biophotonics Int.*, **2004**, *11*, 36–42.
40. Lee, W.; Kim, J. –C. Highly Ordered Porous Alumina with Tailor-Made Pore Structures Fabricated by Pulse Anodization. *Nanotechnology*, **2010**, *21*, article no 485304.
41. Lee, W.; Kim, J. –C.; Gösele, U. Spontaneous Current Oscillations during Hard Anodization of Aluminum under Potentiostatic Conditions. *Adv. Funct. Mater.*, **2010**, *20*, 21–27.
42. Garmire, E. Theory of Quarter-wave-stack Dielectric Mirrors used in a Thin Fabry–Perot Filter. *Appl. Opt.*, **2003**, *42*, 5442–5449.

43. Costa, A. E. B.; Mejía-Salazar, J. R.; Cavalcanti, S. B. Defect Modes in Metamaterial Photonic Supperlattices as Tunneling Resonances in Trilayer Structures. *J. Opt. Soc. Am. B*, **2016**, *33*, 468–473.
44. Yamamoto, Y.; Baba, N.; Tajima, S. Coloured Materials and Photoluminescence Centres in Anodic Film on Aluminium. *Science*, **1981**, *289*, 572–574.
45. Han, H.; Park, S. J.; Jang, J. S.; Ryu, H.; Kim, K. J.; Baik, S.; Lee, W. In *Situ* Determination of the Pore Opening Point during Wet-Chemical Etching of the Barrier Layer of Porous Anodic Aluminum Oxide: Nonuniform Impurity Distribution in Anodic Oxide. *ACS Appl. Mater. Interfaces*, **2013**, *5*, 3441–3448.
46. Ahmed, A. M.; Mehaney, A. Ultra-High Sensitive 1D Porous Silicon Photonic Crystal Sensor Based on the Coupling of Tamm/Fanno Resonances in the Mid-Infrared Region. *Sci. Rep.*, **2019**, *9*, article no 6973.
47. Ghazzal, M. N.; Joseph, M.; Kebaili, H.; De Coninck, J.; Gaigneaux, E. M. Tuning the Selectivity and Sensitivity of Mesoporous Dielectric Multilayers by Modifying the Hydrophobic–Hydrophilic Balance of the Silica Layer. *J. Mater. Chem.*, **2012**, *22*, 22526–22532.
48. Some, S.; Xu, Y.; Kim, Y.; Yoon, Y.; Qin, H.; Kulkarmi, A.; Kim, T.; Lee, H. Highly Sensitive and Selective Gas Sensor Using Hydrophilic and Hydrophobic Graphenes. *Sci. Rep.*, **2013**, *3*, article no 1868.
49. Mejía-Salazar, J. R.; Oliveira, O. N. Jr. Plasmonic Biosensing. *Chem. Rev.*, **2018**, *118*, 10617–10625.
50. Wang, B.; Yu, P.; Wang, W.; Zhang, X.; Kuo, H–. C.; Xu, H.; Wang, Z. M. High-Q Plasmonic Resonances: Fundamentals and Applications. *Adv. Optical Mater.*, **2021**, article no 2001520.

Chapter 6

Chapter 7. Tuning Intrinsic Photoluminescence of Multispectral Nanoporous Anodic Alumina Photonic Structures

UNIVERSITAT ROVIRA I VIRGILI
ENGINEERING OF PHOTONIC STRUCTURES BASED ON NANOPOROUS ANODIC ALUMINA AS AN OPTICAL SENSING PLATFORM
Laura Karen Acosta Capilla

In this chapter, the precise structural engineering and tuning of intrinsic photoluminescence emissions from nanoporous anodic alumina photonic crystals (NAA–PCs) is demonstrated. A smart structural design by a combination of pulse and constant anodization in distinct acid electrolytes makes it possible to engineer a novel heterogenous optical structure consisting of a non-emitting, light-filtering layer in the form of multi-spectral NAA–PC, and an intrinsically light-emitting layer of NAA. MS–NAA–PCs are engineered to feature three intense, well-resolved photonic stopbands, the position of which are spaced across the visible spectrum, from ~380 to 560 nm. These advances pave the way for novel designs of intrinsic, light-emitting NAA-based photonic crystals structures, which could find broad applicability across light technologies such as sensing and biosensing, photodetection, and solar light harvesting.

7.1 Introduction.

Solid-state light-driven luminescence - henceforth “photoluminescence” or PL — is a class of light–matter interaction in which incident photons absorbed by a material’s atoms excite electrons to higher energy levels. Once excited, electrons undergo certain relaxation processes, through which photons are re-radiated or emitted in the form of a light beam.[1] The properties of the emitted photoluminescent beam rely on the electronic band structure of the photo-excited material[2]. Characteristically, PL emissions from solid-state materials with defects in their electronic band structure are spectrally broad, featuring a Gaussian-like emission centered within the vicinity of the exciton resonance — typically at a longer wavelength than that of excitation.[3] Broad PL emissions can be narrowed by distinct strategies to fulfil requirements for specific

applications such as lasing[4], LEDs[5-6], bioimaging[7], and diagnostics and sensing[8-9]. Of all these, engineering the structure of light-emitting materials at the nanoscale in the form of photonic crystals (PCs) enables highly directional emission of light with tunable wavelength by confining, enhancing, and attenuating emitted light at specific, narrow spectral regions[10-11]. PCs are optical structures with allowed and forbidden photonic stopbands that modify the group velocity of incident or emitted photons when these flow through the PCs' structure. Light−matter interactions in PCs can be tuned with precision by engineering their architecture so that regions with high and low refractive indexes are periodically and spatially distributed following specific patterns.[12] A variety of PC forms based on a broad range of materials can be produced to control electromagnetic waves with versatility over the broad spectrum, from UV to IR. Currently, PCs have multiple applications including chemical sensing and biosensing[13-18], photonic encoding[19], lasing[20-25], and photocatalysis[26-27.] Nanoporous PCs are particularly suitable platform materials to tailor photo-induced light emissions, both extrinsically and intrinsically. In the former mode, a host non-photoluminescent nanoporous PC is infiltrated with a photoluminescent material to enhance, filter or guide its light emission[27], while in the latter configuration a photoluminescent nanoporous PC material filters its own PL emission[28]. Nanoporous anodic alumina (NAA) has long been devised as an ideal nanoporous PC platform material due to its cylindrical nanopores with well-defined and highly controllable geometric features.[29-32] NAA is produced by electrochemical oxidation — anodization — of aluminum, which is a cost-effective and fully scalable top–down industrial process compatible with conventional micro- and

nanofabrication. While architecture, dimensions and distribution of nanopores in NAA can be precisely engineered in a variety of NAA-based PCs (NAA–PCs) during anodization[33-35], its intrinsic optical properties — refractive index and photoluminescence — are critically determined by the anodizing acid electrolyte, anodization regime, and post-anodization treatments such as annealing[36]. Origin of PL in NAA is thought to be attributable to two types of photoluminescent centers: (i) F+ centers[37-39] related to ionized oxygen vacancies, and (ii) F– centers associated with carboxylate impurities incorporated from the acid electrolyte during anodization[40-41]. Position and intensity of NAA's PL emission depend intrinsically on the quantity of F+ and F– centers. NAA films produced in oxalic acid feature more intense PL emission than that of its counterparts fabricated in sulfuric or phosphoric acids[42-46]. NAA's PL intensity also decreases with annealing temperature due to elimination of oxygen vacancies and impurities in its structure through crystallographic organization and burning under oxygen atmosphere.[47-52] Pioneering studies on 2D NAA–PCs featuring straight nanopores demonstrated their application as host materials to tune PL emissions from fluorescent dyes infiltrated in their nanoporous matrix. In this system, the red edge of the characteristic photonic stopband (PSB) of NAA–PCs reduces the group velocity of incident photons at that spectral region by the so-called "slow photon" effect. As a result, PL emission is enhanced due to increasing frequency of interactions between exciting photons and light-emitting molecules at that spectral region.[25] An alternative approach would be to tailor the intrinsic photoluminescence of NAA by engineering its structure in the form NAA–PCs.[53-54] Under this configuration, alignment of the NAA–PC's PSB with the Gaussian-like PL emission of NAA would narrow its

linewidth by internally forbidding light propagation at specific spectral regions. Surprisingly, to the best of our knowledge, this system has not been explored yet.

This chapter shows how the intrinsic photoluminescence of NAA can be tuned by engineering its structure in the form of multispectral PCs (MS-NAA–PCs) — NAA–PCs featuring multiple PSBs at specific spectral positions **(Figure 7.1).**

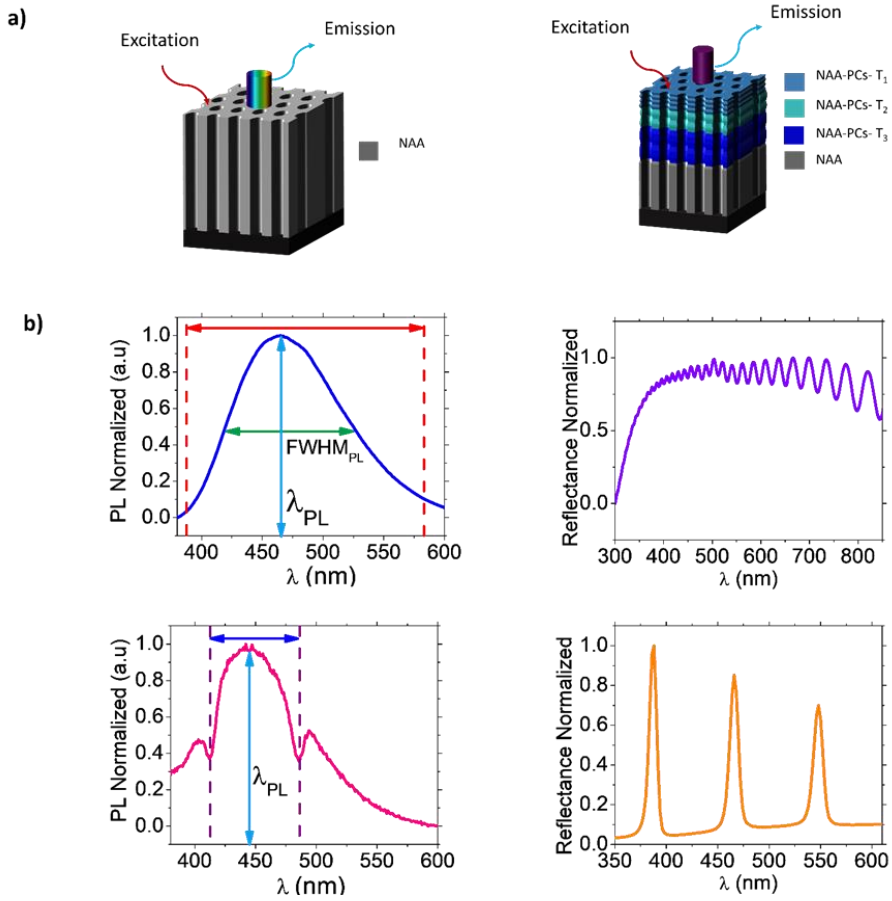

Figure. 7.1 Conceptual illustration showing the mechanism by which MS–NAA–PCs narrow PL emission from NAA by judicious alignment of PSBs. (a) Schematic showing the PL emission of a reference NAA (left) and a MS–NAA–PC (right). (b) Normalized reflection and PL spectra of a NAA film (top) and a MS–NAA–PC (bottom) showing the mechanism by which PSBs in MS–NAA–PCs are harnessed to selectively filter PL emission from NAA, where λ_{PL} and $FWHM_{PL}$ represent the central wavelength position and full width at half maximum of the PL emission of NAA and MS–NAA–PCs, respectively.

Spectral alignment between the three characteristic PSBs of MS–NAA–PCs with the photoluminescence emission of NAA (**Figure 7.1a**) makes it possible to judiciously narrow its linewidth with precision by inhibiting light propagation at specific spectral positions **(Figure 7.1b).** These results create exciting new opportunities to modulate light emission from NAA-based structures, which could have broad implications across optoelectronic disciplines such as lasing, sensing, energy harvesting, and photocatalysis.

7.2 Experimental Details

7.2.1 Fabrication of Reference NAA films

A set of NAA films featuring straight cylindrical nanopores from top to bottom were used as a reference material to quantify bulk PL emission. Al disc were anodized by the two-step process, full details of which are reported elsewhere.[52-56] Briefly, before anodization Al chips were electropolished in a mixture of EtOH and $HClO_4$ 4:1 (v:v) at 20 V and 5 °C for 3 min. Then, the first anodization step was carried out in 0.3 M $H_2C_2O_4$ aqueous electrolyte at 40 V and 5 °C for 20 h. Next, the resulting NAA layer was selectively removed by wet chemical etching in a mixture of 0.2 M H_2CrO4 and 0.4 M H_3PO_4 for 3 h at 70 °C. After this, the second anodization step was performed under the same anodization conditions for a total charge density (integrated current density throughout time per unit of area) of 113.2 C cm^{-2} under voltage control conditions at 40 V to generate a NAA film of 50 µm featuring straight cylindrical nanopores.

7.2.2 Fabrication of MS–NAA–PCs

Fabrication of MS–NAA–PCs was performed following a modified two-step anodization process. Electropolished Al discs were first anodized in a 0.3 M sulfuric acid electrolyte at 5°C under constant voltage at 25 V for 20 h. The NAA film was then chemically dissolved in a mixture of 0.2 M H_2CrO_4 and 0.4 M H_3PO_4 for 3 h at 70 °C. Then, a 10-min second step in the same acid electrolyte at 25 V for 10 min was applied to generate a shuttle layer for homogenous nanopore growth. Then, the anodization process was switched to sinusoidal pulse anodization under current density control conditions.

During this process, a sinusoidal current density input profile was applied to modulate nanopore diameter in depth and generate gradient-index filter PC structures.[59] MS–NAA–PCs consisted of a NAA layer featuring three gradient-index filters generated by judiciously modulating the anodizing current density waveform input into sequential sinusoids with three different pulse periods (i.e., T_1, T_2 and T_3), as described by Equation 7.1:

$$J(t) = \begin{cases} \mathrm{J_1}\sin\left(\frac{2\pi}{\mathrm{T_1}}t\right) + \mathrm{J_0} & 0 \le \mathrm{t} < \mathrm{NT_1} \\ \mathrm{J_1}\sin\left(\frac{2\pi}{\mathrm{T_2}}t\right) + \mathrm{J_0} & \mathrm{NT_1} \le \mathrm{t} < \mathrm{NT_1} + \mathrm{NT_2} \\ \mathrm{J_1}\sin\left(\frac{2\pi}{\mathrm{T_3}}t\right) + \mathrm{J_0} & \mathrm{NT_1} + \mathrm{NT_2} \le \mathrm{t} < \mathrm{NT_1} + \mathrm{NT_2} + \mathrm{NT_3} \end{cases} \quad (7.1)$$

where $J(t)$ is the anodization current density at time t (in seconds), J_1 is the current density amplitude (*in* mA cm^{-2}), T_i (i = 1, 2, 3) is the anodization period i (in seconds) and J_0 is the offset current density (in mA cm^{-2}). The offset current density (J_0), current density amplitude (J_1) and number de periods (N) were kept constant

throughout the anodization process for all MS–NAA–PCs fabricated in this study, while the anodization periods were varied as T_1 = 125 s, T_2 = 150 s, and T_3 = 175 s for N = 100 pulses per period (N_1, N_2 and N_3) (i.e., total of 300 pulses). After this, a 50 μm thick NAA layer produced in 0.3 M oxalic electrolyte (i.e., light-emitting layer) was generated under potentionstatic conditions at 40 V. **Table 7.1** summarizes the fabrication conditions used to fabricate MS–NAA–PCs. After anodization, the remaining aluminum substrate was removed from the backside of MS–NAA–PCs by selective chemical etching in a saturated solution of HCl and $CuCl_2$ for optical characterization.

Table 7.1. Fabrication conditions of MS–NAA–PCs including current density amplitude (J_1), anodization period (T_i) and offset current density (J_0).

	J_0 (mA cm^{-2})	J_1 (mA cm^{-2})	T_1 (s)	T_2 (s)	T_3 (s)	N_1 (pulses)	N_2 (pulses)	N_3 (pulses)
MS-NAA-PCs	1.98	1.41	125	150	175	100	100	100

7.2.3 Optical Characterization of MS–NAA–PCs

Reflection spectra from MS–NAA–PCs were measured from 250 to 900 nm with a resolution of 2 nm at varying angle of incidence, from 8 to 65°, in a PerkinElmer UV–visible–NIR Lambda 950 spectrophotometer. Reflection intensity (R_{PSB}), position of central wavelength (λ_{PSB}), and full width at half-maximum ($FWHM_{PSB}$) of the photonic stopbands (PSBs) of MS–NAA–PCs were estimated from reflection spectra through Gaussian fittings performed in OriginPro8.5®. PL spectra from MS–NAA–PCs were acquired in a fluorescence spectrophotometer (Photon Technology International Inc., Division of Horiba, USA) equipped with a Xe lamp as excitation light

source at room temperature and at an excitation wavelength (λ_{ex}) of 355 nm. PL measurements were performed from the top side of reference NAA films and MS–NAA–PCs, using a commercial bandpass filter with a cutoff wavelength of 350 nm.

7.2.4 Structural Characterization of MS–NAA–PCs

Morphological and structural features of NAA films and MS–NAA–PCs were characterized by a field-emission gun scanning electron microscope (FEG-SEM FEI Quanta 450) operating at an accelerating voltage of 20–25 keV. Characteristic geometric features of MS–NAA–PCs were quantified by analyzing FEG-SEM images in ImageJ software.[60]

7.3. Results and Discussion

7.3.1Fabrication and Structural Characterization of MS–NAA–PCs

Figure 7.2a illustrates the fabrication process used to produce the light-filtering layer of MS–NAA–PCs under sinusoidal current density conditions, including a full-view of a representative anodization profile. **Figure 7.2b** shows magnified views of this sinusoidal pulse anodization process, in which the current density period *(Ti)* — time between consecutive sinusoidal pulses — is increased from 125 to 175 s with a step size of ΔTi = 25 s after each 100 pulses. This input current density profile results in three stacked layers of NAA featuring a modulated nanopore diameter in depth, each of which represents a gradient-index filter with its characteristic PSB. As such, the optical response of the composite NAA–PC features three PSBs, one for each NAA gradient-index filter composing the overall PC structure. It is apparent from these graphs that, under the

fabrication conditions used in this study, the sinusoidal current density input with J_0 = 1.98 mA cm^{-2}, J_1 = 1.41 mA cm^{-2}, T_1 = 125 s, T_2 = 150 s, and T_3 = 175 s for a total of 300 pulses is precisely translated into a sinusoidal voltage output, which mimics the frequency of the input profile. Analysis of this anodization profile indicates that the amplitude of the sinusoidal voltage output slightly increases with increasing T_i, from ~20–25 V at T1 = 125 s to ~20–29 V at T_3, respectively. **Figure 7.3a** shows a top view FEG-SEM image of this NAA–PC structure, which features hexagonally arranged, homogeneously distributed nanopores across its surface. The average nanopore diameter estimated from FEG-SEM image analysis was 17 ± 4 nm, while the interpore distance — distance between center of adjacent nanopores — was measured to be 62 ± 5 nm.

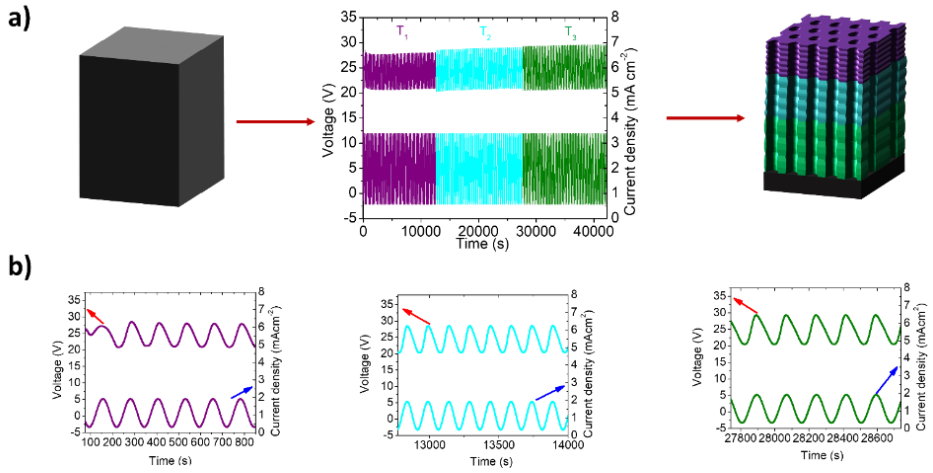

Figure. 7.2 Fabrication of MS–NAA–PCs by sinusoidal pulse anodization. (a) Schematics of fabrication process to produce MS–NAA–PCs by a sinusoidal current density profile with three anodization periods (T_1, T_2 and T_3) including aluminum substrate (left), representative full-view anodization profile with current density input and voltage output (center) and resulting MS–NAA–PC featuring three stacked gradient-index filters (right). (b) Magnified views of sinusoidal current density profile shown in (a) for each anodization period (T_1, T_2 and T_3) demonstrating the precise translation of current density pulses into sinusoidal voltage output pulses.

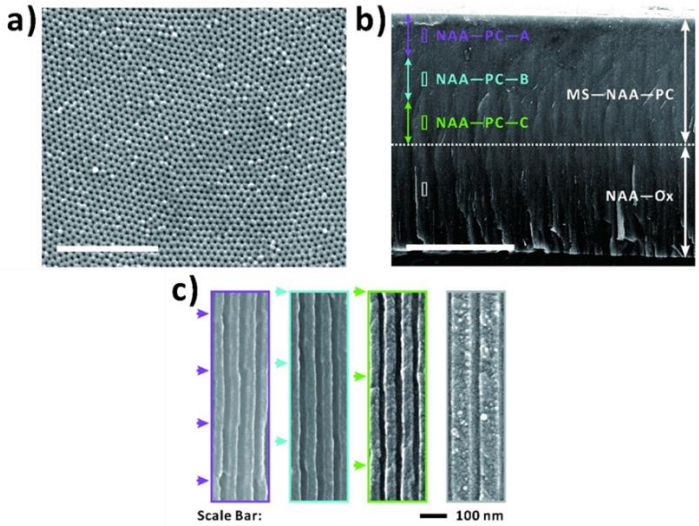

Figure. 7.3. Structural characterization of MS–NAA–PCs. (a) Top view FEG-SEM image of a representative MS–NAA–PC featuring average nanopore diameter and interpore distance of 17 ± 4 nm and 62 ± 5 nm, respectively (scale bar = 1 µm). (b) Full-view cross-sectional FEG-SEM image of a MS–NAA–PC featuring a light-filtering layer at its top and a light-emitting layer at its bottom with thicknesses of 58 ± 1 mm and 50 ± 1 µm, respectively, and NAA–PC–A, NAA–PC–B and NAA–PC–C denote NAA gradient-index filters produced with T_1 = 125 s, T_2 = 150 s, and T_3 = 175 s, respectively, and NAA–Ox corresponds to the light-emitting layer at the bottom of the NAA–PC structures (scale bar = 50 µm). (c) Magnified view cross-sectional FEG-SEM images of color rectangles shown in (b) showing details of nanopore diameter modulations in NAA–PC–A, NAA–PC–B and NAA–PC–C, and straight cylindrical nanopores in NAA–Ox layer (NB: color arrows denote nanopore modulations).

Figure 7.3b shows a general cross-sectional view FEG-SEM image of these NAA–PCs, from which is it possible to discern two main layers: i) a top light-filtering layer formed by three NAA gradient index filters labelled as NAA–PC–A (T_1 = 125 s), NAA–PC–B (T_2 = 150 s) and NAA–PC–C (T_3 = 175 s), which feature modulated nanopore diameter in depth; and ii) a bottom light-emitting layer featuring straight cylindrical nanopores at the bottom labelled as NAA–Ox. The thicknesses of the top and bottom layers were 58 ± 1 and 50 ± 1 µm, respectively, according to FEG-SEM image analysis. **Figure 7.3c** shows a set of magnified cross-sectional views showing details of nanopores at specific positions of the top and bottom layers of the MS–NAA–PC structure. FEG-SEM images of the NAA gradient-index filters

forming the top light-filtering layer reveal nanopore modulations, the period length (L_{TP}) of which increases with the input anodization period (T_i). Analysis of this geometric parameter for NAA–PC–A, NAA–PC–B and NAA–PC–C reveals that L_{TP} increases linearly with T_i at a rate of 2.1 ± 0.1 nm s^{-1}, having values of 210 ± 4, 265 ± 6, and 313 ± 8 nm for T_1, T_2 and T_3, respectively. **Figure 7.3c** also shows a magnified cross-sectional view of the light-emitting layer at the bottom of the MS–NAA–PC structure, which was fabricated in 0.3 M oxalic acid electrolyte at 40 V for a total of ~16 h. This layer features straight cylindrical nanopores with constant diameter from top to bottom. A set of FEG-SEM images of this film from a control NAA–Ox sample used to characterize the bulk PL emission of this layer is shown in **Figure 7.4.** The 50 mm-thick layer features straight cylindrical nanopores with an average diameter of 40 ± 3 nm and an interpore distance of 101 ± 6 nm.

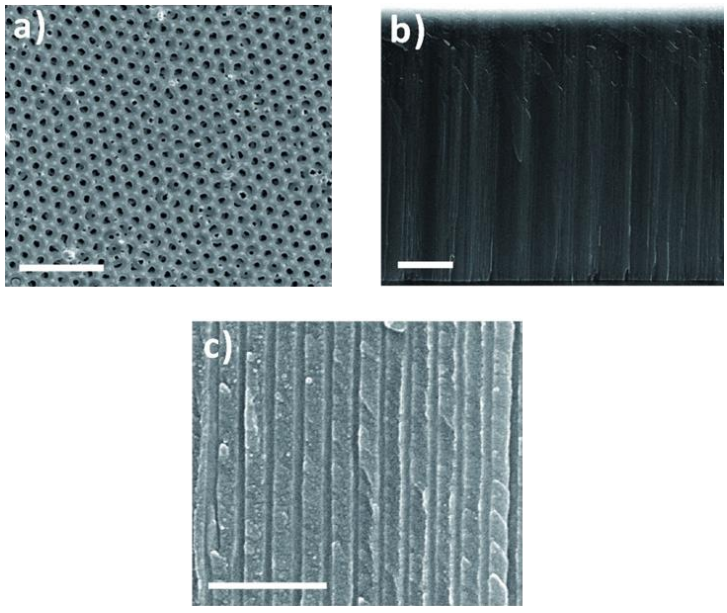

Fig 7.4. Structural characterization of NAA. (a) Top view FEG-SEM image of a representative NAA (scale bar = 500 nm). (b) Full-view cross-sectional FEG-SEM image of a NAA with thicknesses 50 ± 1 mm, (scale bar = 100 mm). (c) Magnified view cross-sectional FEG-SEM showing details of the nanopore s (scale bar = 100 nm).

7.3.2 Optical Characterization of MS–NAA–PCs.

MS–NAA–PCs can be optically described as heterogeneous PC structures with a spectroscopic signature that results from the multiple contributions of the NAA-based gradient-index filters composing their structure (i.e., NAA–PC–A, NAA–PC–B and NAA–PC–C). As such, the reflection spectrum of MS–NAA–PCs features three well-resolved, intense PSBs, the features of which are critically determined by the structural features of each NAA gradient-index filter engineered by the input current density profile.

The light-filtering layer on the top side of MS–NAA–PCs filters the photon-stimulated PL emission from the light-emitting layer at the bottom side of the MS–NAA–PC structure. Therefore, it is critical to characterize and understand the angle-dependence of both light reflection and light emission at the light-filtering and light-emitting layers of the MS–NAA–PC structure, respectively.

7.3.3 Effect of the Incidence Angle in the PSBs of MS–NAA–PCs

The effect of the incidence angle (θ) on the optical features of the PSBs of MS–NAA–PCs was systematically evaluated by reflection spectroscopy (**Figure 7.5a**). **Figure 7.5b** shows the reflection spectra of MS–NAA–PCs at different incidence angles (i.e., 8°, 10°, 15° 20°, 25°, 30°, 35°, 40°, 45°, 50°, 55°, 60° and 65°). **Table 7.2** summarizes the optical features of the three characteristic PSBs of NAA–PC–A, NAA–PC–B, and NAA–PC–C labelled as PSB_1, PSB_2, and PSB_3, including the central wavelength position (λ_{PSB}), reflection intensity (R_{PSB}), and full width at half maximum ($FWHM_{PSB}$), all estimated from Gaussian fittings.

The position of the three PSBs in the reflection spectrum of MS–NAA–PCs blue-shifts, while their intensity decreases with increasing angle of incidence. This result is in good agreement with the Bragg–Snell law, in which the wavelength of the diffracted light depends on the angle of incidence, the periodicity, and the effective refractive index[61-63] of the nanoporous PC as expressed in Equation 7.2:

$$m\lambda_{PSB} = 2L_{TP}\sqrt{n_{eff}^2 - sin^2\theta} \qquad (7.2)$$

where λ_{PSB} is the central wavelength of the PSB, m is the order of the PSB, L_{TP} is the structure periodicity, θ is the angle of incidence, and n_{eff} is the effective refractive index. Analysis of this dependence, summarized in **Figure 7.5c**, shows that λ_{PSB} is blue shifted at rates of −1.22 ± 0.04, −1.49 ± 0.05, and −1.78 ± 0.06 nm deg^{-1} for PSB_1, PSB_2 and PSB_3, respectively.

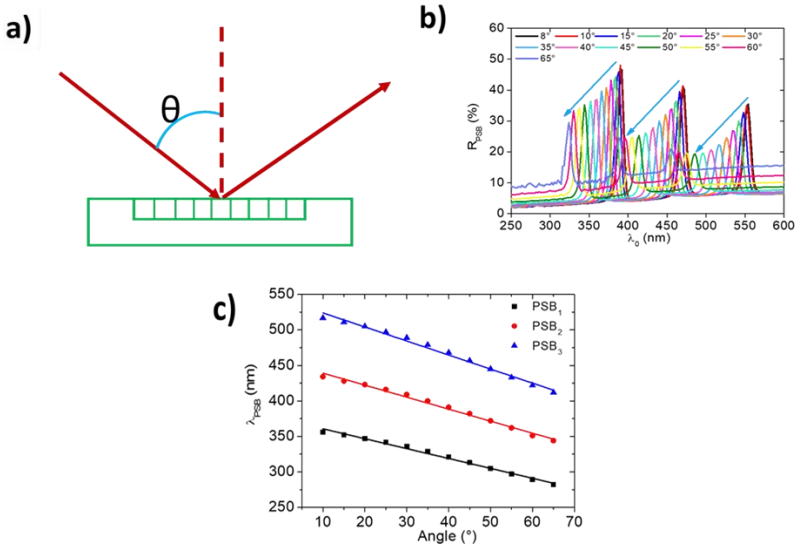

Figure. 7.5. Effect of the incidence angle on the optical features of the PSBs of MS–NAA–PCs. (a) Schematic showing the variation of the incidence angle. (b) Reflection spectra of a representative MS–NAA–PC as a function of angle of incidence, from θ = 8° to 65°. (c) Central wavelength position of MS–NAA–PC's PSB_1, PSB_2 and PSB_3 (λ_{PSB}) as a function of θ.

Table 7.2. Summary of optical features of MS–NAA–PCs.

Angle (°)	Band	λ_{band} (nm)	R_{band} (%)	FWHM (nm)
8	1	390	43.0	8.0
	2	470	35.0	9.5
	3	553	28.0	10
10	1	389	42.6	8.1
	2	469	35.0	9.4
	3	551	28.0	10.2
15	1	387	42.0	8.3
	2	466	33.0	9.8
	3	548	26.0	10.6
20	1	382	40.0	8.5
	2	461	31.0	9.9
	3	541	23.0	11.0
25	1	377	38.5	8.6
	2	455	28.5	10.1
	3	534	20.7	11.5
30	1	372	36.2	8.7
	2	448	26.2	10.3
	3	526	18.2	12.0
35	1	365	35.0	9.0
	2	440	24.1	10.5
	3	516	16.0	12.2
40	1	358	33.0	9.1
	2	431	22.0	10.7
	3	506	14.0	12.3
45	1	351	31.4	9.0
	2	422	20.0	10.6
	3	495	12.4	11.7
50	1	344	29.6	8.8
	2	413	18.2	10.0
	3	485	11.6	10.6
55	1	336	28.0	8.3
	2	404	17.0	9.7
	3	474	10.5	10.5
60	1	329	25.0	8.0
	2	396	15.0	8.9
	3	464	9.0	10.3
65	1	323	19.0	7.8
	2	388	12.5	8.9
	3	455	7.0	9.5

Figure 7.6 shows the dependence of R_{PSB} and $FWHM_{PSB}$ as a function of incidence angle, which indicates that the reflection intensity of the PSB decreases with increasing angle of incidence. Analysis of the fitting lines shown in **Figure 7.6a** denotes that R_{PSB} decreases at rates of –0.37 ± 0.02, –0.39 ± 0.007, –0.38 ± 0.016 a.u. deg^{-1} for PSB_1, PSB_2, and PSB_3, respectively.

It is apparent from **Figure 7.6b** that the dependence of $FWHM_{PSB}$ with angle of incidence follows a Gaussian-like trend, where this optical feature increases until 40° and dramatically decreases > 45° until 65°. Trends for $FWHM_{PSB}$'s PSB_1, PSB_2, and PSB_3, were determined to be:

a) $FWHM_1 = 7.53 + ((64.63)/(34.64 \cdot p/2)) \cdot Exp(-2 \cdot (\theta - 36.59/(34.65))$

b) $FWHM_2 = -4.74 + ((2363.2)/(123.63 \cdot p/2)) \cdot Exp(-2 \cdot (\theta - 33.84/(123.63))$

c) $FWHM_3 = 9.19 + ((125.62)/(33.0 \cdot p/2)) \cdot Exp(-2 \cdot (\theta - 35.92/(33.0))$

from Gaussian fittings, respectively.

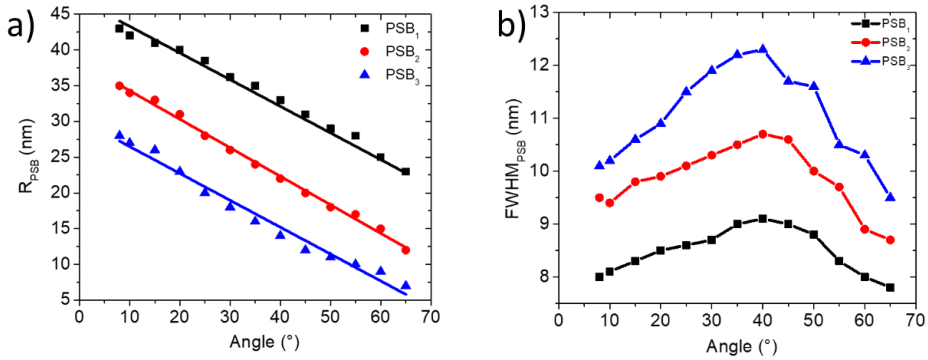

Figure 7.6. Effect of the angle of incidence on the PSB's features of MS–NAA–PCs. **(**a) Reflection intensity of PSB (R_{PSB}) as functions of ϑ. (b) Full width at half-maximum of PSB ($FWHM_{PSB}$) as functions of ϑ.

7.3.4 Effect of the Incidence Angle in the PL of the Light-Emitting Layer in MS–NAA–PCs

Photoluminescence of NAA is attributable to oxygen vacancies distributed across the onion-like composition of anodic alumina, and oxalic impurities incorporated into its structure from the acid electrolyte during the anodization process. Of all types, NAA produced in oxalic acid electrolyte has the highest PL emission.[49-51] Conversely, the characteristic PL emission from NAA produced in sulfuric acid electrolyte is weak and almost negligible by comparison. For this reason, we devised the structure of MS–NAA–PCs featuring a top light-filtering layer having an almost negligible PL emission and a bottom light-emitting layer with strong PL emission. **Figure 7.7a** shows a schematic illustration of the experimental setup used to characterize PL emissions from MS–NAA–PCs.

Figure 7.7b shows the characteristic PL emission at different angles of incidence (from 15° to 85° with an interval of 10°) from a representative 50 µm-thick NAA film fabricated by two-step anodization in oxalic acid electrolyte. The emission spectrum of the NAA film is characterized by a broad, intense Gaussian-like emission band across the 380–600 nm range for all the angles of incidence analyzed. It is apparent from **Figure 7.7c** that the position of the PL band (λ_{PL}) is shifted toward longer wavelengths (i.e., red shift) with increasing angle of incidence, following a sigmoidal trend where λ_{PL} = 475.04 + (445.8—475.04)/1 + Exp (θ–51.67/ 8.82). This graph indicates a slight red shift of λ_{PL} with θ, from 445 nm at 15° to 448 nm at 35°. However, λ_{PL} undergoes a significant shift between 35° and 75°, in which λ_{PL} red-shifts its position from 448 nm to 479 nm, respectively, and it stabilizes its position for θ > 75°.

Figure 7.7d shows the dependence of $FWHM_{PL}$ with the angle of incidence. It is apparent that $FWHM_{PL}$ follows a Gaussian-like trend with θ, where this optical feature initially increases with angle of incidence until 45°. At this angle, $FWHM_{PL}$ achieves its maximum value of 115 ± 1 nm. For θ > 45°, $FWHM_{PL}$ starts to decrease until a minimum of 98 ± 2 nm at an angle of 85°. **Table 7.3** summarizes the dependence of λ_{PL} and $FWHM_{PL}$ with the angle of incidence for a representative light-emitting NAA film produced in oxalic acid electrolyte.

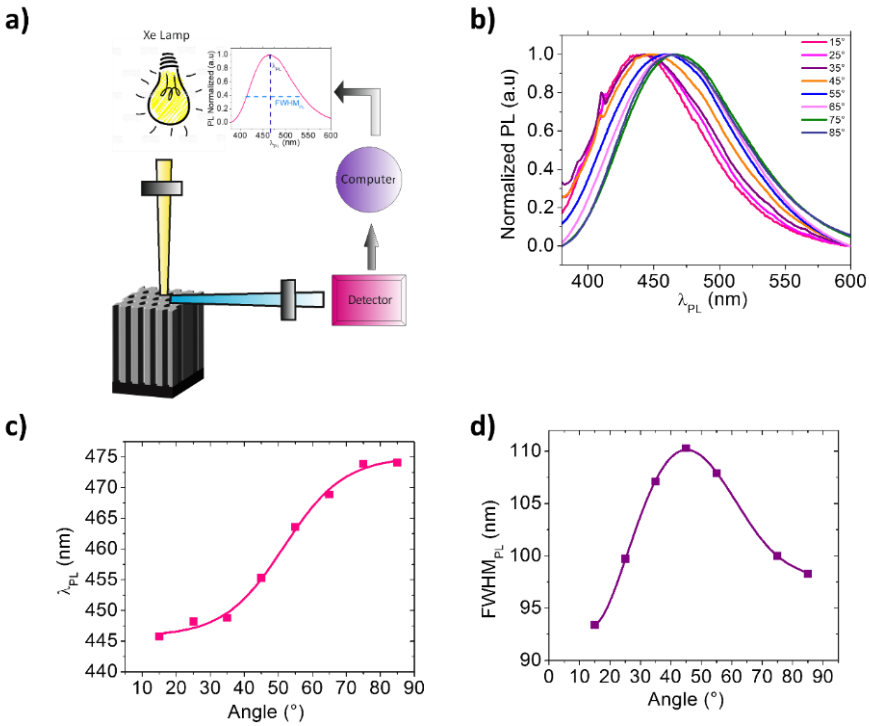

Figure 7.7. Photoluminescent emission from NAA films. (a) Schematic illustration of the PL setup used to characterize PL emission from MS–NAA–PCs and NAA–Ox films. (b) Characteristic Gaussian-like PL emission at varying the angle of incidence, from 15° to 85°, from a reference NAA–Ox film fabricated in oxalic acid electrolyte by two step anodization (NB: λ_{ex} = 350 nm). (c) Dependence of central wavelength position of PL emission (λ_{PL}) with angle of incidence. (d) Dependence of full width at half maximum of PL emission ($FWHM_{PL}$) with angle of incidence.

Table 7.3. Photoluminescence wavelength of NAA–Ox light-emitting layer produced in oxalic acid at different angles.

Angle (°)	PL wavelength (nm)	FWHM (nm)
15	445	93
25	448	100
35	448	107
45	455	110
55	464	108
65	469	105
75	474	100
85	474	98

7.3.5 Photoluminescence of MS–NAA–PCs.

MS–NAA–PCs were fabricated to feature three well-resolved PSBs as specific spectral positions within the PL emission of NAA–Ox films. To this end, the structure of MS–NAA–PCs was judiciously engineered with three stacked gradient-index filters embedded within the same heterogeneous PC structure. These heterogeneous NAA-based PCs were used as model platforms to study for the first time the light-filtering properties of NAA–PCs, harnessing the intrinsic light-emitting properties of NAA. MS–NAA–PCs were mounted on a rotating stage, which allows PL signal to be measured at different angles. Excitation light at 355 nm was shone onto the center of MS–NAA–PCs and the emission was collected from 380 to 600 nm at varying angle of incidence. **Figure 7.8** shows the PL emission of a reference NAA–Ox film (black line), and the reflection (red line) spectrum, and PL emission (blue line) of a MS–NAA–PCs at varying angle of incidence (i.e., 65°, 70°, 75°, and 80° for PL, and

complementary reflection angles of 25°, 20°, 15°, and 10° for reflection, respectively). It is apparent that the generation of three gradient-index filters on top of the light-emitting NAA–Ox layer filters efficiently PL emission by narrowing $FWHM_{PL}$ and shifting λ_{PL} following an angle-dependent pattern. $FWHM_{PL}$ of the PL emission of the NAA–Ox film at 80°, 75°, 70°, and 65° was measured to be 99 ± 2, 100 ± 2, 103 ± 1, and 105 ± 1 nm, respectively **(Figures 7.8a–d)**. Upon the generation of a MS–NAA–PCs, $FWHM_{PL}$ is narrowed to 93 ± 2, 88 ± 2, 97 ± 3, and 88 ± 6 nm at 80°, 75°, 70°, and 65°, respectively. This result indicates that light emission is filtered by the top gradient-index filters. It is also found that λ_{PL} red-shifts its position with decreasing angle of incidence, having values of 443 ± 1, 447 ± 1, 451 ± 1, and 450 ± 1 nm at 80°, 75°, 70°, and 65°, respectively **(Figures 7.8a–d).**

For instance, the PL emission of MS–NAA–PCs at 80° (**Figure 7.8a**) shows two local minima or shoulders at 402 and 473 nm, which would correspond to light-emitting inhibition associated with PSB_1 (389 nm) and PSB_2 (461 nm), respectively. At that angle of incidence, PSB_3 (551 nm) is far from the main Gaussian-like PL emission. Therefore, it is inferred that this gradient-index filter does not contribute to the filtered PL emission from the MS–NAA–PC structure within this spectral region. Upon reduction of the angle of incidence, the characteristic PBSs of the MS–NAA–PC structure undergo a blue shift, which in turn changes the characteristics of the light beam emitted from the underlying NAA film. **Figure 7.8b** shows that the local minima of the PL emission from MS–NAA–PCs at 75° features two local minima at 412 and 486 nm, which would correspond

to light-emitting inhibition associated with PSB_1 (387 nm) and PSB_2 (466 nm), respectively. At that angle of incidence, PSB_3 is located at 548 nm, which is still far from the spectral position of the PL emission and does not contribute significantly to filtering.

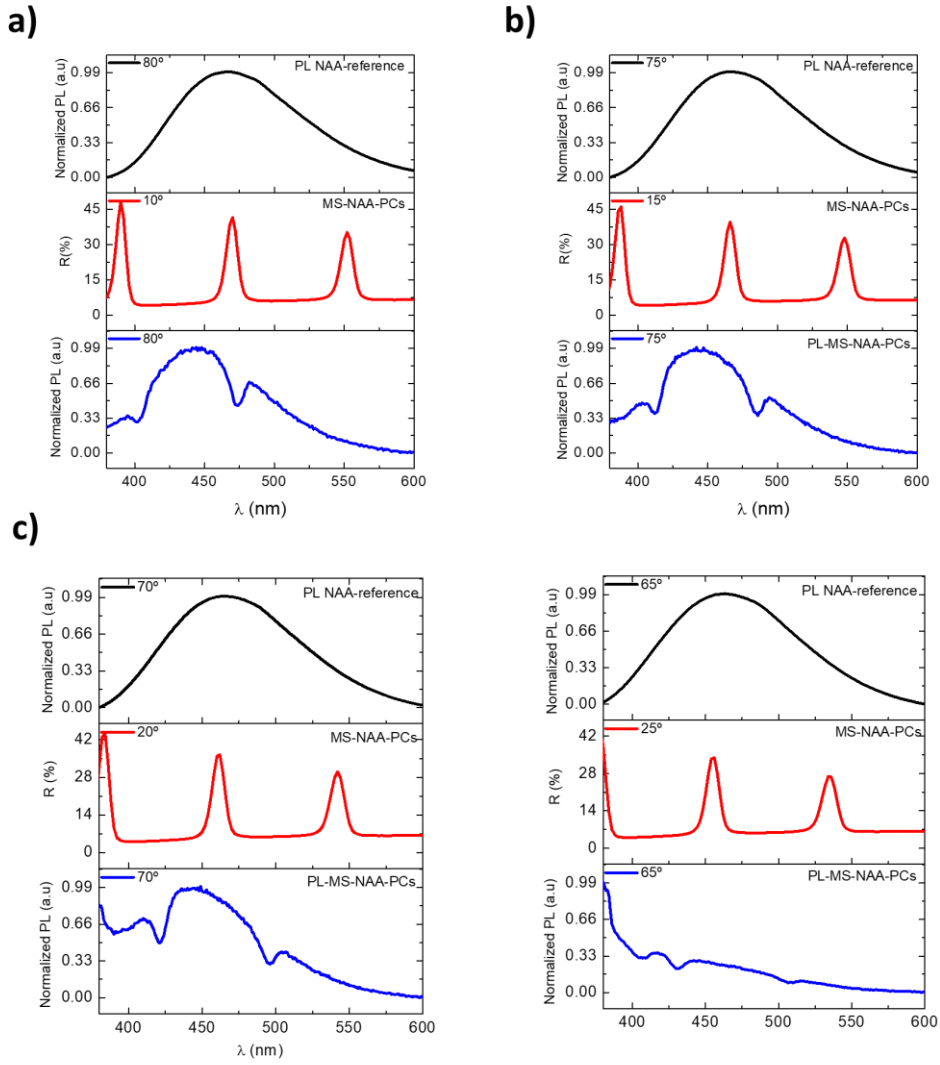

Figure 7.8. Photoluminescence emission of MS–NAA–PC with PL spectra of NAA of oxalic acid as a reference (black line), reflection spectra of MS–NAA–PC (red line), and PL spectra of MS–NAA–PC (blue line) at: (a) 10° (reflection) and 80° (PL emission), (b) 15° (reflection) and 75° (PL emission), (c) 20° (reflection) and 70° (PL emission), and (d) 25° (reflection) and 65° (PL emission) (NB: angles of reflection and emission were complementary at 25° – $\theta_{reflection} + \theta_{emission} = 90$ °).

Figure 7.8c shows that the local minima of the PL emission of MS–NAA–PCs at 70° features two local minima at 421 and 497 nm, which would correspond to light-emitting inhibition associated with PSB_1 (382 nm) and PSB_2 (466 nm), respectively. At that angle of incidence, PSB_3 is located at 541 nm, which is still far from the spectral position of the PL emission and does not contribute significantly to filtering. **Figure 7.8d** shows that the local minima of the PL emission of MS–NAA–PCs at 65 ° features two local minima at 430 and 507 nm, which would correspond to light-emitting inhibition associated with PSB_1 (377 nm) and PSB_2 (455 nm), respectively. At that angle of incidence, PSB_3 is located at 541 nm, which is still far from the spectral position of the PL emission and does not contribute significantly to PL emission filtering.

To gain further insight into the light-filtering properties of MS–NAA–PCs and the dependence of PL emission, we analyzed the optical features of PL emission at distinct angle of incidence. At first glance, **Figure 7.9a** reveals an interesting effect where light emitted from the underlying photoluminescent layer is narrowed and shifted with the angle of incidence. **Figures 7.9b and c** summarize the positions of the characteristic PSB_1, PSB_2, and PSB_3, and the features of the PL emission ($FWHM_{PL}$ and λ_{PL}) from MS–NAA–PCs. It is apparent that the position of PL emission (λ_{PL}) undergoes a slight red shift when the angle of incidence is increased from 65° to 70° (i.e., from 450 to 451 nm, respectively) **(Figure 7.9b**). After this point, the light-filtering layer of MS–NAA–PCs blue-shifts the position of the Gaussian-like PL emission from the light-emitting NAA–Ox layer at the bottom of the heterogenous NAA–PC structure. PL emission from 70° to 85° is found to blue shift linearly from 451 to 437 nm, at a rate of ~–0.93 nm deg^{-1}.

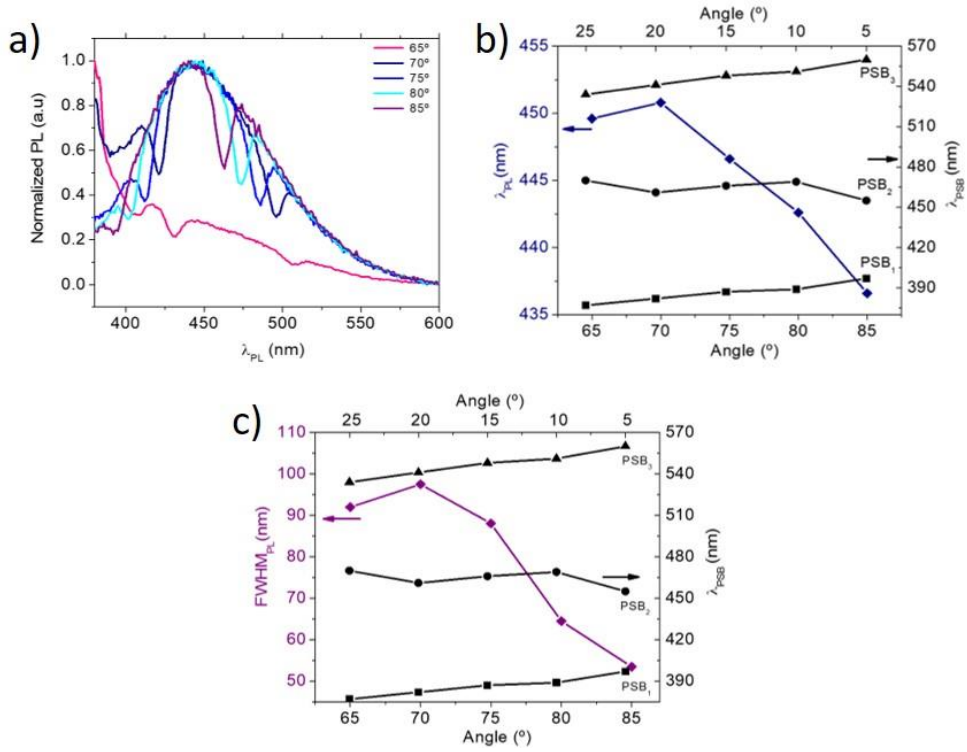

Figure 7.9. Summary of the position of the PSB_1, PSB_2 and PSB_3 and the features of PL emission from MS–NAA–PCs (NB: angles of reflection and emission were complementary at 25° – θ reflection + θ emission = 90°). (a) PL emission from MS–NAA–PCs at 65°, 70°, 75°, 80° and 85°. (b) Dependence of λ_{PL} and the position of the PSB_1, PSB_2 and PSB_3 in MS–NAA–PCs with angle of incidence. (c) Dependence of $FWHM_{PL}$ and the position of the PSB_1, PSB_2 and PSB_3 in MS–NAA–PCs with angle of incidence.

Dependence of $FWHM_{PL}$ with angle of incidence is found to follow a qualitatively similar trend. Initially, PL emission is slightly widened, from 65° to 70°, where this optical feature increases from 92 to 97 nm, respectively (**Figure 7.9c**). However, the light-filtering layer of MS–NAA–PCs can efficiently narrow PL emission from 70° to 85°, where $FWHM_{PL}$ is found to be sharply and linearly narrowed from 97 to 54 nm, at a rate of ~–3.11 nm deg^{-1}. These results clearly demonstrate that a smart structural design of NAA–PCs can be judiciously harnessed to tune and control the features of the intrinsic photoluminescence emission of this highly tailorable platform material.

7.4 Conclusion

In this Chapter, we demonstrated the structural tuning of intrinsic photoluminescence emissions from nanoporous anodic alumina photonic crystals. We have harnessed a smart structural design in which a non-emitting, light-filtering layer in the form of multi-spectral NAA–PC is combined with an intrinsically light-emitting layer of NAA. MS–NAA–PCs feature three intense, well-resolved photonic stopbands, the positions of which can be spaced across the visible spectrum from ~380 to 560 nm. Judicious -emitting NAA layer. This approach makes it possible to engineering of three photonic stopbands in the top light-filtering layer has been demonstrated as an effective approach to narrow and tune photoluminescence emission from an underlying light narrow the width of photoluminescence emission up to ~50 nm, and blue-shift its position for ~15 nm. Inhibition of light emission is accomplished by harnessing forbidden light propagation through the characteristic photonic stopbands of the top light-filtering layer. MS–NAA–PCs enable control over intrinsic photoluminescence of NAA, without the use of external PL emitters such as dyes and fluorophores. These findings provide exciting new opportunities to engineer the intrinsic light-emitting properties of NAA-based photonic crystals structures, which have implications across a variety of photonic technologies such as sensing and biosensing, lasing and light sources, photodetection, photocatalysis, green energy generation and solar light harvesting.

REFERENCES

1. Parker Christie. Photoluminescence of Solutions with Applications to Photochemistry and Analitycal Chemistry. Nature 1968, 220, 1968.
2. Sun, X.; Xu, F.; Li, Z.; Zhang, W. Photoluminescence Properties of Anodic Alumina Membranes with Ordered Nanopore Arrays. *J. Lumin.* **2006**, *121* (2 SPEC. ISS.), 588.
3. Wang, H.; Ferrio, K.; Steel, D. G.; Hu, Y. Z.; Binder, R.; Koch, S. W. Transient Nonlinear Optical Response from Excitation Induced Dephasing in GaAs. Phys. Rev. Lett. 1993, 71 (8), 1261–1264
4. Shkunov, M. N.; Vardeny, Z. V.; DeLong, M. C.; Polson, R. C.; Zakhidov, A. A.; Baughman, R. H. Tunable, Gap-State Lasing in Switchable Directions for Opal Photonic Crystals. *Adv. Funct. Mater.* **2002**, *12* (1), 21–26.
5. Colvin, V.; Sclamp, M. C.; A.P Allvisatos. Light-Emitting Diodes Made from Cadmium Selenide Nanocrystals and a Semiconducting Polymer. *Lett. to Nat.* **1994**, *370*, 775.
6. Lim, J.; Jun, S.; Jang, E.; Baik, H.; Kim, H.; Cho, J. Preparation of Highly Luminescent Nanocrystals and Their Application to Light-Emitting Diodes. *Adv. Mater.* **2007**, *19* (15), 1927–1932.
7. Jaiswal, J. K.; Simon, S. M. Potentials and Pitfalls of Fluorescent Quantum Dots for Biological Imaging. *Trends Cell Biol.* **2004**, *14* (9), 497–504.
8. Chan, W. C. W.; Maxwell, D. J.; Gao, X.; Bailey, R. E.; Han, M.; Nie, S. Luminescent Quantum Dots for Multiplexed Biological Detection and Imaging. *Curr. Opin. Biotechnol.* **2002**, *13* (1), 40–46.
9. Zhang, Y.; Qiu, J.; Gao, M.; Li, P.; Gao, L.; Heng, L.; Tang, B. Z.; Jiang, L. A Visual Film Sensor Based on Silole-Infiltrated SiO2 Inverse Opal Photonic Crystal for Detecting Organic Vapors. *J. Mater. Chem. C* **2014**, *2* (42), 8865–8872.
10. Arsenault, A. C.; Clark, T. J.; Von Freymann, G.; Cademartiri, L.; Sapienza, R.; Bertolotti, J.; Vekris, E.; Wong, S.; Kitaev, V.; Manners, I.; et al. From Colour Fingerprinting to the Control of Photoluminescence in Elastic Photonic Crystals. *Nat. Mater.* **2006**, *5* (3), 179–184.

11. Aoki, K.; Guimard, D.; Nishioka, M.; Nomura, M.; Iwamoto, S.; Arakawa, Y. Coupling of Quantum-Dot Light Emission with a Three-Dimensional Photonic-Crystal Nanocavity. *Nat. Photonics* **2008**, *2* (11), 688–692.
12. Santos, A. Nanoporous Anodic Alumina Photonic Crystals: Fundamentals, Developments and Perspectives. J. Mater. Chem. C **2017**, 5 (23), 5581–5599.
13. Santos, A.; Law, C. S.; Pereira, T.; Losic, D. Nanoporous Hard Data: Optical Encoding of Information within Nanoporous Anodic Alumina Photonic Crystals. Nanoscale **2016**, 8 (15), 8091–8100.
14. Kumeria, T.; Santos, A.; Rahman, M. M.; Losic, D. Advanced Structural Engineering of Nanoporous Photonic Structures: Tailoring Nanopore Architecture to Enhance Sensing Properties. ACS Photonics **2014**, 1, 1298–1306.
15. Biallo, D.; D'Orazio, A.; De Sario, M.; Marrocco, V.; Petruzzelli, V.; Prudenzano, F. Photonic Crystal Sensors. In 2006 International Conference on Transparent Optical Networks; **2006**, 2, 44–48.
16. Macias, G.; Ferré-Borrull, J.; Pallarès, J.; Marsal, L. F. 1-D Nanoporous Anodic Alumina Rugate Filters by Means of Small Current Variations for Real-Time Sensing Applications. Nanoscale Res. Lett. **2014**, 9 (1), 315.
17. Law, C. S.; Lim, S. Y.; Abell, A. D.; Voelcker, N. H.; Santos, A. Nanoporous Anodic Alumina Photonic Crystals for Optical Chemo- and Biosensing: Fundamentals, Advances, and Perspectives. Nanomaterials **2018**, 8 (10), 1–47.
18. A. Santos, T. Pereira, C. S. Law and D. Losic, *Nanoscale*, **2016**, **8**, 14846–14857.
19. Chen, S. W.; Lu, T. C.; Hou, Y. J.; Liu, T. C.; Kuo, H. C.; Wang, S. C. Lasing Characteristics at Different Band Edges in GaN Photonic Crystal Surface Emitting Lasers. Appl. Phys. Lett. 2010, 96 (7), **2008**.
20. Fu, Y.; Zhai, T. Distributed Feedback Organic Lasing in Photonic Crystals. Front. Optoelectron. **2019**, 1–17.
21. Notomi, M.; Suzuki, H.; Tamamura, T. Directional Lasing Oscillation of Two-Dimensional Organic Photonic Crystal Lasers at Several Photonic Band Gaps. Appl. Phys. Lett. **2001**, 78 (10), 1325–1327.

22. Azzini, S.; Gerace, D.; Galli, M.; Sagnes, I.; Braive, R.; Lemaître, A.; Bloch, J.; Bajoni, D. Ultra-Low Threshold Polariton Lasing in Photonic Crystal Cavities. Appl. Phys. Lett. **2011**, 99 (11), 29–32.
23. Yang, W.; Wang, B.; Sun, A.; Liu, J.; Xu, G. Lasing from Dye-Loaded Periodic Anodic Alumina Nanostructure. Mater. Lett. **2016**, 178, 197–200.
24. Masuda, H.; Yamada, M.; Matsumoto, F.; Yokoyama, S.; Mashiko, S.; Nakao, M.; Nishio, K. Lasing from Two-Dimensional Photonic Crystals Using Anodic Porous Alumina. Adv. Mater. **2010**, 2492 (18), 213–216.
25. Lim, S. Y.; Law, C. S.; Markovic, M.; Kirby, J. K.; Abell, A. D.; Santos, A. Engineering the Slow Photon Effect in Photoactive Nanoporous Anodic Alumina Gradient-Index Filters for Photocatalysis. ACS Appl. Mater. Interfaces **2018**, 10 (28), 24124–24136.
26. Liu, L.; Lim, S. Y.; Law, C. S.; Jin, B.; Abell, A. D.; Ni, G.; Santos, A. Light-Confining Semiconductor Nanoporous Anodic Alumina Optical Microcavities for Photocatalysis. J. Mater. Chem. A **2019**, 7 (39), 22514–22529. https://doi.org/10.1039/c9ta08585h.
27. Barth, M.; Gruber, A.; Cichos, F. Spectral and Angular Redistribution of Photoluminescence near a Photonic Stop Band. *Phys. Rev. B - Condens. Matter Mater. Phys.* **2005**, *72* (8), 1–10.
28. Schroden, R. C.; Al-Daous, M.; Stein, A. Self-Modification of Spontaneous Emission by Inverse Opal Silica Photonic Crystals. *Chem. Mater.* **2001**, *13* (9), 2945–2950.
29. Masuda, Hideki and Fukuda, K. Ordered Metal Nanohole Arrays Made by Two-Step Replication of Honeycomb Structures of Anodic Alumina. *Science (80),* **1995**, *268* (3), 1466–1468.
30. Ferré-Borrull, J.; Pallarès, J.; Macías, G.; Marsal, L. F. Nanostructural Engineering of Nanoporous Anodic Alumina for Biosensing Applications. *Materials (Basel).* **2014**, *7* (7), 5225–5253.
31. Lee, W.; Kim, J. C. Highly Ordered Porous Alumina with Tailor-Made Pore Structures Fabricated by Pulse Anodization. *Nanotechnology* **2010**, *21* (48), 1–8.

32. Pashchanka, M.; Schneider, J. J. Self-Ordering Regimes of Porous Anodic Alumina Layers Formed in Highly Diluted Sulfuric Acid Electrolytes. *J. Phys. Chem. C* **2016**, *120* (27), 14590–14596.
33. Hernández-Eguía, L. P.; Ferré-Borrull, J.; Macias, G.; Pallarès, J.; Marsal, L. F. Engineering Optical Properties of Gold-Coated Nanoporous Anodic Alumina for Biosensing. *Nanoscale Res. Lett.* **2014**, *9* (1), 414.
34. Sulka, G. D. *Highly Ordered Anodic Porous Alumina Formation by Self-Organized Anodizing*, 1st ed.; Eftekhari, A., Ed.; Wiley-VCH Verlag GmbH & Co.: Weinheim, **2008**.
35. Shingubara, S. Fabrication of Nanomaterials Using Porous Alumina Templates. *J. Nanoparticle Res.* **2003**, *5* (i), 17–30.
36. Marsal, L. F.; Vojkuvka, L.; Formentin, P.; Pallarés, J.; Ferré-Borrull, J. Fabrication and Optical Characterization of Nanoporous Alumina Films Annealed at Different Temperatures. *Opt. Mater. (Amst).* **2009**, *31* (6), 860–864.
37. Sun, X.; Xu, F.; Li, Z.; Zhang, W. Photoluminescence Properties of Anodic Alumina Membranes with Ordered Nanopore Arrays. *J. Lumin.* **2006**, *121* (2 SPEC. ISS.), 588–594.
38. Huang, G. S.; Wu, X. L.; Mei, Y. F.; Shao, X. F.; Siu, G. G. Strong Blue Emission from Anodic Alumina Membranes with Ordered Nanopore Array. J. Appl. Phys. **2003**, 93 (1), 582–585.
39. Huang, G. S.; Wu, X. L.; Yang, L. W.; Shao, X. F.; Siu, G. G.; Chu, P. K. Dependence of Blue-Emitting Property on Nanopore Geometrical Structure in Al-Based Porous Anodic Alumina Membranes. Appl. Phys. A Mater. Sci. Process. **2005**, 81 (7), 1345–1349.
40. Mukhurov, N. I.; Zhvavyi, S. P.; Gasenkova, I. V.; Terekhov, S. N.; Pershukevich, P. P.; Orlovich, V. A. Photoluminescence of F-Centres in Films of Anodic Alumina. *J. Appl. Spectrosc.* **2010**, *77* (4), 591–597.
41. Du, Y.; Cai, W. L.; Mo, C. M.; Chen, J.; Zhang, L. D.; Zhu, X. G. Preparation and Photoluminescence of Alumina Membranes with Ordered Pore Arrays. *Appl. Phys. Lett.* **1999**, *74* (20), 2951–2953.

42. Rauf, A.; Mehmood, M.; Ahmed, M.; ul Hasan, M.; Aslam, M. Effects of Ordering Quality of the Pores on the Photoluminescence of Porous Anodic Alumina Prepared in Oxalic Acid. *J. Lumin.* **2010**, *130* (5), 792–800.
43. Huang, G. S.; Wu, X. L.; Siu, G. G.; Chu, P. K. On the Origin of Light Emission from Porous Anodic Alumina Formed in Sulfuric Acid. *Solid State Commun.* **2006**, *137* (11), 621–624.
44. Nourmohammadi, A.; Asadabadi, S. J.; Yousefi, M. H.; Ghasemzadeh, M. Photoluminescence Emission of Nanoporous Anodic Aluminum Oxide Films Prepared in Phosphoric Acid. *Nanoscale Res. Lett.* **2012**, *7* (1), 1–7.
45. Vrublevsky, I.; Chernyakova, K.; Ispas, A.; Bund, A.; Gaponik, N.; Dubavik, A. Photoluminescence Properties of Heat-Treated Porous Alumina Films Formed in Oxalic Acid. *J. Lumin.* **2011**, *131* (5), 938–942.
46. Yi-fan Liu, Ya-fang Tu, Sheng-you Huang Zou, Jian-ping Sang, Xian-wu Effect of Etch-Treatment upon the Intensity and Peak Position of Photoluminescence Spectra for Anodic Alumina Films with Ordered Nanopore Array. *J. Mater. Sci. Mater. Electron.* **2009**, *44*, 3370–3375.
47. Santos, A.; Alba, M.; Rahman, M. M.; Formentin, P.; Ferre-Borrull, J.; Pallares, J.; Marsal, L. F. Structural Tuning of Photoluminescence in Nanoporous Anodic Alumina by Hard Anodization in Oxalic and Malonic Acids. *Nanoscale Res. Lett.* **2012**, *7* (1), 1.
48. Reddy, P. R. Morphological Analysis and Photoluminescence Properties of Hydrophilic Porous Anodic Alumina Formed in Oxalic Acid. *J. Mater. Sci. Mater. Electron.* **2016**, *27* (5), 5331–5344.
49. Vrublevsky, I.; Chernyakova, K.; Ispas, A.; Bund, A.; Gaponik, N.; Dubavik, A. Photoluminescence Properties of Heat-Treated Porous Alumina Films Formed in Oxalic Acid. *J. Lumin.* **2011**, *131* (5), 938–942.
50. Stępniowski, W. J.; Nowak-Stępniowska, A.; Bojar, Z. Quantitative Arrangement Analysis of Anodic Alumina Formed by Short Anodizations in Oxalic Acid. *Mater. Charact.* **2013**, *78*.

51. Huang, G. S.; Wu, X. L.; Xie, Y.; Shao, X. F.; Wang, S. H. Light Emission from Silicon-Based Porous Anodic Alumina Formed in 0.5 M Oxalic Acid. *J. Appl. Phys.* **2003**, *94* (4), 2407–2410.
52. Rauf, A.; Mehmood, M.; Ahmed, M.; ul Hasan, M.; Aslam, M. Effects of Ordering Quality of the Pores on the Photoluminescence of Porous Anodic Alumina Prepared in Oxalic Acid. *J. Lumin.* **2010**, *130* (5), 792–800.
53. Santos, A.; Ferré-Borrull, J.; Pallarès, J.; Marsal, L. F. Hierarchical Nanoporous Anodic Alumina Templates by Asymmetric Two-Step Anodization. *Phys. Status Solidi Appl. Mater. Sci.* **2011**, *208* (3), 668–674.
54. Santos, A.; Formentín, P.; Ferré-Borrull, J.; Pallarès, J.; Marsal, L. F. Nanoporous Anodic Alumina Obtained without Protective Oxide Layer by Hard Anodization. *Mater. Lett.* **2012**, *67* (1), 296–299.
55. Santos, A.; Montero-Moreno, J. M.; Bachmann, J.; Nielsch, K.; Formentín, P.; Ferré-Borrull, J.; Pallarès, J.; Marsal, L. F. Understanding Pore Rearrangement during Mild to Hard Transition in Bilayered Porous Anodic Alumina Membranes. *ACS Appl. Mater. Interfaces* **2011**, *3* (6), 1925–1932.
56. Santos, A.; Vojkuvka, L.; Alba, M.; Balderrama, V. S.; Ferré-Borrull, J.; Pallarès, J.; Marsal, L. F. Understanding and Morphology Control of Pore Modulations in Nanoporous Anodic Alumina by Discontinuous Anodization. *Phys. Status Solidi Appl. Mater. Sci.* **2012**, *209* (10), 2045–2048.
57. Hauke, N.; Zabel, T.; Muller, K.; Kaniber, M.; Laucht, A.; Bougeard, D.; Abstreiter, G.; Finley, J. J.; and; Arakawa, Y. Enhanced Photoluminescence Emission from Two- Dimensional Silicon Photonic Crystal Nanocavities. *New J. Phys.* **2010**, *12*, 1–8.
58. Bayindir, M.; Tanriseven, S.; Aydinli, A.; Ozbay, E. Rapid Communication Strong Enhancement of Spontaneous Emission in Amorphous-Silicon-Nitride Photonic Crystal Based Coupled-Microcavity Structures. *Appl. Phys. A Mater. Sci. Process.* **2001**, *127*, 125–127.
59. Acosta, L. K.; Bertó-Roselló, F.; Xifre-Perez, E.; Santos, A.; Ferré-Borrull, J.; Marsal, L. F. Stacked Nanoporous Anodic Alumina Gradient-Index Filters with

Tunable Multispectral Photonic Stopbands as Sensing Platforms. *ACS Appl. Mater. Interfaces* **2019**, *11* (3), 3360–3371.

60. Schneider, C. A.; Rasband, W. S.; Eliceiri, K. W. NIH Image to ImageJ: 25 Years of Image Analysis. *Nat. Methods* **2012**, *9* (7), 671–675.
61. Nemtsev, I. V.; Tambasov, I. A.; Ivanenko, A. A.; Zyryanov, V. Y. Angle-Resolved Reflection Spectroscopy of High-Quality PMMA Opal Crystal. *Photonics Nanostructures - Fundam. Appl.* **2018**, *28*, 37–44.
62. Acosta, L. K.; Berto, F.; Xifre-perez, E.; Law, C. S.; Santos, A.; Ferre, J.; Marsal, L. F. Tunable Nanoporous Anodic Alumina Photonic Crystals by Gaussian Pulse Anodization. **2020**.
63. Mayonado, G.; Mian, S. M.; Robbiano, V.; Cacialli, F. Investigation of The Bragg-Snell Law In Photonic Crystals. **2015**, 60–63.

Chapter 8. Summary and Conclusion

UNIVERSITAT ROVIRA I VIRGILI
ENGINEERING OF PHOTONIC STRUCTURES BASED ON NANOPOROUS ANODIC ALUMINA AS AN OPTICAL SENSING PLATFORM
Laura Karen Acosta Capilla

During the development of this thesis, the engineering of Photonic structures based on Nanoporous Anodic Alumina was explored. Furthermore, different photonic structures were fabricated and used as optical sensor with different analytes such as: D-Glucose, alcohols mixtures and sodium chloride.

In **chapter 2** we presented the state of the art of NAA. In this chapter we presented a summary of the historical background of NAA. The NAA structure, fabrication, anodization techniques as well as the anodization parameters and geometrical characteristics.

In **Chapter 3** we presented the fundamentals of Photonic Structures Based on Nanoporous anodic alumina. The background of this structures was explored. In addition, the different anodization approaches to obtain the most important photonic structures such as: Fabry Pérot interferometers (FPI), Gradient index Filters (GIFs), Distributed Bragg Reflectors (DBRs), microcavities (μCVs), multispectral photonic structures and Bandpass filters (BPFs). Moreover, the potential applications of these structures were presented like optical sensors, Photocatalysis, Drug Delivery and Optical encoding.

In **Chapter 4** we presented the development and optical engineering of stacked nanoporous anodic alumina photonic structures with multispectral bands. (NAA-MPSs) with tunable multi-spectral photonic stopbands for sensing applications. The structure of these photonic crystal (PC) is formed by stacked layers of NAA produced with sinusoidally modified effective medium. The progressive modification of the sinusoidal period during the anodization process enables the generation and precise tuning of the characteristic photonic stopbands. The position of the

forbidden bands presented by these multi-spectral NAA-MPSs can be accurately tuned by varying the anodization period of the anodization current density waveform. Furthermore, we assess the effect of the porosity of the structure on the reflection spectrum by applying a pore widening chemical etching treatment from 0 to 25 min. We also demonstrated the ability of multi-spectral NAA-MPSs structures for sensing applications by detecting small changes of the effective refractive index due to the fluid filling of the pores. Different concentrations of D-glucose have been successfully detected and quantified in real-time. These real-time experiments, carried out by increasing the average pore diameter from 35 nm to 55 nm, indicate that the sensitivity is different for each forbidden band and also it depends on the pore diameter of the multi-spectral NAA-MPS structure: the increment of the pore diameter leads to an enhancement in sensitivity of the photonic crystal structure.

In **Chapter 5** we present a Gaussian pulse anodization approach to generate nanoporous photonic crystals with highly tunable and controllable optical properties across the visible–NIR spectrum. Nanoporous anodic alumina Gaussian photonic crystals (NAA-GPSs) are fabricated in oxalic acid electrolyte by Gaussian pulse anodization a novel form of pulse-like anodization. We evaluate the effect of the Gaussian pulse width in the anodization profile on the optical properties of these photonic crystals by systematically varying this fabrication parameter from 5 to 60 s. The optical features of the characteristic photonic stopband (PSB) of NAA-GPSs position of central wavelength, full width at half maximum and intensity are found to be highly dependent on the Gaussian pulse width, the incidence angle of incoming photons and the nanopore diameter of NAA-GPSs. The effective medium of NAA-GPSs was

assessed by monitoring spectral shifts in their characteristic PSB upon infiltration of their nanoporous structure with analytical solutions of D-glucose of varying concentration (0.0125–1 M). The findings demonstrate that Gaussian pulse anodization is an effective nanofabrication approach to produce highly sensitive NAA-based PC structures with versatile and tunable PSBs across the spectral regions.

In **Chapter 6** Nanoporous anodic alumina optical microcavities (NAA–μQVs) with spectrally tunable resonance band and surface chemistry were used as model light-confining photonic crystal (PC) platforms to elucidate the combined effect of spectral light confinement features and surface chemistry on optical sensitivity nm–1 in water- and organic-based analytical solutions, respectively. The nanoporous architecture of NAA–μQVs featuring two distributed Bragg mirrors with a physical cavity layer in between was engineered by stepwise pulse anodization. Model NAA–μQVs showed well-resolved, spectrally tunable resonance bands ~400 to 800 nm by careful modification of the anodization period in the input STPA profile NAA–μQVs was assessed by analyzing dynamic spectral shifts of NAA–μQVs' resonance band upon infiltration with organic- and aqueous-based analytical solutions of equally varying refractive index, from 1.333 to 1.345 RIU. The findings demonstrated that optical sensitivity of both hydrophilic and hydrophobic NAA–μQVs increases linearly with the position of their characteristic resonance, in both organic and aqueous solutions, due to increasing optical absorbance. Analysis of sensitivity also revealed that hydrophilic NAA–μQVs show ~81 and 35 % superior sensitivity to their hydrophobic counterparts for organic- and aqueous-based analytical solutions, respectively. This chapter provides a new avenue to explore the unique light-confining properties of NAA-based PC

structures for optical sensing applications. Precise design and engineering of structural, optical, and chemical properties of these PCs provide exciting new opportunities to harness distinct forms of light–matter interactions for a broad range of photonic technologies and sensing applications.

In **Chapter 7** We demonstrated the precise structural engineering and tuning of intrinsic photoluminescence emissions from nanoporous anodic alumina photonic crystals (NAA–PCs). A smart structural design by a combination of pulse and constant anodization in distinct acid electrolytes makes it possible to engineer a novel heterogenous optical structure consisting of a non-emitting, light-filtering layer in the form of multi-spectral NAA–PC, and an intrinsically light-emitting layer of NAA. MS–NAA–PCs are engineered to feature three intense, well-resolved photonic stopbands, the position of which are spaced across the visible spectrum, from ~380 to 560 nm. This approach makes it possible to engineering of three photonic stopbands in the top light-filtering layer has been demonstrated as an effective approach to narrow and tune photoluminescence emission from an underlying light narrow the width of photoluminescence emission up to ~50 nm, and blue-shift its position for ~15 nm. Inhibition of light emission is accomplished by harnessing forbidden light propagation through the characteristic photonic stopbands of the top light-filtering layer.

In summary, all the data and work presented in this thesis demonstrated the ability of the Photonic structures based on Nanoporous Anodic Alumina as a potential platform for develop optical sensors.